

Self-consistent simulation of multi-component plasma turbulence and neutral dynamics in the tokamak boundary

Présentée le 5 novembre 2021

Faculté des sciences de base
SPC - Théorie
Programme doctoral en physique

pour l'obtention du grade de Docteur ès Sciences

par

André CALADO COROADO

Acceptée sur proposition du jury

Prof. A. Pasquarello, président du jury
Prof. P. Ricci, directeur de thèse
Prof. J. J. Rasmussen, rapporteur
Prof. F. Militello, rapporteur
Prof. C. Theiler, rapporteur

Abstract

The interaction between neutral particles and the plasma plays a key role in determining the dynamics of the tokamak boundary that, in turn, significantly impact the overall performance of the device. Leveraging the work in Wersal and Ricci [Nucl. Fusion **55**, 123014 (2015)], the present thesis describes the development and implementation in the GBS code of a mass-conserving multi-component self-consistent model to simulate the interplay between neutrals and plasma in the tokamak boundary. The simulation results are shown to be a useful tool to disentangle the physics at play in the tokamak boundary, and in particular for the interpretation of gas puff imaging (GPI).

Developed in the last decade, the GBS code [Ricci *et al*, Plasma Phys. Control. Fusion **54**, 124047 (2012)] allows for self-consistent three-dimensional numerical simulations of the turbulent plasma and neutral dynamics in the tokamak boundary. In GBS, a set of Braginskii equations in the drift limit describes the plasma time evolution, and the neutrals are modelled by solving a kinetic equation using the method of characteristics. While GBS enables simulations in arbitrary magnetic configurations, here we focus on limited plasmas.

We first describe the geometrical operators and proper boundary conditions to ensure that mass conservation is satisfied. In comparison to the previous non-mass-conserving model of GBS, the mass-conserving simulations capture more accurately the sharp transition of the plasma and neutral quantities between the edge and scrape-off layer regions. In addition, we show that mass conserving simulations allow for reliable quantitative studies of particle fluxes in the tokamak boundary.

A multi-component model of the neutral-plasma interaction is then developed by extending the single-component model to the description of a deuterium plasma that includes electrons, D^+ ions, D atoms, D_2 molecules and D_2^+ ions. The molecular dynamics is introduced through a set of drift-reduced Braginskii equations for the D_2^+ species and considering a kinetic equation for D_2 molecules, in addition to the kinetic equation for D atoms, thus resulting in a coupled system of kinetic equations for the atomic and molecular neutral distribution functions. The first multi-component GBS simulations show that, in the relatively long mean-free-path, sheath limited conditions under consideration, most of the D_2 molecules cross the last closed flux surface (LCFS) and are dissociated or ionized in the edge region, thus giving rise to sources of D atoms inside the LCFS. This leads to an inward radial shift of the peak of the plasma source due to ionization of D atoms with respect to the single-component simulations.

The multi-component model is applied to the simulation of GPI diagnostics, where the presence of a molecular gas puff is simulated self-consistently with the plasma and neutral dy-

namics of the tokamak boundary. The injected molecules interact with the boundary plasma, resulting in the emission of light in the D_α wavelength that can be measured to infer the turbulent properties of the plasma. The simulated mechanisms underlying the light emission, which include the excitation of D atoms and dissociation of both D_2 and D_2^+ , provide a reliable tool for the interpretation of GPI experimental measurements. The impact of neutral fluctuations on the D_α emission rate is investigated, as well as the correlation between the D_α emission and the plasma and neutral quantities.

Key words:

plasma physics, controlled fusion, tokamak boundary, scrape-off layer, limited configuration, plasma turbulence, fluid simulations, drift-reduced Braginskii model, kinetic neutral dynamics, neutral-plasma interaction, mass conservation, molecular dynamics, multi-component plasma, gas puff imaging, molecular gas puff, neutral fluctuations

Riassunto

L'interazione tra particelle neutre e il plasma svolge un ruolo fondamentale nel determinare la dinamica al bordo di un tokamak. A sua volta, questa regione ha un impatto significativo sulle prestazioni della macchina. Partendo dal lavoro di Wersal e Ricci [Nucl. Fusion **55**, 123014 (2015)], la presente tesi descrive lo sviluppo e l'implementazione nel codice GBS di un modello a più specie, auto-consistente, che verifica la conservazione della massa, utilizzato per simulare l'interazione tra i neutri e il plasma al bordo di un tokamak. I risultati delle simulazioni si dimostrano uno strumento utile per districare i meccanismi fisici che hanno luogo al bordo di un tokamak, particolarmente per l'interpretazione del GPI, una diagnostica basata sull'iniezione di gas per visualizzare la dinamica del plasma.

Sviluppato nell'ultimo decennio, il codice GBS [Ricci *et al*, Plasma Phys. Cont. Fus. **54**, 124047 (2012)] permette simulazioni numeriche tridimensionali auto-consistenti del plasma e dei neutri. In GBS, un insieme di equazioni fluide nel limite di deriva descrive l'evoluzione temporale della dinamica torbolenta del plasma e i neutri sono modellati risolvendo la loro equazione cinetica. Anche se il codice GBS permette simulazioni in configurazioni magnetiche diverse, nel presente lavoro ci concentriamo su plasmi con un limiter.

Questa tesi comincia con la descrizione degli operatori geometrici e delle condizioni al bordo adeguati per garantire la conservazione della massa. In confronto con il modello precedente di GBS che non conservava la massa, le nuove simulazioni catturano più precisamente la transizione subita delle quantità del plasma e delle particelle neutre attraverso la LCFS (l'ultima superficie di flusso chiusa).

Successivamente, un modello a più specie è sviluppato, estendendo il modello di un plasma ad una sola specie ad uno che è in grado di descrivere un plasma di deuterio composto da elettroni, ioni D^+ , atomi D, molecole D_2 e ioni D_2^+ . La dinamica molecolare è introdotta attraverso le equazioni di Braginskii nel limite di deriva per la specie D_2^+ e considerando un'equazione cinetica per le molecole D_2 , oltre all'equazione per gli atomi. Le prime simulazioni a più specie con il codice GBS dimostrano che, nel regime di trasporto convettivo considerato in questo lavoro, la maggior parte delle molecole D_2 attraversano la LCFS e sono dissociate o ionizzate nella regione del bordo, originando quindi atomi D dentro la LCFS. Questo conduce ad uno spostamento radiale del picco della sorgente di plasma dovuta all'ionizzazione di atomi D verso l'interno del tokamak, rispetto delle simulazioni con una sola specie.

Il modello a più specie è applicato alla simulazione della diagnostica GPI. In questa simulazione, l'iniezione di molecole è simulata in modo auto-consistente con la dinamica del plasma e dei neutri. Le molecole iniettate interagiscono con il plasma e l'interazione risulta nell'e-

missione di luce nella lunghezza d'onda D_α , misurata per inferire le proprietà turbolente del plasma. I meccanismi alla base dell'emissione di luce simulati in questo studio, che includono l'eccitazione di atomi D e la dissociazione di D_2 e D_2^+ , forniscono uno strumento affidabile per l'interpretazione di misure sperimentali prodotte dal GPI. In questo lavoro studiamo l'impatto delle fluttuazioni dei neutri nell'emissione D_α , così come la correlazione tra l'emissione D_α e varie grandezze fisiche del plasma e dei neutri.

Parole chiave:

fisica dei plasmi, fusione controllata, periferia del tokamak, scrape-off layer, limiter, plasmi turbolenti, simulazioni di fluido, modello di Braginskii nel limite di deriva, dinamica cinetica di neutri, interazione neutri-plasma, conservazione di massa, dinamica molecolare, plasma a più specie, gas puff imaging, iniezione di gas molecolare, fluttuazioni dei neutri

Contents

| | |
|--|-----------|
| Abstract (English/Italiano) | i |
| 1 Introduction | 1 |
| 1.1 Controlled nuclear fusion as an energy source | 1 |
| 1.2 The tokamak boundary | 6 |
| 1.3 Simulation models for tokamak boundary | 8 |
| 1.4 Scope and outline of the present Thesis | 9 |
| 2 The mass-conserving GBS model of plasma turbulence and kinetic neutrals | 13 |
| 2.1 Introduction | 14 |
| 2.2 The mass-conserving model for the plasma and neutral particles | 15 |
| 2.2.1 A conserving model for the plasma | 15 |
| 2.2.2 A mass-conserving neutral model | 24 |
| 2.2.3 Mass-conserving boundary conditions | 26 |
| 2.3 Verification of Mass Conservation | 30 |
| 2.4 Simulation Results | 32 |
| 2.4.1 Differences between conserving and non-conserving models | 33 |
| 2.4.2 A conserving model for the plasma | 36 |
| 2.5 Conclusion | 39 |
| 3 A multi-component model of plasma turbulence and kinetic neutral dynamics | 41 |
| 3.1 Introduction | 42 |
| 3.2 Collisional processes in multi-component deuterium plasmas | 44 |
| 3.3 The three-fluid drift-reduced Braginskii equations | 49 |
| 3.4 Boundary conditions | 58 |
| 3.5 The kinetic model for the neutral species and its formal solution | 64 |
| 3.6 First simulation of a multi-component plasma with the GBS code | 74 |
| 3.7 Conclusions | 85 |
| 4 Numerical simulations of Gas Puff Imaging | 87 |
| 4.1 Introduction | 88 |
| 4.2 The GPI diagnostics and D_α emission rate | 91 |
| 4.3 Simulation results | 93 |

Contents

| | | |
|----------|--|------------|
| 4.4 | Analysis of the correlation between the D_α emission and the plasma and neutral quantities | 98 |
| 4.5 | Impact of neutral fluctuations | 105 |
| 4.6 | Conclusion | 112 |
| 5 | Summary and conclusions | 115 |
| A | Proof of mass conservation in the formal solution of the neutral kinetic equation | 119 |
| B | Evaluation of the average electron energy loss and reaction product energies in collisional processes | 123 |
| C | Zhdanov collisional closure | 127 |
| D | List of kernel functions | 133 |
| E | Numerical solution of the neutral equations | 141 |
| | Bibliography | 156 |
| | Acknowledgements | 157 |
| | Curriculum Vitae | 161 |

1 Introduction

1.1 Controlled nuclear fusion as an energy source

Since the rising of civilizations, people join their efforts to grant each other access to basic needs in a safe and comfortable environment. This has always relied on the ability of human communities to exploit the natural resources in order to meet these needs. The industrial revolution of the XVIII and XIX centuries brought a significant increase into this demand, requiring energetic resources for large scale production of goods and transportation. Later in the XIX century, the rising of the first power plants for electric energy generation opened the door for a new electricity-based society. This led to the technological advances of the XX century revolutionizing the means of production and life standards of an ever-increasing number of people. The demand for energy sources grew exponentially in the last century, leading to an unprecedented increase in fossil fuel consumption (coal, oil, gas) and the quest for alternative energy sources. Even today, population growth and the continuous rise of the energy consumption *per capita* make the overall energy consumption rise year after year, despite technological progress allowing for a more efficient energy use [1, 2] (see Fig. 1.1).

Fossil fuel exploitation certainly do not provide the solution for such ever-increasing global energy demand, for two main reasons. First, there is a finite amount of these resources (see Fig. 1.2). Second, fossil fuel burning has led to an increase of the concentration of CO₂ and other pollutants in the atmosphere, leading to severe environmental consequences, of which the increase of greenhouse effect and subsequent man-induced changes in the Earth's climate are the most worrisome [3] (see Fig. 1.3).

Current alternatives to fossil fuels are based on nuclear fission and renewable energy sources. The later include hydro-power, the most relevant contribution on a global scale to date (see Fig. 1.1), and also solar, wind, geothermal and waves. These resources are not exhausted when exploited for electricity generation and, in general, have no associated greenhouse gas emissions. However, the availability of these sources is highly dependent on the geographical, geological and climatological situation of a given country. Moreover, due to the inherent intermittent nature of most of these sources, major developments on energy storage and

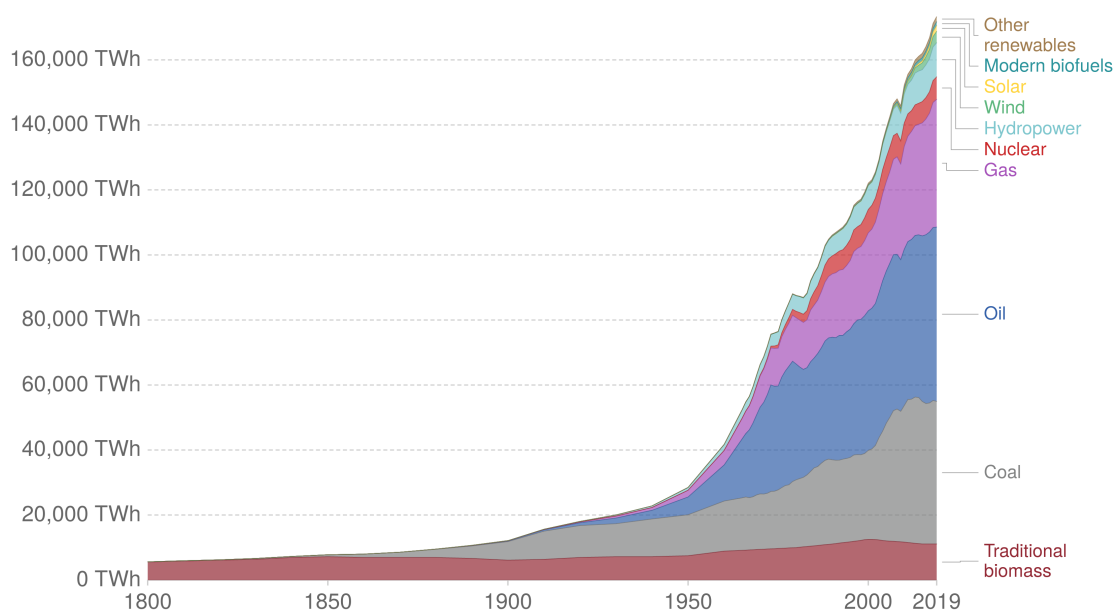


Figure 1.1: Global primary energy consumption by source, according to Vaclav Smil's *Energy Transitions: Global and National Perspectives (Second expanded and updated edition)* (2017) [1] and BP Statistical Review of World Energy [2]. Primary energy is calculated based on the *substitution method* which takes account of the inefficiencies in fossil fuel production by converting non-fossil fuel energy into the energy inputs if they had the same conversion losses as fossil fuels. *Image Source: ourworldindata.org*

management systems are required to take full advantage of their potential [4]. Finally, although recent progress has been reported on making energy generation from renewable sources more efficient, their net power outcome is still largely insufficient to meet global needs.

Nuclear fission has been exploited for the last half century with successful results. The energy density of uranium and other nuclear fission fuels is 5 orders of magnitude larger than that of fossil fuels and the operation of nuclear power plants does not involve pollutant gas emissions. Nuclear fission nowadays contributes with a significant fraction to the overall world electricity generation (see Fig. 1.1). However, being based on a chain reaction and leading to radioactive waste, this energy source suffers from important drawbacks. Release of radioactive isotopes into the environment represents a major threat for the environment and public health. This may happen due to operating an obsolete nuclear power plant in disregard of proper safety procedures (Chernobyl, 1986) or leakage originated by earthquakes or other natural disasters (Fukushima, 2011). Although nuclear accidents of this kind are rare and only responsible for a small number of casualties in comparison with fossil fuel exploitation [5], the public acceptance of these events undermines the possible use of this resource. In addition, storage of radioactive waste generated as a side product of nuclear fission poses a major challenge. Finally, we remark that even fission resources are not renewable on the long term (uranium reserves are expected to last approximately a century if exploited in traditional nuclear power

1.1. Controlled nuclear fusion as an energy source

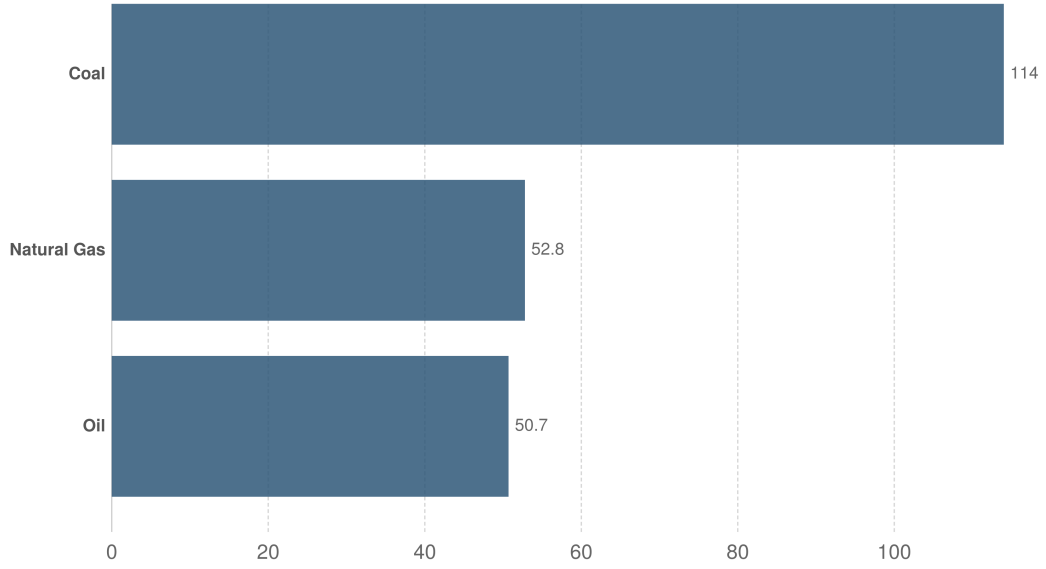


Figure 1.2: Years of fossil fuel reserves (coal, oil and natural gas) left, reported as the reserves-to-product (R/P) ratio which measures the number of years of production left based on known reserves and annual production levels in 2015. These values can change with time, depending on the discovery of new reserves and changes in annual production. Based on data from the BP Statistical Review of World Energy 2016 [7]. *Image Source: ourworldindata.org*

plants at the current consumption rate [6]).

In this context, finding a reliable long-lasting clean energy source that answers mankind's urgent need for energy is one of the great scientific and technological challenges of today. For this reason, controlled fusion has been on the spotlight of scientific research during the last half century. The aim of fusion research is to reproduce the fusion reactions taking place in the stars and to make use of the energy they release to generate electricity. Indeed, the sun, as the other stars with a similar mass, continuously converts hydrogen into helium, thanks to a chain of fusion reactions, generating the energy responsible for most phenomena taking place on Earth.

In the most promising among the set of fusion reactions, a deuterium and tritium nuclei fuse, originating an α particle (helium-4 nucleus) and a neutron,



In this reaction, most of the released energy is carried by the neutron (14.1 MeV), while the energy of the helium nucleus constitutes the remaining 3.5 MeV. In future fusion power plants the energy of the fast neutrons will be deposited in an external blanket and used to generate electricity. On the other hand, the α particles are meant to remain confined and collide with the fresh D,T fuel to deposit their energy and sustain the fusion reaction reducing the need of

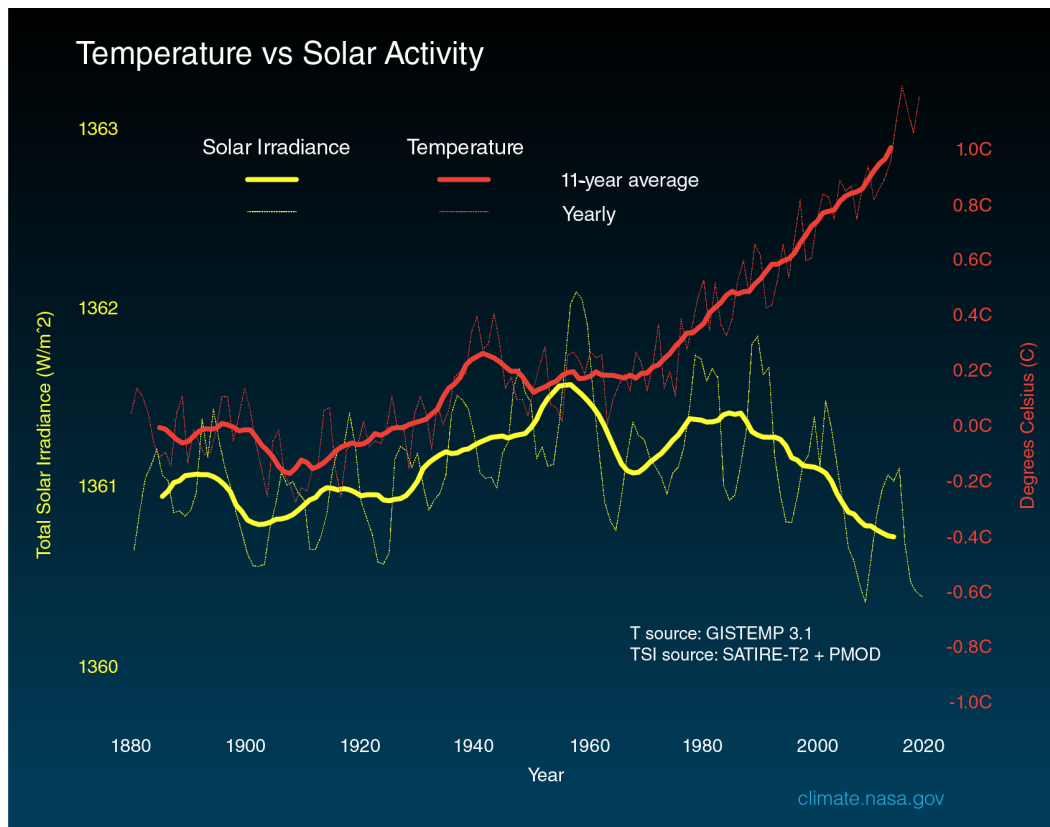


Figure 1.3: Time evolution of the average temperature on the Earth's surface compared to solar irradiance since 1880, considering averages over 11-year periods to eliminate statistical noise associated with annual fluctuations. While the two plots are clearly correlated until 1980, the subsequent divergence of the two strongly suggests an important role of enhanced greenhouse effect on the Earth's climate (Source: NASA/JPL-Caltech).

external heating.

The reaction in Eq. (1.1) is promising if compared to nuclear fission reactions, as the amount of energy it releases is about four times larger (per mass unity), thus resulting in a higher energy density [8, 9]. The fuel for the reaction in Eq. (1.1) is in general easily accessible in nature, since deuterium is abundant in Earth's water (about 35g of deuterium can be found in each cubic metre of sea water [8]). As for tritium, although it does not occur naturally on Earth, it can be bred from lithium, which is present in the Earth's crust. There are some drawbacks of the D-T fusion, such as the non-renewable nature of lithium reserves and the possibility that fast 14.1MeV neutrons activate the wall materials. For this reason, other reactions are also being studied for electricity generation, such as D-D fusion, which releases neutrons with 2.5MeV. Notwithstanding those alternatives, D-T is still the main focus of fusion research, as its energy outcome is larger and the peak cross section is reached at lower temperature [10].

The high temperature necessary for the fusion reaction to occur is due to the small range of

the strong nuclear force and the repulsive nature of the electromagnetic interaction between positively charged nuclei. This makes it necessary an energy of the order of 10keV to bring the fusion isotopes sufficiently close to each other so that the attractive strong nuclear force can overcome the electrostatic repulsion. This energy corresponds to a temperature of the order of 10^8 K. At such high temperatures, matter is in the plasma state, atoms are ionized and matter consists of charged particles, ions and electrons, that interact through electromagnetic fields that they contribute to generate. At the same time, to self-sustain fusion reactions, the plasma has to be confined in a region of space at sufficiently high densities and with sufficiently high confinement times. To achieve self-sustained fusion reactions, experiments must aim at increasing the triple product $nT\tau_E$, with n the plasma density, T the plasma temperature and τ_E the energy confinement time. In fact, the Lawson criterion [11] stipulates that self-sustained energy generation in a nuclear fusion reactor is only possible for $nT\tau_E \gtrsim 3 \times 10^{21} \text{m}^{-3} \text{keVs}$. Achieving this triple product is therefore the main goal of current research, and improving the plasma confinement proves to be a real challenge.

While confinement arises in the Sun as a natural consequence of the gravitational force generated by the mass of the star itself (of the order of 10^{30} kg), man-made devices must follow another strategy to confine the plasma (the mass of the whole Earth itself is about 10^{24} kg, one million times smaller than the sun). The Lorentz force, which the charged particles of the plasma are subject to, $\mathbf{F} = q(\mathbf{E} + \mathbf{v} \times \mathbf{B})$, with q and \mathbf{v} the particle charge and velocity and \mathbf{E} and \mathbf{B} the electric and magnetic field, can be used. In the presence of a magnetic field, because of the Lorentz force, charged particles rotate around the magnetic field lines, while their motion along the direction parallel to the field lines is not constrained. In magnetic confinement fusion devices, of which the stellarator and the tokamak are the most widely exploited examples, a field is created inside a toroidal magnetic chamber, with magnetic field lines closed within the plasma volume ensuring that the plasma remains confined. The magnetic field inside the device cannot be merely toroidal: if that was the case, charged particles would not remain confined as their motion would be affected by drifts arising from the magnetic field curvature and gradient, leading to a loss of confinement. Therefore, a poloidal component is also created to confine the plasma particles.

In a stellarator, both the toroidal and poloidal components of the magnetic field are generated by means of external coils, whose complex design is optimized in order to allow for the magnetic field topologies that best confine the plasma. In contrast, the tokamak (Russian acronym for toroidal magnetic chamber) uses a different approach, as the toroidal magnetic field is created by a series of coils positioned around an axially symmetric torus, while the poloidal field is obtained by exploiting an electromagnetic induction effect. More precisely, the tokamak works as the secondary circuit of a transformer that crosses the center of the torus, with the primary circuit relying on an external magnet. This leads to a toroidal current in the plasma that, in turn, generates a poloidal magnetic field. Additional coils around the torus are used to adjust the shape of the magnetic field. The resulting helical magnetic-field lines lie over nested magnetic flux surfaces, that is geometrical surfaces along which the flux of the magnetic field is constant. The present thesis focuses on the tokamak configuration.

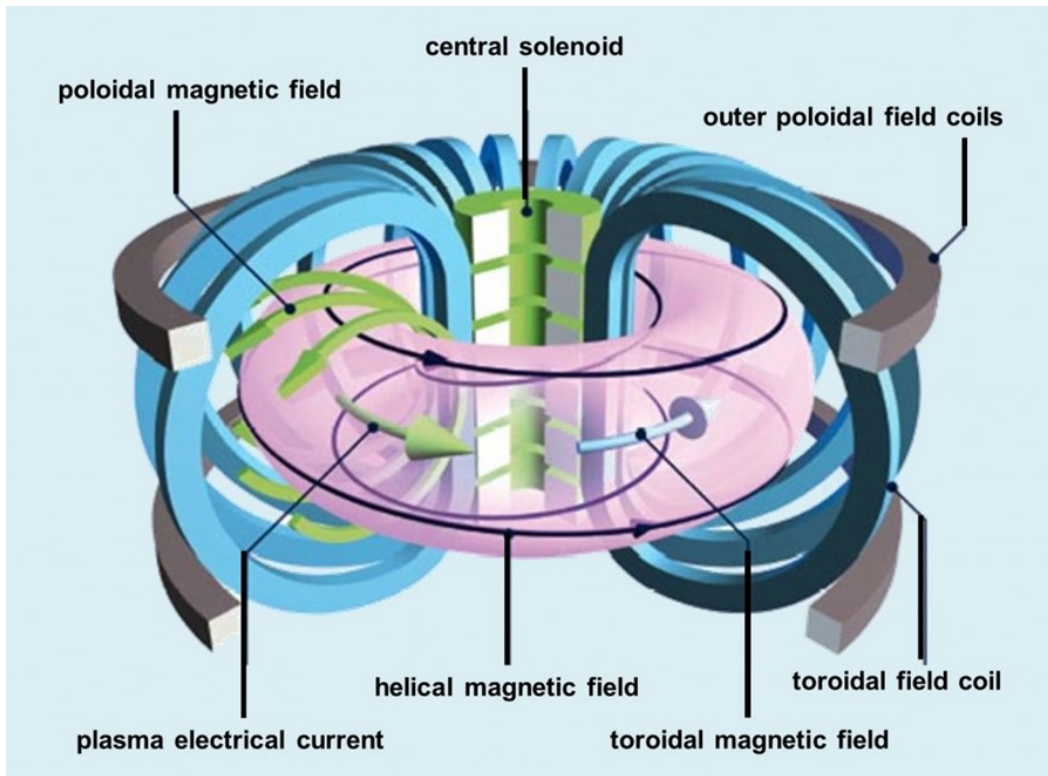


Figure 1.4: The plasma is confined inside a tokamak by means of a helical magnetic field (Source: EUROfusion).

Even though there are some drawbacks of inducing an electric current in the plasma, namely providing a drive for plasma disruptions, the tokamak has been widely studied over the last decades, emerging as a strong candidate for a high performance fusion device. The quality of fusion performances is measured by the gain factor Q , which is the ratio between the energy output and the required power input. The world record for the value of Q was set by JET (Joint European Torus), in the United Kingdom, in 1998, when $Q = 0.67$ was achieved.

Nowadays, the scientific community is joining forces on the construction and future operation of ITER, a large-scale tokamak which is intended to show the feasibility of fusion as an energy source by reaching a gain factor $Q = 10$ in a steady state operation. The first plasma is currently scheduled for December 2025 and ITER is expected to reach the operational target conditions by 2035.

1.2 The tokamak boundary

The plasma volume inside the tokamak can be divided in two regions according to the magnetic field topology: a closed-field line region where the magnetic field lines lie on nested closed flux surfaces and an open-field line region where the magnetic field lines intersect the vessel walls. The two regions are separated by the last closed flux surface (LCFS), or separatrix.

In the closed-field line region, the high density and high temperature plasma is confined and nuclear fusion reactions are set to take place in burning plasma conditions. Temperature and density drop significantly in the outermost layer of the closed-field region, which sets the sharp transition between the core and the open-field line region. We henceforth denote this region as the edge, which extends from the outer core to the LCFS. We remark that the core-edge interface is set based on the change of the plasma pressure scale length and thus it is not strictly defined.

On the other hand, the open-field line region is filled with plasma outflowing from the closed-field line region due to cross-field transport and local ionization events of neutral atoms. Transport is the result of the collisions among charged particles (classical transport), further enhanced by the device toroidal geometry (neoclassical transport), and also the turbulent collective dynamics generated in the plasma as a result of pressure and temperature gradients (turbulent transport). In the open field line region, by flowing along the magnetic field-lines, the plasma particles hit the vessel walls of the device, being recycled and coming back into the plasma as neutrals. For this reason, the open field line region is commonly referred to as the Scrape-Off Layer (SOL).

Successful operation of fusion devices must make sure that the heat load on the vessel wall does not exceed the maximum threshold allowed by the material. The magnetic field lines are made to end on metal plates specifically designed to withstand large heat fluxes (e.g. by active cooling of the material). These can be metal plates, called limiters, which extend radially into the plasma, thus defining the LCFS, or divertor plates, in case the SOL magnetic field lines are diverted away from the core region by creating one or more X-points where the poloidal component of the magnetic field vanishes. In addition to regulating the particle and heat exhaust, the SOL of a magnetic confinement device influences the overall performance of the machine by setting the boundary conditions for plasma and energy confinement. The SOL also plays an important role on fueling, impurity level control and fusion ashes removal [12].

When plasma particles heat the walls, ions and electrons recombine and are recycled into the plasma as neutrals. A fraction of the ions are simply reflected back into the plasma as neutral atoms, preserving their energy, while others are absorbed and then reemitted at the temperature of the wall, in particular when this is saturated. A fraction of the reemitted particles are neutral hydrogen atoms, while others associate to form hydrogen molecules. While neutral atoms are ionized into the plasma, hydrogen molecules are also ionized, but undergo a number of dissociation processes as well. An important part of the plasma fueling thus results from this recycling process [13, 14].

Due to the recycling taking place at the boundary, physical phenomena occurring in the SOL involve the complex interaction between plasma and neutral particles. Indeed, neutrals are present in the tokamak boundary as they are formed also by recombination events within the plasma volume. In addition, they can be injected in the tokamak (for instance, via gas puffing) with the purpose of fuelling, controlling the heat exhaust, or diagnosing the plasma

dynamics. Neutral particles interact with the low-temperature boundary plasma through a number of collisional processes, thus playing a crucial role in determining the dynamics of plasma turbulence in the SOL.

If the plasma densities and temperatures in the SOL are sufficiently low, the neutrals interact weakly with the plasma and ionization takes place mostly inside the LCFS. In this case, there are no large temperature gradients along the SOL and there is a strong flow of plasma particles all along the magnetic field lines towards the limiter/divertor. As a consequence, heat convection dominates heat transport in the SOL. This is referred to as the sheath-limited or convection-limited regime [12].

On the other hand, if the plasma density is increased, the neutral mean free path decreases, which results in a large amount of neutrals being ionized in the open-field line region. As a result, the parallel particle flux in the SOL is significantly reduced, while strong temperature gradients rise because of the cooling effect due to the ionization of neutrals close to the limiter/divertor plates. In this condition, heat transport is mainly conductive. The tokamak is then operated in the so-called conduction-limited or high-recycling regime.

In a divertor configuration, it is possible to extend the high-recycling regime by further decreasing the neutral mean free path, thus leading to a dense cloud of neutral atoms near the divertor plates. As a result, temperature becomes sufficiently low so that volumetric electron-ion recombination becomes important, thus greatly reducing the flux of particles and heat to the divertor. In these conditions, known as the detached regime, a large fraction of heat is radiated, thus making detachment a good candidate for future operation of nuclear fusion reactors [15].

This regime can also be attained by injecting impurities into the system to mimic the role of the neutral cloud and, following this approach, a detached regime can also be obtained in limiter configurations [16, 12].

1.3 Simulation models for tokamak boundary

While the low collisionality of the plasma in the hot dense core of the device demands a kinetic approach for its description, the considerably lower temperature observed in the tokamak boundary, which makes the plasma significantly more collisional, opens the possibility to a fluid description. In the SOL, where most often $k_{\parallel} \lambda_{\text{mfp}} \ll 1$, with λ_{mfp} the electron mean free path and k_{\parallel} the typical plasma perturbation wavenumber, simulations of plasma turbulence can be performed by solving a set of fluid equations, derived following the approach developed by Braginskii [17]. On the other hand, the edge is characterized by a large temperature gradient, setting the transition from low to high collisionality, and therefore the fluid description is valid only to the extent that $k_{\parallel} \lambda_{\text{mfp}} \ll 1$. In addition, with respect to the tokamak core, the simulations of the boundary region must address the neutral-plasma interaction in order to take into account one of the key aspects that determine the plasma dynamics in this region.

Historically, the simulations of the plasma in the tokamak boundary have been based on fluid models that describe cross-field plasma transport by means of a convective-diffusive approach, implemented in codes such as B2 [18, 19], EDGE2D [20], SOLEDGE-2D [21] and TECXY [22]. The neutral dynamics is approached either by using a diffusive fluid model, as in the UEDGE [23] code, or by means of a kinetic description, usually based on a Monte Carlo method, implemented e.g. in the DEGAS2 [24], EIRENE [25], GTNEUT [26] and NEUT2D [27] codes. These simulation models remain the standard of reference, and the study and design of the heat exhaust in magnetically confined fusion devices, such as ITER, strongly relies on simulations carried out by codes that couple these plasma and neutral models, such as the EMC3-EIRENE [28] and SOLPS [29] codes.

During the last decade, first-principles numerical simulations of plasma turbulence in the tokamak boundary have emerged in an attempt to overcome the limitations of diffusive models. Progress has been made possible by the development of several fluid and gyrofluid codes, namely BOUT++ [30] and its derivation Hermes [31], FELTOR [32], GBS [33, 34, 35, 36], GDB [37], GRILLIX [38], HESEL [39] and TOKAM3X [40]. These codes are based on the Braginskii fluid equations taken in the drift limit. Also kinetic codes based on the gyrokinetic model have been considered, e.g. Gkeyll [41] and XGC1 [42, 43]. Notwithstanding the important progress in the development of plasma turbulence codes, their coupling to the simulation of the neutral dynamics is still a challenging open issue.

The coupling of fluid turbulence codes with neutral models is achieved in the BOUT++, nHESEL, TOKAM3X and GBS codes. BOUT++ is a general framework for fluid model-based simulation of turbulence in the tokamak boundary, having allowed for a number of derivations. BOUT++ simulated the neutral-plasma interaction by coupling the gyro-fluid plasma model with a fluid-diffusive description of the neutrals in a linear device geometry [44]. The nHESEL [39] code, consists of the coupling of the HESEL code, which evolves density, electron and ion pressure, and vorticity in a two-dimensional slab geometry, with a one-dimensional diffusive model for neutral atoms generated by dissociation of molecules injected by gas puffs. nHESEL simulations allowed for important insights on the neutral-plasma interaction, such as the influence of blobs on the neutral particle dynamics [45, 39, 46]. In TOKAM3X, the plasma fluid model is coupled with the Monte Carlo code EIRENE [25] that describes the dynamics of neutral species. TOKAM3X-EIRENE simulations of a limited configuration showed that, in a low-density plasma, neutral particle density and flows are weakly affected by the turbulent fluctuations of the plasma [47]. The present thesis focuses on the GBS code.

1.4 Scope and outline of the present Thesis

The GBS code is a three-dimensional global turbulence code that simulates the plasma dynamics in the boundary of magnetic confinement devices. Following a flux-driven approach, GBS describes the plasma dynamics based on a set of Braginskii equations [17] in the drift limit [48], with no separation between fluctuations and equilibrium quantities.

The GBS code started as a two-dimensional fluid turbulence code and it first addressed the plasma dynamics in simple magnetized plasma (SMT) configurations such as TORPEX [49] by evolving the drift-reduced Braginskii equations in the plane perpendicular to the device magnetic field [50, 51]. The parallel dynamics was then included in the model, by using a straight field-line coordinate system. The first three-dimensional version of GBS allowed for global simulations of plasma turbulence in linear devices [52], like LAPD [53], or SMT configurations [54]. GBS was later extended to simulate the tokamak SOL, considering limited magnetic configurations [33]. As described in Ref. [55], the first SOL simulations considered the cold ion limit, neglected electromagnetic effects and made use of the Boussinesq approximation when evaluating the divergence of the polarization flux. Finite ion temperature effects were included later [56], as well as electromagnetic effects [34]. The GBS simulation domain was also extended to give the user the possibility to simulate the edge region. In addition, the Boussinesq approximation was removed [34] in the open field-line region. Moreover, an approach based upon the method of manufactured solutions (MMS) allowed for the full verification of the numerical implementation of the GBS model [57]. In parallel, GBS was adapted to enable the simulation of diverted magnetic configurations, which required the development of a non-straight field line coordinate system and its implementation to treat the presence of X-points [35]. The diverted geometry model of GBS has been exploited to understand the mechanisms underlying intermittent transport in single-null, double-null and snowflake configurations [58, 59, 60].

Since 2015, the limited configuration version of GBS code also addresses the neutral dynamics by means of a kinetic model, thus allowing for self-consistent simulations of plasma turbulence and neutral dynamics [61]. The neutrals and the plasma are coupled via a number of collisional reactions taking place in the plasma volume and recycling processes at the domain boundary. The model described in Ref. [61] considers a single neutral species. A kinetic advection equation for the neutral species is formally solved by applying the method of characteristics (in a similar way to the nSOLT code [62]). This formal solution, which describes the neutral distribution function, is then integrated in the velocity space, thus leading to an integral equation for the neutral density. This equation is then simplified using two assumptions: it is assumed that the time scale of plasma turbulence is larger than the neutral time of flight, which turns the neutral calculation into a static problem, and the neutral parallel motion is also neglected with respect to the characteristic spatial scales of turbulence along the direction parallel to the magnetic field, which reduces the neutral equation to a set of two-dimensional independent equations on the plane perpendicular to the magnetic field. The integral equation for the neutral density obtained within these simplifications is discretized and solved in the whole plasma volume and the domain boundary. The neutral density and neutral outflow to the boundary are then obtained. Once the neutral density in the plasma volume is known, the higher order moments of the neutral distribution function, namely the neutral flux and neutral temperature, are obtained in a straightforward way.

The neutral model implemented in GBS provides a description valid for all ranges of neutral density and mean free path [61]. In fact, it has the advantage of avoiding the assumptions on

the neutral temperature and diffusion coefficients typically considered in fluid-diffusive models. On the other hand, we highlight that the approach to the neutral dynamics implemented in GBS is deterministic, thus avoiding the statistical noise of the Monte Carlo method.

The self-consistent model of the neutral plasma interaction in boundary plasmas has been exploited in Ref. [63] to derive a refined two-point model to link the properties of the plasma in the upstream and divertor regions. This two point-model matches accurately the results from GBS simulations. In fact, it accurately predicts the ratio between the electron temperatures upstream and at the limiter plates in the open field-line region, considering as input parameters the particle and heat sources related to cross-field turbulent transport and the ionization sources along the magnetic field-lines.

GBS simulations were also used to investigate the role of neutral density fluctuations on the D_α emission, as reported in Ref. [64]. For this purpose, a simulation of a diagnostic gas puff located on the low-field side equatorial midplane was performed. The results showed a strong anti-correlation between the neutral density fluctuations and the perturbations of the plasma quantities at distances from the gas puff smaller than the neutral mean free path, $\lambda_{\text{mfp},n}$. However, the neutral density fluctuations were observed to have a small impact on the statistical moments and turbulence properties of the D_α emission, which suggests that neglecting the neutral density fluctuation is a valid approximation when integrating the results of gas puff imaging (GPI) at distances from the gas puff smaller than $\lambda_{\text{mfp},n}$. On the other hand, the GBS simulation also showed that the anti-correlation is weaker when distances from the diagnostic gas puff larger than $\lambda_{\text{mfp},n}$ are considered as the result of non-local shadowing effects due to the fact that the neutrals cross several plasma structures along their path. As a result, the neutral density was found to have a non-negligible impact on the D_α emission at large distances from the gas puff source.

Despite enabling self-consistent simulations of plasma turbulence and neutral dynamics in the tokamak boundary, the GBS model described in Ref. [61] is not mass-conserving. In fact, several approximations are considered in the description of both the plasma and the neutrals, that prevent mass conservation. These assumptions include the simplifications of the device geometry both in the plasma and the neutral models, the use of the Boussinesq approximation and a set of boundary conditions based on assumptions that prevent recycling at the vessel walls from being mass-conserving. In order to account for a fully consistent description of the neutral-plasma interaction and enable mass conservation, the GBS model is improved in the present thesis. The modifications introduced in GBS in order to achieve mass conservation are described in Ch. 2, where the changes implemented in the plasma model, neutral solver and boundary conditions are discussed in detail. The results of the first mass-conserving GBS simulations are also presented and analyzed in Ch.2.

The model developed in Ref. [61] considers one neutral species (D atoms) and the corresponding ion species (D^+), preventing the description of the processes relevant in realistic multi-component plasmas. The multispecies description of the neutral and plasma dynamics

is of particular importance, since the molecular dynamics is expected to play an important role on plasma recycling at the boundary and fuelling. This requires the description of D_2^+ ion dynamics, as well as of both D atoms and D_2 molecules. The multi-component model implemented in GBS to account for different ion and neutral species is the focus of Ch. 3, where the model is presented in detail. The results obtained from the first multi-component GBS simulations are also presented and discussed, being compared with the results from the single-component model.

Finally, we remark that the GPI studies reported in Ref. [64] are based on a single-component plasma framework. The improvement from a single-component to a multi-component description is expected to affect the interpretation of GPI results, as predicted in the studies reported in Ref. [46], based upon fluid simulations of two-dimensional plasmas with multi-component neutrals described by a fluid-diffusive approach. Ch. 4 focuses on the results of multi-component GPI simulations. These results are presented and compared with the ones observed in previous works [46, 64], shedding light on the mechanisms underlying the D_α emission in realistic multi-component plasmas.

The conclusion of the present thesis follows, in Ch. 5. Following the conclusion, a few appendices to the main text are included. App. A presents the proof of mass conservation for the formal solution of the neutral kinetic equation. App. B carries out the derivation of the average energy of the reaction products and the average electron energy loss for the dissociative processes considered in the multi-species model presented in Ch. 3. In App. C, the derivation of the friction and thermal force terms featuring in the velocity and temperature equations in the multi-component plasma description is presented, following the Zhdanov closure [65] and considering the approach described in Ref. [66]. App. D lists the kernel functions used to express the system of equations solved for the neutral species in the multi-component model presented in Ch. 3. Finally, App. E develops the system of equations for the multi-component neutral model in the matrix form which is used for its numerical implementation in GBS.

2 The mass-conserving GBS model of plasma turbulence and kinetic neutrals

In this chapter, the single-component GBS model for the simulation of the tokamak boundary developed in the present thesis is described. This model is mass-conserving to leading order in ρ_{s0}/R_0 , where ρ_{s0} is the ion sound Larmor radius and R_0 is the tokamak major radius at the magnetic axis. A three-dimensional description of plasma turbulence is provided by the two-fluid drift-reduced Braginskii equations, while the neutral atom dynamics model is based on the discretization of the formal solution of the Boltzmann equation, with proper mass-conserving boundary conditions being applied at the vessel walls. The present chapter describes the implementation of this model in GBS, and demonstrate mass conservation. The results of the mass-conserving simulation are then shown and discussed, highlighting the influence that mass conservation has on the profiles of the plasma and neutral quantities. The formation of the electron density profile is also addressed by relating it to the observed radial fluxes of plasma and neutral particles. The present chapter is based on the results published in Ref. [67].

2.1 Introduction

Developed in the last decade, the GBS code [33, 34] has been used to study plasma turbulence in basic plasma physics experiments [54, 52], in tokamak limited configurations [68] and it is now used to perform simulation in diverted configurations [35, 59, 60]. GBS is based on the drift-reduced Braginskii equations for the plasma. In the limited version of GBS, the plasma equations are coupled to a kinetic model for the neutrals [61]. The neutral atom density and higher order moments of the distribution function are computed by solving the kinetic equation through the method of characteristics and discretizing the resulting integral along the neutral path (similarly to the nSOLT code [62]). This method provides a description of all ranges of neutral mean free path [61] while avoiding the statistical noise of the Monte Carlo methods.

By building upon the self-consistent model for the neutral and plasma dynamics implemented in the GBS code and described in Ref. [61], the present chapter describes an improved model aiming at achieving mass conservation in a limited tokamak configuration. The improvements presented here ensure that mass conservation is satisfied to leading order in ρ_{s0}/R_0 (with ρ_{s0} the ion sound Larmor radius and R_0 the tokamak major radius at the magnetic axis), thus allowing for accurate quantitative studies in the tokamak boundary. In fact, the results of the first numerical simulations highlight the crucial role of mass conservation on determining the particle flux in the tokamak boundary, with physical implications, e.g., on the study of the tokamak fueling and the flux of particles and heat flux to the vessel walls.

Mass conservation among the plasma species has already been addressed by other boundary turbulence codes. In GRILLIX [38], plasma particles and energy are conserved by means of a particle source that compensates on average the particle sink at the outermost flux surface. In turn, the Hermes module [31], based on the BOUT++ [30] framework, verifies electron density conservation by implementing the equations in divergence form and relying on finite volume schemes, both in the limiter and divertor configurations. On the other hand, TOKAM3X features conservation of the plasma density, parallel ion momentum, electron and ion energy and charge by implementing the fluid equations in the divergence form [69].

In GBS, the discretization of the solution of the neutral kinetic equation prevents the statistical noise of the Monte Carlo approach from affecting mass conservation in a coupled neutral-plasma model. In fact, by improving the model previously implemented in GBS, presented in Ref. [34], mass conservation is now achieved in GBS to leading order in ρ_{s0}/R_0 . This is made possible thanks to the implementation of i) operators in the plasma equations that consistently take the toroidal geometry into account, avoiding the Boussinesq approximation and geometrical simplifications; ii) solution of the neutral kinetic equation written within proper toroidal geometry; iii) accurate boundary conditions to ensure mass conservation in the description of wall recycling. The resulting model enables self-consistent mass-conserving simulations of the neutral-plasma interaction in the tokamak boundary to leading order in ρ_{s0}/R_0 . These simulations ultimately allow for quantitative studies of particle fluxes. The first

results of the improved model, reported in this chapter, are compared with non-conserving results from previous GBS simulations, highlighting a significant impact of mass conservation. The role of the plasma and neutral fluxes in the formation of the plasma profile is also assessed by varying the plasma density considered in the simulations.

This chapter is structured as follows. After the Introduction, the improved mass-conserving GBS model is presented in Sec. 2.2, focusing separately on the plasma model, the kinetic neutral model, and the boundary conditions. The verification of mass conservation in GBS is the focus of Sec. 2.3. Sec. 2.4 reports on the results of the first mass-conserving simulations carried out with the GBS model presented in this chapter. The differences between the mass-conserving and the non-mass-conserving models are discussed and the role of plasma and neutral particle fluxes on the formation of the plasma density profile is addressed, by performing a density scan. The conclusion of the chapter follows, in Sec. 2.5.

2.2 The mass-conserving model for the plasma and neutral particles

In this chapter, a mass-conserving model to leading order in ρ_{s0}/R_0 is derived for the limiter configuration, where we consider an infinitely thin wedge located on the HFS equatorial mid-plane acting as a toroidal limiter, similarly to Ref. [70]. Also similarly to Ref. [70], we consider a toroidal annulus as the simulation domain, which includes both the open field-line region (SOL) and a fraction of the region inside the LCFS (edge). The mass-conserving plasma equations are presented in Sec. 2.2.1, while the conserving neutral model, consistent with the plasma model and the three-dimensional toroidal geometry, is presented in Sec. 2.2.2. In order to ensure mass conservation in the context of the recycling processes taking place at the domain boundaries, proper boundary conditions are implemented, being the subject under discussion in Sec. 2.2.3.

2.2.1 A conserving model for the plasma

GBS describes plasma turbulence by solving the drift-reduced Braginskii equations [17, 48], as it is justified by the typical low-temperature and high-collisionality plasma conditions in the tokamak boundary. Due to the large amplitude fluctuations, no separation is made between fluctuations and background quantities. The plasma density n , vorticity Ω , the electron and ion temperatures T_e and T_i , and their parallel velocities $v_{\parallel e}$ and $v_{\parallel i}$, are evolved in the electrostatic limit, according to the following system of equations,

$$\begin{aligned} \frac{\partial n}{\partial t} = & -\frac{\rho_*^{-1}}{B} [\phi, n] + \frac{2}{B} [C(p_e) - nC(\phi)] - \nabla \cdot (n v_{\parallel e} \mathbf{b}) \\ & + D_{\perp n} \nabla_{\perp}^2 n + D_{\parallel n} \nabla_{\parallel}^2 n + S_n + n_n v_{iz} - n v_{rec} \end{aligned} \quad (2.1)$$

$$\begin{aligned}
 \frac{\partial \Omega}{\partial t} = & -\nabla \cdot \left[\frac{\rho_*^{-1}}{B^2} [\phi, B\omega] \right] - \nabla \cdot \left[\frac{v_{\parallel i}}{B} \nabla_{\parallel} (B\omega) \right] + \nabla \cdot (j_{\parallel} \mathbf{b}) \\
 & + \frac{2}{B} C(p_e + p_i) + \left[\nabla G_i \cdot \left(\frac{\mathbf{b} \times \mathbf{k}}{B} \right) + G_i \nabla \cdot \left(\frac{\mathbf{b} \times \mathbf{k}}{B} \right) - \frac{2}{3B} C(G_i) \right] \\
 & + \eta_{0\Omega} \nabla_{\parallel}^2 \Omega + D_{\perp \Omega} \nabla_{\perp}^2 \Omega - \nabla \cdot \left[\frac{n_n}{n} (v_{cx} + v_{iz}) \omega \right]
 \end{aligned} \tag{2.2}$$

$$\begin{aligned}
 \frac{\partial v_{\parallel e}}{\partial t} = & -\frac{\rho_*^{-1}}{B} [\phi, v_{\parallel e}] - v_{\parallel e} \nabla_{\parallel} v_{\parallel e} \\
 & + \frac{m_i}{m_e} \left[\frac{v j_{\parallel}}{n} + \nabla_{\parallel} \phi - \frac{\nabla_{\parallel} p_e}{n} - 0.71 \nabla_{\parallel} T_e - \frac{2}{3n} \nabla_{\parallel} G_e \right] \\
 & + D_{\perp v_{\parallel e}} \nabla_{\perp}^2 v_{\parallel e} + D_{\parallel v_{\parallel e}} \nabla_{\parallel}^2 v_{\parallel e} + \frac{n_n}{n} (v_{en} + 2v_{iz}) (v_{\parallel n} - v_{\parallel e})
 \end{aligned} \tag{2.3}$$

$$\begin{aligned}
 \frac{\partial v_{\parallel i}}{\partial t} = & -\frac{\rho_*^{-1}}{B} [\phi, v_{\parallel i}] - v_{\parallel i} \nabla_{\parallel} v_{\parallel i} - \frac{\nabla_{\parallel} p}{n} - \frac{2}{3n} \nabla_{\parallel} G_i \\
 & + D_{\perp v_{\parallel i}} \nabla_{\perp}^2 v_{\parallel i} + D_{\parallel v_{\parallel i}} \nabla_{\parallel}^2 v_{\parallel i} + \frac{n_n}{n} (v_{iz} + v_{cx}) (v_{\parallel n} - v_{\parallel i})
 \end{aligned} \tag{2.4}$$

$$\begin{aligned}
 \frac{\partial T_e}{\partial t} = & -\frac{\rho_*^{-1}}{B} [\phi, T_e] - v_{\parallel e} \nabla_{\parallel} T_e \\
 & + \frac{4T_e}{3B} \left[\frac{C(p_e)}{n} + \frac{5}{2} C(T_e) - C(\phi) \right] \\
 & + \frac{2T_e}{3n} [0.71 \nabla \cdot (j_{\parallel} \mathbf{b}) - n \nabla \cdot (v_{\parallel e} \mathbf{b})] \\
 & + \chi_{\perp e} \nabla_{\perp}^2 T_e + \nabla_{\parallel} \chi_{\parallel e} \nabla_{\parallel} T_e + S_{T_e} \\
 & + \frac{n_n}{n} v_{iz} \left[-\frac{2}{3} E_{iz} - T_e + \frac{m_e}{m_i} v_{\parallel e} \left(v_{\parallel e} - \frac{4}{3} v_{\parallel n} \right) \right] \\
 & - \frac{n_n}{n} v_{en} \frac{m_e}{m_i} \frac{2}{3} v_{\parallel e} (v_{\parallel n} - v_{\parallel e})
 \end{aligned} \tag{2.5}$$

$$\begin{aligned}
 \frac{\partial T_i}{\partial t} = & -\frac{\rho_*^{-1}}{B} [\phi, T_i] - v_{\parallel i} \nabla_{\parallel} T_i + \\
 & \frac{4T_i}{3B} \left[\frac{C(p_e)}{n} - \frac{5}{2} C(T_i) - C(\phi) \right] \\
 & + \frac{2T_i}{3n} [\nabla \cdot (j_{\parallel} \mathbf{b}) - n \nabla \cdot (v_{\parallel i} \mathbf{b})] \\
 & + \chi_{\perp i} \nabla_{\perp}^2 T_i + \nabla_{\parallel} \chi_{\parallel i} \nabla_{\parallel} T_i + S_{T_i} \\
 & + \frac{n_n}{n} (v_{iz} + v_{cx}) \left[T_n - T_i + \frac{1}{3} (v_{\parallel n} - v_{\parallel i})^2 \right],
 \end{aligned} \tag{2.6}$$

2.2. The mass-conserving model for the plasma and neutral particles

with \mathbf{k} the magnetic field curvature vector given by $\mathbf{k} = (\mathbf{b} \cdot \nabla) \mathbf{b}$ and the vector $\boldsymbol{\omega}$ defined as $\boldsymbol{\omega} = (1/B^2)(n\nabla_{\perp}\phi + \nabla_{\perp}p_i)$. Since $\boldsymbol{\omega}$ is related to the plasma vorticity by $\Omega = \nabla \cdot \boldsymbol{\omega}$, the Poisson equation for the electrostatic potential ϕ required to close the system of equations yields

$$\nabla \cdot \left(\frac{n}{B^2} \nabla_{\perp} \phi \right) = \Omega - \nabla \cdot \left(\frac{1}{B^2} \nabla_{\perp} p_i \right). \quad (2.7)$$

We remark that, in Eqs. (2.1-2.7), B denotes the local value of the magnetic field modulus for a given magnetic equilibrium, as required to ensure conservation. We remark that S_{n_e} , S_{T_e} , S_{T_i} in Eqs. (3.19), (2.5) and (2.6) denote respectively the plasma density, electron temperature and ion temperature sources at the edge-core interface, which mimic the plasma and energy outflow from the core into the simulation domain.

In Eqs. (2.1-2.7) and in the rest of the chapter, we use dimensionless quantities. Therefore, the density, n , and the temperatures, T_e and T_i , are normalized to the reference values, n_0 and T_{e0} , while lengths parallel to the magnetic field are normalized to the tokamak major radius, R_0 , lengths perpendicular to the magnetic field are normalized to the ion sound Larmor radius at the magnetic axis, $\rho_{s0} = c_{s0}/\Omega_{ci0}$, where $c_{s0} = T_{e0}/m_i$ is the sound speed and $\Omega_{ci0} = eB_0/m_i$ the ion cyclotron frequency at the magnetic axis (m_i stands for the ion mass and e is the elementary charge). In turn, time is normalized to R_0/c_{s0} . The normalization of all other GBS quantities follows from these normalizations. Precisely, the parallel velocities $v_{\parallel e}$ and $v_{\parallel i}$ are normalized to the ion sound speed c_{s0} , the plasma vorticity Ω is normalized to $n_0 T_{e0}/(\rho_{s0}^2 B_0^2)$, perpendicular diffusion coefficients D_{\perp} and conductivities χ_{\perp} are normalized to $c_{s0} \rho_{s0}^2/R_0$, while the parallel diffusion coefficients D_{\parallel} (added for numerical stability purposes) and conductivities χ_{\parallel} are normalized to $c_{s0} R_0$. We also highlight that, in Eqs. (2.1-2.7), $\rho_{\star} = \rho_{s0}/R_0$ is the normalized ion sound Larmor radius, $\mathbf{b} = \mathbf{B}/B$ is the magnetic field unit vector, $p = n(T_e + T_i)$ is the total pressure and $\nu = en_{e0}R_0/(m_i c_{s0} \sigma_{\parallel})$ is the dimensionless Spitzer resistivity. It is remarked that the Spitzer parallel conductivity is considered. In fact, we assume $\chi_{\parallel e,i} = \chi_{\parallel 0} T_{e,i}^{5/2}$, following the procedure used in previous GBS models (Refs. [33, 34]), but the weaker spatial and temporal variation of the $2/(3n)$ factor is neglected. As a matter of fact, based on previous GBS simulations, we expect that neglecting the $2/(3n)$ factor does not affect our simulation results since conductivity terms are relatively small in the plasma conditions considered, which lie on the border between the sheath-limited and conduction limited regimes. The electron and ion gyroviscous terms (Refs. [33, 34]) in Eqs. (2.3) and (2.4) are given by

$$G_i = -\eta_{0i} \left[2\nabla_{\parallel} v_{\parallel i} + \frac{C(\phi)}{B} + \frac{C(p_i)}{nB} \right], \quad (2.8)$$

$$G_e = -\eta_{0e} \left[2\nabla_{\parallel} v_{\parallel e} + \frac{C(\phi)}{B} - \frac{C(p_e)}{nB} \right]. \quad (2.9)$$

Chapter 2. The mass-conserving GBS model of plasma turbulence and kinetic neutrals

The Poisson brackets, curvature, parallel and perpendicular gradient operators are introduced as

$$[f, g] = \mathbf{b} \cdot (\nabla f \times \nabla g), \quad (2.10)$$

$$C(f) = \frac{B}{2} \left[\nabla \times \left(\frac{\mathbf{b}}{B} \right) \right] \cdot \nabla f \quad (2.11)$$

$$\nabla_{\parallel} f = \mathbf{b} \cdot \nabla f. \quad (2.12)$$

$$\nabla_{\perp} f = [\nabla - \mathbf{b}(\mathbf{b} \cdot \nabla)] f. \quad (2.13)$$

We finally note that ν_{iz} , ν_{cx} , ν_{rec} and ν_{en} are respectively the ionization, charge exchange, recombination and electron-neutral elastic collision rates. Similarly to Ref. [61], these collision rates are evaluated as

$$\nu_{\text{iz}} = n \langle \nu_e \sigma_{\text{iz}}(\nu_e) \rangle, \quad (2.14)$$

$$\nu_{\text{cx}} = n \langle \nu_i \sigma_{\text{cx}}(\nu_i) \rangle, \quad (2.15)$$

$$\nu_{\text{rec}} = n \langle \nu_e \sigma_{\text{rec}}(\nu_e) \rangle, \quad (2.16)$$

$$\nu_{\text{en}} = n \langle \nu_e \sigma_{\text{en}}(\nu_e) \rangle, \quad (2.17)$$

where σ_{iz} , σ_{cx} , σ_{rec} and σ_{en} are the ionization, charge exchange, recombination and electron-neutral elastic collision cross-sections, and ν_e and ν_i denote the electron and ion velocities, respectively. We remark that, while ν_{iz} , ν_{rec} and ν_{en} are evaluated by averaging the collision rates over the electron distribution function, ν_{cx} is obtained by averaging over the ion distribution function [61].

It is remarked that the GBS model presented here does not consider the Boussinesq approximation when evaluating the polarization current density. This constitutes an extension of the work reported in Ref. [34], since the variation of the magnetic field is properly taken into account in the polarization current in both the open and closed field-line regions. This enables the vorticity equation to be written in a mass-conserving form, needed to ensure charge and

2.2. The mass-conserving model for the plasma and neutral particles

mass conservation.

Contrarily to the procedure followed in Hermes [31] and TOKAM3X [40], Eqs. (2.1-2.6) are not expressed in divergence form. This choice is justified by the robust numerical implementation of the Poisson brackets made possible by using the Arakawa scheme [71], similarly to BOUT++ [30]. Moreover, the GBS approach enables a clear separation of the contributions of different physical mechanisms. For example, it allows for the effect of curvature in the $\mathbf{E} \times \mathbf{B}$ convection terms to be isolated in a straightforward way. On the other hand, a careful evaluation of the geometric operators featuring in Eqs. (2.1-2.7) is required for mass conservation to be satisfied. These operators are derived in Ref. [72] taking into account finite aspect ratio effects by assuming a constant aspect ratio $\epsilon = a_0/R_0$, with a_0 the minor radius at the LCFS, and considering the orderings $k_{\parallel}/k_{\perp} \ll 1$ and $k_{\perp}R_0 \gg 1$. This derivation is generalized here to allow for a consistent variation of the inverse aspect ratio $\epsilon(r) = r/R_0$, with r the local minor radius.

We perform the derivation of the geometric operators by assuming an axisymmetric magnetic field,

$$\mathbf{B} = F(\psi)\nabla\varphi + \nabla\psi \times \nabla\varphi, \quad (2.18)$$

where ψ denotes the poloidal magnetic flux function obtained as the solution of the Grad-Shafranov equation, φ represents the toroidal angle, and $F(\psi)$ is the current function that yields the magnetic field toroidal component. In order to express the geometric operators, we introduce the right-handed coordinates set $(\xi^1, \xi^2, \xi^3) = (\theta^*, f(\psi), \varphi)$, where $f(\psi)$ is a magnetic flux coordinate and θ^* is a poloidal angle chosen such that $B^{\varphi} = q(\psi)B^{\theta^*}$, with $B^{\varphi} = \mathbf{B} \cdot \nabla\varphi$ and $B^{\theta^*} = \mathbf{B} \cdot \nabla\theta^*$ the toroidal and poloidal contravariant components of the magnetic field respectively (in general $B^i = \mathbf{B} \cdot \nabla\xi^i$, with $i = 1, 2, 3$), and $q(\psi)$ the safety factor at the magnetic flux ψ , defined as

$$q(\psi) = \frac{1}{2\pi} \int_0^{2\pi} d\theta \frac{B^{\varphi}(\theta, \psi)}{B^{\theta}(\theta, \psi)}, \quad (2.19)$$

with θ the poloidal angle. The reason behind this definition of θ^* is the fact that the magnetic field lines are straight in the (θ^*, φ) plane, which simplifies the numerical implementation of derivatives along the magnetic field. In fact, the $(\theta^*, f(\psi), \varphi)$ coordinate system is advantageous for the numerical implementation of Eqs. (2.1-2.7) because it facilitates the decoupling of the derivatives along the directions parallel and perpendicular to the magnetic field. We then introduce the contravariant metric tensor for this coordinate set, $g^{ij} = \nabla\xi^i \cdot \nabla\xi^j$, the covariant metric tensor, $g_{ij} = \text{Inv}(g^{ij})$ (Inv denotes the inverse matrix), and the coordinate Jacobian $J = 1/\sqrt{\det(g^{ij})} = 1/[\nabla\theta^* \cdot (\nabla f(\psi) \times \nabla\varphi)]$. The magnetic field modulus can be computed from these definitions as $B = \sqrt{B^i B_i}$, with the covariant components of the field being given by

Chapter 2. The mass-conserving GBS model of plasma turbulence and kinetic neutrals

$B_i = g_{ij} B^j$ (Einstein summation convention is used). The magnetic field unit vector is defined through $b_i = B_i/B$, while $c_i = b_i/B$ are the components of the magnetic field unit vector divided by the magnetic field modulus. The Poisson brackets, curvature and parallel gradient operators are computed from the definitions in Eqs. (2.10-2.12) as

$$[\phi, A] = \frac{1}{J} \epsilon_{ijk} b_i \frac{\partial \phi}{\partial \xi^i} \frac{\partial A}{\partial \xi^k}, \quad (2.20)$$

$$C(A) = \frac{B}{2J} \frac{\partial c_m}{\partial \xi^i} \frac{\partial A}{\partial \xi^k} \epsilon_{kjm}, \quad (2.21)$$

$$\nabla_{\parallel} A = \mathbf{b} \cdot \nabla A = b^j \frac{\partial A}{\partial \xi^j}, \quad (2.22)$$

with ϵ_{kjm} the Levi-Civita symbol. Similarly, the second derivative along the direction parallel to the magnetic field is obtained by applying Eq. (2.12) twice,

$$\nabla_{\parallel}^2 A = \mathbf{b} \cdot \nabla (\mathbf{b} \cdot \nabla A) = b^i b^j \frac{\partial^2 A}{\partial \xi^i \partial \xi^j} + b^i \frac{\partial b^j}{\partial \xi^i} \frac{\partial A}{\partial \xi^j}, \quad (2.23)$$

and the perpendicular derivative is defined from Eq. (2.13) as

$$[\nabla_{\perp} A]^i = [g^{ij} - b^i b^j] \partial_j A. \quad (2.24)$$

For simplicity, and following Ref. [72], in the present chapter we consider an equilibrium with circular magnetic flux surfaces and constant current function $F(\psi) = B_0 R_0$. We highlight that considering a more complex magnetic equilibrium would not change the conservation properties of the model, since shaping effects do not impact mass conservation as long as they are implemented consistently. The flux coordinate $f(\psi)$ is chosen as the radial distance from the magnetic axis to a given magnetic flux surface, that is r . This leads to the Jacobian for the (θ^*, r, φ) coordinates being expressed as

$$J(r, \theta^*) = r R_0 \frac{[1 - \epsilon(r)^2]^{3/2}}{[1 - \epsilon(r) \cos(\theta^*)]^2}. \quad (2.25)$$

The magnetic field components, b_i and c_i , can be obtained by using Eqs. (2.18) and (2.25).

Having defined all quantities concerning the magnetic equilibrium, the Poisson bracket operator is derived as

2.2. The mass-conserving model for the plasma and neutral particles

$$[\phi, A] = P_{\theta^* r} [\phi, A]_{\theta^* r} + P_{r\varphi} [\phi, A]_{r\varphi} + P_{\varphi\theta^*} [\phi, A]_{\varphi\theta^*}, \quad (2.26)$$

with its components and respective coefficients defined as

$$[\phi, A]_{\theta^* r} = \frac{\partial \phi}{\partial \theta^*} \frac{\partial A}{\partial r} - \frac{\partial \phi}{\partial r} \frac{\partial A}{\partial \theta^*}, \quad (2.27)$$

$$[\phi, A]_{r\varphi} = \frac{\partial \phi}{\partial r} \frac{\partial A}{\partial \varphi} - \frac{\partial \phi}{\partial \varphi} \frac{\partial A}{\partial r}, \quad (2.28)$$

$$[\phi, A]_{\varphi\theta^*} = \frac{\partial \phi}{\partial \varphi} \frac{\partial A}{\partial \theta^*} - \frac{\partial \phi}{\partial \theta^*} \frac{\partial A}{\partial \varphi}, \quad (2.29)$$

$$P_{\theta^* r} = \frac{b_\varphi}{J}, \quad (2.30)$$

$$P_{r\varphi} = \frac{b_{\theta^*}}{J}, \quad (2.31)$$

$$P_{\varphi\theta^*} = \frac{b_r}{J}. \quad (2.32)$$

The curvature operator is expressed as

$$C(A) = C^r \frac{\partial A}{\partial r} + C^{\theta^*} \frac{\partial A}{\partial \theta^*} + C^\parallel \nabla_\parallel A, \quad (2.33)$$

where the geometric coefficients are given by

$$C^r = -\frac{B}{2J} \frac{\partial c_\varphi}{\partial \theta^*}, \quad (2.34)$$

$$C^{\theta^*} = \frac{B}{2J} \left[\frac{\partial c_\varphi}{\partial r} + \frac{1}{q} \left(\frac{\partial c_{\theta^*}}{\partial r} - \frac{\partial c_r}{\partial \theta^*} \right) \right], \quad (2.35)$$

$$C^\parallel = \frac{B}{2Jb^\varphi} \left(\frac{\partial c_r}{\partial \theta^*} - \frac{\partial c_{\theta^*}}{\partial r} \right). \quad (2.36)$$

We highlight that, while the Poisson bracket operator in Eq. (2.26) is written in (θ^*, r, φ) coordinates, the curvature operator in Eq. (2.33) features derivatives along θ^* , r and the direction parallel to the magnetic field. In fact, parallel derivatives can be directly computed in GBS by taking advantage of the straight-field line coordinate set, (θ^*, r, φ) , as discussed in Ref. [33]. Otherwise, the derivative along the magnetic field would have to be projected into the φ and θ^* directions. This can be derived from Eq. (2.22), yielding

$$\nabla_\parallel = b^\varphi \left[\frac{\partial}{\partial \varphi} + \frac{1}{q} \frac{\partial}{\partial \theta^*} \right]. \quad (2.37)$$

Chapter 2. The mass-conserving GBS model of plasma turbulence and kinetic neutrals

It is then possible to reverse the relation in Eq. (2.37) to write the toroidal derivative in terms of the parallel and poloidal derivatives,

$$\frac{\partial}{\partial \varphi} = \frac{1}{b^\varphi} \nabla_{\parallel} - \frac{1}{q} \frac{\partial}{\partial \theta^*}. \quad (2.38)$$

We can thus use Eq. (2.38) to write the curvature operator in Eq. (2.33) in terms of derivatives along θ^* and the parallel direction instead of derivatives along φ . Regarding the expressions in Eqs. (2.27-2.29) for the Poisson bracket operator, the Arakawa scheme [71] is used to implement them in (θ^*, r, φ) coordinates, taking advantage of the robust stability properties of this numerical scheme.

In comparison with Ref. [72], we do not order $k_{\perp} R_0 \gg 1$ and the divergence of the magnetic field unit vector $\nabla \cdot \mathbf{b}$ is consistently taken into account in the present chapter. Therefore, applying the definition of the divergence of a vector,

$$\nabla \cdot \mathbf{b} = \frac{1}{J} \frac{\partial}{\partial \xi^i} (J b^i), \quad (2.39)$$

one obtains, for a circular axisymmetric magnetic equilibrium,

$$\nabla \cdot \mathbf{b} = -\frac{R_0 b^{\theta^*}}{B} \frac{\partial B}{\partial \theta^*}. \quad (2.40)$$

In turn, the ∇_{\perp} operator in Eq. (2.24) entering the plasma equations via Eq. (2.7) can be expressed by means of Eqs. (2.24) and (2.39) as

$$\nabla_{\perp} \cdot \left[\frac{n}{B^2} \nabla_{\perp} A \right] = \frac{1}{J} \frac{\partial}{\partial \xi^i} \left[J \frac{n}{B^2} (g^{ij} - b^i b^j) \frac{\partial A}{\partial \xi^k} \right]. \quad (2.41)$$

Eq. (2.41) is then developed consistently with the geometry under consideration and keeping only leading order terms in ρ_{s0}/R_0 and k_{\parallel}/k_{\perp} , which yields

$$\begin{aligned} \nabla_{\perp} \cdot \left[\frac{n}{B^2} \nabla_{\perp} A \right] = & N^{rr} \frac{\partial}{\partial r} \left(\frac{n}{B^2} \frac{\partial A}{\partial r} \right) + N^{\theta^* \theta^*} \frac{\partial}{\partial \theta^*} \left(\frac{n}{B^2} \frac{\partial A}{\partial \theta^*} \right) \\ & + \frac{1}{2} N^{r \theta^*} \frac{\partial}{\partial r} \left(\frac{n}{B^2} \frac{\partial A}{\partial \theta^*} \right) + \frac{1}{2} N^{r \theta^*} \frac{\partial}{\partial \theta^*} \left(\frac{n}{B^2} \frac{\partial A}{\partial r} \right), \end{aligned} \quad (2.42)$$

where the geometric coefficients are given by

$$N^{rr} = g^{rr} = 1, \quad (2.43)$$

2.2. The mass-conserving model for the plasma and neutral particles

$$N^{\theta^*\theta^*} = g^{\theta^*\theta^*} + \frac{g^{\varphi\varphi}}{q^2} = \frac{1}{r^2} \frac{1 - \epsilon \cos \theta^*}{1 - \epsilon^2} + \frac{1}{R_0^2} \frac{\sin^2 \theta^* + (1 - \epsilon \cos \theta^*)^2 / q^2}{(1 - \epsilon^2)^2}, \quad (2.44)$$

$$N^{r\theta^*} = 2g^{r\theta^*} = -\frac{2}{R_0} \frac{\sin \theta^*}{1 - \epsilon^2}. \quad (2.45)$$

We remark that the $k_{\parallel}/k_{\perp} \ll 1$ ordering used in the Poisson equation in Eq. (2.7) is not adopted when Eqs. (2.1-2.6) are developed. As a matter of fact, we include derivatives along the magnetic field in the geometrical operators present in those equations. Therefore, while mass is exactly conserved to all orders in k_{\parallel}/k_{\perp} , the energy is only conserved to leading order in k_{\parallel}/k_{\perp} [48].

We highlight that the stencil used within the implementation of the operator in Eq. (2.42) considers $\epsilon(r) = r/R_0$ consistently, therefore taking into account the radial variations of the geometric coefficients. The stencil is implemented by using a second-order centered finite difference scheme, which yields

$$\begin{aligned} \nabla \cdot \left[\frac{n}{B^2} \nabla_{\perp} A \right] = & -\frac{A_{i,j}}{2} \left[\frac{M_{i-1,j}^{rrr} + 2M_{i,j}^{rrr} + M_{i+1,j}^{rrr}}{\Delta r^2} + \frac{M_{i,j-1}^{\theta^*\theta^*} + 2M_{i,j}^{\theta^*\theta^*} + M_{i,j+1}^{\theta^*\theta^*}}{\Delta \theta^{*2}} \right] \\ & + \frac{A_{i+1,j}}{2\Delta r^2} (M_{i+1,j}^{rrr} + M_{i,j}^{rrr}) + \frac{A_{i-1,j}}{2\Delta r^2} (M_{i-1,j}^{rrr} + M_{i,j}^{rrr}) \\ & + \frac{A_{i,j+1}}{2\Delta \theta^{*2}} (M_{i,j+1}^{\theta^*\theta^*} + M_{i,j}^{\theta^*\theta^*}) + \frac{A_{i,j-1}}{2\Delta \theta^{*2}} (M_{i,j}^{\theta^*\theta^*} + M_{i,j-1}^{\theta^*\theta^*}) \\ & + \frac{1}{8\Delta r \Delta \theta^*} \left[A_{i+1,j+1} (M_{i+1,j}^{r\theta^*} + M_{i,j+1}^{r\theta^*}) \right. \\ & + A_{i-1,j-1} (M_{i-1,j}^{r\theta^*} + M_{i,j-1}^{r\theta^*}) \\ & - A_{i-1,j+1} (M_{i-1,j}^{r\theta^*} + M_{i,j+1}^{r\theta^*}) \\ & \left. - A_{i+1,j-1} (M_{i+1,j}^{r\theta^*} + M_{i,j-1}^{r\theta^*}) \right], \end{aligned} \quad (2.46)$$

with the geometric coefficients redefined as $M^{rr} = N^{rr}(n/B^2)$, $M^{r\theta^*} = N^{r\theta^*}(n/B^2)$ and $M^{\theta^*\theta^*} = N^{\theta^*\theta^*}(n/B^2)$.

Finally, we underline that the model equations presented herein reduce to the ones in Ref. [72] when the inverse aspect ratio is approximated by the constant value $\epsilon = a_0/R_0$, thus neglecting the radial variation of ϵ across the poloidal plane. In addition, one would have to consider the limits $k_{\parallel}/k_{\perp} \ll 1$ and $k_{\perp}R_0 \gg 1$, as well as the Boussinesq approximation, to retrieve the model reported in Ref. [72].

2.2.2 A mass-conserving neutral model

Similarly to the model presented in Ref. [61], the neutral-plasma interaction is addressed in GBS by solving the kinetic advection equation for the distribution function of neutral atoms f_n , that is

$$\frac{\partial f_n}{\partial t} + \mathbf{v} \cdot \frac{\partial f_n}{\partial \mathbf{x}} = -v_{iz} f_n - v_{cx} n_n \left(\frac{f_n}{n_n} - \frac{f_i}{n_i} \right) + v_{rec} f_i, \quad (2.47)$$

where n_n and n_i denote the neutral and ion density, respectively, and f_i the ion distribution function. We remark that we neglect collisions between neutral particles and elastic collisions between neutrals and ions. Assuming known plasma properties, we obtain the solution of Eq. (2.47) by using the method of characteristics, writing it as

$$f_n(\mathbf{x}, \mathbf{v}, t) = \int_0^{r'_b} \left[\frac{S(\mathbf{x}', \mathbf{v}, t')}{v} + \delta(r' - r'_b) f_n(\mathbf{x}'_b, \mathbf{v}, t'_b) \right] \times \exp \left[-\frac{1}{v} \int_0^{r'} v_{eff}(\mathbf{x}'', t'') dr'' \right] \frac{J(\mathbf{x}')}{J(\mathbf{x})} dr', \quad (2.48)$$

since the neutrals that contribute to the distribution function at position \mathbf{x} , velocity \mathbf{v} and time t are generated at position $\mathbf{x}' = \mathbf{x} - r' \boldsymbol{\Omega}$ and time $t' = t - r'/v$, with $\boldsymbol{\Omega} = \mathbf{v}/v$ designating the unit vector along the velocity direction and r' the distance between \mathbf{x} and \mathbf{x}' . We remark that the subscript "b" refers to the intersection of the characteristic passing through \mathbf{x} and direction $\boldsymbol{\Omega}$ with the domain boundary. The neutrals are solved in an (R, Z, φ) coordinate set, which is related to the (r, θ) coordinates by $R = R_0 [1 - \epsilon(r) \cos \theta]$ and $Z = R_0 \epsilon(r) \sin \theta$. The Jacobian of this coordinate set is then given by $J(\mathbf{x}) = R(\mathbf{x}) = R_0 [1 - \epsilon(r) \cos \theta]$. The volumetric source of neutrals due to charge-exchange interactions and recombination events occurring within the plasma is represented by the term

$$S(\mathbf{x}', \mathbf{v}, t') = v_{cx}(\mathbf{x}', t') n_n(\mathbf{x}', t') \phi_i(\mathbf{x}', \mathbf{v}, t') + v_{rec}(\mathbf{x}', t') f_i(\mathbf{x}', \mathbf{v}, t'), \quad (2.49)$$

with $\phi_i(\mathbf{x}', \mathbf{v}, t') = m_i / (2\pi T_i) \exp[-m_i v^2 / (2T_i)]$ the velocity distribution of the ions undergoing charge-exchange interactions, which is assumed to be a Maxwellian of temperature T_i . We remark that the volumetric source $S(\mathbf{x}, \mathbf{v}, t)$ is proportional to the neutral density $n_n(\mathbf{x}, t) = \int f_n(\mathbf{x}, \mathbf{v}, t) d\mathbf{v}$, which makes Eq. (2.48) an integral equation for f_n .

The effective cross-section for neutral depletion, $v_{eff}(\mathbf{x}'', t'') = v_{iz}(\mathbf{x}'', t'') + v_{cx}(\mathbf{x}'', t'')$, appearing in Eq. (2.48), takes into account the neutrals removed by ionization or charge-exchange interactions along the path between the source \mathbf{x}' and target \mathbf{x} locations. We note that the neutrals removed by charge-exchange with ions appear as fast neutrals, as described by the source term in Eq. (2.49). The location \mathbf{x}'' is along the integration path, while t'' denotes the time at which a neutral is at position \mathbf{x}'' . The neutral source at the domain boundary is given

by

$$f_n(\mathbf{x}'_b, \mathbf{v}, t'_b) = (1 - \alpha_{\text{refl}})(\Gamma_{\text{out},n} + \Gamma_{\text{out},i})\chi_{\text{in}}(\mathbf{x}_b, \mathbf{v}, T_w) + \alpha_{\text{refl}}[f_n(\mathbf{x}_b, \mathbf{v} - 2\mathbf{v}_\perp) + \Gamma_{\text{out},i}\chi_{\text{in}}(\mathbf{x}_b, \mathbf{v}, T_i)], \quad (2.50)$$

where $\Gamma_{\text{out},n} = \int_{v_\perp < 0} |v_\perp| \cos\theta f_n(\mathbf{x}_b, \mathbf{v}) d\mathbf{v}$ denotes the flux of neutrals outflowing to the boundary, $\Gamma_{\text{out},i}$ is the flux of ions outflowing from the main plasma, which is calculated from the quantities evolved by Eqs. (2.1-2.7), $\mathbf{v}_\perp = v_\perp \hat{\mathbf{n}} = (\mathbf{v} \cdot \hat{\mathbf{n}})\hat{\mathbf{n}}$ is the projection of the particle velocity along the unit vector normal to the boundary pointing towards the plasma $\hat{\mathbf{n}}$, and $\chi_{\text{in}}(\mathbf{x}_b, \mathbf{v}, T_w) = 3m^2/(4\pi T_w^2) \cos(\theta) \exp[-mv^2/(2T_w)]$ is the Knudsen cosine velocity distribution assumed for the reemitted neutrals [61, 73], with $\theta = \arccos(\boldsymbol{\Omega} \cdot \hat{\mathbf{n}})$ and T_w the temperature of neutral particles reemitted at the wall. Eq. (2.50) takes into account that a fraction, α_{refl} , of the neutral particles reaching the wall is reflected, while the remaining fraction is absorbed and then reemitted. Reflected neutrals have a reflected distribution function with respect to the incoming particles, $f_n(\mathbf{x}_b, \mathbf{v} - 2\mathbf{v}_\perp)$. Analogously, the ions outflowing to the boundary recombine with electrons in the wall and are recycled as neutrals, with a fraction α_{refl} of them being reflected and the rest reemitted. For reflected ions we assume a Knudsen cosine velocity distribution $\chi_{\text{in}}(\mathbf{x}_b, \mathbf{v}, T_i)$ and ensure that kinetic energy is conserved by considering the ion temperature T_i instead of wall temperature T_w .

We then solve Eq. (2.48) by considering two approximations that hold within the typical plasma parameters in the tokamak boundary, as explained in detail in Ref. [61]. We assume that the plasma quantities vary over characteristic turbulent time scales, τ_{turb} , which are larger than the characteristic neutral time of flight, τ_n . We also take advantage of the fact that the typical neutral mean free path, $\lambda_{\text{mfp},n} \sim v_{\text{th},n}/\nu_{\text{eff}}$ (with $v_{\text{th},n} = \sqrt{T_n/m_n}$ the neutral thermal velocity, being T_n the neutral temperature and m_n the neutral mass, and $\nu_{\text{eff}} = \nu_{\text{iz}} + \nu_{\text{cx}}$ the effective collision frequency for neutral depletion), is considerably smaller than the typical elongation of turbulent structures along the direction parallel to the magnetic field, $1/k_\parallel \sim R_0$. In fact, assuming a neutral temperature $T_n \sim 2\text{eV}$ and an effective frequency for neutral depletion $\nu_{\text{eff}} \sim 10^5\text{s}^{-1}$, it results $\lambda_{\text{mfp},n} \sim 0.1\text{m}$, which is considerably smaller than $R_0 \sim 1\text{m}$. This allows us to consider all quantities appearing in Eq. (2.48) independent of the parallel coordinate, approximately coincident with the toroidal direction in the limit $|\nabla\psi \times \nabla\varphi| \ll |F(\psi)\nabla\varphi|$ considered in this chapter. As a result of these approximations, Eq. (2.48) reduces to a set of time-independent two-dimensional equations in the poloidal plane. Eq. (2.48) is integrated in the velocity space (v_p, ϑ, v_t) , where v_t denotes the projection of the neutral velocity along the toroidal direction, v_p is the modulus of the projection of the velocity on the poloidal plane and ϑ is the angle between $\boldsymbol{\Omega}$ and the horizontal plane. This approach ultimately leads to a linear integral equation for the neutral density n_n in the poloidal plane,

$$\begin{aligned}
 n_n(\mathbf{x}_p) = & \int_0^{r_b} dr' \int_0^\infty dv_p v_p \int_0^{2\pi} d\vartheta \int_{-\infty}^\infty dv_t \\
 & \times \left\{ \frac{R(\mathbf{x}'_p)}{R(\mathbf{x}_p)} \left[\frac{S(\mathbf{x}'_p, \mathbf{v})}{v_p} + \delta(r' - r'_b) f_n(\mathbf{x}'_{p,b}, \mathbf{v}) \right] \right. \\
 & \left. \times \exp \left[-\frac{1}{v_p} \int_0^{r'} v_{\text{eff}}(\mathbf{x}''_p) dr''_p \right] \right\}, \tag{2.51}
 \end{aligned}$$

where \mathbf{x}_p and \mathbf{x}'_p designate the locations of the target and source of neutral particles within the poloidal cross section and r' denotes the distance between these two points.

The numerical discretization of Eq. (2.51) leads to a matrix equation solved for the neutral particle density $n_n(\mathbf{x}_p)$ and the flux of neutral atoms at the boundary $\Gamma_{\text{out}}(\mathbf{x}_{p,b})$,

$$\begin{bmatrix} n_n \\ \Gamma_{\text{out},n} \end{bmatrix} = \begin{bmatrix} v_{\text{cx}} K_{p \rightarrow p} & K_{b \rightarrow p} \\ v_{\text{cx}} K_{p \rightarrow b} & K_{b \rightarrow b} \end{bmatrix} \begin{bmatrix} n_n \\ \Gamma_{\text{out},n} \end{bmatrix} + \begin{bmatrix} v_{\text{rec}} K_{p \rightarrow p} & K_{b \rightarrow p} \\ v_{\text{rec}} K_{p \rightarrow b} & K_{b \rightarrow b} \end{bmatrix} \begin{bmatrix} n_i \\ \Gamma_{\text{out},i} \end{bmatrix}, \tag{2.52}$$

where the kernel functions K are velocity integrals, their expressions being detailed in Ref. [61]. The kernels link the neutral density n_n at a given location within the plasma volume ("p") and the flux of outflowing neutrals $\Gamma_{\text{out},n}$ at a given location at the domain boundary ("b") with the density and flux of neutrals or ions at all locations. Eq. (2.52) represents a non-homogeneous matrix system, where the homogeneous part describes the contribution of neutrals generated by charge-exchange processes in the plasma volume and the neutrals outflowing to the boundary, while the non-homogeneous part accounts for the neutrals generated by volumetric recombination and ion recycling at the wall.

We highlight that the present thesis takes toroidal geometry into account consistently, by introducing the proper $R(\mathbf{x}'_p)/R(\mathbf{x}_p)$ geometric factor in Eq. (2.51) with respect to the expressions used in Ref. [61]. The geometric factor $R(\mathbf{x}'_p)/R(\mathbf{x}_p)$ consistently takes toroidicity into account, instead of the cylindrical geometry considered in Ref. [61], and is crucial for mass conservation.

2.2.3 Mass-conserving boundary conditions

To ensure mass conservation, proper boundary conditions must be applied to both the plasma and neutrals. We highlight that the domain boundary includes the interface with the limiter plates, the edge-core interface and the vessel outer wall. We focus on the boundary conditions implemented for the plasma fields, as well as the evaluation of the plasma quantities appearing in Eq. (2.50) at the domain boundary, since these quantities provide the boundary conditions for the computation of the neutrals.

We start by considering the boundary conditions for the plasma fields at the limiter plates, where most of the plasma particles end by following the magnetic field lines, being recy-

2.2. The mass-conserving model for the plasma and neutral particles

cled back to the plasma as neutrals. These boundary conditions, imposed at the magnetic-presheath entrance where the ion drift approximation breaks, extend the Bohm-Chodura boundary conditions. Their derivation was first reported in Ref. [74] considering the cold ion limit and extended for the $T_i \neq 0$ case in Ref. [75]. Neglecting plasma gradients along the wall, the plasma boundary conditions at the limiter are given by

$$v_{\parallel i} = \pm \sqrt{T_e F_T} \quad (2.53)$$

$$v_{\parallel e} = \pm \sqrt{T_e} \exp\left(\Lambda - \frac{\phi}{T_e}\right) \quad (2.54)$$

$$\partial_{\theta^*} n = \mp \frac{n}{\sqrt{T_e F_T}} \partial_{\theta^*} v_{\parallel i} \quad (2.55)$$

$$\partial_{\theta^*} \phi = \mp \frac{\sqrt{T_e}}{\sqrt{F_T}} \partial_{\theta^*} v_{\parallel i} \quad (2.56)$$

$$\partial_{\theta^*} T_e = \gamma_e \partial_{\theta^*} \phi \quad (2.57)$$

$$\partial_{\theta^*} T_i = \gamma_i \partial_{\theta^*} \phi \quad (2.58)$$

$$\Omega = -\left(\frac{1}{F_T} (\partial_{\theta^*} v_{\parallel i})^2 \pm \frac{\sqrt{T_e}}{\sqrt{F_T}} \partial_{\theta^*}^2 v_{\parallel i}\right) \quad (2.59)$$

where the \pm signs accounts for magnetic field lines entering or leaving the vessel, $F_T = 1 + T_i/T_e$, $\Lambda = \log[\sqrt{(1/2\pi)(m_i/m_e)}] \simeq 3$. The parameters $\gamma_e = \gamma_i = 0.1$ are numerical coefficients relating the poloidal derivatives of T_e and T_i with the poloidal derivative of the potential at the limiter [74].

On the other hand, *ad hoc* boundary conditions are used at the radial boundaries, where magnetic field lines are parallel to the wall, since no first-principles boundary conditions have been developed so far for the outer vessel wall and the edge-core interface. As a matter of fact, the simulation domain is extended along the radial direction both towards the core and outwards, so that the boundary conditions for the plasma density at the outer vessel walls do not affect significantly the mass conservation properties of the simulation results. For n , T_e , T_i , $v_{\parallel e}$ and $v_{\parallel i}$, homogeneous Neumann boundary conditions are applied and $\Omega = 0$ is set at both the wall and the edge-core interface. Regarding ϕ , we follow an approach similar to the one reported in Ref. [35], using $\phi = \Lambda T_e$ at the wall, with ΛT_e evaluated at the beginning of the

Chapter 2. The mass-conserving GBS model of plasma turbulence and kinetic neutrals

simulation, and $\phi = \phi_0$ at the edge-core interface, with ϕ_0 a properly chosen constant to avoid strong potential gradients.

We now evaluate the flux of ions outflowing to the boundary, $\Gamma_{\text{out},i}$, featuring in Eq. (2.50). This constitutes the primary neutral source in the system and its proper evaluation plays an important role on for mass conservation. We observe that the total ion flux to the boundary is

$$\mathbf{\Gamma}_i = n v_{\parallel i} \mathbf{b} + \mathbf{\Gamma}_{\text{di}} + \mathbf{\Gamma}_{\text{E} \times \text{B}} + \mathbf{\Gamma}_{\text{pol},i}, \quad (2.60)$$

where $n v_{\parallel i} \mathbf{b}$ denotes the parallel ion flux, $\mathbf{\Gamma}_{\text{di}} = -(\nabla p_i \times \mathbf{B})/B^2$ is the ion diamagnetic drift flux, $\mathbf{\Gamma}_{\text{E} \times \text{B}} = (n \mathbf{B} \times \nabla \phi)/B^2$ the $\text{E} \times \text{B}$ drift flux and $\mathbf{\Gamma}_{\text{pol},i} = n \mathbf{v}_{\text{pol},i}$ is the ion polarization drift flux, with the ion polarization velocity written as

$$\mathbf{v}_{\text{pol},i} = -\frac{1}{n \Omega_{\text{ci}0}} \frac{d_i}{dt} \left(\frac{n}{B} \nabla_{\perp} \phi + \frac{1}{B} \nabla_{\perp} p_i \right) - \frac{1}{m_i n \Omega_{\text{ci}0}} \mathbf{b} \times \left[G_i \kappa - \frac{\nabla G_i}{3} \right], \quad (2.61)$$

where $d_i/dt = \partial_t + v_{\parallel i} \mathbf{b} \cdot \nabla + \mathbf{v}_{\text{E} \times \text{B}} \cdot \nabla$. In this chapter, the polarization drift contributions $\mathbf{v}_{\text{pol},i}$ are neglected in the expression of the ion flux to the boundary, since they are smaller than the $\text{E} \times \text{B}$ contribution by a factor of the order of ρ_{s0}/R_0 . Therefore, the expression for the ion flux to the limiter walls considered in the present chapter is given by the projection of Eq. (2.60) along the poloidal direction θ^* ,

$$[\mathbf{\Gamma}_i]_{\text{lim}}^{\theta^*} = n v_{\parallel i} b^{\theta^*} + \mathbf{\Gamma}_{\text{di}}^{\theta^*} + \mathbf{\Gamma}_{\text{E} \times \text{B}}^{\theta^*}, \quad (2.62)$$

with the diamagnetic and $\text{E} \times \text{B}$ flux poloidal components expressed as

$$[\mathbf{\Gamma}_{\text{di}}]^{\theta^*} = -\frac{1}{JB^2} \left[\frac{\partial p_i}{\partial r} B_{\phi} - \frac{\partial p_i}{\partial \phi} B_r \right], \quad (2.63)$$

$$[\mathbf{\Gamma}_{\text{E} \times \text{B}}]^{\theta^*} = -\frac{n}{JB^2} \left[\frac{\partial \phi}{\partial r} B_{\phi} - \frac{\partial \phi}{\partial \phi} B_r \right]. \quad (2.64)$$

We remark that Eq. (2.62) is evaluated locally. In turn, at the vessel wall we consider the radial component of the flux in Eq. (2.60),

$$[\mathbf{\Gamma}_i]_{\text{wall}}^r = \mathbf{\Gamma}_{\text{di}}^r + \mathbf{\Gamma}_{\text{E} \times \text{B}}^r, \quad (2.65)$$

with

$$[\Gamma_{\text{di}}]^r = -\frac{1}{JB^2} \left[-\frac{\partial p_i}{\partial \theta^*} B_\phi + \frac{\partial p_i}{\partial \varphi} B_{\theta^*} \right], \quad (2.66)$$

$$[\Gamma_{\text{E} \times \text{B}}]^r = -\frac{n}{JB^2} \left[-\frac{\partial \phi}{\partial \theta^*} B_\phi + \frac{\partial \phi}{\partial \varphi} B_{\theta^*} \right]. \quad (2.67)$$

The flux of ions perpendicular to the outer wall in Eq. (2.65), being considerably smaller than the flux of ions outflowing towards the limiter in Eq. (2.62), fluctuates and may occasionally reverse direction. This is also due to the *ad hoc* plasma boundary conditions used at the wall. We hence solve this numerical drawback by performing a poloidal and toroidal average of the flux when evaluating $\Gamma_{\text{out},i}$, therefore uniformly redistributing it at the wall.

While the boundary conditions imposed at the limiter and outer wall ensure mass-conservation, the edge-core interface is an open boundary of the simulation domain, which can be crossed by both ions and neutrals, with the plasma outflow from the core compensating the neutral inflow to the core in a steady state situation. In our simulations, the plasma outflowing from the core to the simulation domain is mimicked by a density source near the edge-core interface, S_n . For global mass conservation purposes, we consider a dynamical density source matching the time variation of the volume-integrated plasma density at each time step. As a result, the system evolves to a steady state where the ion flux at the edge-core interface compensates the neutral flux. The mass of the system composed by the ions and the neutrals inside the domain is thus conserved globally and locally, with the density profiles oscillating around a constant steady-state value. Since energy conservation is not the scope of the present chapter, we do not impose energy conservation when modelling the heat outflow from the core into the simulation domain. Instead, the energy outflow from the core is mimicked by temperature sources located at the edge-core interface, S_{T_e} and S_{T_i} , which are described by a gaussian profile of constant amplitude, $S_{T_e} = A_{T_e} \exp(-(r - r_c)^2/w^2)$ and $S_{T_i} = A_{T_i} \exp(-(r - r_c)^2/w^2)$, with r the radial coordinate, $r_c = 0\rho_{s0}$ the radial location of the edge-core boundary, $w = 5\rho_{s0}$ the width of the gaussian source and S_{T_e} and S_{T_i} the electron and ion temperature source amplitudes, respectively.

We remark that the boundary conditions described in the present chapter extend the ones used in previous GBS models (see Refs. [61] and [34]) thanks to the introduction of boundary conditions for the neutral model that account for the leading order drift contributions to the ion flux on top of the parallel motion, while the previous model only considered the parallel ion flow along the magnetic field lines. Therefore, the corrections implemented in the version of GBS reported in this chapter ensure mass conservation to leading order in ρ_{s0}/R_0 .

The model considered here does not include gas puffs for fuelling purposes or other fuelling mechanisms. In fact, in a nuclear fusion reactor, the plasma fuel is expected to be depleted because of the fusion reactions taking place at the core, which has to be compensated by the fuelling from the boundary in order to conserve the total mass of the plasma in the device during operation. We remark that the plasma fuelling can be simulated by using the

model discussed in this chapter, while global and local mass conservation are ensured by also including the modelling of the products of the fusion reactors in a multi-species framework, as well as the presence of a plasma pump for the removal of fusion products. We also note that in order to establish energy conservation in our simulation, the heat exchange between the plasma and the walls has to be described, as well as a more comprehensive description of the collisional heat exchange between different species provided, taking into account the role played by atomic excitation and different energy levels of the hydrogen atom.

2.3 Verification of Mass Conservation

Aiming at verifying the implementation in GBS of the mass-conserving model described in Section 2.2, and composed of the plasma model, Eqs. (2.1-2.7), the boundary conditions, Eqs. (2.53-2.59), and the neutral model, Eq. (2.51), we start by deriving the proper mass conservation law. We remark that the electron continuity equation, Eq. (2.1), can be expressed in divergence form as

$$\frac{\partial n}{\partial t} = -\nabla \cdot \mathbf{\Gamma}_e + n_n v_{iz} + D_{\perp n} \nabla_{\perp}^2 n + D_{\parallel n} \nabla_{\parallel}^2 n, \quad (2.68)$$

where the electron flux $\mathbf{\Gamma}_e$ is expressed as

$$\mathbf{\Gamma}_e = n v_{\parallel e} \mathbf{b} + \mathbf{\Gamma}_{de} + \mathbf{\Gamma}_{E \times B}, \quad (2.69)$$

with $\mathbf{\Gamma}_{E \times B}$ the $\mathbf{E} \times \mathbf{B}$ drift contribution to the electron flux, and $\mathbf{\Gamma}_{de} = (\nabla p_e \times \mathbf{B})/B^2$ the electron diamagnetic drift flux. We note that in Eq. (2.68), as well as in the rest of the present chapter, we neglect the recombination sink term, since the recombination rate is negligible compared to the ones of ionization and charge-exchange at the typical SOL and edge temperatures considered in our simulations.

The ion continuity equation can be derived from Eq. (2.68) by using the vorticity equation, Eq. (2.2), which can also be written in divergence form, $\nabla \cdot \mathbf{j} = 0$, as

$$\nabla \cdot (\mathbf{\Gamma}_i - \mathbf{\Gamma}_e) + \eta_{0\Omega} \nabla_{\parallel}^2 \Omega + D_{\perp \Omega} \nabla_{\perp}^2 \Omega = 0. \quad (2.70)$$

Using Eqs. (2.70) and (2.68), one obtains the ion continuity equation,

$$\frac{\partial n}{\partial t} = -\nabla \cdot \mathbf{\Gamma}_i + n_n v_{iz} + D_{\perp n} \nabla_{\perp}^2 n + D_{\parallel n} \nabla_{\parallel}^2 n - \eta_{0\Omega} \nabla_{\parallel}^2 \Omega - D_{\perp \Omega} \nabla_{\perp}^2 \Omega. \quad (2.71)$$

In what follows, we use $D(n, \Omega) = D_{\perp n} \nabla_{\perp}^2 n + D_{\parallel n} \nabla_{\parallel}^2 n - \eta_{0\Omega} \nabla_{\parallel}^2 \Omega - D_{\perp \Omega} \nabla_{\perp}^2 \Omega$ as a simplified notation. In addition, we note that the solution of the neutral kinetic equation presented in

Eq. (2.51) obeys the conservation relation $n_n v_{iz} = -\nabla \cdot \mathbf{\Gamma}_n$, the detailed demonstration being presented in the Appendix A to this thesis. Thus, the ion continuity equation in Eq. (2.71) can be written in terms of the divergence of the neutral flux, yielding

$$\frac{\partial n}{\partial t} = -\nabla \cdot \mathbf{\Gamma}_i - \nabla \cdot \mathbf{\Gamma}_n + D(n, \Omega), \quad (2.72)$$

which highlights that the variation of the plasma density in time matches the sum of the divergence of the ion and neutral fluxes, apart from numerical diffusion terms featuring in the continuity and vorticity equations, Eqs. (2.1-2.2). We note that Eq. (2.72) states the mass conservation law of the model developed in Section 2.2.

In order to verify Eq. (2.72), we integrate Eq. (2.72) in time and over the poloidal and toroidal directions, thus obtaining a one-dimensional conservation law,

$$\int J d\theta^* d\phi \Delta n = \int_{\Delta t} dt \int J d\theta^* d\phi [-\nabla \cdot (\mathbf{\Gamma}_i + \mathbf{\Gamma}_n) + D(n, \Omega)], \quad (2.73)$$

where $\Delta n = \int_{\Delta t} (\partial n / \partial t) dt$ denotes the local density variation over time. The relative error for mass conservation, normalized to the volume-integrated density variation, is expressed as

$$E(r) = \frac{\int J d\theta^* d\phi \Delta n + \int_{\Delta t} dt \int J d\theta^* d\phi [\nabla \cdot (\mathbf{\Gamma}_i + \mathbf{\Gamma}_n) - D(n, \Omega)]}{\int J d\theta^* d\phi dr |\Delta n| / L_r}, \quad (2.74)$$

with L_r the radial length of the simulation domain.

The error $E(r)$ is evaluated from a set of GBS simulations and presented in Fig. 2.1. We remark that the results shown in Fig. 2.1 are independent of the particular time chosen to evaluate the instantaneous error of mass-conservation.

Our convergence tests show that grid resolution in the radial direction plays a particularly important role in mass conservation. Three different grid resolutions are considered in Fig. 2.1: a coarser grid with $n_{x,p} = 64$ plasma grid points and $n_{x,n} = 10$ neutral grid points in the radial direction, an intermediate grid with $n_{x,p} = 128$ and $n_{x,n} = 18$, and a finer grid with $n_{x,p} = 256$ and $n_{x,n} = 36$. The poloidal and toroidal resolution of the plasma and neutral grids is kept constant in all simulations, with $n_{y,p} = 512$, $n_{z,p} = 64$, $n_{y,n} = 360$, and $n_{z,n} = 64$. Convergence is found in the SOL region, since the error decreases as the grid is refined. In the closed flux surface region, the error is very small for all the simulations. We remark that the peak of $E(r)$ at the LCFS is a consequence of the sharp gradients that are observed between the open and closed field-line regions, ultimately due to the topological transition between the edge and the SOL. This effect is more important if a higher radial resolution is considered, which results from the fact that the grid approaches the topological boundary between the two regions.

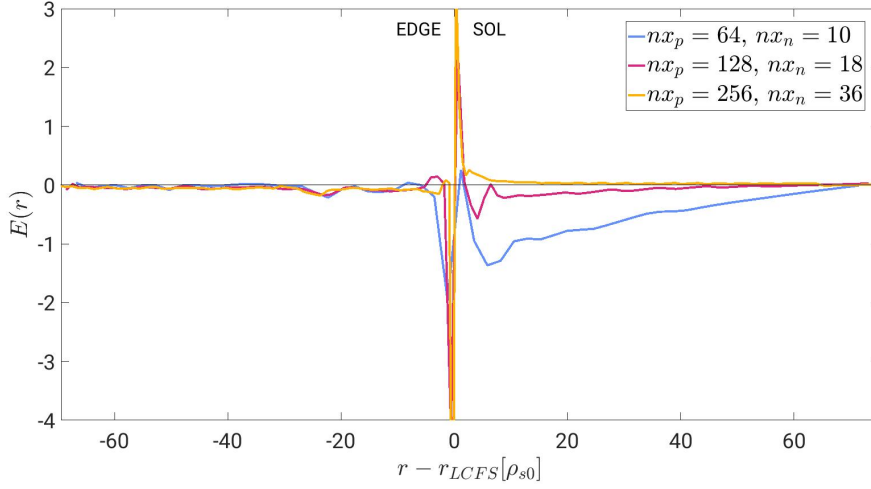


Figure 2.1: Instantaneous error in particle conservation, defined according to Eq. (2.74), evaluated over an interval of two time steps ($\Delta t = 7.5 \times 10^{-5}$) for three combinations of plasma ($n_{x,p} \times n_{y,p} \times n_{z,p}$) and neutral ($n_{x,n} \times n_{y,n} \times n_{z,n}$) grids: i) $(64 \times 512 \times 64)$ and $(10 \times 360 \times 64)$, blue line; ii) $(128 \times 512 \times 64)$ and $(18 \times 360 \times 64)$, red line; iii) $(256 \times 512 \times 64)$ and $(36 \times 360 \times 64)$, green line. Simulation parameters: $R_0/\rho_{s0} = 500$, $q = 3.867$, $n_0 = 2 \times 10^{13} \text{cm}^{-3}$, $T_0 = 20.0 \text{eV}$, $\Omega_{ci} = 5.0 \times 10^7 \text{s}^{-1}$, $T_w = 3.0 \text{eV}$, $\nu = 0.1$, $\eta_{0e} = \eta_{0i} = 1.0$, $\eta_{0\Omega} = 4.0$, $S_{Te} = S_{Ti} = 0.3$, $\chi_{||0} = 0.5$, $D_{||n} = D_{||v_{||e}} = D_{||v_{||i}} = D_{\perp n} = D_{\perp\Omega} = D_{\perp v_{||e}} = D_{\perp v_{||i}} = D_{\perp T_{||e}} = D_{\perp T_{||i}} = 7.0$.

Aiming at a further demonstration of convergence, we obtain a global error measurement by computing the l_2 norm corresponding to the relative error $E(r)$ in Eq. (2.74) for the same pairs of plasma and neutral grid resolution values considered in Fig. (2.1). We evaluate the l_2 norm for the whole domain and then excluding the area around the LCFS where the peaking is observed, which is given by $[x_{LCFS} - 1.5\rho_{s0}, x_{LCFS} + 1.5\rho_{s0}]$. These results are presented in Tab. 2.1, which shows clear convergence for the restricted domain. Therefore, provided the numerical peaking effect is removed, the l_2 norm highlights the convergence, thus reinforcing the conclusions driven from Fig. (2.1).

2.4 Simulation Results

In this section, we present and discuss the results of the first simulations obtained from the mass-conserving GBS model described in Section 2.2. We start by underlining the differences with respect to the non-mass-conserving model previously implemented in GBS. A parameter scan on the plasma density is performed to understand the influence on the plasma density on the mechanisms underlying the neutral-plasma interaction. All results presented in this section refer to time averages over an interval of $\Delta t = 10.0 R_0/c_{s0}$, during the quasi-steady state period of the simulations.

| Plasma resolution (nx_p) | Neutral resolution (nx_n) | l_2 (WD) | l_2 (RD) |
|------------------------------|-------------------------------|----------------------|----------------------|
| 64 | 10 | 6.7×10^{-2} | 6.0×10^{-2} |
| 128 | 18 | 4.0×10^{-2} | 9.5×10^{-3} |
| 256 | 36 | 3.8×10^{-2} | 4.0×10^{-3} |

Table 2.1: Values of the l_2 norm for the relative error $E(r)$ in Eq. (2.74) for different plasma and neutral grid radial resolution (same pairs of values used in Fig. (2.1), considering the whole simulation domain (WD) and for a restricted domain (RD), which excludes the points located in the region around the LCFS where numerical peaking is observed, $[x_{LCFS} - 1.5\rho_{s0}, x_{LCFS} + 1.5\rho_{s0}]$.

2.4.1 Differences between conserving and non-conserving models

To evaluate the impact of mass conservation on the simulations, we compare the mass-conserving model described in the present chapter and the model previously implemented in GBS (described in Ref. [34]). Aiming at disentangling the contributions from each of the modifications implemented in the plasma and the neutral models, we perform a comparison with a hybrid model, which considers a mass-conserving model for the neutrals, but makes use of the previously implemented model for the plasma, featuring inconsistent geometry, the Boussinesq approximation and the $k_{\parallel}/k_{\perp} \ll 1$ and $k_{\perp}R_0 \gg 1$ orderings. For the analysis, we integrate the plasma and neutral quantities over the flux surfaces, which enables the study of the plasma and neutral radial profiles. The plasma and neutral densities are presented in Fig. 2.2, for all three models.

Mass conservation is found to have a significant impact on the simulation results. The mass-conserving simulation shows a considerably higher SOL neutral density that drops significantly in the edge, an effect which is also observed in the hybrid simulations, where the neutrals are described by a mass-conserving model. Therefore, the changes in the neutral density profile arise essentially from the corrections within the neutral model, more precisely from the proper geometric factor, $R(\mathbf{x}'_p)/R(\mathbf{x}_p)$, included in Eq. (2.51). In addition, in the mass-conserving model, the plasma density drop from the closed to the open field-line region is more significant with respect to the one observed in the non-conserving model, while the hybrid model leads to a result that lies somewhere in between. We thus conclude that the changes in the density profile are partly a result of the geometrical corrections within the improved plasma model, mostly thanks to the fact that the radial variation of the inverse aspect ratio $\epsilon(r) = r/R_0$ is now consistently taken into account, but are also partly related to the neutral model corrections. In fact, the modifications in the neutral dynamics also impact the ionization source profiles, which in turn has a decisive influence on the plasma density and ion flux profiles.

We now turn to the analysis of the radial particle fluxes, so as to investigate the mechanisms underlying the changes in the plasma and neutral profiles observed in the mass-conserving model with respect to the one previously implemented in GBS. The radial profiles of the

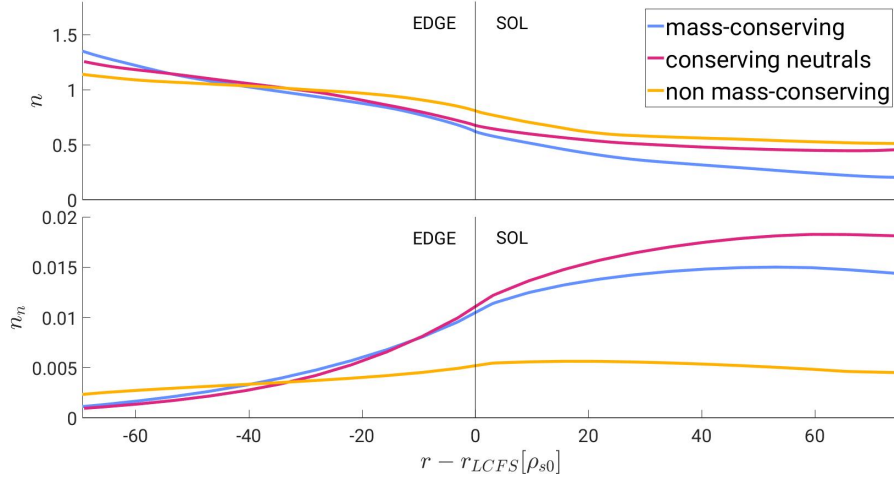


Figure 2.2: Comparison of the radial profiles of plasma density for a non-mass-conserving model, a hybrid version of GBS with conservation properties for the neutrals but not for the plasma and a mass-conserving model, averaged over an interval $\Delta t = 10.0 R_0 / c_{s0}$ from the quasi-steady state period of the simulations. The same parameters considered for the simulations presented in Fig. 2.1 are used, with the plasma and neutral grid sizes $(n_{x,p} \times n_{y,p} \times n_{z,p}) = (255 \times 511 \times 64)$ and $(n_{x,n} \times n_{y,n} \times n_{z,n}) = (24 \times 360 \times 64)$.

radial ion and neutral fluxes are presented in Fig. 2.3, where the contributions from $E \times B$, diamagnetic, and polarization drift fluxes contributing to the overall ion flux are also discriminated. In the mass-conserving simulations, the ion and neutral fluxes are opposite to each other to a good approximation. Hence, the divergence of the ion and neutral fluxes approximately balance each other, apart from small diffusive terms (see Eq. (2.72)). However, this is not the case for the non-conserving model, where the inward-pointing neutral flux remains about constant in the edge and decreases smoothly across the SOL to vanish at the wall, while the outward-pointing ion flux exhibits a rather steep profile, growing sharply from the core to the LCFS and decreasing towards the wall. Regarding the hybrid model, which considers the improvements of the neutral model but not those relative to the plasma, the neutral flux profile is quite similar to the one found for the improved mass-conserving model, since there are no differences in the neutral computation. On the other hand, the combination of the previously implemented non-conserving model for the plasma with the mass-conserving neutral model produces unreliable results for the ion fluxes, especially when close to the edge-core interface.

We further note that the non-conserving model exhibits a relatively large inward-pointing diamagnetic drift flux in the edge and near SOL, which reverses sign in the far SOL. On the other hand, in the mass-conserving model, the diamagnetic flux in Fig. 2.3 is considerably less important and points radially outwards, except in the vicinity of the LCFS. While the polarization drift flux plays a certain role in the near SOL in the non-conserving simulation, it becomes negligible in the whole domain in the mass-conserving simulation. We also highlight

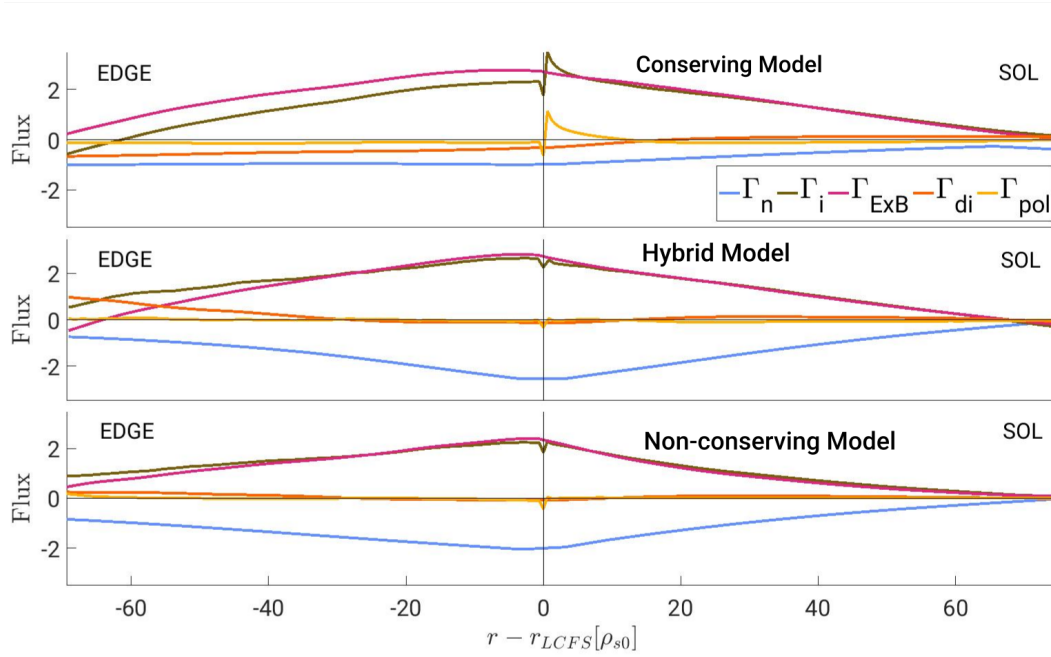


Figure 2.3: Comparison of the radial profiles of radial neutral and ion fluxes for a non-mass-conserving model (top panel), a hybrid version of GBS with conservation properties for the neutrals but not for the plasma (middle panel) and a mass-conserving model (bottom panel), discriminating the contributions of $E \times B$, diamagnetic and polarization drifts, averaged over an interval $\Delta t = 10.0R_0/c_{s0}$ from the quasi-steady state period, using the same grid sizes and parameters considered for the simulations presented in Fig. 2.2.

that our results differ from the conclusions reported in Ref. [37], where the absence of neutrals imposes $\nabla \cdot \Gamma_i = 0$ in a steady state, thus forcing a balance between the $E \times B$ drift flux and the diamagnetic component of the flux. In the simulation results reported in this chapter, the $E \times B$ drift flux is instead balanced by the neutral particle flux, while the diamagnetic contribution is negligible with respect to the $E \times B$ flux component.

As a final remark on the impact of the corrections in the boundary conditions for the neutral calculation, we discuss the relevance of the matching between the flux of ions outflowing to the limiter, $[\Gamma_i]_{\text{lim}}^{\theta^*}$, described in Eq. (2.62), and the flux of recycled neutrals flowing back to the plasma, $[\Gamma_n]_{\text{lim}}^{\theta^*}$. Aiming at this, we consider the same interval $\Delta t = 10.0R_0/c_{s0}$ from the quasi-steady state period used in Figs. 2.2 and 2.3 and we compute the averaged ion and neutral fluxes by integrating along the limiter plates. We then evaluate the relative error, normalized to the total ion flux, i.e.

$$E_{\text{lim}}(r) = \frac{[\Gamma_{\text{i}}]_{\text{lim,tot}}^{\theta^*} - [\Gamma_{\text{n}}]_{\text{lim,tot}}^{\theta^*}}{[\Gamma_{\text{i}}]_{\text{lim,tot}}^{\theta^*}}, \quad (2.75)$$

with

$$[\Gamma_{\text{i}}]_{\text{lim,tot}}^{\theta^*} = \int_{\text{lim}} J d\varphi dr |[\Gamma_{\text{i}}]_{\text{lim}}^{\theta^*}|, \quad (2.76)$$

$$[\Gamma_{\text{n}}]_{\text{lim,tot}}^{\theta^*} = \int_{\text{lim}} J d\varphi dr |[\Gamma_{\text{n}}]_{\text{lim}}^{\theta^*}|. \quad (2.77)$$

The procedure is applied to both sides of the limiter, with $E_{\text{lim}}(r) = 28.3\%$ at the lower plate for the non-conserving boundary conditions and $E_{\text{lim}}(r) = 9.6\%$ for the mas-conserving model, while the upper plate yields $E_{\text{lim}}(r) = 7.2\%$ for the non-conserving model and $E_{\text{lim}}(r) = 2.5\%$ for the simulation considering improved boundary conditions. These values highlight that mass-conserving recycling at the limiter becomes more accurate by a factor of three when the $E \times B$ and diamagnetic drift flux components are included in the expression of the ion flux in the boundary conditions for the neutral model.

2.4.2 A conserving model for the plasma

In this subsection we analyse the results obtained from simulations that consider different values of plasma density, which are obtained by varying the normalization density n_0 . Increasing n_0 makes the reaction rates for ionization, charge-exchange and electron-neutral collisions larger, which affects the plasma and neutral profiles, as shown in Fig. 2.4. In order to isolate the role of the neutrals, all simulations consider the same plasma resistivity ν , as well as the other simulation parameters.

We first consider the lowest density $n_0 = 5.0 \times 10^{12} \text{cm}^{-3}$ case (see Fig. 2.4). The neutral density n_{n} peaks in the SOL close to the limiter plates, where the plasma is recycled, and remains almost constant in the closed field-line region, given the weak interaction of the neutrals with the plasma (an important fraction of neutrals penetrate into the core with no interaction with the plasma in the edge and SOL regions). In fact, because of the higher plasma temperature in the closed field-line region, the ionization source $n_{\text{n}} \nu_{\text{iz}}$ peaks in the vicinity of the limiter, keeping a fairly constant value in the closed-flux surface region on the HFS. The analysis of the cross section profile of charge-exchange, $n_{\text{n}} \nu_{\text{cx}}$, leads to similar conclusions.

Regarding the intermediate density case, $n_0 = 2.0 \times 10^{13} \text{cm}^{-3}$, it is remarked that ionization is predominantly localized near the LCFS, the neutrals penetrating considerably less into the core with respect to the $n_0 = 5.0 \times 10^{12} \text{cm}^{-3}$ case. The spatial distribution of charge-exchange is also characterized by a pronounced peak at the LCFS and a sharp decrease towards the

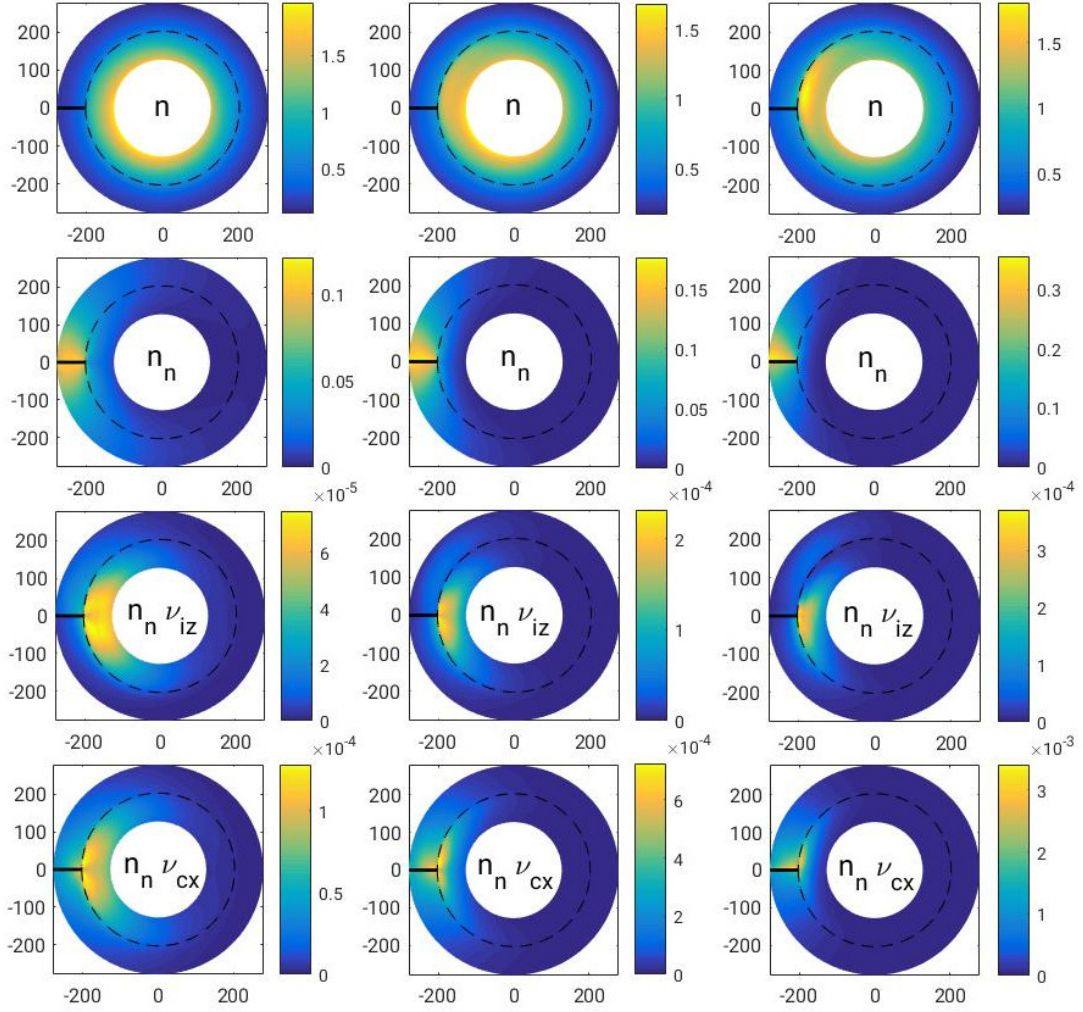


Figure 2.4: Cross sections of plasma density n (first row), neutral density n_n (second row), ionization source $n_n v_{iz}$ (third row) and charge-exchange $n_n v_{cx}$ (fourth row) for a mass-conserving model, considering a time range of $\Delta t = 10.0 R_0 / c_{s0}$ during the simulation quasi-steady state period, for three different normalization densities: $n_0 = 5.0 \times 10^{12} \text{cm}^{-3}$ (left column), $n_0 = 2.0 \times 10^{13} \text{cm}^{-3}$ (center column), and $n_0 = 4.0 \times 10^{13} \text{cm}^{-3}$ (right column). Grid sizes and all other simulation parameters are the same as the ones used for the simulations presented in Fig. 2.2.

edge-core interface. Due to the weaker penetration of the neutrals into the core and the strong ionization in the closed field-line region, a significant drop in the neutral density between the SOL and the edge-core interface is found. Analogously, since most of the ionizations occur near the LCFS, a significant plasma density source is present in the edge near the limiter, resulting in a smooth variation of n in the closed field-line region on the HFS.

Regarding the largest density considered in our scan, $n_0 = 4.0 \times 10^{13} \text{cm}^{-3}$, the simulation results exhibit a strong concentration of the ionization and charge-exchange interactions in

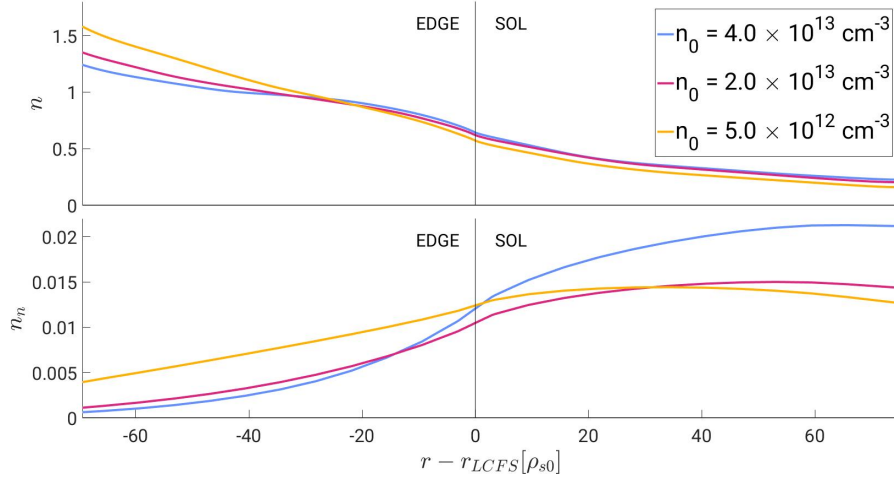


Figure 2.5: Radial plot of the time, toroidally and poloidally averaged density of plasma (top panel) and neutrals (bottom panel) within a mass-conserving model, considering a time range of $\Delta t = 10.0 R_0 / c_{s0}$ during the quasi-steady state period, for three different values of the normalization density: $n_0 = 5.0 \times 10^{12} \text{ cm}^{-3}$ (green line), $n_0 = 2.0 \times 10^{13} \text{ cm}^{-3}$ (red line) and $n_0 = 4.0 \times 10^{13} \text{ cm}^{-3}$ (blue line). Grid sizes and all other simulation parameters are the same as the ones used for the simulations presented in Fig. 2.2.

the proximity of the LCFS, with an extremely weak penetration of neutrals across the edge. Thus, neutral density drop between the SOL and edge regions is further enhanced, while the plasma density peaks in the closed field-line region close to the limiter.

A more quantitative comparison of the radial profiles of n and n_n is presented in Fig. 2.5. We remark that, while small values of n_0 flatten the n_n profile in the edge and SOL regions, the variation of n_0 has a weak influence on the radial profile of n (keeping all other parameters constant. In fact, the variation of v , which is ultimately related to density, strongly influences the plasma profile, as discussed in Ref. [76]).

On the other hand, density has a pronounced impact on the radial particle fluxes. As presented in Fig. 2.6, at low density, the flux of neutrals increases radially in the SOL region, from the wall to the LCFS, due to the increasing number of neutrals recycled into the plasma. Then, the neutral flux Γ_n remains roughly constant in the edge region, since few neutrals are ionized on their way to the core. As expected, the ion flux is approximately opposite to the neutral flux, with the dominant contribution arising from the $E \times B$ drift, both in the edge and SOL regions, and considerably smaller contributions from the diamagnetic and polarization drift fluxes. In addition, a strong radial decrease of the neutral flux is observed from the LCFS to the edge-core interface at high density, as most neutrals are ionized within the edge close to the LCFS. As imposed by mass conservation, the ion flux is opposite to the neutral flux also in this case. In fact, at high density, the ion flux increases radially, from the core to the LCFS. The reason behind the radial increase of the ion flux is the fact that, at high densities, a large number of

neutrals are ionized in the edge region, thus generating the ions that contribute to increase the flux from the core to the LCFS. Beyond the LCFS, the ion flux decreases gradually, as the ions flow to the limiter plates where they are recycled. Nonetheless, the relative contributions to the ion flux do not change, as the flux profile is mostly determined by the $E \times B$ drift contribution in the whole simulation domain.

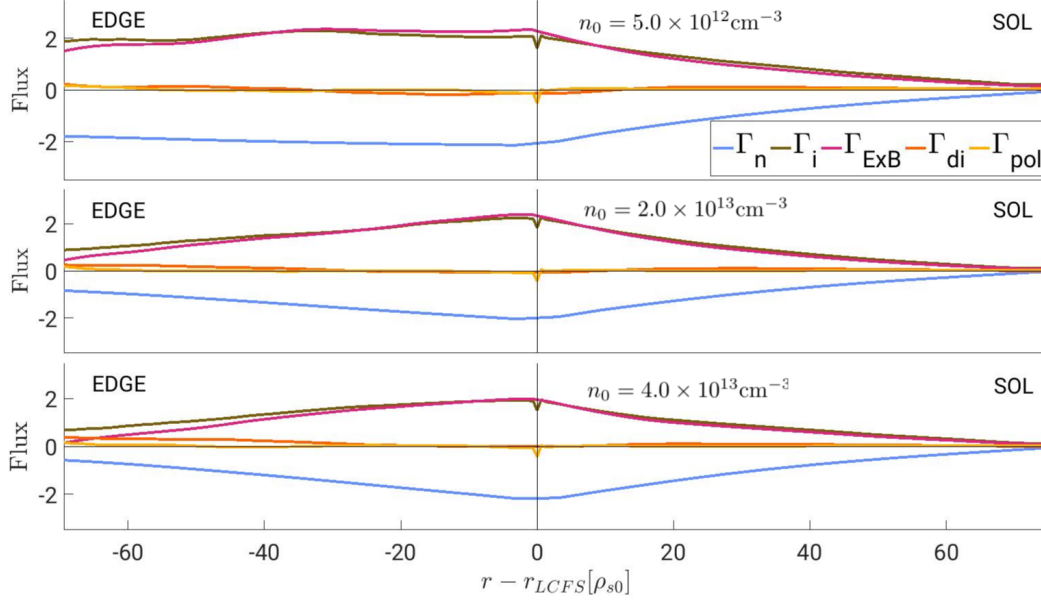


Figure 2.6: Time, toroidally and poloidally averaged radial fluxes of neutrals and ions, discriminating the contributions of $E \times B$, diamagnetic and polarization drifts, for a mass-conserving model, considering an average over a time interval $\Delta t = 10.0 R_0 / c_{s0}$ during the quasi-steady state period, for three different values of the normalization density: $n_0 = 5.0 \times 10^{12} \text{cm}^{-3}$ (top panel), $n_0 = 2.0 \times 10^{13} \text{cm}^{-3}$ (middle panel), and $n_0 = 4.0 \times 10^{13} \text{cm}^{-3}$ (bottom panel). Grid sizes and all other simulation parameters are the same as the ones used for the simulations presented in Fig. 2.2.

2.5 Conclusion

In this chapter, a mass-conserving model to leading order in ρ_{s0} / R_0 for the study of the neutral-plasma interaction in the tokamak boundary is presented. The numerical implementation of this model in the GBS code is described in detail and the first simulation results are shown and discussed.

The model relies on the drift-reduced two-fluid Braginskii equations for the description of plasma turbulence and addresses the dynamics of neutral atoms by solving the neutral kinetic equation, using the method of characteristics and discretizing the resulting formal solution. In order to ensure mass conservation, ions and neutrals considered as a whole, proper boundary conditions are implemented at the walls, thus accounting for mass-conserving recycling, and toroidal geometry is consistently accounted for. More precisely, we consider the radial

variation of the inverse aspect ratio $\epsilon = a_0/R_0$ throughout the code, we avoid the orderings $k_{\parallel}/k_{\perp} \ll 1$ and $k_{\perp}R_0 \gg 1$ in Eqs. (2.1-2.6), and we consistently take into account toroidicity effects in the neutral calculations. We remark that the changes implemented in GBS also ensure that the model conserves energy apart from terms (such as collisional heat exchange and ohmic heating) missing in the temperature equations, which should nevertheless be negligible in the edge and SOL conditions considered in this work (collisional heat exchange and ohmic heating), the presence of boundaries, the energy losses due to the ionization and recombination interactions and the use of the $k_{\parallel}/k_{\perp} \ll 1$ ordering in the Poisson equation. We highlight that a proof of the energy conservation law for the drift-reduced Braginskii model is reported in Ref. [48].

The mass-conserving model is implemented in the GBS code and convergence tests lead to the conclusion that mass conservation is satisfied. The comparison with the non-mass-conserving previously implemented model highlights the significant role played by mass conservation on the simulation results. In fact, when the mass-conserving model described in this chapter is taken into account, plasma and neutral quantities exhibit a larger drop across the LCFS and more pronounced differences are found between the SOL and edge regions.

The analysis of the simulation results reveal that the ion particle flux is mostly determined by the $E \times B$ drift and balances the neutral flux, as expected. A set of simulations performed by varying the plasma density n_0 , while keeping ν and other parameters constant, show that higher densities lead to weaker neutral penetration across the edge, as ionization and charge-exchange peak closer to the LCFS. As a consequence, high density simulations exhibit a stronger neutral density drop from the SOL towards the edge-core interface. In addition, the density scan highlights the impact of density on the radial particle fluxes, as the weaker neutral penetration associated with higher densities leads to a stronger drop of the neutral flux across the closed field-line region, from the LCFS to the edge-core interface. The ion flux points opposite to the neutral flux, as imposed by mass conservation, and is mostly determined by the $E \times B$ component over the entire domain and for all densities considered.

We highlight that the mass-conserving model presented in this chapter is implemented for the study of limited tokamak configurations. The implementation of mass conservation in diverted configurations [35, 60] can be performed by following the steps described in the present chapter.

3 A multi-component model of plasma turbulence and kinetic neutral dynamics

In this chapter, we describe a self-consistent model for the simulation of a multi-component deuterium plasma in the tokamak boundary. The plasma dynamics are described by means of a set of drift-reduced Braginskii equations for each species, which include electrons, deuterium atomic ions and deuterium molecular ions. On the other hand, deuterium atoms and molecules are addressed by considering a kinetic advection equation for each neutral species, which are solved by using the method of characteristics. The models describing the plasma and neutral species are coupled through a set of collisional interactions, which include dissociation, ionization, charge-exchange and recombination processes. In this chapter, the derivation of the plasma and neutral models is presented in detail, including its boundary conditions, and their numerical implementation is discussed. The results of the first GBS simulations of a multi-component plasma are also shown and analyzed with respect to results from the single-component plasma model discussed in Ch. 2. We highlight that the content of the present chapter is submitted for publication to Nuclear Fusion [77].

3.1 Introduction

The plasma boundary of tokamak devices is characterized by the presence of several ion and neutral species, interacting through a complex set of collisional reactions [78, 12]. For instance, not only neutral atoms, but also molecules play a relevant role in the plasma dynamics at the boundary. Molecules are generated by processes such as the plasma recycling at the vessel walls and gas puffing. In fact, ions and electrons, which flow along the magnetic-field lines or across them due to turbulent transport, eventually end at the vessel walls, where they recombine and re-enter the plasma as neutral particles. These neutrals can keep the energy of the incoming ion, which effectively undergoes a reflection process, or they can be emitted at the wall temperature, following the absorption of the incoming ion. In the later case, a significant fraction of the atoms associate to form molecules, which are then reemitted back to the plasma [79]. The exact probability of a reflection process, as well as the probability that atoms associate into molecules, depend on the physical properties of the material constituting the limiter or divertor plates [24]. Moreover, neutral molecules can be externally injected to fuel the plasma, reduce the heat flux to the vessel wall (by decreasing the plasma temperature and hence enhancing volumetric recombination), or for diagnostic purposes, providing indirect measurements of the plasma quantities.

Neutral atoms and molecules are ionized, leading to atomic and molecular ions, thus generating a multi-component plasma. Molecules and molecular ions also undergo dissociative processes, through which they are split into mono-atomic species. Recombination, charge-exchange, elastic and inelastic collisions also come into play. All these collisional reactions transform neutral particles into ions and electrons and vice versa, change the temperature of the plasma species due to the energy required to trigger ionization and dissociation processes and also impact the velocity of the plasma species. As a consequence, due to the plasma dynamics in the boundary being strongly influenced by the interactions with neutrals, simulations of the tokamak plasma boundary should account for its multi-component nature and consider the multiple collisional interactions, in order to enable reliable quantitative predictions.

Multi-component plasmas are typically described by a fluid-diffusive model, usually simplifying the Braginskii equations for the plasma species by modelling cross-field transport through empirical anomalous transport coefficients. This approach is followed by the B2 [18, 19], EDGE2D [20], EMC3 [80], SOLEDGE-2D [21] and TECXY [22] codes. Neutral particle species can also be described by means of a diffusive fluid approach [81], e.g. in the UEDGE code [23]. However, the validity of diffusive models is limited to small values of the neutral mean free path, $\lambda_{\text{mfp},n}$. Hence, these models can not be applied when $\lambda_{\text{mfp},n}$ is of the order of the plasma gradient scale length, which is often the case in the tokamak boundary. This leads to neutrals being more commonly modelled by means of a kinetic description valid for all ranges of mean free path. These models, which usually rely on Monte Carlo methods, are implemented in the DEGAS2 [24], EIRENE [25], GTNEUT [26] and NEUT2D [27] codes. In fact, research on heat exhaust typically requires integrated neutral-plasma simulations of the

tokamak boundary, which often couple above mentioned fluid-diffusive multi-component plasma models and Monte Carlo-based models for the neutral species, e.g. B2-EIRENE [25], EDGE2D-EIRENE [82], EMC3-EIRENE [28] and SOLPS [29]).

Aiming at shedding light on cross-field transport processes, plasma turbulence simulations in the tokamak boundary based on fluid and gyrofluid [30, 31, 32, 33, 34, 35, 36, 37, 38, 39, 40] and kinetic codes [41, 42, 43] have made possible significant progress in the comprehension of the underlying mechanisms of turbulence and cross-field transport in a single-ion species boundary plasma. On the other hand, multi-component plasma simulations including turbulent transport are still in their very beginning. Progress was achieved thanks to the coupling of the SOLEDGE2D [83] and TOKAM3X [40] codes. The resulting SOLEDGE3X code now enables multi-component plasma simulations, addressing the neutral species by means of the EIRENE Monte Carlo code. The investigations undertaken with SOLEDGE3X focused on the study of carbon impurities in the tokamak boundary [66]. Progress was also achieved by coupling the two-dimensional fluid code HESEL [39] with a one-dimensional fluid-diffusive model for the neutral particles, including both atoms and molecules. The resulting nHESEL [45, 39, 46] code thus enables the simulation of a single-ion plasma, featuring the interactions with three neutral species: cold hydrogen molecules puffed into the system, warm atoms resulting from the dissociation of the hydrogen molecules and hot hydrogen atoms generated by charge-exchange processes. This model was used to describe fueling in the presence of gas puffs, as well as the formation of a density shoulder in the tokamak boundary at a high gas puffing rate.

In the present chapter, we describe the development and numerical implementation in the GBS code of a multi-component model, addressing the multi-species plasma dynamics by means of a set of fluid drift-reduced Braginskii equations while describing the neutrals by solving a kinetic advection equation for each species. This chapter generalizes the implementation of the interaction between the neutrals and the plasma in GBS first described in Ref. [61] for single-ion species plasmas, which was later improved in order to verify mass-conservation, as described in Ch. 2. While the methodology presented in this chapter can be extended to include an arbitrary number of particle species and the corresponding more complex scenarios, we consider a deuterium plasma, featuring five different species: three charged particle species, namely electrons (e^-), monoatomic deuterium ions (D^+) and diatomic deuterium ions (D_2^+), and two neutral species, including deuterium atoms (D) and molecules (D_2). We highlight that D^- and D_3^+ ions, neglected here, may also be important in detachment conditions, as they play an important role in molecular assisted recombination (MAR) processes, such as dissociative recombination, dissociated attachment and by mutual neutralization [81, 84, 85].

The model described in this chapter represents the first implementation of a kinetic multi-species model that avoids the statistical noise from the Monte Carlo method. As a matter of fact, the neutral kinetic advection equations, valid for any values of the mean free path of neutral species, are solved by using the method of characteristics and integrating the formal solution in the velocity space. The resulting system of coupled integral equations for the

Chapter 3. A multi-component model of plasma turbulence and kinetic neutral dynamics

density of neutral species is discretized, enabling for the density of neutral particles to be found. The model has the potential to provide the fundamental elements required for the description and understanding of the mechanisms taking place in the boundary, including the fueling and gas puff imaging, where molecular dynamics plays an important role.

The results of the first simulation based on the multi-component GBS model are described in the present chapter, shedding light on the processes related to plasma fueling. More precisely, still considering the limited configuration and plasma parameters between the sheath-limited and high recycling regimes, we show that molecular dissociation has an impact on the space distribution of ionization and the plasma profiles, compared to single-component simulations.

The present chapter is organized as follows. After the Introduction, the collisional processes at play in the multi-component deuterium plasma model implemented in GBS are presented in Sec. 3.2. The drift-reduced Braginskii equations describing a multi-component plasma are derived, in Sec. 3.3, extending the approach followed in the single-component version of GBS described in Ch. 2. In Sec. 3.4, the multi-component boundary conditions applied at the tokamak wall are introduced. The kinetic model for the neutral species is presented in Sec. 3.5, which also describes the numerical implementation of the model, a generalization of the approach initially developed in Ref. [61] and then improved as described in Sec. 2.2.2 for a single neutral species model. Finally, we present in Sec. 3.6 the results of the first multi-component plasma GBS simulations, discussing the effect of the molecules on the plasma dynamics, with respect to the results from the single-ion species plasma simulations presented in Ch. 2. The summary follows, in Sec. 3.7.

3.2 Collisional processes in multi-component deuterium plasmas

The model presented in this chapter aims at describing a multi-component deuterium plasma. Analogously to Refs. [81], [86] and [87], we consider a plasma featuring the e , D^+ and D_2^+ species and we consider the D and D_2 neutral species. D_2 molecules are generated by the association of atoms at the vessel walls and by external injection. A fraction of D_2 molecules are ionized, thus generating D_2^+ ions, while dissociative processes give rise to mono-atomic ions, D^+ , and neutrals, D , which are also ionized, leading to D^+ . We highlight that the resulting five-species model differs from the three-species model used in the previous GBS simulations of a single-ion species plasma [61] considered in Ch. 2, where only mono-atomic deuterium ions and neutrals are evolved. We remark that, by introducing the tools required to describe the fundamental processes at play in multi-component plasmas, the model presented in this chapter can be extended to account for more complex scenarios, featuring several plasma and neutral species.

The plasma and neutral species are coupled by a number of collisional processes, which include ionization, recombination, charge-exchange, dissociation, and elastic collisions between electrons and neutrals. These processes appear in the models describing the neutral and plasma as sources and sinks of particles and heat, as well as friction terms. Table 3.1 lists

3.2. Collisional processes in multi-component deuterium plasmas

the collisional processes considered in our multi-component model, as well as their respective reaction rates.

We remark that ν_e , ν_{D^+} and $\nu_{D_2^+}$ denote the modulus of the electron, D^+ and D_2^+ velocities respectively, while their densities are represented by n_e , n_{D^+} and $n_{D_2^+}$. On the other hand, $\sigma_{iz,D}$ and σ_{iz,D_2} are the cross sections of the ionization of D and D_2 respectively, σ_{rec,D^+} and σ_{rec,D_2^+} denote the cross sections for recombination of D^+ and D_2^+ with electrons, σ_{e-D} and σ_{e-D_2} refer to the cross sections of elastic collisions between electrons and D and D_2 respectively, σ_{diss,D_2} and σ_{diss,D_2^+} represent the dissociation cross sections of D_2 and D_2^+ , $\sigma_{diss-iz,D_2}$ and $\sigma_{diss-iz,D_2^+}$ are the cross sections for dissociative ionization of D_2 and D_2^+ , $\sigma_{diss-rec,D_2^+}$ denotes the cross section of dissociative recombination of D_2^+ ions and, finally, σ_{cx,D^+} , σ_{cx,D_2^+} , $\sigma_{cx,D-D^+}$ and σ_{cx,D_2-D^+} are the cross sections for $D - D^+$, $D_2 - D_2^+$, $D - D_2^+$ and $D_2 - D^+$ charge-exchange interactions. In the present work, the distinction between fundamental and excited states for atoms, molecules and ions is neglected. As a matter of fact, we use the total cross section for each process considering the sum over the accessible electronic states of the reactants and products, following Refs. [84] and [85]. By applying momentum and energy conservation considerations, we compute the velocity and energy of the collision products, too. Since these also depend on the electronic states of the reactants and products, we average over the states relevant to a given reaction, taking into account the cross section of each state. The derivation of these values is detailed in App. B.

By considering Krook collision operators, the collision rates for ionization, recombination, elastic collisions and dissociative processes are computed as the average over the electron velocity distribution function, thus neglecting the velocity of the massive particle involved in the collision (D , D_2 , D^+ or D_2^+) when computing the relative velocity between the electron and the other particle. As a matter of fact, electrons have considerably larger thermal velocity than ions or neutrals. As for charge-exchange processes between D^+ ions and the neutral species D and D_2 , given the weak dependence of the cross section on the ion-neutral relative velocity [12], we neglect the neutral particle velocity (D or D_2) when evaluating the relative velocity of the colliding particles (the velocity of a neutral particle is usually smaller than the ion velocity). Therefore, the reaction rates σ_{cx,D^+} and σ_{cx,D_2-D^+} are computed by averaging over the distribution function of the D^+ species, which we assume to be described by a Maxwellian with temperature T_{D^+} . We follow the same approach when computing the cross section of charge-exchange interactions between D_2^+ ions and the D_2 and D neutrals, by averaging the cross sections σ_{cx,D_2^+} and $\sigma_{cx,D-D_2^+}$ over the D_2^+ velocity distribution function, which we assume to be a Maxwellian of temperature $T_{D_2^+}$.

The $\langle \nu \sigma \rangle$ products for most of the reactions considered in Table 3.1 are obtained from the AMJUEL [84] and HYDEL [85] databases (precise references for each cross section listed in Table 1 of Ref. [87]). We remark that, although these databases present the cross sections for hydrogen plasmas, we assume in this chapter that they apply also to deuterium. We highlight that the cross section for the $e^- - D$ elastic collisions is obtained from Ref. [88] (page 40, Table 2), while the $e^- - D_2$ elastic collision cross section is computed from Ref. [89] (page 917, Table

Table 3.1: Collisional processes considered and their respective reaction rates.

| Collisional process | Equation | Reaction Frequency |
|---------------------------------------|---|---|
| Ionization of D | $e^- + D \rightarrow 2e^- + D^+$ | $\nu_{iz,D} = n_e \langle \nu_e \sigma_{iz,D}(\nu_e) \rangle$ |
| Recombination of D^+ and e^- | $e^- + D^+ \rightarrow D$ | $\nu_{rec,D^+} = n_e \langle \nu_e \sigma_{rec,D^+}(\nu_e) \rangle$ |
| $e^- - D$ elastic collisions | $e^- + D \rightarrow e^- + D$ | $\nu_{e-D} = n_e \langle \nu_e \sigma_{e-D}(\nu_e) \rangle$ |
| Ionization of D_2 | $e^- + D_2 \rightarrow 2e^- + D_2^+$ | $\nu_{iz,D_2} = n_e \langle \nu_e \sigma_{iz,D_2}(\nu_e) \rangle$ |
| Recombination of D_2^+ and e^- | $e^- + D_2^+ \rightarrow D_2$ | $\nu_{rec,D_2^+} = n_e \langle \nu_e \sigma_{rec,D_2^+}(\nu_e) \rangle$ |
| $e^- - D_2$ elastic collisions | $e^- + D_2 \rightarrow e^- + D_2$ | $\nu_{e-D_2} = n_e \langle \nu_e \sigma_{e-D_2}(\nu_e) \rangle$ |
| Dissociation of D_2 | $e^- + D_2 \rightarrow e^- + D + D$ | $\nu_{diss,D_2} = n_e \langle \nu_e \sigma_{diss,D_2}(\nu_e) \rangle$ |
| Dissociative ionization of D_2 | $e^- + D_2 \rightarrow 2e^- + D + D^+$ | $\nu_{diss-iz,D_2} = n_e \langle \nu_e \sigma_{diss-iz,D_2}(\nu_e) \rangle$ |
| Dissociation of D_2^+ | $e^- + D_2^+ \rightarrow e^- + D + D^+$ | $\nu_{diss,D_2^+} = n_e \langle \nu_e \sigma_{diss,D_2^+}(\nu_e) \rangle$ |
| Dissociative ionization of D_2^+ | $e^- + D_2^+ \rightarrow 2e^- + 2D^+$ | $\nu_{diss-iz,D_2^+} = n_e \langle \nu_e \sigma_{diss-iz,D_2^+}(\nu_e) \rangle$ |
| Dissociative recombination of D_2^+ | $e^- + D_2^+ \rightarrow 2D$ | $\nu_{diss-rec,D_2^+} = n_e \langle \nu_e \sigma_{diss-rec,D_2^+}(\nu_e) \rangle$ |
| Charge-exchange of D^+, D | $D^+ + D \rightarrow D + D^+$ | $\nu_{cx,D} = n_{D^+} \langle \nu_{D^+} \sigma_{cx,D^+}(\nu_{D^+}) \rangle$ |
| Charge-exchange of D_2^+, D_2 | $D_2^+ + D_2 \rightarrow D_2 + D_2^+$ | $\nu_{cx,D_2} = n_{D_2^+} \langle \nu_{D_2^+} \sigma_{cx,D_2^+}(\nu_{D_2^+}) \rangle$ |
| Charge-exchange of D_2^+, D | $D_2^+ + D \rightarrow D_2 + D^+$ | $\nu_{cx,D-D_2^+} = n_{D_2^+} \langle \nu_{D_2^+} \sigma_{cx,D-D_2^+}(\nu_{D_2^+}) \rangle$ |
| Charge-exchange of D_2, D^+ | $D_2 + D^+ \rightarrow D_2^+ + D$ | $\nu_{cx,D_2-D^+} = n_{D^+} \langle \nu_{D^+} \sigma_{cx,D_2-D^+}(\nu_{D^+}) \rangle$ |

13). The cross section for the $D_2 - D_2^+$ charge-exchange reaction is in turn taken from the HYDEL database (H.4, reaction 4.3.1), while the cross sections from the ALADDIN database [90] (obtained from Refs. [91, 92]) are used for the $D - D_2^+$ charge-exchange interaction. For all the other reactions, the cross sections from the AMJUEL database [84] are considered. The $\langle \nu \sigma \rangle$ product for the collisional processes considered in this chapter is plotted as a function of the temperature of the colliding particle in Fig. 3.1.

We henceforth focus on the computation of the velocity and energy of their products. For charge-exchange interactions following the general form $A + B^+ \rightarrow A^+ + B$, we assume that, while A and B^+ exchange an electron, their velocities are not affected and energy is conserved. As a result, the A^+ ion is released from the charge-exchange collision with the velocity of A , and B is released with the velocity of B^+ . For the $e^- + D \rightarrow e^- + D$ elastic collisions, because of the large electron to deuterium mass ratio, we consider that the D velocity is not impacted by the collision, while the electron is emitted isotropically in the reference frame of the massive particle following a Maxwellian distribution function, $\Phi_e[\mathbf{v}_D, T_{e,e-D}] = [m_e/(2\pi T_{e,e-D})]^{3/2} \exp[-m_e(\mathbf{v} - \mathbf{v}_D)^2/(2T_{e,e-D})]$, which is centered at the velocity of the incoming D particle, $\mathbf{v}_D = \int \mathbf{v} f_D d\mathbf{v} / \int f_D d\mathbf{v}$. The temperature $T_{e,e-D}$ is, in turn, established by energy conservation considerations. More precisely, we observe that the average energy of the incoming electrons consists of the sum of the kinetic energy associated with the fluid velocity, \mathbf{v}_e , and the thermal contribution, $(3/2)T_e$. On the other hand, the energy of the outgoing electrons has a contribution arising from the collective velocity of the re-emitted particles, \mathbf{v}_D , and a thermal contribution, $T_{e,e-D}$. It follows that $T_{e,e-D}$ verifies the balance

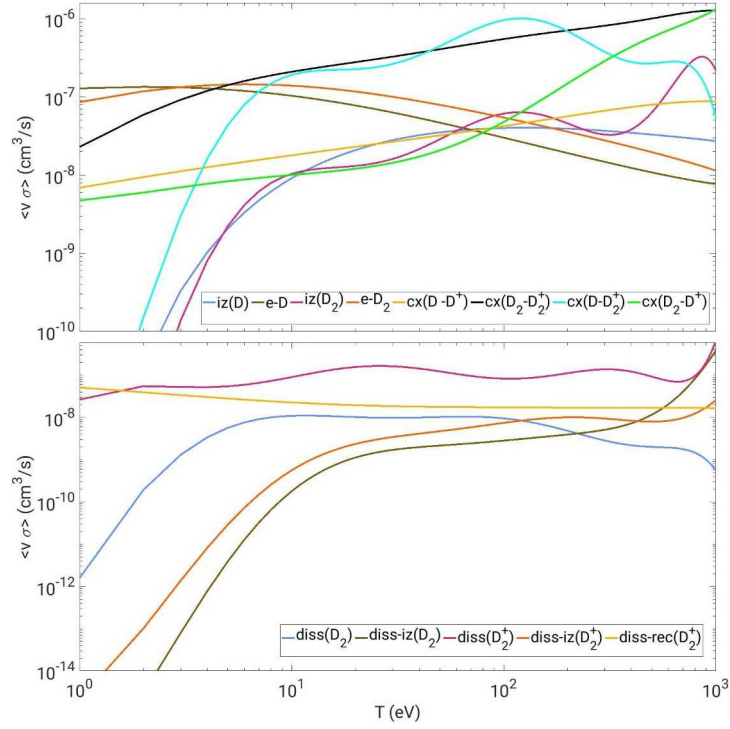


Figure 3.1: $\langle v\sigma \rangle$ product for the collisional processes considered in this chapter. Ionization processes, elastic collisions and charge-exchange processes are displayed on the top panel, dissociative reactions on the bottom panel. The $\langle v\sigma \rangle$ product is plotted as a function of the temperature of the colliding particle.

described by $3T_e/2 + m_e v_e^2/2 = T_{e,e-D} + m_e v_D^2/2$. The elastic collisions between electrons and D_2 are then described in a similar way. The re-emitted electrons have a distribution of velocities $\Phi_e[v_{D_2}, T_{e,e-D_2}]$, with $T_{e,e-D_2}$ obtained from an analogous conservation law, expressed as $3T_e/2 + m_e v_e^2/2 = T_{e,e-D_2} + m_e v_{D_2}^2/2$.

Considering the electrons generated by ionization of D, we assume that they are described by the Maxwellian distribution $\Phi_e[v_D, T_{e,iz(D)}]$ centered at the fluid velocity of the D atom v_D , with $T_{e,iz(D)}$ accounting for the ionization energy loss, $\langle E_{iz} \rangle$, its value being presented in Table 3.2. More precisely, $T_{e,iz(D)}$ satisfies the energy conservation law, $3T_e/2 + m_e v_e^2/2 = 2[T_{e,iz(D)} + m_e v_D^2/2] + \langle E_{iz,D} \rangle$, since the reaction gives rise to two electrons with the same properties. A similar approach is followed for the ionization of D_2 , with the two emitted electrons being described by a Maxwellian $\Phi_e[v_{D_2}, T_{e,iz(D_2)}]$ centered at the velocity of the D_2 molecules, v_{D_2} , and with temperature $T_{e,iz(D_2)}$ obtained from $3T_e/2 + m_e v_e^2/2 = 2[T_{e,iz(D_2)} + m_e v_{D_2}^2/2] + \langle E_{iz,D_2} \rangle$, with $\langle E_{iz,D_2} \rangle$ the average energy loss due to ionization of D_2 (see Table 3.2). We highlight that we neglect multi-step ionization processes when we compute the cross section for ionization of D and D_2 , adopting the same procedure for all the other reactions induced by impacting electrons, such as the dissociative processes.

We also apply the same procedure used for ionization processes to describe the properties of the electrons generated by dissociative processes. The electron created by dissociation of D_2 is described by the Maxwellian $\Phi_e[\mathbf{v}_{D_2}, T_{e,\text{diss}(D_2)}]$ centered around \mathbf{v}_{D_2} and with temperature $T_{e,\text{diss}(D_2)}$ obtained from $3T_e/2 + m_e v_{D_2}^2/2 = T_{e,\text{diss}(D_2)} + m_e v_{D_2}^2/2 + \langle E_{\text{diss},D_2} \rangle$. Regarding dissociation of D_2^+ , the resulting electron is analogously modelled by a Maxwellian $\Phi_e[\mathbf{v}_{D_2^+}, T_{e,\text{diss}(D_2^+)}]$ centered at the velocity of the D_2^+ ion and with temperature $T_{e,\text{diss}(D_2^+)}$ given by the corresponding energy conservation law expressed as $3T_e/2 + m_e v_{D_2^+}^2/2 = T_{e,\text{diss}(D_2^+)} + m_e v_{D_2^+}^2/2 + \langle E_{\text{diss},D_2^+} \rangle$. On the other hand, dissociative ionization of D_2 gives rise to two electrons, their Maxwellian distribution function, $\Phi_e[\mathbf{v}_{D_2}, T_{e,\text{diss-iz}(D_2)}]$, being centered around the D_2 velocity, \mathbf{v}_{D_2} , and characterized by a temperature $T_{e,\text{diss-iz}(D_2)}$, obtained from $3T_e/2 + m_e v_{D_2}^2/2 = 2 \left[T_{e,\text{diss-iz}(D_2)} + m_e v_{D_2}^2/2 \right] + \langle E_{\text{diss-iz},D_2} \rangle$. Similarly, we assume that the electrons generated by dissociative ionization of D_2^+ are described by a Maxwellian $\Phi_e[\mathbf{v}_{D_2^+}, T_{e,\text{diss-iz}(D_2^+)}]$ centered at $\mathbf{v}_{D_2^+}$ and with temperature $T_{e,\text{diss-iz}(D_2^+)}$ obtained from energy conservation, $3T_e/2 + m_e v_{D_2^+}^2/2 = 2 \left[T_{e,\text{diss-iz}(D_2^+)} + m_e v_{D_2^+}^2/2 \right] + \langle E_{\text{diss-iz},D_2^+} \rangle$.

The evaluation of the temperature of the D atoms and D^+ ions released from dissociative reactions is based on the modelling of these reactions as Franck-Condon dissociation processes. These temperatures are summarized in Table 3.2 and rely on data from Ref. [85]. The calculations are detailed in the App. B. We highlight that the values for the average electron energy loss due to dissociative processes take into account the energy lost by an electron when exciting the D_2 molecule or D_2 molecular ion before dissociation takes place. This contrasts with other work (see e.g. Ref. [46]) where the energy inherent to the dissociation process is taken into account. Our approach is justified by the fact that the effective electron energy loss associated with a given dissociative process accounts for the energy required to excite the molecule, which, in turn, comprises the energy cost of dissociation, the kinetic energy of the products and the radiation emitted due to deexcitation of the products. We also highlight that these particles are emitted isotropically in the frame of the centre of mass of the incoming D_2 or D_2^+ particle. Thus, we assume that the D atoms generated by dissociation of D_2 molecules, for example, follow a Maxwellian distribution $\Phi_D[\mathbf{v}_{D_2}, T_{D,\text{diss}(D_2)}]$. Similarly, we describe the neutral D atoms and D^+ ions produced by dissociative-ionization of D_2 molecules by the Maxwellian distributions $\Phi_D[\mathbf{v}_{D_2}, T_{D,\text{diss-iz}(D_2)}]$ and $\Phi_{D^+}[\mathbf{v}_{D_2}, T_{D,\text{diss-iz}(D_2)}]$ respectively, with the temperature $T_{D,\text{diss-iz}(D_2)}$ listed in Table 3.2 and evaluated in App. B. In turn, $\Phi_D[\mathbf{v}_{D_2^+}, T_{D,\text{diss}(D_2^+)}]$ and $\Phi_{D^+}[\mathbf{v}_{D_2^+}, T_{D,\text{diss}(D_2^+)}]$ are the Maxwellian distributions of D atoms and D^+ ions generated by dissociation of D_2^+ ions, where $\mathbf{v}_{D_2^+}$ denotes the fluid velocity of the D_2^+ ion population that includes the leading order components (see Sec. 3.3). Moreover, dissociative-ionization of D_2^+ gives rise to D^+ ions that are described by a Maxwellian distribution $\Phi_{D^+}[\mathbf{v}_{D_2^+}, T_{D,\text{diss-iz}(D_2^+)}]$. Finally, we remark that the D atoms and D^+ generated by dissociative-recombination of D_2^+ are described by the Maxwellian distributions $\Phi_D[\mathbf{v}_{D_2^+}, T_{D,\text{diss-rec}(D_2^+)}]$ and $\Phi_{D^+}[\mathbf{v}_{D_2^+}, T_{D,\text{diss-rec}(D_2^+)}]$ respectively, with $T_{D,\text{diss-rec}(D_2^+)}$ denoting the average thermal energy of the reaction products.

3.3. The three-fluid drift-reduced Braginskii equations

Table 3.2: Average electron energy loss and average energy of reaction products for the ionization and dissociative processes included in the model.

| Collisional process | e^- Energy loss | Temperature of products |
|--|--|--|
| Ionization of D | $\langle E_{iz,D} \rangle = 13.60\text{eV}$ | _____ |
| Ionization of D_2 | $\langle E_{iz,D_2} \rangle = 15.43\text{eV}$ | _____ |
| Dissociation of D_2 | $\langle E_{diss,D_2} \rangle \simeq 14.3\text{eV}$ | $T_{D,diss(D_2)} \simeq 1.95\text{eV}$ |
| Dissociative ionization of D_2 ($E_e < 26\text{eV}$) | $\langle E_{diss-iz,D_2} \rangle \simeq 18.25\text{eV}$ | $T_{D,diss-iz(D_2)} \simeq 0.25\text{eV}$ |
| Dissociative ionization of D_2 ($E_e > 26\text{eV}$) | $\langle E_{diss-iz,D_2} \rangle \simeq 33.6\text{eV}$ | $T_{D,diss-iz(D_2)} \simeq 7.8\text{eV}$ |
| Dissociation of D_2^+ | $\langle E_{diss,D_2^+} \rangle \simeq 13.7\text{eV}$ | $T_{D,diss(D_2^+)} \simeq 3.0\text{eV}$ |
| Dissociative ionization of D_2^+ | $\langle E_{diss-iz,D_2^+} \rangle \simeq 15.5\text{eV}$ | $T_{D,diss-iz(D_2^+)} \simeq 0.4\text{eV}$ |
| Dissociative recombination of D_2^+ | _____ | $T_{D,diss-rec(D_2^+)} \simeq 11.7\text{eV}$ |

3.3 The three-fluid drift-reduced Braginskii equations

The plasma turbulent dynamics is described by a fluid model based on a Braginskii set of equations for each plasma species. Their derivation starts from the kinetic equations for e^- , D^+ and D_2^+ , which must include the terms arising from the neutral-plasma interactions. These equations generalise the ones considered in the single-ion species model introduced in Refs. [34, 61], by adding the new collisional terms listed in Table 3.1, as well as an equation describing the D_2^+ ions. The kinetic equations yield

$$\begin{aligned}
\frac{\partial f_e}{\partial t} + \mathbf{v} \cdot \frac{\partial f_e}{\partial \mathbf{x}} + \mathbf{a} \cdot \frac{f_e}{\partial \mathbf{v}} = & \nu_{iz,D} n_D \left[2\Phi_e[\mathbf{v}_D, T_{e,iz(D)}] - \frac{f_e}{n_e} \right] \\
& + \nu_{e-D} n_D \left[\Phi_e[\mathbf{v}_D, T_{e,en(D)}] - \frac{f_e}{n_e} \right] - \nu_{rec,D^+} \frac{n_{D^+}}{n_e} f_e + \nu_{iz,D_2} n_{D_2} \left[2\Phi_e[\mathbf{v}_{D_2}, T_{e,iz(D_2)}] - \frac{f_e}{n_e} \right] \\
& + \nu_{e-D_2} n_{D_2} \left[\Phi_e[\mathbf{v}_{D_2}, T_{e,en(D_2)}] - \frac{f_e}{n_e} \right] - \nu_{rec,D_2^+} \frac{n_{D_2^+}}{n_e} f_e \\
& + \nu_{diss,D_2} n_{D_2} \left[\Phi_e[\mathbf{v}_{D_2}, T_{e,diss(D_2)}] - \frac{f_e}{n_e} \right] + \nu_{diss-iz,D_2} n_{D_2} \left[2\Phi_e[\mathbf{v}_{D_2}, T_{e,diss-iz(D_2)}] - \frac{f_e}{n_e} \right] \\
& + \nu_{diss-iz,D_2^+} n_{D_2^+} \left[2\Phi_e[\mathbf{v}_{D_2^+}, T_{e,diss-iz(D_2^+)}] - \frac{f_e}{n_e} \right] \\
& + \nu_{diss,D_2^+} n_{D_2^+} \left[\Phi_e[\mathbf{v}_{D_2^+}, T_{e,diss(D_2^+)}] - \frac{f_e}{n_e} \right] - \nu_{diss-rec,D_2^+} n_{D_2^+} \frac{f_e}{n_e} + C(f_e),
\end{aligned} \tag{3.1}$$

$$\begin{aligned}
\frac{\partial f_{D^+}}{\partial t} + \mathbf{v} \cdot \frac{\partial f_{D^+}}{\partial \mathbf{x}} + \mathbf{a} \cdot \frac{f_{D^+}}{\partial \mathbf{v}} = & \nu_{iz,D} f_D - \nu_{rec,D^+} f_{D^+} \\
& - \nu_{cx,D} \left(\frac{n_D}{n_{D^+}} f_{D^+} - f_D \right) + \nu_{cx,D-D_2^+} f_D - \nu_{cx,D_2-D^+} \frac{n_{D_2}}{n_{D^+}} f_{D^+} \\
& + \nu_{diss-iz,D_2} f_{D_2} + 2\nu_{diss-iz,D_2^+} f_{D_2^+} + \nu_{diss,D_2^+} f_{D_2^+} + C(f_{D^+}),
\end{aligned} \tag{3.2}$$

and

$$\begin{aligned}
 \frac{\partial f_{D_2^+}}{\partial t} + \mathbf{v} \cdot \frac{\partial f_{D_2^+}}{\partial \mathbf{x}} + \mathbf{a} \cdot \frac{\partial f_{D_2^+}}{\partial \mathbf{v}} &= \nu_{iz,D_2} f_{D_2} - \nu_{rec,D_2^+} f_{D_2^+} \\
 - \nu_{cx,D_2} \left(\frac{n_{D_2}}{n_{D_2^+}} f_{D_2^+} - f_{D_2} \right) &- \nu_{cx,D_2-D^+} f_{D_2} - \nu_{cx,D-D_2^+} \frac{n_D}{n_{D_2^+}} f_{D_2^+} \\
 - \left(\nu_{diss-iz,D_2^+} + \nu_{diss,D_2^+} + \nu_{diss-rec,D_2^+} \right) f_{D_2^+} &+ C(f_{D_2^+}).
 \end{aligned} \tag{3.3}$$

In Eqs. (3.1-3.3), \mathbf{v} denotes the particle velocity, \mathbf{a} the particle acceleration due to the Lorentz Force, and $\partial/\partial \mathbf{x}$ the gradient in real space and $\partial/\partial \mathbf{v}$ in the velocity space. The $C(f_e)$, $C(f_{D^+})$ and $C(f_{D_2^+})$ terms refer to the Coulomb collisions between charged particles influencing the e , D^+ and D_2^+ distribution functions, respectively.

The three-fluid Braginskii equations (for a plasma featuring e^- , D^+ and D_2^+) are obtained by computing the first three moments of the kinetic equations for each species in the limit $\Omega_{cD^+} \tau_{D^+} \gg 1$, with $\Omega_{cD^+} = eB/m_{D^+}$ the cyclotron frequency (m_{D^+} stands for the D^+ ion mass and e represents the elementary charge) and τ_{D^+} the characteristic Coulomb collision time for D^+ ions. The Braginskii equations, including the neutral-plasma interaction terms, can be derived by following the steps presented in Ref. [48], taking the form

$$\begin{aligned}
 \frac{\partial n_e}{\partial t} + \nabla \cdot (n_e \mathbf{v}_e) &= n_D \nu_{iz,D} - n_{D^+} \nu_{rec,D^+} + n_{D_2} \nu_{iz,D_2} - n_{D_2^+} \nu_{rec,D_2^+} \\
 + n_{D_2} \nu_{diss-iz,D_2} + n_{D_2^+} \nu_{diss-iz,D_2^+} - n_{D_2^+} \nu_{diss-rec,D_2^+},
 \end{aligned} \tag{3.4}$$

$$\begin{aligned}
 \frac{\partial n_{D^+}}{\partial t} + \nabla \cdot (n_{D^+} \mathbf{v}_{D^+}) &= n_D \nu_{iz,D} - n_{D^+} \nu_{rec,D^+} + n_D \nu_{cx,D-D_2^+} - n_{D_2} \nu_{cx,D_2-D^+} \\
 + n_{D_2} \nu_{diss-iz,D_2} + n_{D_2^+} (2\nu_{diss-iz,D_2^+} + \nu_{diss,D_2^+}),
 \end{aligned} \tag{3.5}$$

$$\begin{aligned}
 \frac{\partial n_{D_2^+}}{\partial t} + \nabla \cdot (n_{D_2^+} \mathbf{v}_{D_2^+}) &= n_{D_2} \nu_{iz,D_2} - n_{D_2^+} \nu_{rec,D_2^+} + n_{D_2} \nu_{cx,D_2-D^+} - n_D \nu_{cx,D-D_2^+} \\
 - n_{D_2^+} (\nu_{diss-iz,D_2^+} + \nu_{diss,D_2^+} + \nu_{diss-rec,D_2^+}),
 \end{aligned} \tag{3.6}$$

$$\begin{aligned}
 m_e n_e \frac{d_e v_{e\alpha}}{dt} &= -\frac{\partial p_e}{\partial x_\alpha} - \frac{\partial \Pi_{e\alpha\beta}}{\partial x_\beta} - e n_e [E_\alpha + (\mathbf{v}_e \times \mathbf{B})_\alpha] + R_{e\alpha} \\
 + m_e [n_D (2\nu_{iz,D} + \nu_{e-D}) (v_{D\alpha} - v_{e\alpha}) + n_{D_2} (2\nu_{iz,D_2} + \nu_{e-D_2}) (v_{D_2\alpha} - v_{e\alpha}) \\
 + 2n_{D_2} \nu_{diss-iz,D_2} (v_{D_2\alpha} - v_{e\alpha}) + 2\nu_{diss-iz,D_2^+} n_{D_2^+} (v_{D_2^+\alpha} - v_{e\alpha}) \\
 + n_{D_2^+} \nu_{diss,D_2^+} (v_{D_2^+\alpha} - v_{e\alpha}) + n_{D_2} \nu_{diss,D_2} (v_{D_2\alpha} - v_{e\alpha})],
 \end{aligned} \tag{3.7}$$

3.3. The three-fluid drift-reduced Braginskii equations

$$\begin{aligned}
m_D n_{D^+} \frac{d_{D^+} v_{D^+ \alpha}}{dt} &= -\frac{\partial p_{D^+}}{\partial x_\alpha} - \frac{\partial \Pi_{D^+ \alpha \beta}}{\partial x_\beta} + e n_{D^+} [E_\alpha + (\mathbf{v}_{D^+} \times \mathbf{B})_\alpha] + R_{D^+ \alpha} \\
&+ m_D \left[n_D (v_{iz,D} + v_{cx,D} + v_{cx,D-D_2^+}) (v_{D\alpha} - v_{D^+ \alpha}) + n_{D_2} v_{diss-iz,D_2} (v_{D_2 \alpha} - v_{D^+ \alpha}) \right. \\
&\left. + n_{D_2^+} (2v_{diss-iz,D_2^+} + v_{diss,D_2^+}) (v_{D_2^+ \alpha} - v_{D^+ \alpha}) \right], \tag{3.8}
\end{aligned}$$

$$\begin{aligned}
m_{D_2} n_{D_2^+} \frac{d_{D_2^+} v_{D_2^+ \alpha}}{dt} &= -\frac{\partial p_{D_2^+}}{\partial x_\alpha} - \frac{\partial \Pi_{D_2^+ \alpha \beta}}{\partial x_\beta} + e n_{D_2^+} [E_\alpha + (\mathbf{v}_{D_2^+} \times \mathbf{B})_\alpha] + R_{D_2^+ \alpha} \\
&+ m_{D_2} n_{D_2} (v_{iz,D_2} + v_{cx,D_2} + v_{cx,D_2-D^+}) (v_{D_2 \alpha} - v_{D_2^+ \alpha}), \tag{3.9}
\end{aligned}$$

$$\begin{aligned}
\frac{3}{2} n_e \frac{d_e T_e}{dt} + p_e \nabla \cdot \mathbf{v}_e &= -\nabla \cdot \mathbf{q}_e - \Pi_{e\alpha\beta} \frac{\partial v_{e\beta}}{\partial x_\alpha} + Q_e \\
&+ n_D v_{iz,D} \left[-E_{iz,D} - \frac{3}{2} T_e + \frac{3}{2} m_e \mathbf{v}_e \cdot \left(\mathbf{v}_e - \frac{4}{3} \mathbf{v}_D \right) \right] - n_D v_{e-D} m_e \mathbf{v}_e \cdot (\mathbf{v}_D - \mathbf{v}_e) \\
&+ n_{D_2} v_{iz,D_2} \left[-E_{iz,D_2} - \frac{3}{2} T_e + \frac{3}{2} m_e \mathbf{v}_e \cdot \left(\mathbf{v}_e - \frac{4}{3} \mathbf{v}_{D_2} \right) \right] - n_{D_2} v_{e-D_2} m_e \mathbf{v}_e \cdot (\mathbf{v}_{D_2} - \mathbf{v}_e) \\
&+ n_{D_2} v_{diss,D_2} [-E_{diss,D_2} + m_e \mathbf{v}_e \cdot (\mathbf{v}_e - \mathbf{v}_{D_2})] \\
&+ n_{D_2} v_{diss-iz,D_2} \left[-E_{diss-iz,D_2} - \frac{3}{2} T_e + \frac{3}{2} m_e \mathbf{v}_e \cdot \left(\mathbf{v}_e - \frac{4}{3} \mathbf{v}_{D_2} \right) \right] \\
&+ n_{D_2^+} v_{diss,D_2^+} \left[-E_{diss,D_2^+} + m_e \mathbf{v}_e \cdot (\mathbf{v}_e - \mathbf{v}_{D_2^+}) \right] \\
&+ n_{D_2^+} v_{diss-iz,D_2^+} \left[-E_{diss-iz,D_2^+} - \frac{3}{2} T_e + \frac{3}{2} m_e \mathbf{v}_e \cdot \left(\mathbf{v}_e - \frac{4}{3} \mathbf{v}_{D_2^+} \right) \right], \tag{3.10}
\end{aligned}$$

$$\begin{aligned}
\frac{3}{2} n_{D^+} \frac{d_{D^+} T_{D^+}}{dt} + p_{D^+} \nabla \cdot \mathbf{v}_{D^+} &= -\nabla \cdot \mathbf{q}_{D^+} - \Pi_{D^+ \alpha \beta} \frac{\partial v_{D^+ \beta}}{\partial x_\alpha} + Q_{D^+} \\
&+ n_D (v_{iz,D} + v_{cx,D} + v_{cx,D-D_2^+}) \left[\frac{3}{2} (T_D - T_{D^+}) + \frac{m_{D^+}}{2} (\mathbf{v}_D - \mathbf{v}_{D^+})^2 \right] \\
&+ n_{D_2} v_{diss-iz,D_2} \left[\frac{3}{2} (T_{D^+,diss-iz(D_2)} - T_{D^+}) + \frac{m_{D^+}}{2} (\mathbf{v}_{D_2} - \mathbf{v}_{D^+})^2 \right] \\
&+ 2n_{D_2^+} v_{diss-iz,D_2^+} \left[\frac{3}{2} (T_{D^+,diss-iz(D_2^+)} - T_{D^+}) + \frac{m_{D^+}}{2} (\mathbf{v}_{D_2^+} - \mathbf{v}_{D^+})^2 \right] \\
&+ n_{D_2^+} v_{diss,D_2^+} \left[\frac{3}{2} (T_{D^+,diss(D_2^+)} - T_{D^+}) + \frac{m_{D^+}}{2} (\mathbf{v}_{D_2^+} - \mathbf{v}_{D^+})^2 \right], \tag{3.11}
\end{aligned}$$

$$\begin{aligned}
\frac{3}{2} n_{D_2^+} \frac{d_{D_2^+} T_{D_2^+}}{dt} + p_{D_2^+} \nabla \cdot \mathbf{v}_{D_2^+} &= -\nabla \cdot \mathbf{q}_{D_2^+} - \Pi_{D_2^+ \alpha \beta} \frac{\partial v_{D_2^+ \beta}}{\partial x_\alpha} + Q_{D_2^+} \\
&+ n_{D_2} (v_{cx,D_2} + v_{iz,D_2} + v_{cx,D_2-D^+}) \left[\frac{3}{2} (T_{D_2^+} - T_{D_2^+}) + \frac{m_{D_2^+}}{2} (\mathbf{v}_{D_2} - \mathbf{v}_{D_2^+})^2 \right], \tag{3.12}
\end{aligned}$$

where $\Pi_{e\alpha\beta}$ denotes the component of the stress tensor along the α and β directions, \mathbf{R}_e the friction force acting on the electrons, \mathbf{q}_e the electron heat flux density, Q_e the electron heat

Chapter 3. A multi-component model of plasma turbulence and kinetic neutral dynamics

generated by Coulomb collisions and $d_e/dt = \partial/\partial t + (\mathbf{v}_e \cdot \nabla)$ the electron advective derivative. The equivalent notation is used for the D^+ and D_2^+ species.

Similarly to what was done in the derivation of the single-ion species model presented in Ch. 2, we consider the $d/dt \ll \Omega_{cD^+}$ and $k_\perp \rho_{D^+} \ll 1$ orderings, which are valid in typical conditions of the tokamak boundary. This leads to the derivation of the drift-limit of the Braginskii equations, keeping only leading order components in $(1/\Omega_{cD^+})d/dt$ in the electron perpendicular velocity, i.e. $\mathbf{v}_{\perp e} = \mathbf{v}_{\perp e0} = \mathbf{v}_{E \times B} + \mathbf{v}_{de}$, with $\mathbf{v}_{E \times B} = (\mathbf{E} \times \mathbf{B})/B^2$ the $E \times B$ drift and $\mathbf{v}_{de} = (\mathbf{B} \times \nabla p_e)/(en_e B^2)$ the electron diamagnetic drift, thus neglecting electron inertia. The D^+ perpendicular velocity is analogously decomposed as $\mathbf{v}_{\perp D^+} = \mathbf{v}_{\perp D^+0} + \mathbf{v}_{pol,D^+} + \mathbf{v}_{fric,D^+}$, where the leading order perpendicular velocity,

$$\mathbf{v}_{\perp D^+0} = \mathbf{v}_{E \times B} + \mathbf{v}_{dD^+}, \quad (3.13)$$

is defined as the sum of the $E \times B$ drift and the diamagnetic drift, $\mathbf{v}_{dD^+} = (\mathbf{B} \times \nabla p_{D^+})/(en_{D^+} B^2)$. The polarization drift,

$$\mathbf{v}_{pol,D^+} = -\frac{1}{n_{D^+} \Omega_{cD^+}} \frac{d_{D^+}}{dt} \left(\frac{n_{D^+}}{B} \nabla_\perp \phi + \frac{1}{B} \nabla_\perp p_{D^+} \right) + \frac{1}{m_{D^+} n_{D^+} \Omega_{cD^+}} \mathbf{b} \times \left[G_{D^+} \mathbf{k} - \frac{\nabla G_{D^+}}{3} \right], \quad (3.14)$$

is of higher order than $\mathbf{v}_{\perp D^+0}$ in the $d/dt \ll \Omega_{cD^+}$ expansion, as it is shown in Ref. [48]. The drift velocity due to friction between D^+ ions and the other species,

$$\begin{aligned} \mathbf{v}_{fric,D^+} = & \frac{n_D}{n_{D^+}} \frac{\nu_{cx,D} + \nu_{iz,D} + \nu_{cx,D-D_2^+}}{\Omega_{cD^+}} (\mathbf{v}_{\perp D} - \mathbf{v}_{\perp D^+0}) \times \mathbf{b} + \frac{n_{D_2}}{n_{D^+}} \frac{\nu_{iz-diss,D_2}}{\Omega_{cD^+}} (\mathbf{v}_{\perp D_2} - \mathbf{v}_{\perp D^+0}) \times \mathbf{b} \\ & + \frac{n_{D_2^+}}{n_{D^+}} \frac{2\nu_{diss-iz,D_2^+} + \nu_{diss,D_2^+}}{\Omega_{cD^+}} (\mathbf{v}_{\perp D_2^+0} - \mathbf{v}_{\perp D^+0}) \times \mathbf{b}, \end{aligned} \quad (3.15)$$

is of higher order in $(1/\Omega_{cD^+})d/dt$, too. This term features contributions from collisions of D^+ with D , D_2 and D_2^+ particles. Assuming $\nu_D \lesssim \nu_{D^+}$, $\nu_{D_2} \lesssim \nu_{D^+}$ and $\nu_{D_2^+} \lesssim \nu_{D^+}$, and noticing that $\nu/\Omega_{cD^+} \ll 1$, we obtain $\nu_{fric,D^+} \sim (\nu/\Omega_{cD^+})\nu_{D^+} \ll \nu_{D^+}$. Hence, we approximate \mathbf{v}_{D^+} and $\mathbf{v}_{D_2^+}$ with their respective leading order components, i.e. $\mathbf{v}_{\perp D^+} \simeq \mathbf{v}_{\perp D^+0}$ and $\mathbf{v}_{\perp D_2^+} \simeq \mathbf{v}_{\perp D_2^+0}$, in Eq. (3.15). In Eqs. (3.14) and (3.15), the gyroviscous term for D^+ ions, $G_{D^+} = -\eta_{0D^+} [2\nabla_\parallel \nu_{\parallel D^+} + C(\phi)/B + C(p_{D^+})/(Z_{D^+} n_{D^+} B)]$, the D^+ viscosity η_{0D^+} , is introduced, as well as the magnetic field curvature vector $\mathbf{k} = (\mathbf{b} \cdot \nabla) \mathbf{b}$, the gradient along the magnetic field $\nabla_\parallel = \mathbf{b} \cdot \nabla$, the gradient perpendicular to the magnetic field $\nabla_\perp = \nabla - \mathbf{b} \nabla_\parallel$ and the magnetic field unit vector $\mathbf{b} = \mathbf{B}/B$.

A similar approach is followed when deriving the drift-limit of the D_2^+ velocity, as the $d/dt \ll$

3.3. The three-fluid drift-reduced Braginskii equations

$\Omega_{cD_2^+}$ ordering remains valid in typical tokamak boundary conditions. The perpendicular velocity of D_2^+ ions is therefore written as $\mathbf{v}_{\perp D_2^+} = \mathbf{v}_{\perp D_2^+ 0} + \mathbf{v}_{\text{pol}, D_2^+} + \mathbf{v}_{\text{fric}, D_2^+}$, with

$$\mathbf{v}_{\perp D_2^+ 0} = \mathbf{v}_{E \times B} + \mathbf{v}_{dD_2^+} \quad (3.16)$$

the leading order component, with $\mathbf{v}_{dD_2^+} = (\mathbf{B} \times \nabla p_{D_2^+}) / (en_{D_2^+} B^2)$. We remind that $\mathbf{v}_{\text{pol}, D_2^+}$ is the polarization drift velocity and $\mathbf{v}_{\text{fric}, D_2^+}$ denotes the drift velocity arising from friction between D_2^+ ions and other species. Their respective expressions are

$$\mathbf{v}_{\text{pol}, D_2^+} = -\frac{1}{n_{D_2^+} \Omega_{cD_2^+}} \frac{d_{D_2^+}}{dt} \left(\frac{n_{D_2^+}}{B} \nabla_{\perp} \phi + \frac{1}{B} \nabla_{\perp} p_{D_2^+} \right) + \frac{1}{m_{D_2^+} n_{D_2^+} \Omega_{cD_2^+}} \mathbf{b} \times \left[G_{D_2^+} \mathbf{k} - \frac{\nabla G_{D_2^+}}{3} \right], \quad (3.17)$$

and

$$\mathbf{v}_{\text{fric}, D_2^+} = \frac{n_{D_2}}{n_{D_2^+}} \frac{v_{iz, D_2} + v_{cx, D_2} + v_{cx, D_2-D^+}}{\Omega_{cD_2^+}} \left(\mathbf{v}_{\perp D_2} - \mathbf{v}_{\perp D_2^+ 0} \right) \times \mathbf{b}, \quad (3.18)$$

with $G_{D_2^+} = -\eta_{0D_2^+} \left[2\nabla_{\parallel} v_{\parallel D_2^+} + C(\phi)/B + C(p_{D_2^+})/(n_{D_2^+} B) \right]$ the D_2^+ gyroviscous term and $\eta_{0D_2^+}$ the corresponding viscosity. We note that approximation $\mathbf{v}_{\perp D_2} \simeq \mathbf{v}_{\perp D_2^+ 0}$ is used in Eq. (3.18).

To obtain an expression for the parallel friction forces and parallel heat fluxes and close the Braginskii equations, we apply the collisional closure developed by Zhdanov in Ref. [65], following the formulation presented in Refs. [66, 93], which facilitates the numerical implementation. The use of this procedure in the context of the multi-species plasma considered in the present chapter is detailed in App. C, where we make use of the fact that the $n_{D_2^+}$ is significantly smaller than the n_{D^+} , i.e. $n_{D_2^+}/n_{D^+} \ll 1$, for typical tokamak boundary conditions, which in turn allows us to write $n_e \simeq n_{D^+}$ thanks to quasi-neutrality. On the other hand, the contributions from the perpendicular components of the heat fluxes in the terms $\nabla \cdot \mathbf{q}_e$ and $\nabla \cdot \mathbf{q}_{D^+}$ appearing in the T_e and T_{D^+} equations, respectively, are evaluated by assuming the $\Omega_{ce} \tau_e \gg 1$, $\omega_{D^+} \tau_{cD^+} \gg 1$ limits (typical time between collisions considerably larger than cyclotron frequency), which significantly simplifies the expressions, following the same approach described in [17] and in agreement with the single-ion species model [33, 34]. This approach is generalised to evaluate the term arising from the perpendicular component of $\nabla \cdot \mathbf{q}_{D_2^+}$ in the $T_{D_2^+}$ equation, Eq. (3.12). We also highlight that the collisional heat exchange terms, i.e. Q_e , Q_{D^+} and $Q_{D_2^+}$, in Eqs. (3.10-3.12), are neglected in the derivation of the drift-limit of the Braginskii equations, as they are assumed to be of higher order in ρ_{s0}/R_0 , similarly to the single-component GBS model presented in Refs. [33, 34] and in Ch. 2 of this thesis.

Therefore, the drift-reduced Braginskii system of equations includes the continuity equation for the electron species, the continuity equation for the D_2^+ species, the vorticity equations

Chapter 3. A multi-component model of plasma turbulence and kinetic neutral dynamics

that ensures quasi-neutrality, $n_e = n_{D^+} + n_{D_2^+}$, and the equations for the parallel velocities and temperature of all species. They take the form

$$\begin{aligned} \frac{\partial n_e}{\partial t} = & -\frac{\rho_*^{-1}}{B} [\phi, n_e] + \frac{2}{B} [C(p_e) - n_e C(\phi)] - \nabla \cdot (n_e v_{\parallel e} \mathbf{b}) + \mathcal{D}_{n_e} \nabla_{\perp}^2 n_e + S_{n_e} \\ & + n_D v_{iz,D} - n_{D^+} v_{rec,D^+} + n_{D_2} v_{iz,D_2} - n_{D_2^+} v_{rec,D_2^+} \\ & + n_{D_2} v_{diss-iz,D_2} + n_{D_2^+} v_{diss-iz,D_2^+} - n_{D_2^+} v_{diss-rec,D_2^+}, \end{aligned} \quad (3.19)$$

$$\begin{aligned} \frac{\partial n_{D_2^+}}{\partial t} = & -\frac{\rho_*^{-1}}{B} [\phi, n_{D_2^+}] - \nabla \cdot (n_{D_2^+} v_{\parallel D_2^+} \mathbf{b}) - \frac{2}{B} [n_{D_2^+} C(T_{D_2^+}) + T_{D_2^+} C(n_{D_2^+}) + n_{D_2^+} C(\phi)] \\ & + \mathcal{D}_{n_{D_2^+}} \nabla_{\perp}^2 n_{D_2^+} + S_{n_{D_2^+}} + n_{D_2} v_{iz,D_2} - n_{D_2^+} v_{rec,D_2^+} + n_{D_2} v_{cx,D_2-D^+} - n_D v_{cx,D-D^+} \\ & - n_{D_2^+} (v_{diss-iz,D_2^+} + v_{diss,D_2^+} + v_{diss-rec,D_2^+}), \end{aligned} \quad (3.20)$$

$$\begin{aligned} \frac{\partial \Omega}{\partial t} = & -\nabla \cdot \left[\frac{\rho_*^{-1}}{B} ([\phi, B\Omega_{D^+}] + 2[\phi, B\omega_{D_2^+}]) \right] - \nabla \cdot \left[\frac{v_{\parallel D^+}}{B} \nabla_{\parallel} (B\Omega_{D^+}) + \frac{v_{\parallel D_2^+}}{B} \nabla_{\parallel} (B\omega_{D_2^+}) \right] \\ & + \frac{2}{B} [n_e C(T_e) + T_e C(n_e) + n_{D^+} C(T_{D^+}) + T_{D^+} C(n_{D^+}) + n_{D_2^+} C(T_{D_2^+}) + T_{D_2^+} C(n_{D_2^+})] \\ & + \nabla \cdot (j_{\parallel} \mathbf{b}) + \left[\nabla G_{D^+} \cdot \left(\frac{\mathbf{b} \times \mathbf{k}}{B} \right) + G_{D^+} \nabla \cdot \left(\frac{\mathbf{b} \times \mathbf{k}}{B} \right) - \frac{2}{3B} C(G_{D^+}) \right] \\ & + \left[\nabla G_{D_2^+} \cdot \left(\frac{\mathbf{b} \times \mathbf{k}}{B} \right) + G_{D_2^+} \nabla \cdot \left(\frac{\mathbf{b} \times \mathbf{k}}{B} \right) - \frac{2}{3B} C(G_{D_2^+}) \right] + \eta_{0\Omega} \nabla_{\parallel}^2 \Omega + \mathcal{D}_{\perp\Omega} \nabla_{\perp}^2 \Omega \\ & - \nabla \cdot \left[\frac{2n_{D_2}}{n_{D_2^+}} (v_{cx,D_2} + v_{iz,D_2} + v_{cx,D_2-D^+}) \omega_{D_2^+} \right] - \nabla \cdot \left[\frac{n_D}{n_{D^+}} (v_{cx,D} + v_{iz,D} + v_{cx,D-D^+}) \omega_{D^+} \right] \\ & - \nabla \cdot \left[\frac{n_{D_2}}{n_{D^+}} v_{di-iz,D_2} \omega_{D^+} \right] + \nabla \cdot \left[\frac{n_{D_2^+}}{n_{D^+}} (2v_{di-iz,D_2^+} + v_{di,D_2^+}) (\omega_{D_2^+} - \omega_{D^+}) \right], \end{aligned} \quad (3.21)$$

$$\begin{aligned} \frac{\partial v_{\parallel e}}{\partial t} = & -\frac{\rho_*^{-1}}{B} [\phi, v_{\parallel e}] - v_{\parallel e} \nabla_{\parallel} v_{\parallel e} + \frac{m_D}{m_e} \left[\nabla_{\parallel} \phi - \frac{\nabla_{\parallel} p_e}{n_e} - \frac{2}{3n_e} \nabla_{\parallel} G_e - 0.71 \nabla_{\parallel} T_e \right] \\ & - \frac{m_D}{m_e} v (v_{\parallel e} - v_{\parallel D^+}) + \mathcal{D}_{v_{\parallel e}} \nabla_{\perp}^2 v_{\parallel e} + \frac{1}{n_e} [n_D (2v_{iz,D} + v_{e-D}) (v_{\parallel D} - v_{\parallel e}) \\ & + n_{D_2} (2v_{iz,D_2} + v_{e-D_2}) (v_{\parallel D_2} - v_{\parallel e}) + n_{D_2} (2v_{diss-iz,D_2} + v_{diss,D_2}) (v_{\parallel D_2} - v_{\parallel e}) \\ & + n_{D_2^+} (2v_{diss-iz,D_2^+} + v_{diss,D_2^+}) (v_{\parallel D_2^+} - v_{\parallel e})], \end{aligned} \quad (3.22)$$

$$\begin{aligned}
 \frac{\partial v_{\parallel D^+}}{\partial t} = & -\frac{\rho_*^{-1}}{B}[\phi, v_{\parallel D^+}] - v_{\parallel D^+} \nabla_{\parallel} v_{\parallel D^+} - \nabla_{\parallel} \phi - \frac{\nabla_{\parallel} p_D^+}{n_{D^+}} - \frac{2}{3n_{D^+}} \nabla_{\parallel} G_{D^+} + 0.71 \frac{n_e}{n_{D^+}} \nabla_{\parallel} T_e \\
 & - v \frac{n_e}{n_{D^+}} (v_{\parallel D^+} - v_{\parallel e}) + \mathcal{D}_{v_{\parallel D^+}} \nabla_{\perp}^2 v_{\parallel D^+} + \frac{1}{n_{D^+}} \left[n_D (v_{iz,D} + v_{cx,D} + v_{cx,D-D_2^+}) (v_{\parallel D} - v_{\parallel D^+}) \right. \\
 & \left. + n_{D_2^+} v_{\text{diss-iz},D_2} (v_{\parallel D_2} - v_{\parallel D^+}) + n_{D_2^+} (2v_{\text{diss-iz},D_2^+} + v_{\text{diss},D_2^+}) (v_{\parallel D_2^+} - v_{\parallel D^+}) \right], \quad (3.23)
 \end{aligned}$$

$$\begin{aligned}
 \frac{\partial v_{\parallel D_2^+}}{\partial t} = & -\frac{\rho_*^{-1}}{B}[\phi, v_{\parallel D_2^+}] - v_{\parallel D_2^+} \nabla_{\parallel} v_{\parallel D_2^+} + \frac{1}{2} \left[-\nabla_{\parallel} \phi - \frac{\nabla p_{D_2^+}}{n_{D_2^+}} - \frac{2}{3n_{D_2^+}} \nabla_{\parallel} G_{D_2^+} \right] \\
 & + \mathcal{D}_{v_{\parallel D_2^+}} \nabla_{\perp}^2 v_{\parallel D_2^+} + \frac{n_{D_2}}{n_{D_2^+}} (v_{iz,D_2} + v_{cx,D_2} + v_{cx,D_2-D^+}) (v_{\parallel D_2} - v_{\parallel D_2^+}), \quad (3.24)
 \end{aligned}$$

$$\begin{aligned}
 \frac{\partial T_e}{\partial t} = & -\frac{\rho_*^{-1}}{B}[\phi, T_e] - v_{\parallel e} \nabla_{\parallel} T_e + \frac{4T_e}{3B} \left[\frac{C(p_e)}{n_e} + \frac{5}{2} C(T_e) - C(\phi) \right] - \frac{2T_e}{3} \nabla \cdot (v_{\parallel e} \mathbf{b}) \\
 & + \frac{2}{3n_e} \frac{1.62}{v} [n_e T_e (\nabla_{\parallel} T_e) \nabla \cdot \mathbf{b} + \nabla_{\parallel} (n_e T_e \nabla_{\parallel} T_e)] - \frac{2}{3} 0.71 T_e \nabla \cdot (v_{\parallel e} - v_{\parallel D^+}) \mathbf{b} \\
 & - \frac{2}{3} 0.71 \left(\frac{T_e}{n_e} \nabla_{\parallel} n_e + \nabla_{\parallel} T_e \right) (v_{\parallel e} - v_{\parallel D^+}) + \chi_{\perp e} \nabla_{\perp}^2 T_e + \nabla_{\parallel} (\chi_{\parallel e} \nabla_{\parallel} T_e) + S_{T_e} \\
 & + \frac{n_D}{n_e} v_{iz,D} \left[-\frac{2}{3} E_{iz,D} - T_e + \frac{m_e}{m_D} v_{\parallel e} \left(v_{\parallel e} - \frac{4}{3} v_{\parallel D} \right) \right] - \frac{n_D}{n_e} v_{e-D} \frac{m_e}{m_D} \frac{2}{3} v_{\parallel e} (v_{\parallel D} - v_{\parallel e}) \\
 & + \frac{n_{D_2}}{n_e} v_{iz,D_2} \left[-\frac{2}{3} E_{iz,D_2} - T_e + \frac{m_e}{m_D} v_{\parallel e} \left(v_{\parallel e} - \frac{4}{3} v_{\parallel D_2} \right) \right] - \frac{n_{D_2}}{n_e} v_{e-D_2} \frac{m_e}{m_D} \frac{2}{3} v_{\parallel e} (v_{\parallel D_2} - v_{\parallel e}) \quad (3.25) \\
 & + \frac{n_{D_2}}{n_e} v_{\text{diss},D_2} \left[-\frac{2}{3} E_{\text{diss},D_2} + \frac{2}{3} \frac{m_e}{m_D} v_{\parallel e} (v_{\parallel e} - v_{\parallel D_2}) \right] \\
 & + \frac{n_{D_2}}{n_e} v_{\text{diss-iz},D_2} \left[-\frac{2}{3} E_{\text{diss-iz},D_2} - T_e + \frac{m_e}{m_D} v_{\parallel e} \left(v_{\parallel e} - \frac{4}{3} v_{\parallel D_2} \right) \right] \\
 & + \frac{n_{D_2^+}}{n_e} v_{\text{diss},D_2^+} \left[-\frac{2}{3} E_{\text{diss},D_2^+} + \frac{2}{3} \frac{m_e}{m_D} v_{\parallel e} (v_{\parallel e} - v_{\parallel D_2^+}) \right] \\
 & + \frac{n_{D_2^+}}{n_e} v_{\text{diss-iz},D_2^+} \left[-\frac{2}{3} E_{\text{diss-iz},D_2^+} - T_e + \frac{m_e}{m_D} v_{\parallel e} \left(v_{\parallel e} - \frac{4}{3} v_{\parallel D_2^+} \right) \right],
 \end{aligned}$$

$$\begin{aligned}
\frac{\partial T_{D^+}}{\partial t} = & -\frac{\rho_*^{-1}}{B} [\phi, T_{D^+}] - \nu_{\parallel D^+} \nabla_{\parallel} T_{D^+} + \frac{4}{3} \frac{T_{D^+}}{B} \left[-C(\phi) + \frac{C(p_e + p_{D_2^+})}{n_{D^+}} \right] \\
& - \frac{2T_{D^+}}{3n_{D^+}} \left[n_e \nabla \cdot (\nu_{\parallel e} \mathbf{b}) - n_{D_2^+} \nabla \cdot (\nu_{\parallel D_2^+} \mathbf{b}) + \nu_{\parallel e} \nabla_{\parallel} n_e - \nu_{\parallel D_2^+} \nabla_{\parallel} n_{D_2^+} - \nu_{\parallel D^+} \nabla_{\parallel} n_{D^+} \right] \\
& - \frac{10}{3} \frac{T_{D^+}}{B} C(T_{D^+}) + \frac{2}{3n_{D^+}} \frac{2.32}{\sqrt{2}\nu} \sqrt{\frac{m_e}{m_D}} \nabla \cdot (n_e T_{D^+} \nabla_{\parallel} T_{D^+}) \mathbf{b} \\
& + \chi_{\perp D^+} \nabla_{\perp}^2 T_{D^+} + \nabla_{\parallel} (\chi_{\parallel D^+} \nabla_{\parallel} T_{D^+}) + S_{T_{D^+}} \\
& + \frac{1}{n_{D^+}} \left\{ n_D \left(\nu_{iz,D} + \nu_{cx,D} + \nu_{cx,D-D_2^+} \right) \left[T_D - T_{D^+} + \frac{1}{3} (\nu_{\parallel D} - \nu_{\parallel D^+})^2 \right] \right. \\
& + n_{D_2} \nu_{\text{diss-iz},D_2} \left[T_{D^+, \text{diss-iz}(D_2)} - T_{D^+} + \frac{1}{3} (\nu_{\parallel D_2} - \nu_{\parallel D^+})^2 \right] \\
& + 2n_{D_2^+} \nu_{\text{diss-iz},D_2^+} \left[T_{D^+, \text{diss-iz}(D_2^+)} - T_{D^+} + \frac{1}{3} (\nu_{\parallel D_2^+} - \nu_{\parallel D^+})^2 \right] \\
& \left. + n_{D_2^+} \nu_{\text{diss},D_2^+} \left[T_{D^+, \text{diss}(D_2^+)} - T_{D^+} + \frac{1}{3} (\nu_{\parallel D_2^+} - \nu_{\parallel D^+})^2 \right] \right\}
\end{aligned} \tag{3.26}$$

and

$$\begin{aligned}
\frac{\partial T_{D_2^+}}{\partial t} = & -\frac{\rho_*^{-1}}{B} [\phi, T_{D_2^+}] - \nu_{\parallel D_2^+} \nabla_{\parallel} T_{D_2^+} - \frac{4}{3} \frac{T_{D_2^+}}{B} \left[C(\phi) + \frac{C(p_{D_2^+})}{n_{D_2^+}} \right] - \frac{10}{3} \frac{T_{D_2^+}}{B} C(T_{D_2^+}) \\
& - \frac{2T_{D_2^+}}{3} \nabla \cdot (\nu_{\parallel D_2^+} \mathbf{b}) + \frac{2}{3n_{D_2^+}} \frac{0.92}{\sqrt{2}\nu} \sqrt{\frac{m_e}{m_D}} \nabla \cdot (n_e T_{D^+} \nabla_{\parallel} T_{D^+}) \mathbf{b} \\
& + \chi_{\perp D_2^+} \nabla_{\perp}^2 T_{D_2^+} + \nabla_{\parallel} (\chi_{\parallel D_2^+} \nabla_{\parallel} T_{D_2^+}) + S_{T_{D_2^+}} \\
& + \frac{n_{D_2}}{n_{D_2^+}} (\nu_{cx,D_2} + \nu_{iz,D_2} + \nu_{cx,D_2-D^+}) \left[T_{D_2^+} - T_{D_2} + \frac{2}{3} (\nu_{\parallel D_2} - \nu_{\parallel D_2^+})^2 \right].
\end{aligned} \tag{3.27}$$

In Eqs. (3.19-3.27) we introduce $[A, B] = \mathbf{b} \cdot (\nabla A \times \nabla B)$, $C(A) = (B/2) [\nabla \times (\mathbf{b}/B)] \cdot \nabla A$ and the plasma vorticity $\Omega = \Omega_{D^+} + 2\Omega_{D_2^+}$, with the D^+ contribution being given by $\Omega_{D^+} = \nabla \cdot \boldsymbol{\omega}_{D^+} = \nabla \cdot [(n_{D^+}/B^2) \nabla_{\perp} \phi + (1/B^2) \nabla_{\perp} p_{D^+}]$ and an analogous D_2^+ contribution, $\Omega_{D_2^+}$. The system is closed by the generalized Poisson equation, which is obtained by inverting the definition of the plasma vorticity, Ω , yielding

$$\nabla_{\perp} \cdot \left[\frac{n_{D^+} + 2n_{D_2^+}}{B^2} \nabla_{\perp} \phi \right] = \Omega - \nabla_{\perp} \cdot \left[\frac{1}{B^2} \nabla_{\perp} (p_{D^+} + 2p_{D_2^+}) \right]. \tag{3.28}$$

We highlight that the electron gyroviscous term in Eq. (3.22) is defined by analogy with the ion gyroviscous terms, $G_e = -\eta_{0e} [2\nabla_{\parallel} \nu_{\parallel e} + C(\phi)/B - C(p_e)/(n_e B)]$. When writing Eq. (2.70), we avoid the Boussinesq approximation and take into account all components of the velocity of

the ion species D^+ and D_2^+ , including the higher order polarization and friction contributions. On the other hand, when expressing the advective derivative for the ion species, d_{D^+}/dt and $d_{D_2^+}/dt$, we keep only the leading order components of the perpendicular velocity, $v_{\perp D^+0}$ and $v_{\perp D_2^+0}$, neglecting \mathbf{v}_{pol} and \mathbf{v}_{fric} . We consistently neglect the friction and polarization drifts in the continuity equation for D_2^+ . We remark that this is still a reasonable approach within the conditions considered in the present work, given that the density of D_2^+ ions is smaller than the density of the main ion species by several orders of magnitude. We also note that the terms of higher order in $1/\Omega_{cD_2^+} d/dt$ in the perpendicular velocity of D_2^+ ions are neglected when $\nabla \cdot \mathbf{v}_{D_2^+}$ is written in the temperature equations, Eqs. (3.26) and (3.27), this assumption being required to avoid explicit time derivatives featuring in the polarization drift velocity, $\mathbf{v}_{\text{pol}, D_2^+}$. However, all terms are considered in the divergence of the perpendicular velocity of D^+ ions in Eq. (3.26), as we use $\nabla \cdot \mathbf{j} = 0$ to write $\nabla \cdot \mathbf{v}_{D^+}$ in terms of $\nabla \cdot \mathbf{v}_e$ and $\nabla \cdot \mathbf{v}_{D_2^+}$. Finally, when taking the divergence of these terms, we consider $\nabla \cdot \mathbf{v}_D \ll \nabla \cdot \mathbf{v}_{D^+}$ to neglect the contribution of the velocity of D atoms, which is valid since $\rho_{s,D^+} \ll \lambda_{\text{mfp},D}$ (with $\rho_{s,D^+} = c_{s,D^+}/\Omega_{c,D^+}$ the sound Larmor radius of D^+ ions, $c_{s,D^+} = \sqrt{T_e/m_{D^+}}$ the D^+ ions sound speed and $\lambda_{\text{mfp},D}$ the mean free path of a D atoms). This relation is also generalized to the other neutral and ion species, namely D_2 molecules and D_2^+ ions, which enables us to neglect the contribution of the divergence of the velocities of neutral particles when compared to the divergence of ion velocities. Similarly to Ch. 2 for the single-component plasma, S_{n_e} , $S_{n_{D^+}}$, S_{T_e} , $S_{T_{D^+}}$ and $S_{T_{D_2^+}}$ in Eqs. (3.19-3.27) represent the density and temperature source terms for the different plasma species. We highlight that, while neglecting the polarization drift of the D_2^+ species is reasonable in the present chapter, this could not be done if multiple ion species with similar densities were considered, e.g. in the simulation of a $D-T$ plasma. The polarization drift of both D^+ and T^+ would have to be taken into account, which would require a different time integration scheme with respect to the one used in GBS. A multispecies model for the 2D simulation of a $D-T$ plasma is presented in detail in Ref. [94].

We remark that dimensionless units are used in Eqs. (3.19-3.27) and in the rest of this chapter, similarly to Ch. 2. The densities, n_e , n_{D^+} and $n_{D_2^+}$, are normalized to the reference value n_0 , while temperatures, T_e , T_{D^+} and $T_{D_2^+}$, are normalized to the respective reference values, T_{e0} , T_{D^+0} and $T_{D_2^+0} = T_{D^+0}$, which are also related through the dimensionless quantity $\tau = T_{D^+0}/T_{e0}$. In turn, lengths along the magnetic field are normalized to the tokamak major radius, R_0 , lengths in a direction perpendicular to the magnetic field are normalized to the ion sound Larmor radius, $\rho_{s0} = c_{s0}/\Omega_{cD^+0}$, where $c_{s0} = T_{e0}/m_{D^+}$ is the normalized D^+ ion sound speed and $\Omega_{cD^+0} = eB_0/m_{D^+}$ is the D^+ ion cyclotron frequency at the magnetic axis, and time is normalized to R_0/c_{s0} . All the other normalizations follow, namely the parallel velocities, $v_{\parallel e}$, $v_{\parallel D^+}$ and $v_{\parallel D_2^+}$, normalized to c_{s0} , the plasma vorticity Ω , normalized to $n_0 T_{e0}/(\rho_{s0}^2 B_0^2)$, the perpendicular diffusion coefficients D_{\perp} and conductivities χ_{\perp} , normalized to $c_{s0} \rho_{s0}^2/R_0$, and finally the parallel diffusion coefficients D_{\parallel} and conductivities χ_{\parallel} , normalized to $c_{s0} R_0$. Normalized quantities are used in the rest of the chapter, except when explicitly mentioned. We remark that we have defined the parameter $\rho_{\star} = \rho_{s0}/R_0$ as the ratio between the D^+ ion sound Larmor radius and the tokamak major radius R_0 . We also note that v is the dimensionless

Chapter 3. A multi-component model of plasma turbulence and kinetic neutral dynamics

resistivity given by $\nu = (e^2 n_{e0} R_0) / (m_D c_{s0} \sigma_{\parallel})$, with the parallel conductivity defined in terms of the electron characteristic time τ_e as $\sigma_{\parallel} = e^2 n_e \tau_e / (0.51 m_e)$.

We conclude with a couple of remarks on Eqs. (3.19-3.27). At first, we remark that the parallel conductivity featuring in the temperature equations for electrons is expressed in the form $\chi_{\parallel,e} = \chi_{\parallel,0,e} T_e^{5/2}$, where the Spitzer temperature dependence is retained, while we neglect the weaker space and time dependence of the $2/(3n_e)$ factor, in a similarly approach to the one followed in the single-component plasma model of GBS [33, 34] discussed in Ch. 2. An identical procedure is followed when considering χ_{\parallel,D^+} and χ_{\parallel,D_2^+} . This approximation is expected not to affect significantly the results of simulations in the tokamak boundary conditions considered in the present work, which have parameters between the sheath-limited and conduction-limited regimes, where the contributions of conductivity are expected to be small. We also mention that, because the D_2^+ density typically drops to very low values, numerical issues may appear in the equations for $v_{\parallel D_2^+}$ and $T_{D_2^+}$, arising from terms featuring a $1/n_{D_2^+}$ dependence. In order to develop a more robust numerical approach, we evolve the parallel flux and pressure of the D_2^+ ion species, $\Gamma_{\parallel D_2^+} = n_{D_2^+} v_{\parallel D_2^+}$ and $p_{D_2^+} = n_{D_2^+} T_{D_2^+}$, instead of $v_{\parallel D_2^+}$ and $T_{D_2^+}$. The equations modelling the time evolution of $\Gamma_{\parallel D_2^+}$ and $p_{D_2^+}$ are

$$\frac{\partial \Gamma_{\parallel D_2^+}}{\partial t} = \frac{\partial n_{D_2^+}}{\partial t} v_{\parallel D_2^+} + n_{D_2^+} \frac{\partial v_{\parallel D_2^+}}{\partial t}, \quad (3.29)$$

and

$$\frac{\partial p_{D_2^+}}{\partial t} = \frac{\partial n_{D_2^+}}{\partial t} T_{D_2^+} + n_{D_2^+} \frac{\partial T_{D_2^+}}{\partial t}, \quad (3.30)$$

with $\partial_t n_{D_2^+}$, $\partial_t v_{\parallel D_2^+}$ and $\partial_t T_{D_2^+}$ being given, respectively, by Eqs. (3.20), (3.24) and (3.27). We remark that, when presenting the results of simulations, we focus on the parallel flux, $\Gamma_{\parallel D_2^+}$, and pressure, $p_{D_2^+}$.

3.4 Boundary conditions

The boundary conditions implemented in the single-component GBS model presented in Ch. 2 are extended in the present chapter to include the molecular ion species D_2^+ . Similarly to the single-ion species model, the simulation domain boundary includes the limiter plates, the outer wall and the interface with the core, which is excluded since the low plasma collisionality does not enable a description based on a fluid model.

We start by considering the boundary conditions at the limiter plates, where the plasma particles end as a result of the flow parallel to the magnetic field. Hence, those are the boundary conditions that more significantly influence the simulation dynamics. Similarly to Ch. 2, the boundary conditions are imposed at the interface between the collisional pre-sheath

(CP) and the magnetic pre-sheath (MP), which are derived from the Bohm-Chodura boundary conditions, following the approach described in Ref. [74] in the cold ion limit and generalized in Ref. [75] to account for finite ion temperature. In this chapter, we extend this procedure for a multi-ion species plasma. For this purpose, we use the (y, x, z) coordinates, being z the direction of the magnetic field, x the direction perpendicular to the magnetic field and parallel to the limiter surface, and y the direction perpendicular to both x and z (all spatial coordinates are normalized to ρ_{s0} while the other quantities follow the same normalizations used for Eqs. (3.19-3.27)). We also introduce the coordinate perpendicular to the limiter plate, expressed as $s = y\cos\alpha + z\sin\alpha$, where α denotes the angle between the magnetic field line and the plane of the limiter.

We remark that, to describe the steady-state dynamics of the multi-species plasma in the CP, we make use of the continuity equation for the D^+ and D_2^+ species (with quasi-neutrality providing the electron density) and the parallel momentum equations for e^- , D^+ and D_2^+ . These can be written, in a steady state, as

$$\nabla \cdot (n_{D^+} \mathbf{v}_{D^+}) = S_{p,D^+}, \quad (3.31)$$

$$\nabla \cdot (n_{D_2^+} \mathbf{v}_{D_2^+}) = S_{p,D_2^+}, \quad (3.32)$$

$$n_e(\mathbf{v}_e \cdot \nabla) \mathbf{v}_e = -n_e \mathbf{E} - n_e \mathbf{v}_{D^+} \times \mathbf{B} - \nabla p_e + \mathbf{S}_{m,e}, \quad (3.33)$$

$$n_{D^+} (\mathbf{v}_{D^+} \cdot \nabla) \mathbf{v}_{D^+} = n_{D^+} \mathbf{E} + n_{D^+} \mathbf{v}_{D^+} \times \mathbf{B} - \nabla p_{D^+} + \mathbf{S}_{m,D^+} \quad (3.34)$$

and

$$n_{D_2^+} (\mathbf{v}_{D_2^+} \cdot \nabla) \mathbf{v}_{D_2^+} = n_{D_2^+} \mathbf{E} + n_{D_2^+} \mathbf{v}_{D_2^+} \times \mathbf{B} - \nabla p_{D_2^+} + \mathbf{S}_{m,D_2^+}, \quad (3.35)$$

with S_{p,D^+} and S_{p,D_2^+} the particle sources for D^+ and D_2^+ , and $\mathbf{S}_{m,e}$, \mathbf{S}_{m,D^+} and \mathbf{S}_{m,D_2^+} the momentum sources for e^- , D^+ and D_2^+ .

From Eqs. (3.31-3.35) and following the approach described in Ref. [75], we obtain a system of five equations for $\partial_s n_{D^+}$, $\partial_s n_{D_2^+}$, $\partial_s v_{\parallel D^+}$ and $\partial_s v_{\parallel D_2^+}$, $\partial_s \phi$ for the interface between the CP and the MP border, considering $m_e/m_{D^+} \ll 1$ and assuming the isothermal approximation for both ions and electrons. Moreover, we remark that, at the MP entrance, gradients along the x direction are assumed weaker than gradients along s by a factor $\epsilon = \rho_{s0}/L_n \simeq \rho_{s0}/L_{T_e} \simeq \rho_{s0}/L_\phi \ll 1$, with L_n , L_{T_e} and L_ϕ respectively the gradient scale lengths of n_e , T_e and ϕ along the x direction. At the same time, we neglect finite Larmor radius (FLR) effects and, to express

Chapter 3. A multi-component model of plasma turbulence and kinetic neutral dynamics

the y and x velocity components of each ion species, D^+ and D_2^+ , we include only the leading order terms in $(1/\Omega_{cD^+})d/dt$ (see Eqs. (3.13) and (3.16)). This leads to

$$v_{y,D^+} = v_{y,E \times B} + v_{y,dD^+}, \quad (3.36)$$

$$v_{x,D^+} = v_{x,E \times B} + v_{x,dD^+}, \quad (3.37)$$

$$v_{y,D_2^+} = v_{y,E \times B} + v_{y,dD_2^+} \quad (3.38)$$

and

$$v_{x,D_2^+} = v_{x,E \times B} + v_{x,dD_2^+}, \quad (3.39)$$

where $v_{y,E \times B}$ and $v_{x,E \times B}$ are respectively the y and x components of the $E \times B$ drift velocity, v_{y,dD^+} and v_{x,dD^+} are the y and x components of the D^+ diamagnetic drift velocity and v_{y,dD_2^+} and v_{x,dD_2^+} are the y and x components of the D_2^+ diamagnetic velocity. The velocity of the D^+ ions along the s direction is written as $v_{s,D^+} = v_{\parallel D^+} \sin \alpha + v_{y,D^+} \cos \alpha$. We also define the velocity of the D^+ ions along the s direction excluding the diamagnetic contribution, that is $v'_{s,D^+} = v_{s,D^+} - v_{y,dD^+} \cos \alpha$, and similarly for the D_2^+ ions, yielding $v'_{s,D_2^+} = v_{s,D_2^+} - v_{y,dD_2^+} \cos \alpha$. The system in Eqs. (3.31-3.35) is then written as

$$v_{s,D^+} \partial_s n_{D^+} + n_{D^+} \sin \alpha \partial_s v_{\parallel D^+} - \partial_x n_{D^+} \cos \alpha \partial_s \phi = S_{p,D^+}, \quad (3.40)$$

$$v_{s,D_2^+} \partial_s n_{D_2^+} + n_{D_2^+} \sin \alpha \partial_s v_{\parallel D_2^+} - \partial_x n_{D_2^+} \cos \alpha \partial_s \phi = S_{p,D_2^+}, \quad (3.41)$$

$$n_{D^+} v_{s,D^+} \partial_s v_{\parallel D^+} + n_{D^+} (\sin \alpha - \partial_x v_{\parallel D^+} \cos \alpha) \partial_s \phi + T_{D^+} \sin \alpha \partial_s n_{D^+} = S_{\parallel m,D^+}, \quad (3.42)$$

$$n_{D_2^+} v_{s,D_2^+} \partial_s v_{\parallel D_2^+} + n_{D_2^+} (\sin \alpha - \partial_x v_{\parallel D_2^+} \cos \alpha) \partial_s \phi + T_{D_2^+} \sin \alpha \partial_s n_{D_2^+} = S_{\parallel m,D_2^+} \quad (3.43)$$

and

$$\sin \alpha T_e \partial_s n_e - \sin \alpha n_e \partial_s \phi = S_{\parallel m,e}, \quad (3.44)$$

where $S_{\parallel m, D^+} = \mathbf{S}_{m, D^+} \cdot \mathbf{b}$, $S_{\parallel m, D_2^+} = \mathbf{S}_{m, D_2^+} \cdot \mathbf{b}$ and $S_{\parallel m, e} = \mathbf{S}_{m, e} \cdot \mathbf{b}$. We make use of the quasi-neutrality condition, $n_e = n_{D^+} + n_{D_2^+}$, to obtain a system of five linear equations, which is expressed in matrix form as $\mathbf{M}\mathbf{x} = \mathbf{S}$, with

$$\mathbf{M} = \begin{pmatrix} v'_{s, D^+} & n_{D^+} \sin \alpha & 0 & 0 & -\cos \alpha \partial_x n_{D^+} \\ T_{D^+} \sin \alpha & n_{D^+} v'_{s, D^+} & 0 & 0 & n_{D^+} (\sin \alpha - \partial_x v_{\parallel D^+} \cos \alpha) \\ 0 & 0 & v'_{s, D_2^+} & n_{D_2^+} \sin \alpha & -\cos \alpha \partial_x n_{D_2^+} \\ 0 & 0 & T_{D_2^+} \sin \alpha & n_{D_2^+} v'_{s, D_2^+} & n_{D_2^+} (\sin \alpha - \partial_x v_{\parallel D_2^+} \cos \alpha) \\ \sin \alpha T_e & 0 & \sin \alpha T_e & 0 & -(n_{D^+} + n_{D_2^+}) \sin \alpha \end{pmatrix}, \quad (3.45)$$

$$\mathbf{x} = \begin{pmatrix} \partial_s n_{D^+} \\ \partial_s n_{D_2^+} \\ \partial_s v_{\parallel D^+} \\ \partial_s v_{\parallel D_2^+} \\ \partial_s \phi \end{pmatrix} \quad (3.46)$$

and

$$\mathbf{S} = \begin{pmatrix} S_{p, D^+} \\ S_{p, D_2^+} \\ S_{\parallel m, D^+} \\ S_{\parallel m, D_2^+} \\ S_{\parallel m, e} \end{pmatrix}. \quad (3.47)$$

Following the same approach as [74, 75], we observe that, although the source terms are important in the CP, they become small with respect to the gradient terms at the MP entrance. This enables the assumption that $|\Sigma_j M_{ij} X_j| \gg |S_i|$. Thus, the linear system $\mathbf{M}\mathbf{x} = \mathbf{S}$ reduces to $\mathbf{M}\mathbf{x} = 0$ at the MP entrance. We then solve $\det(\mathbf{M}) = 0$ with respect to v'_{s, D^+} to obtain the non-trivial solution valid at the MP entrance. For this purpose, we follow Ref. [95] to relate the parallel velocity of the D_2^+ ion species, $v_{\parallel D_2^+}$, to the parallel velocity of the D^+ ions, $v_{\parallel D^+}$,

$$v_{\parallel D_2^+} = \sqrt{\frac{m_{D^+}}{m_{D_2^+}}} v_{\parallel D^+} = \frac{v_{\parallel D^+}}{\sqrt{2}}. \quad (3.48)$$

We also assume $n_{D_2^+}/n_e \ll 1$ (and therefore $n_{D^+} \simeq n_e$) and keep only zero order terms in ϵ , thus neglecting all derivatives along the x direction. The condition $\det(\mathbf{M}) = 0$ then yields

$$v'_{s, D^+} = \pm \sqrt{T_e F_T} \sin \alpha \quad (3.49)$$

Chapter 3. A multi-component model of plasma turbulence and kinetic neutral dynamics

where the \pm signs stand for the magnetic field lines entering/leaving the vessel and we have defined $F_T = 1 + \tau T_{D^+} / T_e$. We also remark that $v'_{s,D^+} = v_{\parallel D^+} \sin \alpha$, since we neglect $v_{y,E \times B} \cos \alpha = \partial_x \phi \cos \alpha$, to obtain the boundary condition for $v_{\parallel D^+}$ at the limiter,

$$v_{\parallel D^+} = \pm \sqrt{T_e F_T}. \quad (3.50)$$

The expressions of the boundary conditions for the other plasma quantities then follow. As a matter of fact, Eq. (3.42) can be inverted to express $\partial_s \phi$ in terms of $\partial_s v_{\parallel D^+}$, which yields

$$\partial_s \phi = -\frac{v'_{s,D^+} \partial_s v_{\parallel D^+}}{F_T \sin \alpha} = \mp \frac{\sqrt{T_e}}{\sqrt{F_T}} \partial_s v_{\parallel D^+}. \quad (3.51)$$

We make use of Eq. (3.44) to express $\partial_s n_e$ in terms of $\partial_s \phi$, that is

$$\partial_s n_e = \frac{n_e}{T_e} \partial_s \phi = \mp \frac{n_e}{\sqrt{T_e F_T}} \partial_s v_{\parallel D^+} \quad (3.52)$$

and, applying $n_{D^+} = n_e$, we obtain

$$\partial_s n_{D^+} = n_e / T_e \partial_s \phi = \mp \frac{n_e}{\sqrt{T_e F_T}} \partial_s v_{\parallel D^+} \quad (3.53)$$

Regarding the density of the D_2^+ ions, we use Eq. (3.41), deriving the boundary condition given by

$$\partial_s n_{D_2^+} = \mp n_{D_2^+} / \sqrt{T_e F_T} \partial_s v_{\parallel D^+}. \quad (3.54)$$

To derive the boundary conditions for T_e , T_{D^+} and $T_{D_2^+}$, we note that temperature gradients along the direction perpendicular to the wall are small compared to the gradients of the other physical quantities. In fact, Ref. [74, 75] shows that $\partial_s T_e \sim \partial_s T_{D^+} \simeq 0.1 \partial_s \phi$. In the present chapter, we also follow this prescription and assume $\partial_s T_e = \partial_s T_{D^+} = \partial_s T_{D_2^+} = 0.1 \partial_s \phi$ (we note that our tests show that imposing $\partial_s T_e = \partial_s T_{D^+} = \partial_s T_{D_2^+} = 0$ does not noticeably impact the results of the simulation).

To obtain the boundary condition for Ω at the MP entrance, we apply its definition, $\Omega = \nabla \cdot [(n_{D^+} / B^2) \nabla_{\perp} \phi + (1 / B^2) \nabla_{\perp} p_{D^+}] + \nabla \cdot [(n_{D_2^+} / B^2) \nabla_{\perp} \phi + (1 / B^2) \nabla_{\perp} p_{D_2^+}]$, and we write the second order derivatives in the directions perpendicular to the magnetic field retaining only derivatives along the y direction, making use of $\partial_x^2 \ll \partial_y^2$. Given that $\partial_y B = 0$ at the limiter, the $1 / B^2$ factor is taken constant when computing the derivatives featuring in the definition of Ω . We write the derivatives along the y direction in terms of derivatives along s and consider

$T_{D_2^+} = T_{D^+}$ (for simplicity), which finally yields

$$\Omega = -\cos\alpha \left[\partial_s(n_e + n_{D_2^+})\partial_s\phi + T_{D^+}\partial_s^2(n_e + n_{D_2^+}) + (n_e + n_{D_2^+})\partial_s^2\phi \right]. \quad (3.55)$$

We now use Eqs. (3.52) and (3.54) to express $\partial_s n_e$ and $\partial_s n_{D^+}$ in terms of $\partial_s\phi$ and start from Eq. (3.51) to obtain the final expression of the boundary condition for Ω , that is

$$\Omega = -(n_e + n_{D_2^+})F_T\cos^2\alpha \left[\pm \frac{\sqrt{T_e}}{\sqrt{F_T}}\partial_s^2 v_{\parallel D^+} \mp \frac{1}{\sqrt{T_e}F_T}(\partial_s v_{\parallel D^+})^2 \right]. \quad (3.56)$$

Finally, we remark that the boundary condition for the electron parallel velocity is obtained from the analysis of the electron kinetic distribution function at the MP entrance. As discussed in Ref. [74], this yields

$$v_{\parallel e} = \sqrt{T_e} \left[\pm \exp\left(\Lambda - \frac{\phi}{T_e}\right) \right], \quad (3.57)$$

where $\Lambda = \log[\sqrt{(1/2\pi)(m_i/m_e)}] \simeq 3$.

On the other hand, at the vessel outer wall and the edge-core interface, *ad hoc* boundary conditions are considered, similarly to the approach used in the single-ion species GBS model [74, 75, 34] considered in Ch. 2. As a matter of fact, a set of first-principles boundary conditions is yet to be derived for such boundaries. We reduce the effect of these *ad hoc* boundary conditions on the results of the simulation by radially extending the simulation domain towards the wall and the core, as in the model presented in Ch. 2. We impose homogeneous Neumann boundary conditions to n_e , n_{D^+} , T_e , T_{D^+} , $T_{D_2^+}$, $v_{\parallel e}$, $v_{\parallel D^+}$ and $v_{\parallel D_2^+}$. Given that the density of D_2^+ ions is expected to be very low at the edge-core interface (no D_2^+ ions outflow from the core), we use Dirichlet boundary conditions at the edge-core interface for $n_{D_2^+}$, setting it to a very small value (we choose $n_{D_2^+} = \exp(-5)$, and we notice that this value has a small impact on the results), while homogenous Neumann boundary conditions are considered at the outer wall. The boundary conditions considered for the other quantities follow the same approach described in Ch. 2. More precisely, we also use Dirichlet boundary conditions for the vorticity, setting $\Omega = 0$ at both the wall and the core interface. We follow the approach presented in Ref. [35] for the ϕ boundary conditions, considering $\phi = \Lambda T_e$ at the vessel wall and $\phi = \phi_0$ at the core interface, where ϕ_0 is a constant value chosen to prevent large gradients of ϕ .

3.5 The kinetic model for the neutral species and its formal solution

We now extend the approach followed in Ref. [61] and improved in Ch. 2 for a single-neutral species model. We consider one kinetic equation for each neutral species, namely D atoms and D₂ molecules, which compute their respective distribution functions, f_D and f_{D_2} . The result is a set of coupled equations, yielding

$$\begin{aligned} \frac{\partial f_D}{\partial t} + \mathbf{v} \cdot \frac{\partial f_D}{\partial \mathbf{x}} = & -\nu_{iz,D} f_D - \nu_{cx,D} \left(f_D - \frac{n_D}{n_{D^+}} f_{D^+} \right) + \nu_{rec,D^+} f_{D^+} \\ & + \nu_{cx,D_2-D^+} \left(\frac{n_{D_2}}{n_{D^+}} f_{D^+} \right) - \nu_{cx,D-D_2^+} f_D + 2\nu_{diss,D_2} f_{D_2} + \nu_{diss-iz,D_2} f_{D_2} \\ & + \nu_{diss,D_2^+} f_{D_2^+} + 2\nu_{diss-rec,D_2^+} f_{D_2^+}, \end{aligned} \quad (3.58)$$

and

$$\begin{aligned} \frac{\partial f_{D_2}}{\partial t} + \mathbf{v} \cdot \frac{\partial f_{D_2}}{\partial \mathbf{x}} = & -\nu_{iz,D_2} f_{D_2} - \nu_{cx,D_2} \left(f_{D_2} - \frac{n_{D_2}}{n_{D_2^+}} f_{D_2^+} \right) \\ & + \nu_{rec,D_2^+} f_{D_2^+} - \nu_{cx,D_2-D^+} f_{D_2} + \nu_{cx,D-D_2^+} \left(\frac{n_D}{n_{D_2^+}} f_{D_2^+} \right) \\ & - \nu_{diss,D_2} f_{D_2} - \nu_{diss-iz,D_2} f_{D_2}. \end{aligned} \quad (3.59)$$

We then obtain the formal solution of Eqs. (3.58) and (3.59) by applying the method of characteristics, assuming that the plasma quantities are known. This leads to

$$\begin{aligned} f_D(\mathbf{x}, \mathbf{v}, t) = & \int_0^{r'_b} \left[\frac{S_D(\mathbf{x}', \mathbf{v}, t')}{v} + \delta(r' - r'_b) f_D(\mathbf{x}'_b, \mathbf{v}, t'_b) \right] \\ & \times \exp \left[-\frac{1}{v} \int_0^{r'} \nu_{eff_D}(\mathbf{x}'', t'') dr'' \right] \frac{J(\mathbf{x}')}{J(\mathbf{x})} dr' \end{aligned} \quad (3.60)$$

and

$$\begin{aligned} f_{D_2}(\mathbf{x}, \mathbf{v}, t) = & \int_0^{r'_b} \left[\frac{S_{D_2}(\mathbf{x}', \mathbf{v}, t')}{v} + \delta(r' - r'_b) f_{D_2}(\mathbf{x}'_b, \mathbf{v}, t'_b) \right] \\ & \times \exp \left[-\frac{1}{v} \int_0^{r'} \nu_{eff_{D_2}}(\mathbf{x}'', t'') dr'' \right] \frac{J(\mathbf{x}')}{J(\mathbf{x})} dr'. \end{aligned} \quad (3.61)$$

The solutions introduced in Eq. (3.60-3.61) describe the distribution functions of D and

3.5. The kinetic model for the neutral species and its formal solution

D_2 at position \mathbf{x} , velocity \mathbf{v} and time t as the result of the neutrals generated at a location $\mathbf{x}' = \mathbf{x} - r'\mathbf{\Omega}$, in the plasma volume or at the boundary, and at time $t' = t - r'/v$, where $\mathbf{\Omega} = \mathbf{v}/v$ is the unit vector aligned with the neutral velocity and r' is the distance measured from \mathbf{x}' to \mathbf{x} (the subscript "b" designates the intersection point between the domain boundary and the characteristic starting at \mathbf{x} with direction $\mathbf{\Omega}$). Since the neutrals are solved on the (R, Z) coordinate system, with R the distance from the torus axis and Z the vertical coordinate measured from the equatorial midplane, the integral includes the Jacobian corresponding to this coordinate system, expressed as $J(\mathbf{x}) = R(\mathbf{x})$. We highlight that the volumetric source associated with the collisional processes in Eq. (3.60) is written as

$$\begin{aligned} S_D(\mathbf{x}', \mathbf{v}, t') = & v_{\text{cx},D}(\mathbf{x}', t') n_D(\mathbf{x}', t') \Phi_{[\mathbf{v}_{D^+}, T_{D^+}]}(\mathbf{x}', \mathbf{v}, t') + v_{\text{cx},D_2-D^+}(\mathbf{x}', t') n_{D_2}(\mathbf{x}', t') \Phi_{[\mathbf{v}_{D^+}, T_{D^+}]}(\mathbf{x}', \mathbf{v}, t') \\ & + v_{\text{rec},D^+}(\mathbf{x}', t') n_{D^+}(\mathbf{x}', \mathbf{v}, t') \Phi_{[\mathbf{v}_{D^+}, T_{D^+}]}(\mathbf{x}', \mathbf{v}, t') + 2v_{\text{diss},D_2}(\mathbf{x}', t') n_{D_2}(\mathbf{x}', t') \Phi_{[\mathbf{v}_{D_2}, T_{D,\text{diss}(D_2)}]}(\mathbf{x}', \mathbf{v}, t') \\ & + v_{\text{diss-iz},D_2}(\mathbf{x}', t') n_{D_2}(\mathbf{x}', t') \Phi_{[\mathbf{v}_{D_2}, T_{D,\text{diss-iz}(D_2)}]}(\mathbf{x}', \mathbf{v}, t') + v_{\text{diss},D_2^+}(\mathbf{x}', t') n_{D_2^+}(\mathbf{x}', \mathbf{v}, t') \Phi_{[\mathbf{v}_{D_2^+}, T_{D,\text{diss}(D_2^+)}]}(\mathbf{x}', \mathbf{v}, t') \\ & + 2v_{\text{diss-rec},D_2^+}(\mathbf{x}', t') n_{D_2^+}(\mathbf{x}', \mathbf{v}, t') \Phi_{[\mathbf{v}_{D_2^+}, T_{D,\text{diss-rec}(D_2^+)}]}(\mathbf{x}', \mathbf{v}, t') \end{aligned} \quad (3.62)$$

since D ions can be created in the plasma volume by $D - D^+$ and $D_2 - D^+$ charge-exchange interactions, recombination of D^+ ions with electrons, dissociation of D_2 molecules into two D atoms, dissociative ionization of D_2 into D and D^+ , dissociation of D_2^+ ions into D and D^+ , and dissociative recombination of D_2^+ into two D atoms.

Similarly, D_2 molecules are generated in the plasma by charge-exchange collisions between D_2 molecules and D_2^+ ions or D atoms and D_2^+ ions, or by recombination of D_2^+ ions with electrons. Therefore, the volumetric source term in Eq. (3.61) is

$$\begin{aligned} S_{D_2}(\mathbf{x}', \mathbf{v}, t') = & v_{\text{cx},D_2}(\mathbf{x}', t') n_{D_2}(\mathbf{x}', t') \Phi_{[\mathbf{v}_{D_2^+}, T_{D_2^+}]}(\mathbf{x}', \mathbf{v}, t') + v_{\text{rec},D_2^+}(\mathbf{x}', t') n_{D_2^+}(\mathbf{x}', \mathbf{v}, t') \Phi_{[\mathbf{v}_{D_2^+}, T_{D_2^+}]}(\mathbf{x}', \mathbf{v}, t') \\ & + v_{\text{cx},D-D_2^+}(\mathbf{x}', t') n_D(\mathbf{x}', t') \Phi_{[\mathbf{v}_{D_2^+}, T_{D_2^+}]}(\mathbf{x}', \mathbf{v}, t'). \end{aligned} \quad (3.63)$$

We note that $\Phi_{[\mathbf{v}_{D^+}, T_{D^+}]}(\mathbf{x}', \mathbf{v}, t') = [m_{D^+}/(2\pi T_{D^+})]^{3/2} \exp[-m_{D^+}(\mathbf{v} - \mathbf{v}_{D^+})^2/(2T_{D^+})]$ is a Maxwellian distribution function that describes the D^+ ion population, centered at the ion velocity $\mathbf{v}_{D^+}(\mathbf{x}', t')$, including only the leading order components, $\mathbf{v}_{D^+} = v_{\parallel D^+} \mathbf{b} + \mathbf{v}_{\perp D^+0}$, and based on the D^+ temperature, $T_{D^+}(\mathbf{x}', t')$. In addition, $\Phi_{[\mathbf{v}_{D_2^+}, T_{D_2^+}]}(\mathbf{x}', \mathbf{v}, t')$ is a Maxwellian distribution describing the D_2^+ ions and follows a similar definition. We remark that, when we evaluate the average velocity of the Maxwellian distributions describing neutrals generated from D_2 and D_2^+ , we neglect \mathbf{v}_{D_2} and $\mathbf{v}_{D_2^+}$ with respect to \mathbf{v}_{D^+} , i.e. we assume $|\mathbf{v}_{D_2}| \lesssim |\mathbf{v}_{D^+}|$ and $|\mathbf{v}_{D_2^+}| \lesssim |\mathbf{v}_{D^+}|$. We also note that the temperature $T_{D,\text{diss}(D_2)}$ is the average thermal energy of D atoms generated by dissociation of D_2 molecules, presented in Table 3.2 and calculated in App. B. The

Chapter 3. A multi-component model of plasma turbulence and kinetic neutral dynamics

energy of the neutral D atoms generated by the other dissociative processes is computed using a similar approach.

The effective frequencies for depletion of neutral particles are given by

$$\nu_{\text{eff,D}}(\mathbf{x}'', t'') = \nu_{\text{iz,D}}(\mathbf{x}'', t'') + \nu_{\text{cx,D}}(\mathbf{x}'', t'') + \nu_{\text{cx,D-D}_2^+}(\mathbf{x}'', t'') \quad (3.64)$$

and

$$\begin{aligned} \nu_{\text{eff,D}_2}(\mathbf{x}'', t'') &= \nu_{\text{iz,D}_2}(\mathbf{x}'', t'') + \nu_{\text{cx,D}_2}(\mathbf{x}'', t'') + \nu_{\text{cx,D}_2-\text{D}^+}(\mathbf{x}'', t'') \\ &+ \nu_{\text{diss,D}_2}(\mathbf{x}'', t'') + \nu_{\text{diss-iz,D}_2}(\mathbf{x}'', t''), \end{aligned} \quad (3.65)$$

since the volumetric sinks of D atoms are associated with ionization or charge-exchange with D^+ or D_2^+ , while depletion of D_2 is related to ionization, charge-exchange with D_2^+ or D^+ , dissociation or dissociative ionization.

There is also a contribution to the neutral distribution functions in Eqs. (3.60) and (3.61) related to plasma recycling taking place at the boundary walls. Therefore, we now focus on the neutral processes occurring there. Similarly to the single-ion species model discussed in Ch. 2, a fraction, $\alpha_{\text{refl}}(\mathbf{x}'_b)$, of the D_2^+ ions that reach the boundary walls is reflected back into the plasma, after recombination with electrons and formation of D_2 neutrals. The remaining fraction, $1 - \alpha_{\text{refl}}(\mathbf{x}'_b)$, is absorbed and reemitted at wall temperature as D_2 , also after recombining with an electron. Similar considerations are valid when describing the D_2 neutrals that reach the boundary, i.e. the D_2 molecules are assumed to be reflected or reemitted with the same probability as D_2^+ .

Turning now to the atomic species, since the wall temperature is low, a fraction, β_{assoc} , of the D^+ and D particles absorbed at the walls associate and reenter the plasma as D_2 molecules. The remaining D^+ ions and D neutrals reaching the boundaries are reflected or reemitted, similarly to D_2^+ ions and D_2 particles, with the same probability of reflection, $\alpha_{\text{refl}}(\mathbf{x}'_b)$. As a result, the distribution functions at the vessel, $f_{\text{D}}(\mathbf{x}'_b, \mathbf{v}, t')$ and $f_{\text{D}_2}(\mathbf{x}'_b, \mathbf{v}, t')$, for $\nu_p = \mathbf{v} \cdot \hat{\mathbf{n}} > 0$ (with $\hat{\mathbf{n}}$ the unit vector normal to the boundary) are written as

$$\begin{aligned} f_{\text{D}}(\mathbf{x}'_b, \mathbf{v}, t') &= (1 - \alpha_{\text{refl}}(\mathbf{x}'_b)) \Gamma_{\text{reem,D}}(\mathbf{x}'_b, t') \chi_{\text{in,D}}(\mathbf{x}'_b, \mathbf{v}) \\ &+ \alpha_{\text{refl}}(\mathbf{x}'_b) \left[f_{\text{out,D}}(\mathbf{x}'_b, \mathbf{v} - 2\mathbf{v}_p, t') + \frac{\Gamma_{\text{out,D}^+}(\mathbf{x}'_b, t')}{\nu_p} \Phi_{[\mathbf{v}_{\text{refl}(\text{D}^+)}, T_{\text{D}^+}]}(\mathbf{x}'_b, \mathbf{v}, t') \right] \end{aligned} \quad (3.66)$$

and

3.5. The kinetic model for the neutral species and its formal solution

$$f_{D_2}(\mathbf{x}'_b, \mathbf{v}, t') = (1 - \alpha_{\text{refl}}(\mathbf{x}'_b)) \Gamma_{\text{reem}, D_2}(\mathbf{x}'_b, t') \chi_{\text{in}, D_2}(\mathbf{x}'_b, \mathbf{v}) + \alpha_{\text{refl}}(\mathbf{x}'_b) \left[f_{\text{out}, D_2}(\mathbf{x}'_b, \mathbf{v} - 2\mathbf{v}_p, t') + \frac{\Gamma_{\text{out}, D_2^+}(\mathbf{x}'_b, t')}{v_p} \Phi_{[\mathbf{v}_{\text{refl}}(D_2^+), T_{D_2^+}]}(\mathbf{x}'_b, \mathbf{v}, t') \right]. \quad (3.67)$$

At first, we analyse the contributions of reflected particles in Eqs. (3.66-3.67). The reflected D and D₂ are described by the distribution functions $f_{\text{out}, D}(\mathbf{x}'_b, \mathbf{v} - 2\mathbf{v}_p, t')$ and $f_{\text{out}, D_2}(\mathbf{x}'_b, \mathbf{v} - 2\mathbf{v}_p, t')$, since $\mathbf{v} - 2\mathbf{v}_p$ is the velocity of the neutrals which are reflected when flowing towards the wall, where $\mathbf{v}_p = v_p \hat{\mathbf{n}}$ denotes the velocity along the direction normal to the wall surface. On the other hand, we address the contributions from the D⁺ and D₂⁺ ions reflected at the walls by considering the projection of the flux of outflowing D⁺ and D₂⁺ along the direction normal to the boundary surface, which are given respectively by $\Gamma_{\text{out}, D^+}(\mathbf{x}'_b) = -\Gamma_{\text{out}, D^+}(\mathbf{x}'_b) \cdot \hat{\mathbf{n}}$ and $\Gamma_{\text{out}, D_2^+}(\mathbf{x}'_b) = -\Gamma_{\text{out}, D_2^+}(\mathbf{x}'_b) \cdot \hat{\mathbf{n}}$. These fluxes include the contributions of the plasma flow parallel to the magnetic-field lines and the leading order perpendicular drifts, more precisely the $E \times B$ and diamagnetic drifts, yielding

$$\Gamma_{\text{out}, D^+}(\mathbf{x}'_b) = n_{D^+} v_{\parallel D^+} \mathbf{b} + n_{D^+} \mathbf{v}_{\perp D^+} \cdot 0 \quad (3.68)$$

and

$$\Gamma_{\text{out}, D_2^+}(\mathbf{x}'_b) = n_{D_2^+} v_{\parallel D_2^+} \mathbf{b} + n_{D_2^+} \mathbf{v}_{\perp D_2^+} \cdot 0, \quad (3.69)$$

We assume that the velocity distribution of the D neutrals generated by reflection of D⁺ ions is described by a Maxwellian centered at the velocity, $\mathbf{v}_{\text{refl}}(D^+) = \mathbf{v}_{D^+} - 2\mathbf{v}_{pD^+}$, with $\mathbf{v}_{pD^+} = (\mathbf{v}_{D^+} \cdot \hat{\mathbf{n}}) \hat{\mathbf{n}}$, and with temperature of the incoming D⁺ ions, T_{D^+} , given by $\Phi_{[\mathbf{v}_{\text{refl}}(D^+), T_{D^+}]}(\mathbf{x}', \mathbf{v}, t')$. Similarly, the D₂ neutrals arising from reflection of D₂⁺ ions are assumed to follow a Maxwellian distribution, $\Phi_{[\mathbf{v}_{\text{refl}}(D_2^+), T_{D_2^+}]}(\mathbf{x}', \mathbf{v}, t')$, being $\mathbf{v}_{\text{refl}}(D_2^+) = \mathbf{v}_{D_2^+} - 2\mathbf{v}_{pD_2^+}$, with $\mathbf{v}_{pD_2^+} = (\mathbf{v}_{D_2^+} \cdot \hat{\mathbf{n}}) \hat{\mathbf{n}}$ and $T_{D_2^+}$ the temperature of the incoming D₂⁺ ions.

We now focus on the contributions in Eqs. (3.66-3.67) that account for the reemission of neutrals from the boundary, which are written in terms of

$$\Gamma_{\text{reem}, D}(\mathbf{x}'_b) = (1 - \beta_{\text{assoc}}) [\Gamma_{\text{out}, D}(\mathbf{x}'_b) + \Gamma_{\text{out}, D^+}(\mathbf{x}'_b)] \quad (3.70)$$

and

$$\Gamma_{\text{reem}, D_2}(\mathbf{x}'_b) = \Gamma_{\text{out}, D_2}(\mathbf{x}'_b) + \Gamma_{\text{out}, D_2^+}(\mathbf{x}'_b) + \frac{\beta_{\text{assoc}}}{2} [\Gamma_{\text{out}, D}(\mathbf{x}'_b) + \Gamma_{\text{out}, D^+}(\mathbf{x}'_b)]. \quad (3.71)$$

Chapter 3. A multi-component model of plasma turbulence and kinetic neutral dynamics

In addition to the projections of the ion fluxes to the boundary, $\Gamma_{\text{out},D_2^+}$ and $\Gamma_{\text{out},D_2^+}$, Eqs. (3.70) and (3.71) account for the projections along the direction normal to the boundary of the fluxes of D atoms and D_2 molecules outflowing to the limiter and walls, $\Gamma_{\text{out},D}$ and Γ_{out,D_2} . These are defined based on the neutral fluxes directed towards the boundary (with $v_p < 0$) as

$$\Gamma_{\text{out},D}(\mathbf{x}'_b) = - \int_{v_p < 0} (\mathbf{v}_p \cdot \mathbf{n}) f_D(\mathbf{x}'_b, \mathbf{v}) d\mathbf{v} \quad (3.72)$$

and

$$\Gamma_{\text{out},D_2}(\mathbf{x}'_b) = - \int_{v_p < 0} (\mathbf{v}_p \cdot \mathbf{n}) f_{D_2}(\mathbf{x}'_b, \mathbf{v}) d\mathbf{v}. \quad (3.73)$$

We assume that the velocity distribution of the reemitted particles follows the Knudsen cosine law for a given wall temperature, T_w , which for the D atoms yields

$$\chi_{\text{in},D}(\mathbf{x}'_b, \mathbf{v}) = \frac{3}{4\pi} \frac{m_D^2}{T_w^2} \cos(\theta) \exp\left(-\frac{m_D v^2}{2T_w}\right), \quad (3.74)$$

while the expression for D_2 molecules is similarly given by

$$\chi_{\text{in},D_2}(\mathbf{x}'_b, \mathbf{v}) = \frac{3}{4\pi} \frac{m_{D_2}^2}{T_w^2} \cos(\theta) \exp\left(-\frac{m_{D_2} v^2}{2T_w}\right). \quad (3.75)$$

We then follow an approach identical to the one described in Ref. [61] to obtain a set of time-independent two-dimensional integral equations for n_D and n_{D_2} , enabling the numerical implementation of the formal solution in Eqs. (3.60) and (3.61). First, we take advantage of the fact that the typical neutral time of flight is shorter than the characteristic turbulence timescales, $\tau_n \ll \tau_{\text{turb}}$, a condition which is denote in Ref. [61] as the neutral adiabatic regime. This allows for the approximation $t' = t$ in Eqs. (3.60-3.67) or, equivalently, $\partial_t f_D = 0$ and $\partial_t f_{D_2} = 0$ in Eqs. (3.58-3.59). We also note that the neutral mean free path is typically smaller than the characteristic elongation of turbulent structures along the magnetic field direction, $\lambda_{\text{mfp},n} k_{\parallel} \ll 1$. Therefore, our description of neutral motion is reduced to the analysis of a set of independent two-dimensional planes perpendicular to the magnetic field, which coincide approximately with the poloidal planes. Finally, integrating Eqs. (3.60-3.61) over the velocity space, we obtain a system of two coupled equations for the densities of D atoms and D_2 molecules, written as

$$n_D(\mathbf{x}_\perp) = \int_D dA' \frac{1}{r'_\perp} \int_0^\infty dv_\perp v_\perp \int_0^\infty dv_\parallel \left\{ \frac{S_D(\mathbf{x}'_\perp, \mathbf{v})}{v_\perp} \exp \left[-\frac{1}{v_\perp} \int_0^{r'_\perp} v_{\text{eff},D}(\mathbf{x}''_\perp) dr''_\perp \right] \right\} \\ + \int_{\partial D} da'_b \frac{\cos\theta'}{r'_{\perp b}} \int_0^\infty dv_\perp v_\perp \int_0^\infty dv_\parallel \left\{ f_D(\mathbf{x}'_{\perp b}, \mathbf{v}) \exp \left[-\frac{1}{v_\perp} \int_0^{r'_\perp} v_{\text{eff},D}(\mathbf{x}''_\perp) dr''_\perp \right] \right\}, \quad (3.76)$$

and

$$n_{D_2}(\mathbf{x}_\perp) = \int_D dA' \frac{1}{r'_\perp} \int_0^\infty dv_\perp v_\perp \int_0^\infty dv_\parallel \left\{ \frac{S_{D_2}(\mathbf{x}'_\perp, \mathbf{v})}{v_\perp} \exp \left[-\frac{1}{v_\perp} \int_0^{r'_\perp} v_{\text{eff},D_2}(\mathbf{x}''_\perp) dr''_\perp \right] \right\} \\ + \int_{\partial D} da'_b \frac{\cos\theta'}{r'_{\perp b}} \int_0^\infty dv_\perp v_\perp \int_0^\infty dv_\parallel \left\{ f_{D_2}(\mathbf{x}'_{\perp b}, \mathbf{v}) \exp \left[-\frac{1}{v_\perp} \int_0^{r'_\perp} v_{\text{eff},D_2}(\mathbf{x}''_\perp) dr''_\perp \right] \right\}. \quad (3.77)$$

We remark that the geometrical arguments presented in Ref. [61] are used when considering the integral along the neutral path and the integral along the angle describing the perpendicular velocity, that is

$$\int_0^{r'_{\perp,b}} dr'_\perp \int_0^{2\pi} d\vartheta F(\mathbf{x}_\perp, \mathbf{x}'_\perp) = \int_D dA' \frac{1}{r'_\perp} F(\mathbf{x}_\perp, \mathbf{x}'_\perp), \quad (3.78)$$

where dA' is the area element in the two-dimensional poloidal plane and $F(\mathbf{x}_\perp, \mathbf{x}'_\perp)$ is a generic function. We also use

$$\int_0^{r'_{\perp,b}} dr'_\perp \int_0^{2\pi} d\vartheta \delta(r'_\perp - r'_{\perp b}) F(\mathbf{x}_\perp, \mathbf{x}'_\perp) = \int_{\partial D} da'_b \frac{\cos\theta'}{r'_{\perp b}} F(\mathbf{x}_\perp, \mathbf{x}'_{\perp b}), \quad (3.79)$$

with da'_b designating a line element along the boundary of D , which we write as ∂D , and $\theta' = \arccos(\Omega_\perp \cdot \hat{\mathbf{n}})$.

We also express the volumetric source terms featuring in Eqs. (3.62) and (3.63), $S_D(\mathbf{x}', \mathbf{v})$ and $S_{D_2}(\mathbf{x}', \mathbf{v})$, in terms of n_D and n_{D_2} , and the distribution functions of the neutral species at the boundary appearing in Eqs. (3.66) and (3.63), f_D and f_{D_2} , in terms of Γ_{out,D^+} , $\Gamma_{\text{out},D_2^+}$, $\Gamma_{\text{out},D}$ and Γ_{out,D_2} . For the density of D_2 molecules, n_{D_2} , this is expressed as

$$\begin{aligned}
n_{D_2}(\mathbf{x}_\perp) = & \int_D n_{D_2}(\mathbf{x}'_\perp) \nu_{\text{cx}, D_2}(\mathbf{x}'_\perp) K_{p \rightarrow p}^{D_2, D_2^+}(\mathbf{x}_\perp, \mathbf{x}'_\perp) dA' \\
& + \int_{\partial D} (1 - \alpha_{\text{refl}}(\mathbf{x}'_{\perp, b})) \Gamma_{\text{out}, D_2}(\mathbf{x}'_{\perp, b}) K_{b \rightarrow p}^{D_2}(\mathbf{x}_\perp, \mathbf{x}'_{\perp, b}) da'_b \\
& + \int_{\partial D} (1 - \alpha_{\text{refl}}(\mathbf{x}'_{\perp, b})) \frac{\beta_{\text{assoc}}}{2} \Gamma_{\text{out}, D}(\mathbf{x}'_{\perp, b}) K_{b \rightarrow p}^{D_2}(\mathbf{x}_\perp, \mathbf{x}'_{\perp, b}) da'_b \\
& + \int_D n_D(\mathbf{x}'_\perp) \nu_{\text{cx}, D-D_2^+}(\mathbf{x}'_\perp) K_{p \rightarrow p}^{D_2, D_2^+}(\mathbf{x}_\perp, \mathbf{x}'_\perp) dA' + n_{D_2[\text{rec}(D_2^+)]}(\mathbf{x}_\perp) \\
& + n_{D_2[\text{out}(D_2^+)]}(\mathbf{x}_\perp) + n_{D_2[\text{out}(D^+)]}(\mathbf{x}_\perp),
\end{aligned} \tag{3.80}$$

while for the density of D atoms, n_D , this is written as

$$\begin{aligned}
n_D(\mathbf{x}_\perp) = & \int_D n_D(\mathbf{x}'_\perp) \nu_{\text{cx}, D}(\mathbf{x}'_\perp) K_{p \rightarrow p}^{D, D^+}(\mathbf{x}_\perp, \mathbf{x}'_\perp) dA' \\
& + \int_D n_{D_2}(\mathbf{x}'_\perp) \nu_{\text{cx}, D_2-D^+}(\mathbf{x}'_\perp) K_{p \rightarrow p}^{D, D^+}(\mathbf{x}_\perp, \mathbf{x}'_\perp) dA' \\
& + \int_D 2n_{D_2}(\mathbf{x}'_\perp) \nu_{\text{diss}, D_2}(\mathbf{x}'_\perp) K_{p \rightarrow p}^{D, \text{diss}(D_2)}(\mathbf{x}_\perp, \mathbf{x}'_\perp) dA' \\
& + \int_D n_{D_2}(\mathbf{x}'_\perp) \nu_{\text{diss-iz}, D_2}(\mathbf{x}'_\perp) K_{p \rightarrow p}^{D, \text{diss-iz}(D_2)}(\mathbf{x}_\perp, \mathbf{x}'_\perp) dA' \\
& + \int_{\partial D} (1 - \alpha_{\text{refl}}(\mathbf{x}'_{\perp, b})) (1 - \beta_{\text{assoc}}) \Gamma_{\text{out}, D}(\mathbf{x}'_{\perp, b}) K_{b \rightarrow p}^{D, \text{reem}}(\mathbf{x}_\perp, \mathbf{x}'_{\perp, b}) da'_b \\
& + n_{D[\text{rec}(D^+)]}(\mathbf{x}_\perp) + n_{D[\text{out}(D^+)]}(\mathbf{x}_\perp) + n_{D[\text{diss}(D_2^+)]}(\mathbf{x}_\perp).
\end{aligned} \tag{3.81}$$

Replacing ν_p in Eqs. (3.73) and (3.72), the projections of the fluxes of D_2 and D along the direction normal to the boundary are written respectively as $\Gamma_{\text{out}, D_2}(\mathbf{x}'_{\perp, b}) = - \int_{\cos(\theta) < 0} \nu_\perp \cos \theta f_{D_2}(\mathbf{x}'_{\perp, b}, \mathbf{v}_\perp) d\mathbf{v}_\perp$ and $\Gamma_{\text{out}, D}(\mathbf{x}'_{\perp, b}) = - \int_{\cos(\theta) < 0} \nu_\perp \cos \theta f_D(\mathbf{x}'_{\perp, b}, \mathbf{v}_\perp) d\mathbf{v}_\perp$. Then, replacing $f_{D_2}(\mathbf{x}'_{\perp, b}, \mathbf{v}_\perp)$ and $f_D(\mathbf{x}'_{\perp, b}, \mathbf{v}_\perp)$ by their expressions as given in Eqs. (3.66) and (3.67), these fluxes are rewritten in terms of n_D , n_{D_2} , Γ_{out, D^+} , $\Gamma_{\text{out}, D_2^+}$, $\Gamma_{\text{out}, D}$ and Γ_{out, D_2} as

$$\begin{aligned}
\Gamma_{\text{out}, D_2}(\mathbf{x}_{\perp, b}) = & \int_D n_{D_2}(\mathbf{x}'_\perp) \nu_{\text{cx}, D_2}(\mathbf{x}'_\perp) K_{p \rightarrow b}^{D_2, D_2^+}(\mathbf{x}_\perp, \mathbf{x}'_\perp) dA' \\
& + \int_{\partial D} (1 - \alpha_{\text{refl}}(\mathbf{x}'_{\perp, b})) \Gamma_{\text{out}, D_2}(\mathbf{x}'_{\perp, b}) K_{b \rightarrow b}^{D_2}(\mathbf{x}_\perp, \mathbf{x}'_{\perp, b}) da'_b \\
& + \int_{\partial D} (1 - \alpha_{\text{refl}}(\mathbf{x}'_{\perp, b})) \frac{\beta_{\text{assoc}}}{2} \Gamma_{\text{out}, D}(\mathbf{x}'_{\perp, b}) K_{b \rightarrow b}^{D_2}(\mathbf{x}_\perp, \mathbf{x}'_{\perp, b}) da'_b \\
& + \int_D n_D(\mathbf{x}'_\perp) \nu_{\text{cx}, D-D_2^+}(\mathbf{x}'_\perp) K_{p \rightarrow b}^{D_2, D_2^+}(\mathbf{x}_\perp, \mathbf{x}'_\perp) dA' \\
& + \Gamma_{\text{out}, D_2[\text{rec}(D_2^+)]}(\mathbf{x}_\perp) + \Gamma_{\text{out}, D_2[\text{out}(D_2^+)]}(\mathbf{x}_\perp) + \Gamma_{\text{out}, D_2[\text{out}(D^+)]}(\mathbf{x}_\perp),
\end{aligned} \tag{3.82}$$

and

$$\begin{aligned}
\Gamma_{\text{out},D}(\mathbf{x}_{\perp,b}) = & \int_D n_D(\mathbf{x}'_{\perp}) v_{\text{cx},D}(\mathbf{x}'_{\perp}) K_{p \rightarrow b}^{D,D^+}(\mathbf{x}_{\perp}, \mathbf{x}'_{\perp}) dA' \\
& + \int_D n_{D_2}(\mathbf{x}'_{\perp}) v_{\text{cx},D_2 \rightarrow D^+}(\mathbf{x}'_{\perp}) K_{p \rightarrow b}^{D,D^+}(\mathbf{x}_{\perp}, \mathbf{x}'_{\perp}) dA' \\
& + \int_D 2n_{D_2}(\mathbf{x}'_{\perp}) v_{\text{diss},D_2}(\mathbf{x}'_{\perp}) K_{p \rightarrow b}^{D,\text{diss}(D_2)}(\mathbf{x}_{\perp}, \mathbf{x}'_{\perp}) dA' \\
& + \int_D n_{D_2}(\mathbf{x}'_{\perp}) v_{\text{diss-iz},D_2}(\mathbf{x}'_{\perp}) K_{p \rightarrow b}^{D,\text{diss-iz}(D_2)}(\mathbf{x}_{\perp}, \mathbf{x}'_{\perp}) dA' \\
& + \int_{\partial D} (1 - \alpha_{\text{refl}}(\mathbf{x}'_{\perp,b})) (1 - \beta_{\text{assoc}}) \Gamma_{\text{out},D}(\mathbf{x}'_{\perp,b}) K_{b \rightarrow b}^{D,\text{reem}}(\mathbf{x}_{\perp}, \mathbf{x}'_{\perp,b}) da'_b \\
& + \Gamma_{D[\text{rec}(D^+)]}(\mathbf{x}_{\perp}) + \Gamma_{D[\text{out}(D^+)]}(\mathbf{x}_{\perp}) + \Gamma_{D[\text{diss}(D_2^+)]}(\mathbf{x}_{\perp}),
\end{aligned} \tag{3.83}$$

We remark that the densities and fluxes of neutral particles in Eqs. (3.80-3.83) are multiplied by a factor $1 - \alpha_{\text{refl}}(\mathbf{x}'_{\perp,b})$ in order to consider only the contribution of particles that are reemitted at the boundary, hence excluding reflection. We note that reflection of neutral particles is included in the definition of the kernel functions featuring in Eqs. (3.76-3.77).

We now turn to the definition of the kernel functions appearing in Eqs. (3.80-3.83). These are defined as integrals in the velocity space for a given pair of source (\mathbf{x}'_{\perp}) and target (\mathbf{x}_{\perp}) locations. Exemplifying for $K_{p \rightarrow p}^{D_2,D_2^+}(\mathbf{x}_{\perp}, \mathbf{x}'_{\perp})$, the kernel function measures the number of D_2 neutrals arriving at a location \mathbf{x}_{\perp} in the plasma volume (p) as a result of collisions involving neutralization of D_2^+ ions at a location \mathbf{x}'_{\perp} inside the plasma volume (p). Its expression is given by

$$K_{p \rightarrow p}^{D_2,D_2^+}(\mathbf{x}_{\perp}, \mathbf{x}'_{\perp}) = K_{p \rightarrow p, \text{dir}}^{D_2,D_2^+}(\mathbf{x}_{\perp}, \mathbf{x}'_{\perp}) + \alpha_{\text{refl}} K_{p \rightarrow p, \text{refl}}^{D_2,D_2^+}(\mathbf{x}_{\perp}, \mathbf{x}'_{\perp}). \tag{3.84}$$

which splits the contributions to n_{D_2} arising from the direct path of length $r'_{\perp, \text{dir}}$ connecting \mathbf{x}_{\perp} and \mathbf{x}'_{\perp} , $K_{p \rightarrow p, \text{dir}}^{D_2,D_2^+}(\mathbf{x}_{\perp}, \mathbf{x}'_{\perp})$, and the path referring to the trajectory of neutrals that are reflected at the boundary, $K_{p \rightarrow p, \text{refl}}^{D_2,D_2^+}(\mathbf{x}_{\perp}, \mathbf{x}'_{\perp})$. Both $K_{p \rightarrow p, \text{dir}}^{D_2,D_2^+}$ and $K_{p \rightarrow p, \text{refl}}^{D_2,D_2^+}$ follow the same expression,

$$K_{p \rightarrow p, \text{path}}^{D_2,D_2^+}(\mathbf{x}_{\perp}, \mathbf{x}'_{\perp}) = \int_0^{\infty} \frac{1}{r'_{\perp, \text{path}}} \Phi_{\perp}[\mathbf{v}_{\perp, D_2^+}, T_{D_2^+}](\mathbf{x}'_{\perp}, \mathbf{v}_{\perp}) \exp \left[-\frac{1}{v_{\perp}} \int_0^{r'_{\perp, \text{path}}} v_{\text{eff}, D_2}(\mathbf{x}''_{\perp}) dr''_{\perp} \right] dv_{\perp}, \tag{3.85}$$

where $\text{path} = \{\text{dir}, \text{refl}\}$ and $r'_{\perp, \text{path}}$ denotes the distance between \mathbf{x}_{\perp} and \mathbf{x}'_{\perp} along the path (for the direct trajectory $r'_{\perp, \text{dir}}$ is the distance between the two points along a straight line, while for the reflected trajectory $r'_{\perp, \text{refl}}$ is computed as the sum of the distance between \mathbf{x}'_{\perp} and the boundary and the distance from the boundary to \mathbf{x}_{\perp}). We remark that $\Phi_{\perp}[\mathbf{v}_{\perp, D_2^+}, T_{D_2^+}](\mathbf{x}'_{\perp}, \mathbf{v}_{\perp})$ is

Chapter 3. A multi-component model of plasma turbulence and kinetic neutral dynamics

the integral along the parallel velocity of the D_2^+ Maxwellian distribution function, $\Phi_{\perp}[\mathbf{v}_{\perp D_2^+}, T_{D_2^+}](\mathbf{x}'_{\perp}, \mathbf{v}_{\perp}) = \int_{-\infty}^{\infty} \Phi_{\perp}[\mathbf{v}_{\perp D_2^+}, T_{D_2^+}](\mathbf{x}', \mathbf{v}_{\perp}) d v_{\parallel}$. We also note that $K_{p \rightarrow p, \text{dir}}^{D_2, D_2^+}$ in Eq. (3.85) is valid if the points are optically connected, i.e. if the straight line connecting the two points does not cross the core nor the limiter plates. Otherwise, if the points are not optically connected, $K_{p \rightarrow p, \text{dir}}^{D_2, D_2^+} = 0$ is defined. As for $K_{p \rightarrow p, \text{refl}}^{D_2, D_2^+}$, we highlight that, following the same approach presented in Ref. [61] and considered in Ch. 2, we neglect reflection at the outer walls, while ions and neutrals can be reflected at the limiter plates. The other kernels appearing in Eqs. (3.76-3.77) follow the same structure as $K_{p \rightarrow p}^{D_2, D_2^+}$, and they take into account possible direct and reflected paths connecting the two points. The form of these kernels is detailed in App. D.

Turning now to the evaluation of the non-homogeneous terms appearing in Eqs. (3.80-3.83), i.e. the terms that are not proportional to n_D nor n_{D_2} , we start by looking at the contribution of the ions recycled at the wall. As a matter of fact, the contribution to the density of neutral D atoms of reflection and reemission of D^+ ions that reach the boundary and recombine with electrons is written as

$$n_{D[\text{out}, D^+]}(\mathbf{x}_{\perp}) = \int_{\partial D} \Gamma_{\text{out}, D^+}(\mathbf{x}'_{\perp, b}) \left[(1 - \alpha_{\text{refl}}(\mathbf{x}'_{\perp, b})) (1 - \beta_{\text{assoc}}) K_{b \rightarrow p}^{D, \text{reem}}(\mathbf{x}_{\perp}, \mathbf{x}'_{\perp, b}) + \alpha_{\text{refl}}(\mathbf{x}'_{\perp, b}) K_{b \rightarrow p}^{D, \text{refl}}(\mathbf{x}_{\perp}, \mathbf{x}'_{\perp, b}) \right] d a'_b, \quad (3.86)$$

where Γ_{out, D^+} is defined in Eq. (3.68). Similarly, the recombination of D_2^+ ions with electrons at the walls that are then either reflected or reemitted as D_2 , and the recombination of D^+ ions with electrons at the walls and the following association into D_2 molecules contribute to the density of the D_2 species. These contributions can be expressed as

$$n_{D_2[\text{out}, D_2^+]}(\mathbf{x}_{\perp}) = \int_{\partial D} \Gamma_{\text{out}, D_2^+}(\mathbf{x}'_{\perp, b}) \left[(1 - \alpha_{\text{refl}}(\mathbf{x}'_{\perp, b})) K_{b \rightarrow p}^{D_2, \text{reem}}(\mathbf{x}_{\perp}, \mathbf{x}'_{\perp, b}) + \alpha_{\text{refl}}(\mathbf{x}'_{\perp, b}) K_{b \rightarrow p}^{D_2, \text{refl}}(\mathbf{x}_{\perp}, \mathbf{x}'_{\perp, b}) \right] d a'_b, \quad (3.87)$$

and

$$n_{D_2[\text{out}, D^+]}(\mathbf{x}_{\perp}) = \int_{\partial D} \Gamma_{\text{out}, D^+}(\mathbf{x}'_{\perp, b}) \left[(1 - \alpha_{\text{refl}}(\mathbf{x}'_{\perp, b})) \frac{\beta_{\text{assoc}}}{2} K_{b \rightarrow p}^{D_2, \text{reem}}(\mathbf{x}_{\perp}, \mathbf{x}'_{\perp, b}) \right] d a'_b. \quad (3.88)$$

We also define the non-homogeneous contributions to the flux of neutrals at the boundary, $\Gamma_{\text{out}, D}$ and Γ_{out, D_2} , arising from the ions outflowing to the wall. Following a similar approach to the one described for the contributions to $n_{\text{out}, D}$ and n_{out, D_2} , these are expressed as

3.5. The kinetic model for the neutral species and its formal solution

$$\begin{aligned} \Gamma_{\text{out},D_2[\text{out},D_2^+]}(\mathbf{x}_\perp,b) &= \int_{\partial D} \Gamma_{\text{out},D_2^+}(\mathbf{x}'_\perp,b) \left[(1 - \alpha_{\text{refl}}(\mathbf{x}'_\perp,b)) K_{b \rightarrow b}^{D_2,\text{reem}}(\mathbf{x}_\perp,b,\mathbf{x}'_\perp,b) \right. \\ &\quad \left. + \alpha_{\text{refl}}(\mathbf{x}'_\perp,b) K_{b \rightarrow b}^{D_2,\text{refl}}(\mathbf{x}_\perp,b,\mathbf{x}'_\perp,b) \right] da'_b, \end{aligned} \quad (3.89)$$

$$\Gamma_{\text{out},D_2[\text{out},D^+]}(\mathbf{x}_\perp,b) = \int_{\partial D} \Gamma_{\text{out},D^+}(\mathbf{x}'_\perp,b) \left[(1 - \alpha_{\text{refl}}(\mathbf{x}'_\perp,b)) \frac{\beta_{\text{assoc}}}{2} K_{b \rightarrow b}^{D_2,\text{reem}}(\mathbf{x}_\perp,b,\mathbf{x}'_\perp,b) \right] da'_b, \quad (3.90)$$

and

$$\begin{aligned} \Gamma_{\text{out},D[\text{out},D^+]}(\mathbf{x}_\perp,b) &= \int_{\partial D} \Gamma_{\text{out},D^+}(\mathbf{x}'_\perp,b) \left[(1 - \alpha_{\text{refl}}(\mathbf{x}'_\perp,b)) (1 - \beta_{\text{assoc}}) K_{b \rightarrow b}^{D,\text{reem}}(\mathbf{x}_\perp,b,\mathbf{x}'_\perp,b) \right. \\ &\quad \left. + \alpha_{\text{refl}}(\mathbf{x}'_\perp,b) K_{b \rightarrow b}^{D,\text{refl}}(\mathbf{x}_\perp,b,\mathbf{x}'_\perp,b) \right] da'_b. \end{aligned} \quad (3.91)$$

We then turn to the evaluation of the contributions to the neutral particles featuring in Eqs. (3.80-3.83) generated by volumetric processes involving the ion species D^+ and D_2^+ . The contribution to the D_2 density from D_2^+ recombination processes is expressed as

$$n_{D_2[\text{rec},D_2^+]}(\mathbf{x}_\perp) = \int_D n_{D_2^+}(\mathbf{x}'_\perp) v_{\text{rec},D_2^+}(\mathbf{x}'_\perp) K_{p \rightarrow p}^{D_2,D_2^+}(\mathbf{x}_\perp,\mathbf{x}'_\perp) dA', \quad (3.92)$$

while the contribution to the flux of D_2 to the boundary, also associated to D_2^+ recombination events, is written as

$$\Gamma_{\text{out},D_2[\text{rec},D_2^+]}(\mathbf{x}_\perp) = \int_D n_{D_2^+}(\mathbf{x}'_\perp) v_{\text{rec},D_2^+}(\mathbf{x}'_\perp) K_{p \rightarrow b}^{D_2,D_2^+}(\mathbf{x}_\perp,\mathbf{x}'_\perp) dA'. \quad (3.93)$$

Similar contributions from volumetric recombination processes are considered for the D neutral species. The contribution to the D density from D^+ recombination is given by

$$n_{D[\text{rec},D^+]}(\mathbf{x}_\perp) = \int_D n_{D^+}(\mathbf{x}'_\perp) v_{\text{rec},D^+}(\mathbf{x}'_\perp) K_{p \rightarrow p}^{D,D^+}(\mathbf{x}_\perp,\mathbf{x}'_\perp) dA', \quad (3.94)$$

Chapter 3. A multi-component model of plasma turbulence and kinetic neutral dynamics

and a similar definition is considered for the flux of D,

$$\Gamma_{\text{out,D[rec,D}^+]}(\mathbf{x}_\perp) = \int_{\text{D}} n_{\text{D}^+}(\mathbf{x}'_\perp) v_{\text{rec,D}^+}(\mathbf{x}'_\perp) K_{p \rightarrow b}^{\text{D,D}^+}(\mathbf{x}_\perp, \mathbf{x}'_\perp) dA'. \quad (3.95)$$

Finally, the contribution to n_{D} from the dissociation of D_2^+ ions featuring in Eq. (3.81) is defined as

$$\begin{aligned} n_{\text{D[diss(D}_2^+)]}(\mathbf{x}_\perp) &= \int_{\text{D}} n_{\text{D}_2^+}(\mathbf{x}'_\perp) v_{\text{diss,D}_2^+}(\mathbf{x}'_\perp) K_{p \rightarrow p}^{\text{D,diss(D}_2^+)}(\mathbf{x}_\perp, \mathbf{x}'_\perp) dA' \\ &+ \int_{\text{D}} 2n_{\text{D}_2^+}(\mathbf{x}'_\perp) v_{\text{diss-rec,D}_2^+}(\mathbf{x}'_\perp) K_{p \rightarrow p}^{\text{D,diss-rec(D}_2^+)}(\mathbf{x}_\perp, \mathbf{x}'_\perp) dA'. \end{aligned} \quad (3.96)$$

and, similarly, the dissociation of D_2^+ ions gives rise to a contribution to $\Gamma_{\text{out,D}}$ in Eq. (3.83) defined as

$$\begin{aligned} \Gamma_{\text{out,D[diss(D}_2^+)]}(\mathbf{x}_\perp) &= \int_{\text{D}} n_{\text{D}_2^+}(\mathbf{x}'_\perp) v_{\text{diss,D}_2^+}(\mathbf{x}'_\perp) K_{p \rightarrow b}^{\text{D,diss(D}_2^+)}(\mathbf{x}_\perp, \mathbf{x}'_\perp) dA' \\ &+ \int_{\text{D}} 2n_{\text{D}_2^+}(\mathbf{x}'_\perp) v_{\text{diss-rec,D}_2^+}(\mathbf{x}'_\perp) K_{p \rightarrow b}^{\text{D,diss-rec(D}_2^+)}(\mathbf{x}_\perp, \mathbf{x}'_\perp) dA'. \end{aligned} \quad (3.97)$$

The system of coupled kinetic equations for the neutral species is discretized on a regular cartesian grid in the (R, Z) plasma and written in matrix form, in order to obtain the corresponding numerical solution by factorizing the matrix and solving the system. We describe the details of the numerical implementation of the neutral model in App. E.

3.6 First simulation of a multi-component plasma with the GBS code

In this section, we present the results from the first turbulence simulations in the tokamak boundary based on the multi-component plasma model implemented in the GBS code and described in the present chapter, in Secs. 3.2-3.5. Analogously to the simulations reported in Refs. [33, 61] and in Ch. 2 of the present thesis, we consider a tokamak with an infinitesimally thin toroidal limiter at the HFS equatorial midplane, with major radius $R_0/\rho_{s0} = 500$, and we simulate a three-dimensional domain, considering an annular cross section that includes both the edge and the device SOL. The radial length of the domain is $S_{\text{rad}} = 150\rho_{s0}$ and the poloidal length at the core interface is $S_{\text{pol}} = 800\rho_{s0}$. Given that we consider the limiter to extend over $75\rho_{s0}$, both the open and closed field-line regions have a radial width of $75\rho_{s0}$, corresponding to half the domain size along the radial direction.

3.6. First simulation of a multi-component plasma with the GBS code

The simulation presented in this chapter considers the following parameters: $q = 3.992$, $n_0 = 2 \times 10^{13} \text{cm}^{-3}$, $T_0 = 20.0 \text{eV}$, $\tau = 1$, $\Omega_{\text{ci}} = 5.0 \times 10^7 \text{s}^{-1}$, $T_W = 0.3 \text{eV}$, $\nu = 0.1$, $S_{T_e} = S_{T_i} = 0.3$, $\eta_{0e} = \eta_{0D^+} = 1.0$, $\eta_{0\Omega} = 4.0$, $\chi_{\parallel 0,e} = 0.5$, $\chi_{\parallel 0,D^+} = 0.05$, $\chi_{\parallel 0,D_2^+} = 0.05$, $D_{\parallel n_e} = 0.5$, $D_{\parallel n_{D_2^+}} = 0.0$, $D_{\parallel \nu_{\parallel e}} = 0.5$, $D_{\parallel \nu_{\parallel D^+}} = 0.0$, $D_{\parallel \nu_{\parallel D_2^+}} = 0.5$, and $D_{\perp n_e} = 21.0$, $D_{\perp n_{D_2^+}} = D_{\perp \Omega} = D_{\perp \nu_{\parallel e}} = D_{\perp \nu_{\parallel D^+}} = D_{\perp \nu_{\parallel D_2^+}} = D_{\perp T_e} = D_{\perp T_{D^+}} = D_{\perp T_{D_2^+}} = 7.0$. Regarding the probability of a reflection process occurring at the limiter, we note that it has a strong dependence on the particle energy and the properties of the wall material (see Ref. [12]). In this simulation, reflection of ions and neutrals takes place at the limiter plates with a given probability $\alpha_{\text{refl,lim}}$, which we take constant along the limiter surface. We thus write the fraction of particles being reflected at the boundary as

$$\alpha_{\text{refl}}(\mathbf{x}'_{\perp,b}) = \begin{cases} \alpha_{\text{refl,lim}} \neq 0 & \text{if } \mathbf{x}'_{\perp,b} \text{ is located at limiter walls} \\ 0 & \text{if } \mathbf{x}'_{\perp,b} \text{ is located at the outer and inner boundary.} \end{cases} \quad (3.98)$$

Since we choose to consider metallic boundaries, we assume a value identical to the one adopted in Ref. [61] and in Ch. 2 of this thesis, $\alpha_{\text{refl,lim}} = 0.8$, with the remaining fraction of the incoming particles being absorbed and reemitted when the wall is saturated. We also assume that most of the absorbed D atoms associate into D_2 molecules at the tokamak boundary (see Refs. [79, 96]), thus being reemitted as D_2 molecules. We therefore take $\beta_{\text{assoc}} = 0.95$.

Regarding the numerical parameters of the simulations, the plasma grid resolution is $n_{x,p} \times n_{y,p} \times n_{z,p} = 255 \times 511 \times 64$, while the resolution of the neutral grid is $n_{x,n} \times n_{y,n} \times n_{z,n} = 24 \times 138 \times 64$. The time step is $3.75 \times 10^{-5} R_0 / c_s$, with the neutral quantities being evaluated every $\Delta t = 0.1 R_0 / c_s$. Although convergence studies based on the multispecies model presented in this chapter have not been developed, convergence on plasma and neutral grid refinement has been studied within the context of single-component simulations. The conclusions presented in Ref. [36], which we expect to remain valid in the multi-species model presented in this chapter, confirm that our results are converged with respect to the frequency of neutral calculation.

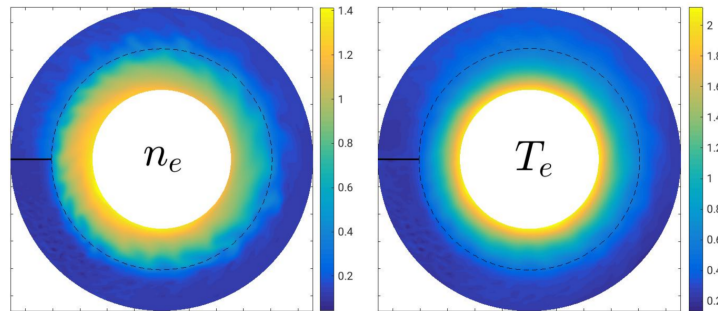


Figure 3.2: Typical poloidal snapshot of the electron density (n_e) and electron temperature (T_e) taken from the turbulent quasi-steady state of the multi-component plasma simulation described in the present chapter.

Chapter 3. A multi-component model of plasma turbulence and kinetic neutral dynamics

The simulation results presented here refer to the quasi-steady state regime, reached after a transient, when the plasma and neutral profiles oscillate around constant equilibrium values. We highlight that, similarly to the results from single-component GBS simulations, the plasma behaviour is turbulent in the edge and especially in the SOL, as it can be observed in the poloidal snapshots of electron density (n_e) and temperature (T_e) presented in Fig. 3.2. We perform toroidal and time averages of the plasma quantities evolved by Eqs. (3.19-3.27) and (3.28) over a time interval of $\Delta t \simeq 10R_0/c_{s0}$. Poloidal cross section plots of these quantities are shown in Fig. 3.3. In Fig. 3.4, we present the poloidal cross section plots of the density of the neutral atoms and molecules, n_D and n_{D_2} respectively, and the neutral-plasma collisional interaction terms considered in our model. The results of these multi-species simulations are compared with respect to a single-component plasma simulation considering the same parameter values. We present in Fig. 3.5 the time and toroidal averages of the plasma and neutral quantities from the single-species simulation which we find relevant to compare with the results from the multi-species simulation.

We start by focusing on some general considerations on the densities of the plasma and neutral particles. The plots in Fig. 3.3 show that the density of the molecular ion species D_2^+ is between three and four orders of magnitude smaller than the density of the main ion species D^+ , which agrees with the assumption $n_{D_2^+}/n_{D^+} \ll 1$ considered in Eqs. (3.22-3.27) for the derivation of the parallel friction and heat flux terms and in Eqs. (3.40-3.44) to obtain the boundary conditions at the limiter plates. We note that the density of D_2^+ peaks just inside the LCFS close to the limiter, since most of the D_2 molecules cross the open-field line region without interacting due to the low electron densities and temperatures in the SOL and are then dissociated and/or ionized by the denser and warmer plasma inside the LCFS. As a matter of fact, $n_{D_2^+}$ matches the profile of the molecular ionization source $n_{D_2}v_{iz,D_2}$ shown in Fig. 3.4, which also peaks in the edge near the limiter. On the other hand, Fig. 3.4 shows that n_D and n_{D_2} are similar to n_{D^+} near the limiter plates, while being about one order of magnitude smaller than n_{D^+} in the rest of the SOL and up to two orders of magnitude smaller inside the LCFS. Moreover, looking at the relative importance of D and D_2 , Fig. 3.4 shows that n_{D_2} is larger than n_D by a factor between two and three in the SOL around the limiter, while n_D is larger than n_{D_2} inside the LCFS at the HFS equatorial midplane, as a result of the higher values of electron density and temperature, which lead to the dissociation of D_2 molecules in this region.

We then turn our attention to the asymmetry of the plasma density and flow. As a matter of fact, a slight up-down asymmetry in the edge region is observed in the profiles of n_e and n_{D^+} , which are noticeably larger below the equatorial midplane than above it. This can also be observed in the poloidal snapshot of n_e in Fig. 3.2. At the same time, the profiles of $v_{\parallel e}$ and $v_{\parallel D^+}$ reveal that electrons and D^+ ions flow in the counterclockwise direction in the edge region (see Fig. 3.3). Since most neutrals are ionized inside the LCFS and in the vicinity of the limiter, the plasma particles resulting from the ionization processes flow downwards, which leads to a slightly larger density of e^- and D^+ below the equatorial midplane of the device. We highlight that the n_{D^+} and $v_{\parallel D^+}$ profiles obtained from simulations based on the single-component model of

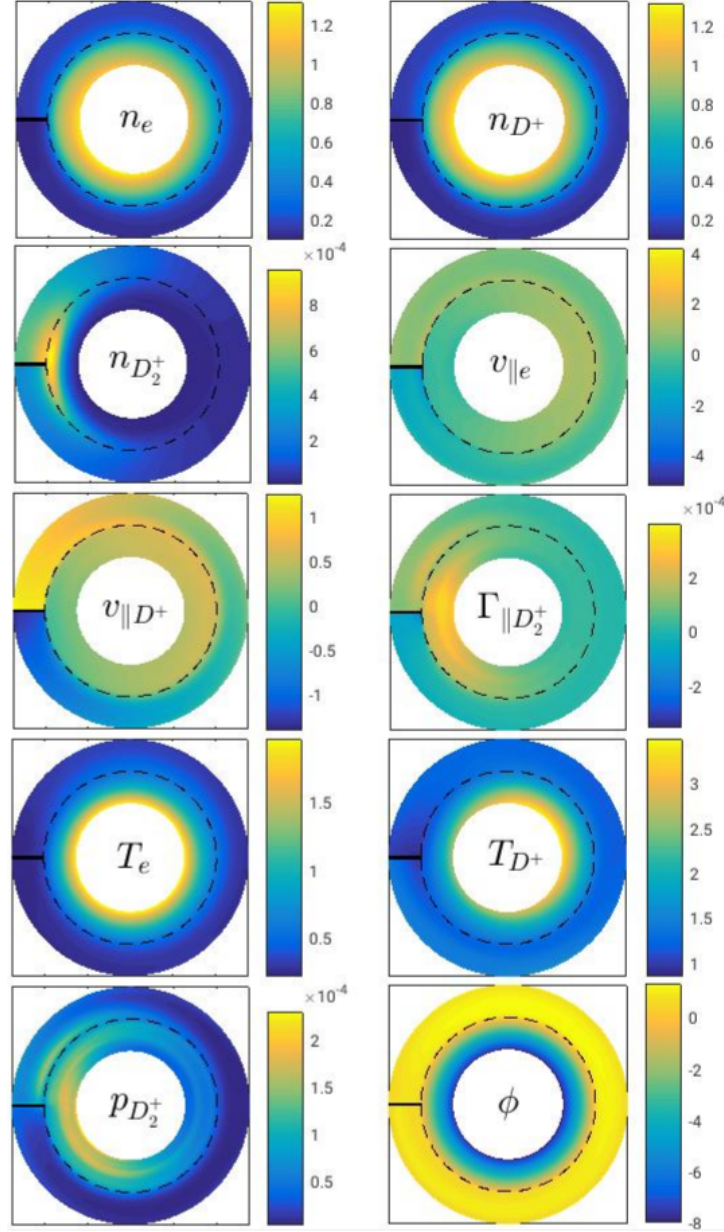


Figure 3.3: Cross section plots of the electron density (n_e), D^+ density (n_{D^+}), D_2^+ density ($n_{D_2^+}$), electron parallel velocity ($v_{||e}$), D^+ parallel velocity ($v_{||D^+}$), D_2^+ parallel velocity ($v_{||D_2^+}$), electron temperature (T_e), D^+ temperature (T_{D^+}), D_2^+ temperature ($T_{D_2^+}$) and electrostatic potential (ϕ), toroidal and time-averaged over an interval of $\Delta t = 10.1 R_0 / c_{s0}$ from the quasi-steady state of the multi-component plasma simulation.

GBS are slightly different, as illustrated in Fig. 3.5. In the single-component simulation, an up-down asymmetry is also observed in the n_{D^+} profile. However, this asymmetry is related to the ionization source $n_D v_{iz}$ being larger in the edge region below the limiter than above it, due to larger recycling rates at the lower limiter plate. In fact, in contrast to the multispecies case,

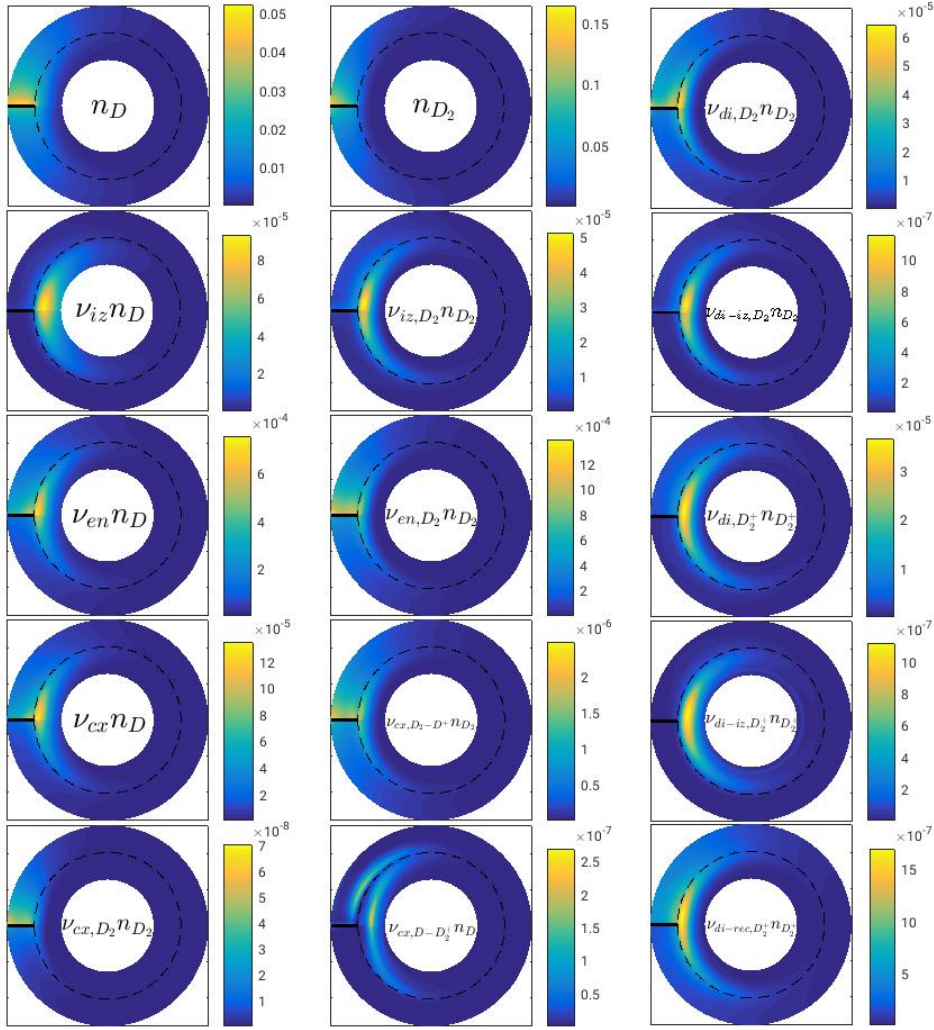


Figure 3.4: Cross section plots of the neutral species densities and source terms resulting from the neutral-plasma interaction, toroidal and time-averaged over an interval of $\Delta t = 10.1 R_0 / c_{s0}$ from the quasi-steady state of the multi-component plasma simulation described.

the $\nu_{\parallel D^+}$ is characterized by a counterclockwise parallel flow of D^+ ions in the edge below the midplane, while the parallel flow is directed clockwise above it.

Another important observation arising from the multi-component plasma simulation is the higher recycling rates in the region above the limiter than below, which is highlighted by the up-down asymmetry observed in the profiles of the densities of n_D and n_{D_2} in Fig. 3.4. This suggests that the parallel flux of plasma in the SOL region towards the limiter plates is larger above the equatorial midplane, which agrees with the up-down asymmetry shown in Fig. 3.3 for the poloidal profiles of n_{D^+} and $\nu_{\parallel D^+}$. A deep investigation of the reason behind this behaviour calls for a careful analysis of the turbulent dynamics in the SOL, taking also into account the other components of the flux beyond the parallel flow. Nonetheless, the simulation results suggest that this up-down asymmetry may be related to the counterclockwise flow of

plasma in the edge observed in the profile of $v_{\parallel D^+}$.

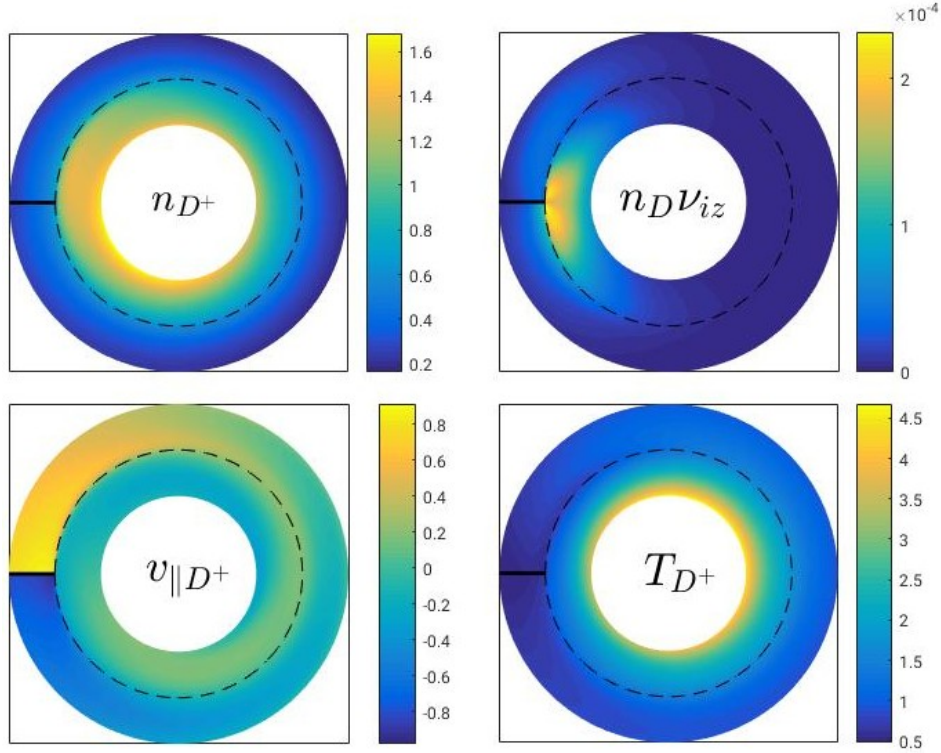


Figure 3.5: Cross section plots of plasma density $n = n_e = n_{D^+}$, ion parallel velocity $v_{\parallel D^+}$, ion temperature T_{D^+} and ionization source term $n_D v_{iz}$, toroidal and time-averaged over an interval of $\Delta t = 10.1 R_0 / c_{s0}$ from a quasi-steady state single-component plasma simulation. The grid sizes and simulation parameters are the same as the ones considered in the multi-component simulations, except for the wall re-emission temperature, which is set to $T_W = 3.0\text{eV}$, to mimic Franck-Condon dissociation processes, and $D_{\perp n_e} = 7.0$.

Moreover, n_{D^+} is observed to be slightly larger in the HFS with respect to the LFS, which is related to the existence of D^+ sources in the HFS around the midplane. This result agrees with the conclusions driven from the single-species simulation, where n_{D^+} is also found to be larger in the HFS as a consequence of the ionization source, $n_D v_{iz}$.

Focusing now on the temperature of the plasma species, we observe that the T_e profile presents a behaviour identical to the one verified in single-component plasma simulations. A clear asymmetry between the HFS and the LFS is observed for T_{D^+} , whose profile is also very similar to the results obtained from a single-component simulation presented in Fig. 3.5. As a matter of fact, the temperature is considerably lower on the HFS compared to the LFS, which is related to the generation of cold D^+ ions inside the LCFS due to the ionization of D atoms, dissociative processes and charge-exchange collisions. This becomes particularly important in the region above the limiter, where larger recycling rates are observed. On the other hand, the profile of $p_{D_2^+}$ peaks inside the LCFS at the HFS, where the majority of the D_2^+ ions are generated by ionization of D_2 molecules generated at the limiter. The up-down asymmetry

Chapter 3. A multi-component model of plasma turbulence and kinetic neutral dynamics

of the $p_{D_2^+}$ profile around the limiter plates is also related to the asymmetry of the recycling rates. As an aside note, we highlight that, since it is strongly related to the T_e profile [97], the electrostatic potential profile obtained from the multi-component simulations is identical to the one observed for the single-component plasma model.

Focusing on the neutral-plasma interaction terms presented in Fig. 3.4, we start by noticing that ionization processes are in general considerably more important in the edge region at the HFS. We also highlight that the ionization frequencies have similar profiles for both atoms and molecules. However, $n_{D_2} \nu_{iz,D_2}$ peaks in the vicinity of the LCFS, while $n_D \nu_{iz,D}$ peaks further inside the LCFS and shows a larger spread along the radial direction. In fact, D_2 molecules are generated in the SOL and are dissociated and/or ionized in the proximity of the LCFS, where the plasma is warmer and denser. In contrast, although most D atoms are generated in the SOL, they are also a product of dissociation of D_2 molecules in the edge. This effect shifts the maximum of $n_D \nu_{iz,D}$ radially inwards and increases the radial spread of the ionization source, when compared to single-component plasma simulations. Since n_D is larger than n_{D_2} in the edge, the maximum of $n_D \nu_{iz,D}$ is also almost two times larger than the maximum of $n_{D_2} \nu_{iz,D_2}$.

Regarding collisions between electrons and neutral particles, we note that the reactions involving D_2 are more important in the SOL, taking place mostly in the area surrounding the limiter plates, where a larger number of neutral molecules are generated. Reactions with D_2 are less important in the edge, as most molecules are dissociated and/or ionized due to the higher densities and temperatures. On the other hand, elastic collisions between electrons and D atoms peak inside the LCFS, which is because the cross sections of these reactions are larger in the edge region due to the higher plasma density and temperature and because of the presence of D atoms generated by molecular dissociation. We remark that elastic collisions and charge-exchange reactions are more frequent above the limiter, which follows from the previous discussion on the strong up-down asymmetry. As for charge-exchange reactions, we observe that their spatial distribution is similar to the one of collision between electrons and neutral particles. The charge-exchange reactions between the molecular species ($D_2 - D_2^+$ collisions) are less important than the interactions between mono-atomic species ($D - D^+$ collisions) by three to four orders of magnitude, which results from the small $n_{D_2^+}$ to n_{D^+} ratio. In addition, the terms related to charge-exchange interactions between D_2 molecules and D^+ ions ($D_2 - D^+$ collisions) are two orders of magnitude smaller than the ones between the atomic species ($D - D^+$ collisions), in the region of the domain where these interactions are important. Finally, charge-exchange interactions between D_2^+ ions and D atoms is three orders of magnitude less important than $D - D^+$ collisions, which is a consequence of $n_D \nu_{cx,D-D_2^+}$ being proportional to $n_{D_2^+}$.

We finally analyse the dissociative reactions, which constitute a sink of molecular species D_2 and D_2^+ and sources of D atoms and D^+ ions. Dissociation of D_2 and D_2^+ , described by the terms $n_{D_2} \nu_{di,D_2}$ and $n_{D_2^+} \nu_{di,D_2^+}$ respectively, which do not involve ionization nor recombination processes, are the dominant dissociation processes, as their frequencies are similar to the reaction rates of the ionization processes. We highlight that dissociation of D_2 molecules peaks

just above the limiter plate (where most D_2 molecules are generated) and in the edge region, in the proximity of the LCFS, and then it becomes considerably smaller in the core, given that n_{D_2} drops rapidly across the edge. In contrast, dissociation of D_2^+ ions is very small in the SOL, where the density of D_2^+ is negligible (at the typical electron temperature of the SOL, ionization of D_2 has a very small cross section), and is important only inside the LCFS, where D_2^+ ions are generated. The $n_{D_2^+} \nu_{di,D_2^+}$ profile thus closely follows the $n_{D_2^+}$ profile, exhibiting a larger radial spread with respect to the dissociation of D_2 . As for dissociative ionization of D_2 and D_2^+ , $n_{D_2} \nu_{di-iz,D_2}$ and $n_{D_2^+} \nu_{di-iz,D_2^+}$ respectively, we observe that the rates are smaller by one to two orders of magnitude compared to the dissociation of D_2 and D_2^+ and peak in the edge region even further inside. This is related to the fact that the energy required to trigger dissociative ionization processes is significantly larger than the one required to dissociate the particles without ionizing them, as shown in Table 3.2. Therefore, these processes are only important in the edge region, where densities and temperatures are sufficiently high to make these cross sections significant. This is in particular the case of $n_{D_2^+} \nu_{di-iz,D_2^+}$, since this term is also proportional to the density of D_2^+ ions, which is relevant only inside the LCFS. However, we remark that these reactions become considerably less important towards the core, as very few D_2 and D_2^+ cross the edge region without being dissociated. Regarding dissociative-recombination of D_2^+ particles, $n_{D_2^+} \nu_{di-rec,D_2^+}$, its amplitude is also smaller than that of dissociation by one to two orders of magnitude and follows very closely the $n_{D_2^+}$ profile, as there is no energy threshold to trigger the reaction, contrarily to dissociative ionization processes.

The results described above lead to a global picture of the main processes determining the dynamics of D_2 molecules in the tokamak boundary. Although some D_2 are dissociated in the open field-line region, most of them cross the LCFS and are dissociated into D atoms within a short distance, as they interact with the plasma of the edge, of higher density and temperature. The remaining D_2 molecules penetrate further inwards and are ionized by the increasingly warmer and denser plasma, giving rise to D_2^+ ions, which in turn have very short lifetimes, since they are rapidly dissociated into D^+ ions and D atoms.

We remark that, due to the low plasma density of the SOL, in the multi-component as well as in the single-component simulations, a considerable amount of D atoms generated in the SOL (emitted at the limiter or created by dissociation of D_2 molecules) penetrate in the edge, where ionization takes place due to the higher plasma density and temperature. However, the presence of the D sources inside the LCFS in the multi-component simulations shifts the spatial distribution of ionization, $n_D \nu_{iz}$, towards the core with respect to the results from single-component simulations, as shown in Fig. 3.5. Therefore, these results highlight the importance of considering molecular dynamics when describing the neutral-plasma interaction in the boundary of a tokamak. A parameter scan on the electron density and temperature will allow broader physical conclusions to be drawn from the multi-component model of the neutral-plasma interaction presented here. In particular, increasing plasma density and temperature is expected to reduce the penetration of both D atoms and D_2 molecules, thus shifting the dissociation and ionization sources/sinks radially outwards.

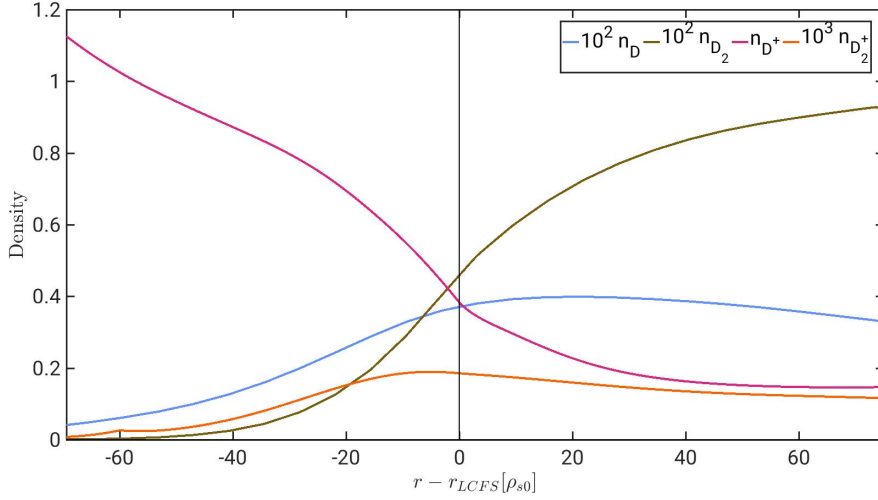


Figure 3.6: Radial profiles of the ions and neutrals species densities, averaged over the toroidal and poloidal directions, evaluated over an interval of $\Delta t = 10.1 R_0 / c_{s0}$ from a quasi-steady state simulation.

To conclude, we also present radial plots of the particle densities (Fig. 3.6) and radial fluxes (Fig. 3.7), which are obtained by evaluating the average of these quantities in time and in the toroidal and poloidal directions. In Fig. 3.7, we separate the contributions of the $E \times B$, diamagnetic and polarization drifts to the flux of the ion species, D^+ and D_2^+ . On the other hand, Fig. 3.8 presents the results from the single-component simulations. The n_{D^+} profile in Fig. 3.6 is similar to the one in Fig. 3.8 obtained from the single-component plasma simulation, with a large density gradient region near the LCFS and a density shoulder forming in the far SOL. In turn, the density of D_2^+ is small in the whole domain and peaks in the edge, across the LCFS, where most D_2 molecules are ionized, and decreases rapidly towards the core, due to the small penetration of D_2 molecules in the warmer and denser plasma in that region. We remark that the D_2^+ ions observed in the open-field line region result mostly from charge-exchange interactions between D_2 and D^+ (see Fig. 3.4) and the ionization of D_2 molecules reemitted from the limiter and vessel wall.

Regarding the neutral species, we note that n_D peaks in the SOL, close to the LCFS, and decreases radially outwards, while in the single-component plasma simulation n_D increases monotonically radially towards the wall. This is the consequence of the dissociation of D_2 molecules into D atoms in the edge and near SOL, as well as the association of D atoms into D_2 molecules at the limiter plates and the vessel wall. On the other hand, we observe that n_{D_2} decreases monotonically from the outer wall to the interface with the core, since D_2 molecules are generated in the open-field line region as the result of recycling processes and are lost due to dissociation and ionization processes which take place mostly in the edge and near SOL.

The dissociation of D_2 molecules also affects the radial flux of D, Γ_D , presented in Fig. 3.7. In contrast with the single-component plasma simulation presented in Fig. 3.8, Γ_D points

3.6. First simulation of a multi-component plasma with the GBS code

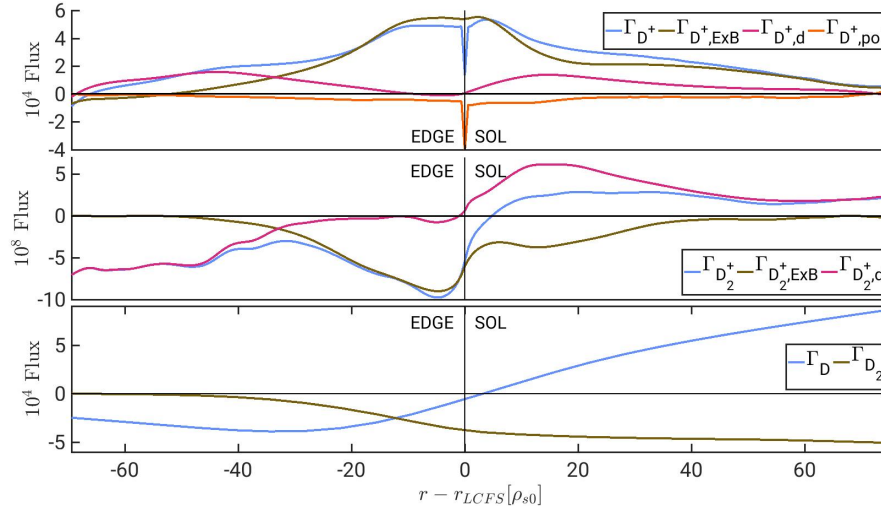


Figure 3.7: Radial profiles of the radial flux for D^+ ions (top), D_2^+ ions (middle) and neutral species D and D_2 (bottom), averaged over the toroidal and poloidal directions, evaluated over an interval of $\Delta t = 10.1 R_0 / c_{s0}$ from the quasi-steady state multi-component plasma simulation. The components of the D^+ and D_2^+ radial flux are discriminated.

radially inwards in the edge, reversing sign in the SOL, which is a consequence of the release of D atoms due to the dissociation of D_2 molecules, of particular importance close to the LCFS. Moreover, the D atoms reaching the outer wall associate and are reemitted as D_2 molecules, thus contributing to the outward flux of D . The multi-component plasma simulation shows that Γ_D peaks in the edge, while for a single-component model Γ_D is maximum at the LCFS. This is due to the D atoms that are generated in the edge region close to the LCFS in a multi-component model, compensating their ionization. At the same time, we remark that the radial flux of D_2 molecules, Γ_{D_2} , points radially inwards in the whole domain (see Fig. 3.7). As a matter of fact, Γ_{D_2} is roughly constant in the SOL, because the loss of D_2 molecules due to dissociation is compensated by the D_2 molecules recycled at the limiter. Then, Γ_{D_2} decreases in the edge as a result of the molecular dissociation and ionization (due to the larger values of plasma density and temperature in the closed field-line region), thus becoming negligible towards the core.

Focusing now on the dynamics of the ion species, we highlight that the radial flux of D^+ ions points radially outwards across the whole domain and is mostly determined by the dominant $E \times B$ flux except in the proximity of the core, where the diamagnetic flux dominates over the $E \times B$ flux. The polarization drift contribution is negligible in the whole domain. We also note that the flux increases across the edge region from the core to the LCFS, peaks in the near SOL and gradually decreases across the SOL. This significantly differs from the profile of the ion flux in the single-component plasma simulation (see Fig. 3.8), where the flux peaks at the LCFS. This difference between the two models is related to the location of the ionization source $n_D v_{iz}$. As a matter of fact, while the source has a smooth profile and peaks at the LCFS in the single-component simulation, the ionization source peaks further inside the edge in

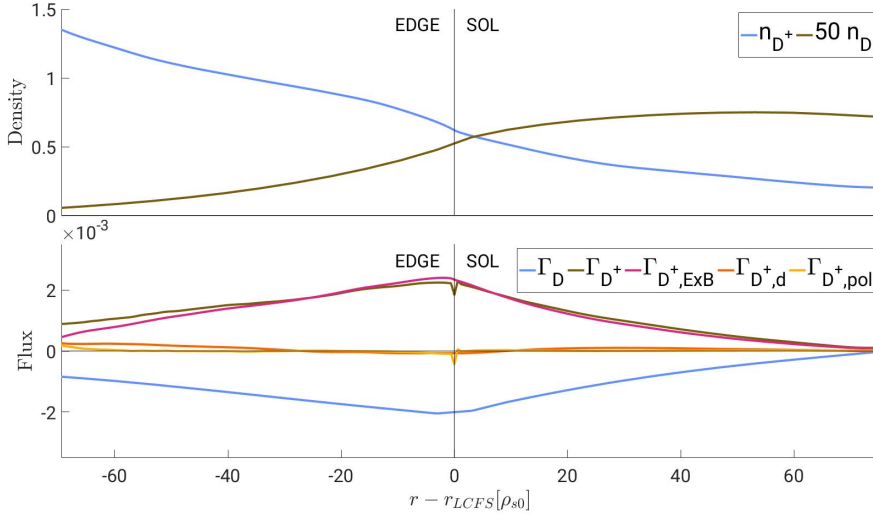


Figure 3.8: Radial profiles of density (top) and radial flux (bottom) for the D^+ and D species, averaged over the toroidal and poloidal directions, evaluated over an interval of $\Delta t = 10.1 R_0 / c_{s0}$ from a quasi-steady state single-component plasma situation. The components behind the radial ion flux are discriminated. Plasma and neutral grid resolution, as well as simulation parameters, are the same considered in Fig. 3.5.

the multi-component model, leading to a sharp increase of the D^+ flux in the edge, in the proximity of the LCFS.

We remark that, as seen in Fig. 3.7, the radial flux of D_2^+ ions points radially outwards in the SOL, but is directed radially inwards in the edge. This is a consequence of the fact that most D_2^+ are generated in the vicinity of the LCFS, where the D_2 molecules are ionized by the warmer and denser plasma. The D_2^+ radial flux is determined by the balance between the inward pointing $E \times B$ and outward pointing diamagnetic drift components in the SOL, by the $E \times B$ flux in the edge close to the LCFS, and by the diamagnetic component towards the core.

We also note that the inward pointing D_2^+ flux, $\Gamma_{D_2^+}$, is sharply peaked in the edge, in the vicinity of the LCFS. This is because most D_2^+ ions are generated by ionization of D_2 molecules in that region and are dissociated shortly afterwards, having travelled a negligible distance. Indeed, the spatial location of the peak of $\Gamma_{D_2^+}$ matches to the one of the $n_{D_2^+}$ profile in Fig. 3.6. We highlight that the contribution to the flux of D_2^+ arising from the polarization drift is not represented in Fig. 3.7 because it is neglected in our model. Finally, $\Gamma_{D_2^+}$ is three to four orders of magnitude smaller than Γ_{D^+} , which is a consequence of the small ratio $n_{D_2^+} / n_{D^+}$. Since the polarization drift component is expected to be small compared to the total ion flux of D_2^+ molecules, $\Gamma_{D_2^+}$, we conclude that neglecting the polarization drift terms in Eqs. (3.19-3.27) has indeed a negligible impact on the results of the simulation.

We must highlight that the D_2^+ flux is very small compared to the flux of the main ion species, D^+ , since the density of D_2^+ ions is about four orders of magnitude smaller than the density of D^+ . This may allow to neglect the D_2^+ ion species, by assuming that they are instantly

dissociated into a D atom and a D^+ ion. In the future, we will repeat the simulation presented here while considering instantaneous dissociation of D_2^+ to clarify the impact of taking the finite lifetime of D_2^+ ions into account.

3.7 Conclusions

In this chapter we present a multi-component plasma model for the self-consistent description of the neutral and plasma dynamics in the tokamak boundary, which is implemented in the GBS code. A deuterium plasma is simulated in the edge and SOL regions of a tokamak, featuring electrons, D^+ and D_2^+ ions, D atoms and D_2 molecules. The models that describe the neutrals and the plasma dynamics are coupled by means of a number of collisional processes, which are responsible for the introduction of neutral-plasma interaction terms both in the plasma and the neutral equations. The collisional reactions considered in this chapter include ionization, elastic collisions between electrons and neutral particles, charge-exchange collisions and dissociative processes. The multi-component plasma model is based upon the Braginskii fluid equations derived in the drift-limit, which extend the single-ion species model to account for D_2^+ ions. The closure considered in the present chapter follows the approach developed by Zhdanov. Regarding the neutral particles, the model used in the single-neutral species model of GBS [61] is extended to address the effect of the molecular species, D_2 . As a matter of fact, in the model presented in this chapter, the neutrals are computed by solving two coupled kinetic equations for the D and D_2 species by using the method of characteristics. The resulting system of linear integral equations are then discretized and solved with respect to the densities of neutral species, n_D and n_{D_2} .

The results from the first simulation based upon the multi-component model, considering a toroidally limited plasma, are also described. These results bear some considerable differences compared to the results from simulations carried out by using the single-ion component model implemented in GBS. An up-down asymmetry is observed in the n_e and n_{D^+} density profiles, with larger densities being observed below the equatorial midplane. This is related to the counterclockwise parallel flow of the edge plasma, as reported in the profiles of $v_{\parallel e}$, $v_{\parallel D^+}$ and $v_{\parallel D_2^+}$. This feature also leads to larger recycling rates and higher neutral density in the upper side of the limiter, compared to the region below the limiter plates. In addition, the density of the neutral atoms and molecules, n_D and n_{D_2} , is found to be about one order of magnitude smaller than n_{D^+} in the open-field line region and two orders of magnitude smaller in the edge, while $n_{D_2^+}$ is about three to four orders of magnitude smaller than n_{D^+} , even in the edge close to the LCFS, where $n_{D_2^+}$ peaks.

Taking into account the molecular dynamics also allowed multi-component plasma simulations to grasp the influence of D_2 molecules on the plasma fuelling. In fact, most D_2 particles are generated at the limiter close to the LCFS. A large fraction of D_2 molecules cross the LCFS and reach the edge, where they are typically dissociated into atomic D as a result of the interaction with the high density and temperature plasma. The D atoms thus generated and

Chapter 3. A multi-component model of plasma turbulence and kinetic neutral dynamics

the remaining D_2 molecules are then ionized inside the edge, with the D_2^+ ions being dissociated shortly afterwards as a consequence of the high electron densities and temperatures. Therefore, the simulation results reveal an inward radial shift of the peak of the ionization of D atoms, compared to the results from the single-ion species simulations.

The radial profiles of the densities and radial fluxes are also influenced by the inclusion of molecules. The radial flux of D^+ is observed to increase sharply in the edge, in the vicinity of the LCFS as a result of the ionization source peaking in that region. The flux of D^+ then remains high in the proximity of the LCFS and decreases sharply in the near SOL, where the ion sinks at the limiter are dominant over the sources of D^+ . This constitutes a difference with respect to the D^+ flux observed in the results from a single-ion species simulation, where a maximum is reported at the LCFS. On the other hand, the D density peaks in the SOL due to the D_2 molecules dissociated in that region. This is also the reason for the sign reversal of the radial flux of D atoms in the far SOL, where Γ_D points radially outwards. On the other hand, the inward flux of D atoms increases radially inwards inside the LCFS, since D atoms are also generated in the proximity of the LCFS by D_2 dissociation.

To conclude, the results presented in this chapter highlight that the multi-component model for the self-consistent description of the neutral-plasma interaction provide a description of a deuterium plasma capturing the molecular dynamics and its overall influence on the other plasma and neutral quantities. Therefore, the model can be used to address a multi-component plasma and more than one neutral species at a kinetic level when carrying out self-consistent first-principles simulations of plasma turbulence in the tokamak boundary. The procedure described in this chapter can be extended to include other species of plasma particles or neutrals, as well as the corresponding additional collisional processes. The model can also be implemented in a diverted tokamak configuration (featuring one or various X-points), where multi-component simulations are important to shed some light on the high recycling and detachment regimes.

4 Numerical simulations of Gas Puff Imaging

This chapter presents the results of gas puff imaging (GPI) studies carried out by exploiting the multi-component model described in Ch. 3. The research reported here aims at extending the results of previous works on the simulation of GPI to the case of a multi-component deuterium plasma in a three-dimensional domain. The simulations are performed in a toroidally-limited plasma with gas puff sources located at the LFS equatorial midplane. The D_α emission arising from the excitation of D atoms and the contributions from dissociation of D_2 molecules and D_2^+ ions, which is observed to dominate over the other components in the proximity of the wall, are considered. The statistical moments and the turbulence properties, computed for the different components of the D_α emission, as well as the relevant plasma and neutral quantities, are investigated. The correlation functions between the D_α emission rate and the plasma and neutral quantities, namely the electron density, n_e , electron temperature, T_e , and density of neutral atoms, n_D , are also evaluated considering in detail each contribution to the D_α emission and analysing the correlation functions between these quantities in the simulation domain. The results shown in this chapter highlight the importance of considering the neutral fluctuations when interpreting the measurements of the D_α emission rate, especially in the edge, where the perturbations of the neutral density have a more significant impact on the D_α emission.

4.1 Introduction

Gas puff imaging (GPI) is one of the fundamental diagnostics currently used to evaluate the turbulent evolution of a plasma in the boundary of tokamak devices [98, 99, 100, 101]. The GPI diagnostics is based on the injection of neutral particles at a specific toroidal location. The neutral particles interact with the plasma via a number of collisional processes and give rise to emission of light as a result of atomic deexcitation. Given that the plasma boundary is a medium of low optical density, the emitted light interacts weakly with the plasma and can be measured by one or more high temporal and spatial resolution cameras. The cameras register the integrated light emitted along the respective lines of sight. Using an horizontal and a vertical camera, a tomographic reconstruction of the two-dimensional light emission profile is also made possible.

Optical filters allow for the fast cameras to select a specific spectral line of interest within the visible range, depending on the composition of the plasma. In the case of a deuterium plasma, measurements most often focus on the D_α line of the Balmer series [98, 100, 102, 103], which is the result of the deexcitation of a deuterium atom from the second excited state $D^*(n=3)$ to the first excited state $D^*(n=2)$. Several atomic and molecular processes account for the presence of deuterium atoms in the $D^*(n=3)$ state. These processes include impact excitation of D atoms in the fundamental ($n=1$) state and a variety of dissociative processes of the diatomic deuterium species, D_2 and D_2^+ . As a result, it is difficult in experiments to identify the source of D_α emission, even though the majority is expected to come from impact excitation of D atoms. Moreover, the D_α emission following each excitation process has a complex dependence on a number of parameters, which makes it even more difficult to interpret D_α measurements. Therefore, assumptions have to be made, based on the properties of the diagnosed plasma, to guide the interpretation of experimental results.

The effect of molecular dynamics is often neglected when interpreting D_α emission in experiments [102, 104], therefore excluding the contribution of dissociative processes in the interpretation of the D_α emission source, which is thus ascribed to electron impact excitation. The emission rate is thus modelled as [99, 100, 103, 64]

$$D_{\alpha, \text{Exc}} = n_e n_D r_{\alpha, \text{Exc}}(n_e, T_e), \quad (4.1)$$

with n_e the electron density, n_D the density of D atoms and $r_{\alpha, \text{Exc}}(n_e, T_e)$ the emission rate coefficient for impact excitation of D to the second excited state $D^*(n=3)$. The dependence of r_α on the electron density and temperature, n_e and T_e respectively, is theoretically calculated, based on a collisional-radiative model [105]. In addition, it is often assumed that D_α emission depends weakly on the neutral density perturbations. As a consequence, n_D is assumed constant in Eq. (4.1) and n_D fluctuations are not taken into account in the analysis. Finally, electron density and temperature fluctuations are assumed strongly correlated in the SOL region [102, 104]. With these assumptions, the electron pressure can be inferred from the D_α

emission measurements, which ultimately allows for the study of boundary turbulence. A more accurate interpretation of D_α emission is made possible by disentangling the dependence of the D_α emission on n_e , n_D and T_e . This can be obtained by measuring the light emission resulting from three different spectral lines, similarly to the experiments carried out with He-lines in the Alcator C-Mod tokamak [98] and the TJ-II stellarator [106]. However, if molecular dissociation becomes a non-negligible source of D_α emission with respect to impact excitation, the use of different spectral lines is not sufficient to disentangle the complexity underlying the D_α emission.

A number of numerical simulations, based on different approaches, have been performed to disentangle the complexity of the interpretation of GPI results over the last decades. On the one hand, GPI simulations were carried out assuming that neutral density perturbations are negligible, focusing therefore on the turbulent dynamics of the plasma [102, 103, 104, 107]. On the other hand, the effect of neutral fluctuations were addressed while considering time-independent plasma profiles or using analytical models for plasma perturbations [100, 108, 109, 110]. Efforts to jointly address the plasma and neutral dynamics on GPI simulations have been reported only in the last decade.

The first attempt of a self-consistent description of fast camera data is described in Ref. [111], where two-dimensional simulations of plasma turbulence and a mono-energetic neutral model are used. In Ref. [64], the GBS code is used to simulate D_α emission from GPI diagnostics with a model of plasma turbulence and neutral dynamics. The three-dimensional drift-reduced Braginskii equations for a single-component deuterium plasma (D^+ and e^-) are solved, coupled with a kinetic model for deuterium atoms, D , in the SOL of a limited tokamak configuration with a toroidal limiter on the HFS equatorial plane. A gas puff source is introduced at the LFS equatorial midplane, consisting of the injection of D atoms from the wall. Since the model does not take into account molecular dynamics, the D atoms are injected into the domain at a temperature of 3eV, in order to model D atoms generated by Franck-Condon dissociation of D_2 molecules. The study focuses on the D_α line of the Balmer series, reporting on the correlation between the D_α emission, the electron density, n_e , the electron temperature, T_e , and the deuterium atom density, n_D . Results show that n_e , T_e and D_α emission are all strongly correlated, particularly in the SOL. As for n_D fluctuations, different results are reported at distances from the gas puff location smaller or larger than $\lambda_{mfp,D}$, in particular a strong anti-correlation between n_D and the plasma quantities is observed at a distance from the gas puff location smaller than $\lambda_{mfp,D}$. In fact, positive perturbations of n_e and T_e lead to higher ionization rates, thus resulting in lower n_D . As a consequence, n_D and D_α emission rates are also strongly anti-correlated in that region. However, while the D atom density has an effect on the amplitude of the D_α emission rate, according to Eq. (4.1), the impact on the statistical moments and turbulence properties of the D_α emission remains limited. Ref. [64] concludes that neglecting the n_D fluctuations remains as a valid assumption for interpreting GPI measurements at distances from the gas puff source smaller than $\lambda_{mfp,D}$, the main effect of assuming constant n_D being an underestimate of the plasma quantities n_e , T_e from the interpretation of D_α emission. On the other hand, Ref. [64] shows that, for distances from the

gas puff source larger than $\lambda_{\text{mfp,D}}$, the D atom density is influenced by non-local shadowing effects due to the interaction of the atoms with a number of structures on their way across the plasma. As a matter of fact, when crossing positive perturbations of n_e and T_e , atoms are more likely to be ionized and do not penetrate further into the plasma, thus leading to small n_D in the edge, regardless of the local values of n_e and T_e . This non-local shadowing effect [64] hence weakens the anti-correlation between n_D and the plasma quantities, n_e and T_e , as one moves radially inwards. At the same time, the anti-correlation between n_D and the D_α emission rate decreases, becoming a positive correlation at distances from the gas puff source larger than $\lambda_{\text{mfp,D}}$. Therefore, n_D fluctuations have a more significant impact on the statistical moments and turbulence characteristics of the D_α emission at distances larger than $\lambda_{\text{mfp,D}}$, where n_D fluctuations should be taken into account when considering GPI measurements.

The nHESEL code [45, 39, 46] has also been used to investigate the physics behind the GPI emission. nHESEL self-consistently simulates the neutral-plasma interaction in a two-dimensional domain, relying on a fluid model of single-component plasma turbulence coupled with a diffusive model for multiple neutral species. In Ref. [46], nHESEL simulations explore the effect of molecular dissociation on the correlation between n_D and plasma quantities in the presence of blob events. Three different neutral species are considered: thermal deuterium molecules, D_2 , injected into the system via gas puffing, thermal Helium atoms, He, and non-thermal deuterium atoms, D, that comprise warm atoms directly generated by Franck-Condon dissociation of molecular deuterium and hot atoms resulting from charge-exchange interactions with D^+ ions.

As described in Ref. [46], dissociative processes lead to volumetric sinks of D_2 and sources of D atoms, while ionization constitutes a sink of D. Since there are no volumetric sources of D_2 , an enhancement of n_e and T_e due to a blob enhances dissociative processes and thus leads to a decrease of n_{D_2} . Therefore, n_{D_2} is anti-correlated with n_e and T_e (similarly to n_D in Ref. [46]). On the other hand, the competition between dissociation and ionization events, that constitute a source and a sink of D atoms respectively, determines the effect of blob-induced plasma perturbations on the n_D fluctuations. In Ref. [46], this balance is expressed as

$$S_D = n_{D_2} [2\nu_{\text{diss}(D_2)}(T_e) + \nu_{\text{diss-iz}(D_2)}(T_e)] - n_D \nu_{\text{iz}}(T_e), \quad (4.2)$$

where ν_{diss} , $\nu_{\text{diss-iz}}$ and ν_{iz} are the dissociation, dissociative-ionization and ionization rates, all proportional to n_e . If $S_D > 0$, an increase of n_e leads to an increase of S_D , and therefore a correlation between n_D and n_e . In contrast, if $S_D < 0$, n_D is anti-correlated with n_e , similarly to the observations in Ref. [64]. In Ref. [46] a parameter η is also introduced, defined as the ratio between the D sources and sinks,

$$\eta = \frac{n_{D_2} [2\nu_{\text{diss}(D_2)} + \nu_{\text{diss-iz}(D_2)}]}{n_D \nu_{\text{iz}}} = \frac{n_{D_2}}{n_D} \frac{[2\nu_{\text{diss}(D_2)} + \nu_{\text{diss-iz}(D_2)}]}{\nu_{\text{iz}}}, \quad (4.3)$$

with correlation between n_e and n_D found for $\eta > 1$ and anti-correlation for $0 < \eta < 1$. The value of η is determined partly by the n_{D_2}/n_D ratio and partly by the ratio between the reaction rates of volumetric sources and sinks, which depend on the electron temperature. As the authors highlight in Ref. [46], the temperature-dependent term is always larger than 1, approaching 1.7 at large electron temperature. Therefore, as long as $n_{D_2}/n_D > 0.58$, correlation ($\eta > 1$) is always observed. The numerical simulation presented in Ref. [46] points out $\eta > 1$ in the SOL, where n_{D_2} is large, and $\eta < 1$ in the edge, because of the large temperature observed inside the separatrix and the resulting low D_2 density. The findings reported in Ref. [46] thus suggest that n_D is correlated with D_α emission in the SOL and anti-correlated in the edge. This conclusion contrasts with the one in Ref. [64] where, by not taking into account D_2 dissociation, n_D perturbations are found to be anti-correlated with the plasma density and temperature perturbations in most of the domain, particularly in the SOL.

The present chapter leverages the studies presented in Ref. [64] and extends them to the case of a multi-component deuterium plasma by using the GBS model presented in Ch. 3. This includes two ion species, D^+ and D_2^+ , and two neutral species, D atoms and D_2 molecules, thus allowing for molecular dissociation to be taken into account. Our goal is to understand the impact of the multi-component plasma dynamics on GPI diagnostics, extending the work reported in Ref. [46] by using a global three-dimensional model to describe the tokamak boundary and addressing the neutrals by discretizing a kinetic advection equation for each species. The kinetic approach allows us to account for all values of the mean free path for the neutral species, with no need to distinguish particles of the same species according to their temperature and origin. In addition to Ref. [46], we also aim at evaluating the contribution to the D_α emission from dissociation of molecular species, D_2 and D_2^+ , and compare it with the main source due to excitation of D atoms.

This chapter is structured as follows: after this Introduction, a brief description of the simulation of the gas puff setup is presented in Sec. 4.2. We then present the simulation results in Sec. 4.3. These results are further discussed in Sec. 4.4, where we evaluate the correlations between the quantities involved in the computation of the D_α emission rate, and in Sec. 4.5, where we address the impact of the fluctuations of the density of neutral species on the interpretation of GPI results. The conclusions follow in Sec. 4.6.

4.2 The GPI diagnostics and D_α emission rate

The simulations described here leverage the self-consistent multi-component model for plasma turbulence and kinetic neutrals in the tokamak boundary implemented in GBS and presented in Ch. 3. We consider therefore a limited plasma, with toroidal limiter on the equatorial HFS limiter. The GPI diagnostics is implemented by adding a low-intensity gas puff at the equatorial midplane on the LFS. We assume that the gas puff extends over the full toroidal direction and it is independent of the toroidal angle, to simplify our scenario and its analysis. The gas puff injects D_2 molecules at wall temperature at the outer chamber wall,

Chapter 4. Numerical simulations of Gas Puff Imaging

which does coincide with the boundary of the simulation domain. This contrasts with Ref. [64], where the injected molecules are assumed to undergo Franck-Condon dissociation outside the simulation domain and enter it as D atoms at a temperature of 3eV. As a matter of fact, the results obtained from the first multi-component GBS simulation presented in Ch. 3 show that penetration of D₂ molecules across the SOL into the edge is important, at least in the plasma conditions considered in our simulations (in the transition between the sheath-limited and conduction-limited regimes), highlighting the importance of properly modelling the puffing of D₂ molecules from the domain boundary.

Following Ref. [64], the distribution function of the D₂ molecules injected for the GPI diagnostics from the domain boundary is described by

$$f_{D_2, \text{gp}}(y, \mathbf{v}) = S_{\text{gp}} \exp\left(-\frac{(y - y_{\text{gp}})^2}{2(\Delta y_{\text{gp}})^2}\right) \chi_{\text{in}, D_2}(\mathbf{v}), \quad (4.4)$$

where S_{gp} is the puffing rate (equivalent to the flux of puffed molecules), y is the poloidal coordinate along the outer wall, y_{gp} is the poloidal coordinate of the center of the gas puff, Δy_{gp} is the gas puff width and $\chi_{\text{in}}(\mathbf{v})$ is the velocity distribution of the puffed D₂ molecules, which is assumed to follow the Knudsen cosine law,

$$\chi_{D_2, \text{in}}(\mathbf{v}) = \frac{3}{4\pi} \frac{m_{D_2}}{T_w^2} \cos(\theta) \exp\left(-\frac{m_{D_2} v^2}{2T_w}\right). \quad (4.5)$$

In Eq. (4.4), following the definition introduced in the previous chapters, we define the angle $\theta = \arccos(\hat{\Omega} \cdot \hat{\mathbf{n}})$, with the unit vector $\hat{\Omega} = \mathbf{v}/v$ being along the direction of the neutral velocity, and the unit vector normal to the boundary $\hat{\mathbf{n}}$ pointing towards the plasma volume. In the present work, we consider a temperature $T_w = 0.3\text{eV}$, $y_{\text{gp}} = 400\rho_{s0}$ (the gas puff is located at the equatorial outboard midplane) and $\Delta y_{\text{gp}} = 20\rho_{s0}$.

In the present thesis, similarly to Ref. [64], we focus on the local emission rate from the Balmer D _{α} line. However, in addition to the D _{α} emission resulting from electron impact excitation of D atoms, dissociation of molecular species D₂ and D₂⁺ is also taken into account as sources of D _{α} emission. The total D _{α} emission rate is hence expressed as

$$D_\alpha = D_{\alpha, \text{Exc}} + D_{\alpha, \text{Diss}(D_2)} + D_{\alpha, \text{Diss}(D_2^+)}, \quad (4.6)$$

where $D_{\alpha, \text{Exc}}$ is the contribution from the excitation of D atoms to the excited state D* ($n = 3$) defined in Eq. (4.1), while

$$D_{\alpha, \text{Diss}(D_2)} = n_e n_{D_2} r_{\alpha, \text{Diss}(D_2)}(n_e, T_e), \quad (4.7)$$

is the contribution from dissociation of D_2 molecules into two D atoms, one of which in the excited state D^* ($n = 3$). Finally,

$$D_{\alpha, \text{Diss}(D_2^+)} = n_e n_{D_2^+} r_{\alpha, \text{Diss}(D_2^+)}(n_e, T_e), \quad (4.8)$$

is the contribution that joins the dissociation of D_2^+ molecular ions into one D^+ ion and one D atom in the excited state D^* ($n = 3$) and the dissociative-recombination of D_2^+ molecular ions into two D atoms, one of them in the excited state D^* ($n = 3$). We recall that n_{D_2} is the density of D_2 molecules and $n_{D_2^+}$ the density of D_2^+ ions. We also remark that the emission rate coefficient for dissociation of D_2 molecules generating a D^* ($n = 3$) atom, $r_{\alpha, \text{Diss}(D_2)}(n_e, T_e)$, as well as the emission rate coefficient for dissociation or dissociative recombination of D_2^+ generating a D^* ($n = 3$) atom, $r_{\alpha, \text{Diss}(D_2^+)}(n_e, T_e)$, are obtained from a collisional-radiative model [112]. For the emission rate coefficient $r_{\alpha, \text{Diss}(D_2)}(n_e, T_e)$, we use the values made available in the OpenADAS database, similarly to Ref. [64]. Other molecular processes accounting for D_α emission, such as dissociative-ionization of D_2 , are neglected here because their cross sections are considerably smaller than the ones of the processes considered here.

4.3 Simulation results

The simulation of GPI presented here considers a simulation with the same parameters as the one described in Ch. 3, where the diagnostic gas puff described in Sec. 4.2 is introduced. After a transient phase, a quasi-steady state is reached, characterized by constant plasma profiles resulting from the balance between sources and sinks. Our analysis focuses on a time interval $\Delta t = 40R_0/c_{s0}$ during the quasi-steady state phase and targets mostly the LFS region around the diagnostic gas puff ($350\rho_{s0} < y < 450\rho_{s0}$), where D_α light emission following the injected particles is important. Similarly to Ch. 3, we highlight that the results presented here are expected to depend strongly on the simulation parameters considered.

We first perform time and toroidal averages of the plasma and neutral quantities relevant for the study of D_α emission, namely the electron density, n_e , the electron temperature, T_e , the D atom density, n_D , the D_2 molecule density, n_{D_2} , and the D_2^+ ion density, $n_{D_2^+}$. We also study the number of particles ionized/dissociated per unit volume and unit time, i.e. $n_D \nu_{iz}$, $n_{D_2} \nu_{iz, D_2}$, $n_{D_2} \nu_{\text{Diss}(D_2)}$ and $n_{D_2^+} \nu_{\text{Diss}(D_2^+)}$. The time and toroidal averages of these quantities are presented in the poloidal cross sections shown in Fig. 4.1. We remark that the $40R_0/c_{s0}$ time interval over which the average is performed is considerably larger than the characteristic timescales of turbulent events. Toroidal averaging is enabled by the axisymmetry of the considered configuration.

We note that the cross section plots of the plasma and neutral quantities, n_e , n_D , D_2 , n_{D_2} , $n_{D_2^+}$ and T_e , are similar to the ones observed in the simulations reported in Ch. 3 for the first multi-component plasma simulation, the difference being only in the region close to the gas

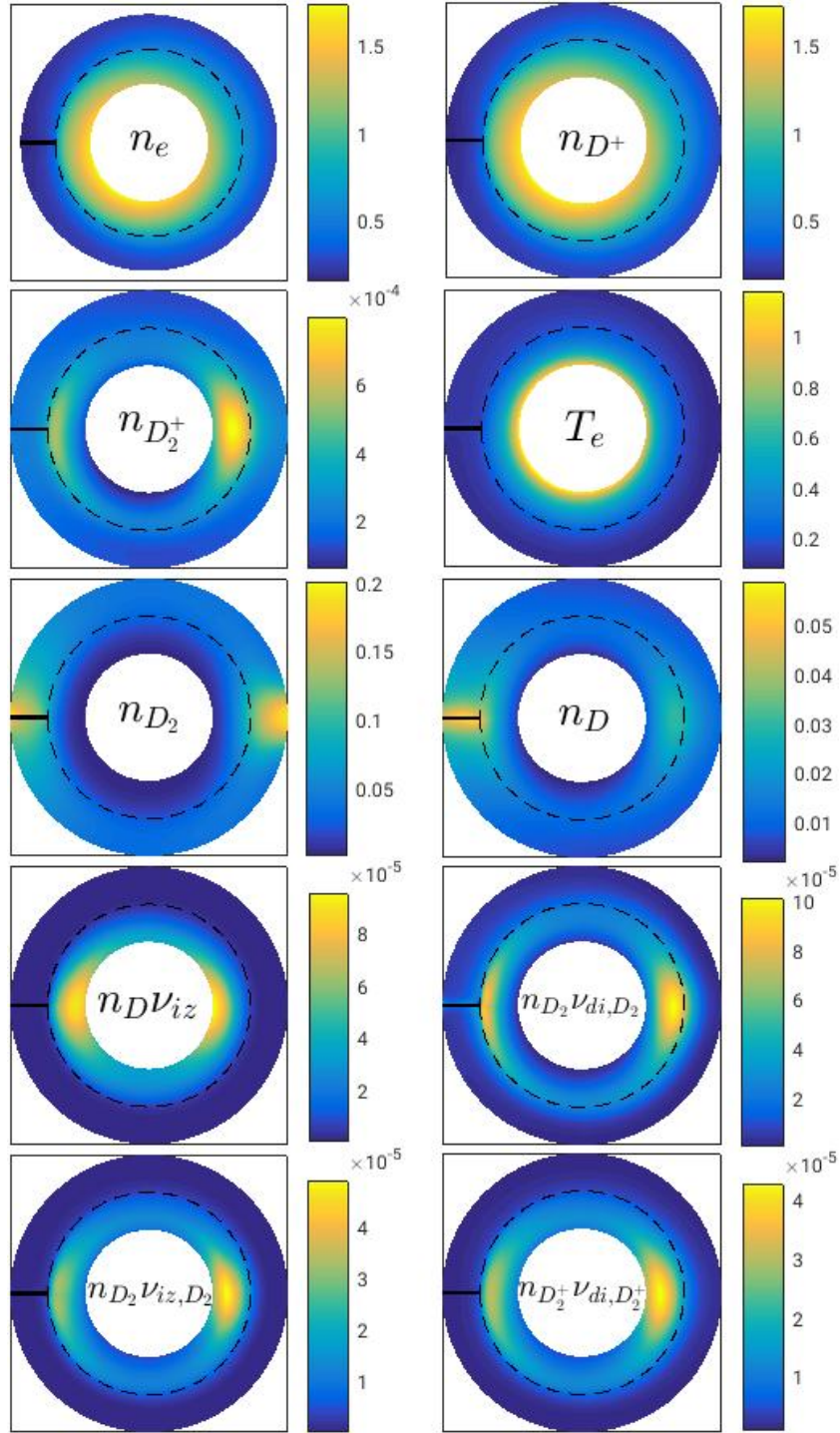


Figure 4.1: Poloidal cross section of time and toroidal-averaged plasma quantities (n_e , $n_{D_2^+}$, and T_e), neutral particle densities (n_D , n_{D_2}), ionization sources ($n_D \nu_{iz}$ and $n_{D_2} \nu_{iz, D_2}$) and dissociation rates ($n_{D_2} \nu_{Diss(D_2)}$ and $n_{D_2^+} \nu_{Diss(D_2^+)}$).

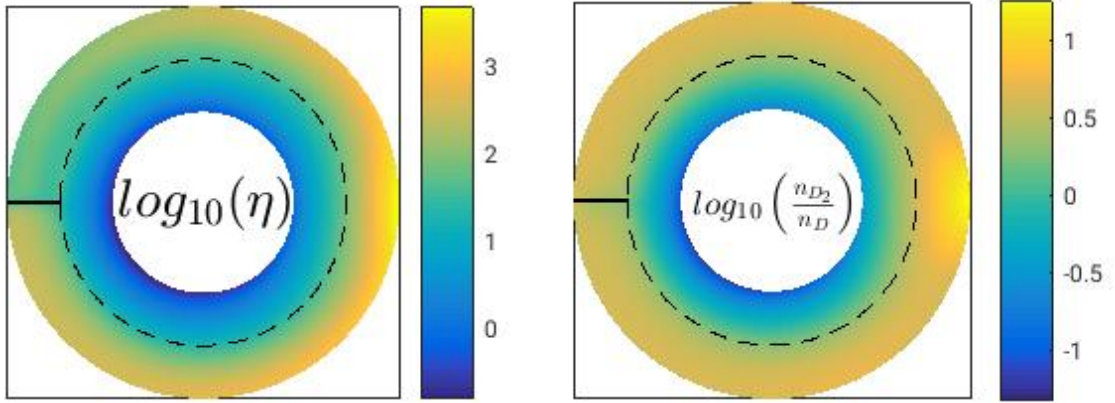


Figure 4.2: Poloidal cross section of the logarithm of η and the logarithm of n_{D_2}/n_D .

puff at the LFS. As a consequence of the GPI injection, n_{D_2} peaks in the proximity of the outer wall at the LFS equatorial midplane, where the gas puff is located. We remark that, due to the SOL conditions considered in this simulation, namely the low T_e values observed in the SOL at the LFS, the D_2 mean free path is larger than the SOL width, $\lambda_{\text{mfp},D_2} \simeq 95\rho_{s0}$. As a consequence, most D_2 molecules cross the SOL without interacting with the plasma and are only dissociated/ionized inside the LCFS, which has an important impact on the D_α emission profile. As a result of the large λ_{mfp,D_2} , the density of D atoms peaks in the edge, close to the LCFS, and the density of D_2^+ ions also peaks further inside. In fact, as shown in Fig. 4.1, dissociation of D_2 molecules peaks inside the LCFS and ionization of D_2 molecules, which requires more energy compared to dissociation, peaks further inside, where the values of n_e and T_e are higher. On the other hand, since dissociative processes have in general larger cross sections than ionization at the same temperature (see Fig. 3.1), most D_2^+ ions are dissociated shortly after being generated. This is confirmed by Fig. 4.1, that shows that dissociation of D_2^+ occurs where the ionization of D_2 takes place. Finally, ionization of D peaks close to the core, a consequence of the fact that most D atoms are generated in the edge region and then ionized when they enter in contact with the warmer and denser plasma in the innermost region of the domain.

We remark that, while the radial profiles of n_e and T_e are similar to the ones presented in Ref. [64], the D atom density, n_D , is different, since it peaks inside the LCFS, which is a consequence of the dissociative processes taking place in the edge where D atoms are generated. On the other hand, the D_2 density, n_{D_2} , peaks in the SOL close to the outer wall, while D_2^+ peaks in the edge, where the high plasma density and temperature maximizes the ionization of D_2 molecules.

We also focus on the value of the correlation parameter η , redefined from Eq. (4.2) consistently with the multi-component plasma model under consideration, so as to take into account all possible sources and sinks of D atoms (see the list of collisional processes described in Table 3.1), yielding

$$\eta = \frac{n_{D_2} [2\nu_{\text{diss}(D_2)} + \nu_{\text{diss-iz}(D_2)}] + n_{D_2^+} [2\nu_{\text{diss-rec}} + \nu_{\text{diss}}]}{n_D [\nu_{\text{iz}} + \nu_{\text{cx,D-D}_2^+}]} \quad (4.9)$$

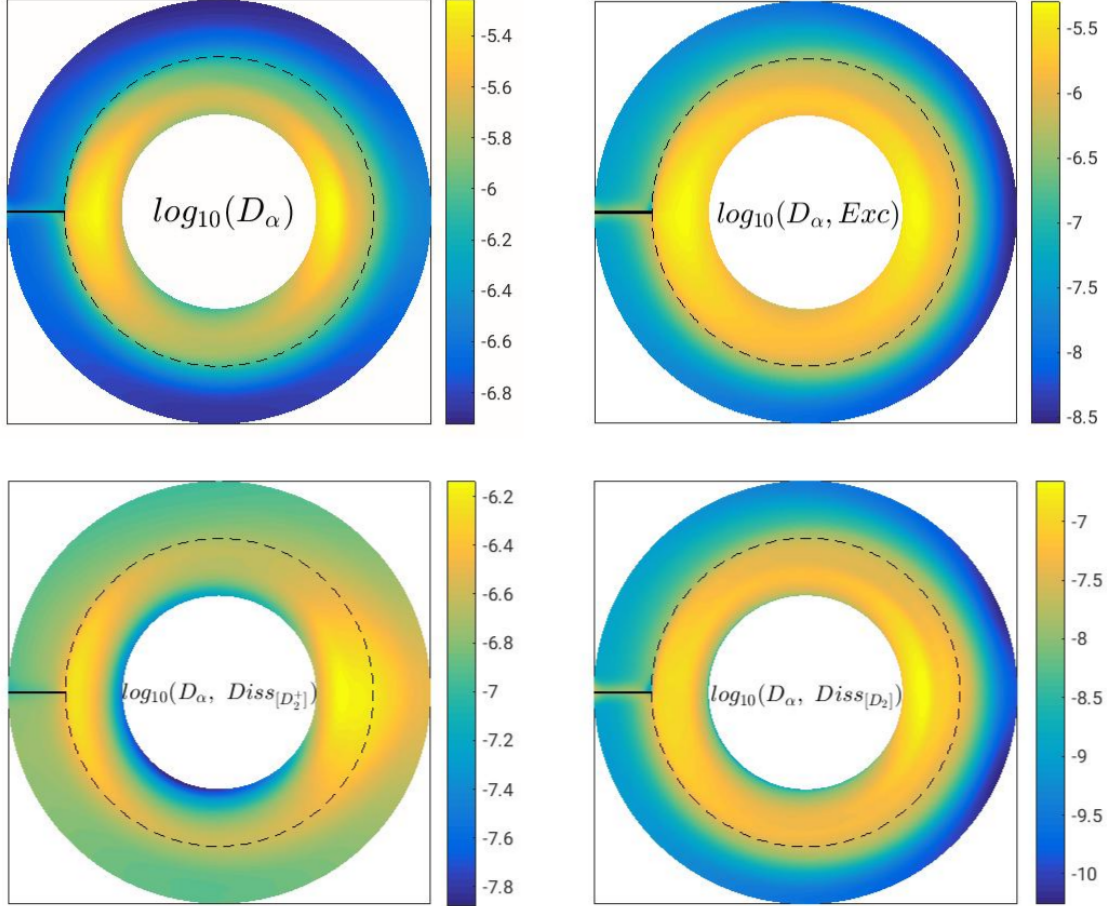


Figure 4.3: The logarithm of the time and toroidal averaged D_α emission and of its contributions, $D_{\alpha, \text{Exc}}$, $D_{\alpha, \text{Diss}(D_2)}$ and $D_{\alpha, \text{Diss}(D_2^+)}$, are represented in the poloidal plane.

Given the values of the reaction rates of the collisional processes, which are plotted in Fig. 3.1, for typical densities and temperatures in the plasma boundary, the term referring to the dissociation of D_2 dominates the numerator of Eq. (4.2), while ionization of D dominates over $D - D_2^+$ charge-exchange in the denominator. Therefore, for typical SOL and edge parameters, $\eta \simeq (n_{D_2}/n_D)(2\nu_{\text{Diss}(D_2)}/\nu_{\text{iz}})$, similarly to the expression reported in Eq. (3) from Ref. [46]. Thus, $\eta > 1$ holds whenever $n_{D_2}/n_D \gtrsim 0.6$ is satisfied.

The time and toroidal average of the logarithm of η and of the logarithm of n_{D_2}/n_D are plotted in Fig. 4.2 on a poloidal cross section. Due to the considerable penetration of D_2 molecules across the LCFS, $n_{D_2}/n_D > 1$ is observed in the SOL and in a significant portion of the edge,

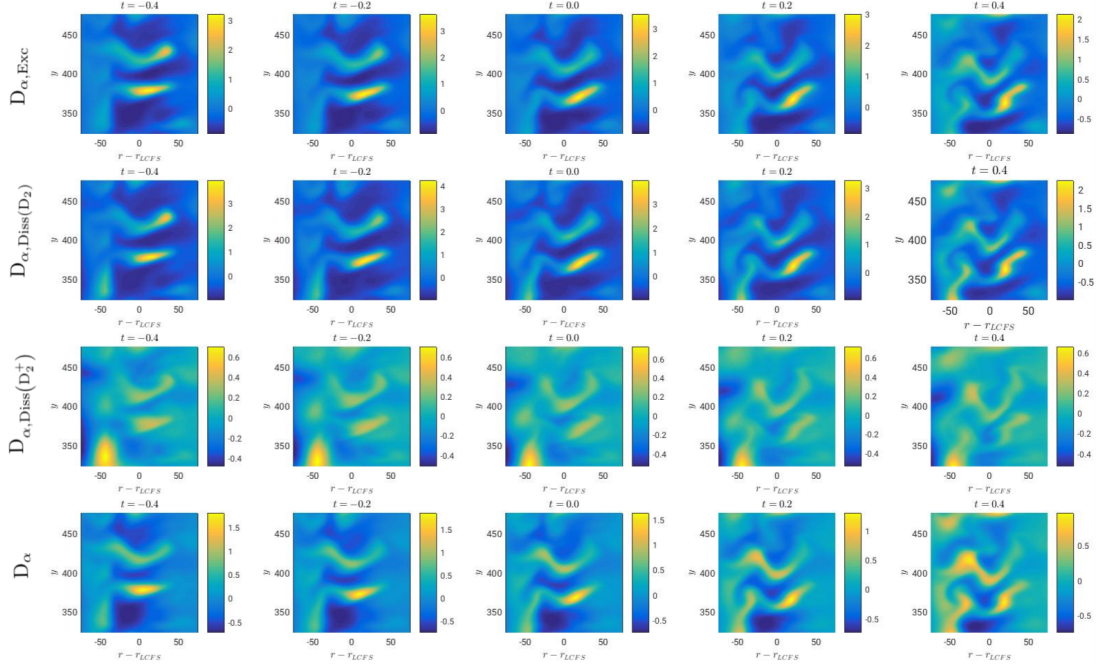


Figure 4.4: Five snapshots of the normalized fluctuations of each component of the D_α emission, separated by $0.2R_0/c_{s0}$. The $D_{\alpha,Exc}$, $D_{\alpha,Diss(D_2)}$ and $D_{\alpha,Diss(D_2^+)}$ contributions and the total D_α emission are shown in the first, second, third and fourth rows, respectively.

especially at the LFS equatorial midplane, where the diagnostic D_2 gas puff is present. As a result, $\eta > 1$ holds in most of the domain while $\eta < 1$ is verified only in a restricted portion of the edge region closer to the core. This implies that, except for the region close to the core, the number of D atoms generated by dissociative processes per unit time and unit volume is larger than the number of D atoms depleted per unit time and unit volume due to ionization events, with n_D being positively correlated with n_e and T_e . This is in line with the results reported in Ref. [46] and contrasts with the conclusions in Ref. [64] based on single-component simulations carried out with GBS. Nevertheless, we highlight that results are highly dependent on the specific SOL conditions considered, which are characterized by a lower electron temperature than the one usually found in typical SOL plasmas. In the case of a higher temperature SOL, we expect a shift radially outwards of the regions observed in this simulation.

Following Ref. [64], Fig. 4.3 presents time and toroidally averaged poloidal cross sections of the total D_α emission rate and the contributions from the three sources contributing to it, in logarithmic scale. We highlight that the excitation of D atoms, $D_{\alpha,Exc}$, is the main source of D_α emission, peaking in the edge. On the other hand, the contribution from dissociation of D_2 , $D_{\alpha,Diss(D_2)}$, is one to two orders of magnitude smaller than $D_{\alpha,Exc}$. The $D_{\alpha,Diss(D_2)}$ contribution peaks in the edge, close to the core, because of the high plasma densities and temperatures in this region, even though the density of D_2 molecules is small. Regarding the contribution from dissociation of D_2^+ , $D_{\alpha,Diss(D_2^+)}$, we highlight that it peaks in the edge, close to the LCFS. While

it is smaller than $D_{\alpha,\text{Exc}}$ by a factor of about five in the edge region, it becomes the dominant source of D_{α} emission in the far SOL.

Typical snapshots that represent the time evolution of the D_{α} emission rate are presented in Figs. 4.4, where the analysis is restricted to the GPI injection, i.e. at the LFS around the equatorial midplane, $350\rho_{s0} < y < 450\rho_{s0}$. The normalized perturbation of the total D_{α} emission, computed as $(D_{\alpha} - \langle D_{\alpha} \rangle) / \langle D_{\alpha} \rangle$, with $\langle D_{\alpha} \rangle$ the time and toroidally averaged D_{α} emission rate, is considered, as well as of its three sources, computed analogously. The snapshots are separated by time intervals of $0.2R_0/c_{s0}$. The $D_{\alpha,\text{Exc}}$ and $D_{\alpha,\text{Diss}(D_2)}$ emissions display a similar profile, while $D_{\alpha,\text{Diss}(D_2^+)}$ fluctuations, despite bearing an overall qualitative resemblance to the other emission profiles, peak at different locations. The plots of the fluctuations of the total D_{α} emission rate, follow the profiles of the snapshots of $D_{\alpha,\text{Exc}}$ in the edge and near SOL, since this is the dominant source of D_{α} emission in that region, and are similar to the plots of $D_{\alpha,\text{Diss}(D_2^+)}$ in the far SOL, where it dominates. A parameter scan on the plasma density and temperature will extend the present study. In particular, we expect that, at larger values of the electron density and temperature, the whole dynamics is shifted further out towards the far SOL, as the mean free path of D_2 molecules decreases.

4.4 Analysis of the correlation between the D_{α} emission and the plasma and neutral quantities

Since the measurements of D_{α} emission provided by GPI diagnostics are used to infer the properties of the plasma and neutrals, understanding the correlations between the D_{α} emission and these properties is of crucial importance for an accurate interpretation of the GPI measurements. We then evaluate the correlations between the D_{α} emission rate and the n_e , n_D , n_{D_2} , $n_{D_2^+}$ and T_e (the quantities associated with the D_{α} emission). For this purpose, following the same procedure as in Ref. [64], we make use of the Spearman rank coefficient of correlation [113], which varies between -1 (if two functions are totally anti-correlated) and 1 (in case they are perfectly correlated).

Fig. 4.5 shows the Spearman correlations between the quantities involved in the calculation of the emissivity rate associated with the excitation of D atoms, $D_{\alpha,\text{Exc}}$. The electron density and temperature are strongly correlated, especially in the edge region. On the other hand, the correlation between the neutral density n_D and the plasma quantities, n_e and T_e , is different from the one observed in Ref. [64]. In fact, n_D is correlated with n_e in the SOL, with the correlation increasing towards the LCFS. The correlation function peaks in the edge, close to the LCFS, and then decreases sharply, becoming negative towards the core. A similar behavior is found for the Spearman correlation between n_D and T_e , with the correlation in the SOL and the anti-correlation in the edge being even stronger compared to the correlation between n_D and T_e . This is due to the mechanisms behind the generation and depletion of D atoms in the SOL and edge regions. In fact, in the SOL region, positive fluctuations of plasma density and temperature enhance the dissociation of the D_2 molecules injected by the gas puff from the

4.4. Analysis of the correlation between the D_α emission and the plasma and neutral quantities

outer wall, which results in an increase in the D atom density. Hence n_e and T_e are positively correlated with n_D . Around the LCFS, the density of D_2 molecules decreases while the density of D atom increases. However, the source of D atoms due to molecular dissociation is still more important than their sink due to ionization processes, since the plasma temperature remains lower than the ionization threshold. As a result, in agreement with Ref. [46], the correlations between n_D and n_e and between n_D and T_e remain positive.

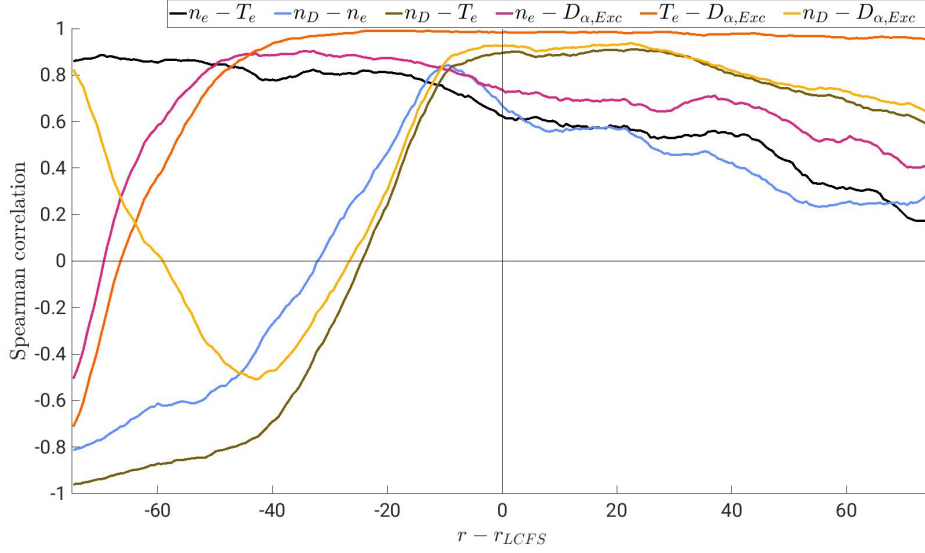


Figure 4.5: Radial plot of the Spearman correlation function between the quantities involved in the $D_{\alpha,Exc}$ emission, at the LFS equatorial midplane (all quantities are averaged in time and along the toroidal direction).

Deep in the edge, the high temperature leads to an ionization sink that dominates over dissociation sources. Therefore, local positive fluctuations of n_e and T_e lead to the decrease of D atom density, thus resulting in an anti-correlation between n_D and the plasma quantities, n_e and T_e . The result observed in Ref. [64] is thus recovered, but only for the warmer and denser plasma in the edge.

Turning to the D_α emission rate due to atom excitation, we observe that it is strongly correlated with the plasma quantities n_e and T_e , as expected from (Eq. 4.1), in the SOL and around the LCFS. The D_α emission is also positively correlated with n_D . This results from Eq. (4.1) and from the fact that n_e , T_e and n_D are also positively correlated with one another, which agrees with the conclusions in Ref. [46]. On the other hand, the correlation function between $D_{\alpha,Exc}$ and the plasma quantities n_e and T_e falls sharply and becomes negative towards the core. In fact, at the high densities and temperatures of this region, the density of neutral atoms drops to very low values, reducing significantly the D_α emission due to atom excitation. As a result, the D_α emission rate in Eq. (4.1) becomes more sensitive to fluctuations of n_D rather than perturbations of the plasma quantities, which explains why $D_{\alpha,Exc}$ is anti-correlated with n_e and T_e in this region, while strongly correlated with n_D . This also highlights the importance of taking into account the neutral density fluctuations when interpreting

D_α emission measurements close to the core, as D_α emission rates may become mostly determined by n_D fluctuations. We note that the result of the single-component simulation in Ref. [64] is retrieved in the edge. In this region, n_D is sufficiently large that it does not constrain the D_α emission. In these conditions, the n_D perturbations are less important than the fluctuations of n_e and T_e , leading to a positive correlation between $D_{\alpha,Exc}$ and n_e and T_e in most of the edge region and a negative correlation with the atom density, n_D .

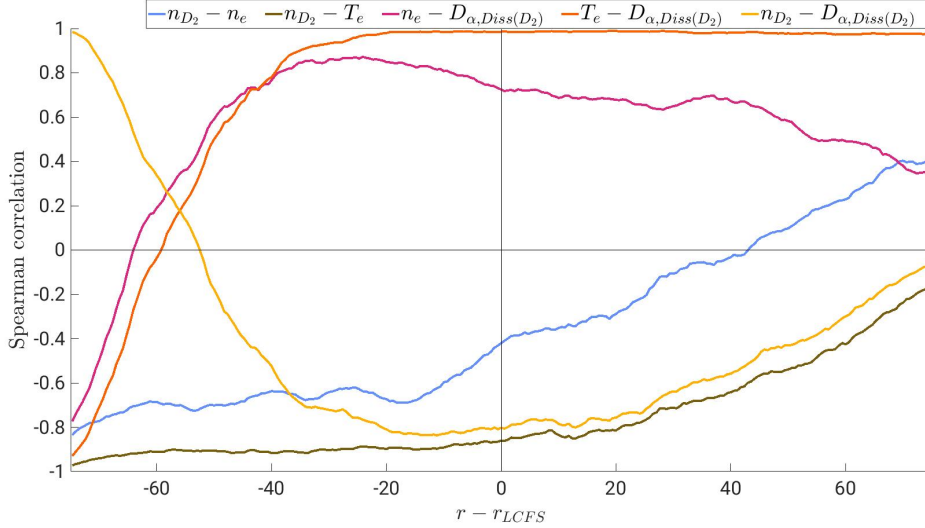


Figure 4.6: Radial plot of the Spearman correlation function between the quantities involved in the $D_{\alpha,diss(D_2)}$ emission, at the LFS equatorial midplane (all quantities are averaged in time and along the toroidal direction).

Fig. 4.6 shows the Spearman correlation function between the variables involved in the D_α emission rate associated with the dissociation of D_2 molecules, $D_{\alpha,Diss(D_2)}$. It is observed that n_{D_2} and T_e are strongly anti-correlated in the whole domain, since positive perturbations of T_e are associated with enhanced ionization of D_2 molecules and hence smaller n_{D_2} . Similarly, n_{D_2} is anti-correlated with n_e in the edge and in the near SOL, where large plasma densities result in a large rate of molecular dissociation and hence smaller density of D_2 molecules. The correlation becomes positive in the far SOL, closer to the gas puff source, where the density of D_2 molecules is larger. In fact, the gas puff is expected to enhance plasma fuelling, i.e. larger densities of D_2 molecules will ultimately lead to an increase of n_e . These results are similar to the ones obtained in Ref. [64] for the D_α emission due to excitation of D atoms in a single-component plasma. Regarding the $D_{\alpha,Diss(D_2)}$, we observe that it is correlated with n_e and T_e in the SOL and in most of the edge region. In particular, the $D_{\alpha,Diss(D_2)} - T_e$ correlation is strong in the SOL. Towards the core, the density of D_2 molecules drops, making $D_{\alpha,Diss(D_2)}$ very small and strongly dependent on the n_{D_2} fluctuations. Therefore, $D_{\alpha,Diss(D_2)}$ is more sensitive to the fluctuations of n_{D_2} than the perturbations of the plasma quantities, similarly to the dependence of $D_{\alpha,Exc}$ on n_D . As a result, $D_{\alpha,Diss(D_2)}$ becomes anti-correlated with n_e and T_e in the proximity of the core. In contrast, the emission rate is strongly correlated with the density of D_2 molecules near the core, but reduces sharply when one moves radially outwards,

4.4. Analysis of the correlation between the D_α emission and the plasma and neutral quantities

as n_{D_2} is no longer negligible and hence no longer regulates $D_{\alpha, \text{Diss}(D_2)}$.

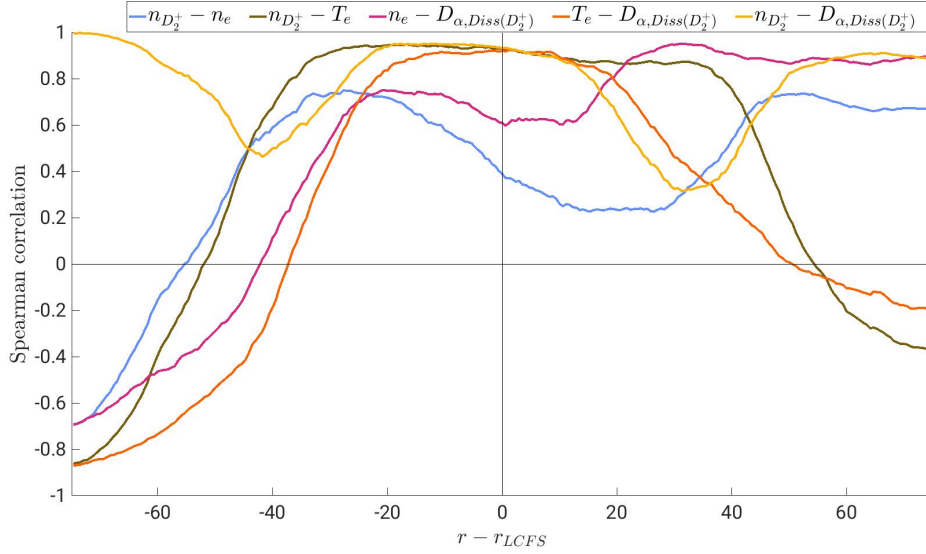


Figure 4.7: Radial plot of the Spearman correlation function between the quantities involved in the $D_{\alpha, \text{diss}(D_2^+)}$ emission, at the LFS equatorial midplane (all quantities are averaged in time and along the toroidal direction).

Focusing now on the analysis of the D_α emission due to dissociation and dissociative recombination of D_2^+ ions, $D_{\alpha, \text{Diss}(D_2^+)}$ (see Fig. 4.7), we start by highlighting the strong correlation between the density of D_2^+ ions and n_e in the SOL and in most of the edge, since positive n_e perturbations enhance the ionization of D_2 molecules and hence increase $n_{D_2^+}$ in these regions. However, since D_2^+ ions have a short lifetime, being destroyed by dissociative processes whose cross sections are larger than the cross section of ionization of D_2 molecules, the correlation between $n_{D_2^+}$ and n_e is also strongly influenced by the density of n_{D_2} molecules. As a matter of fact, towards the core, n_{D_2} drops to residual values, resulting in fewer D_2 molecules that can be ionized than D_2^+ ions that can be dissociated. As a consequence, positive fluctuations of n_e lead mostly to enhanced dissociation of D_2^+ ions and therefore negative $n_{D_2^+}$ fluctuations, which turns into an anti-correlation between $n_{D_2^+}$ and n_e . The Spearman correlation function between $n_{D_2^+}$ and T_e follows a similar behaviour, i.e. anti-correlation close to the core and correlation in the edge and near SOL, but in the far SOL where anti-correlation between these two quantities is observed. This is due to the fact that, at the typical temperatures of the far SOL, dissociation of D_2^+ ions dominates over ionization of D_2 molecules (see Fig. 3.1). Therefore, while positive temperature fluctuations result in the generation of D_2^+ ions, they also increase the rate of depletion of D_2^+ ions due to dissociative processes even more significantly. As a consequence, positive T_e perturbations lead to negative $n_{D_2^+}$ fluctuations in this region.

Since the density of D_2^+ ions is very small everywhere and hence decisively constrains the $D_{\alpha, \text{Diss}(D_2^+)}$ emission rate, the $D_{\alpha, \text{Diss}(D_2^+)}$ emission rate is correlated with $n_{D_2^+}$ in the whole domain. The correlation is particularly strong near the core, at the LCFS and in the proximity of the outer wall. The correlation function between $D_{\alpha, \text{Diss}(D_2^+)}$ and T_e is positive in most of

the domain (higher temperatures are related to larger emissivity coefficients and increased ionization of D_2 molecules), the exception being the proximity to the core and to the outer wall, where an anti-correlation is found between $D_{\alpha, \text{Diss}(D_2^+)}$ and T_e due to the anti-correlation between $n_{D_2^+}$ and T_e . Similarly, $D_{\alpha, \text{Diss}(D_2^+)}$ is correlated with n_e in the SOL and in most of the edge, where $n_{D_2^+}$ is correlated with n_e , but an anti-correlation between $D_{\alpha, \text{Diss}(D_2^+)}$ and n_e is observed close to the core, where fluctuation of $n_{D_2^+}$ and n_e are also anti-correlated.

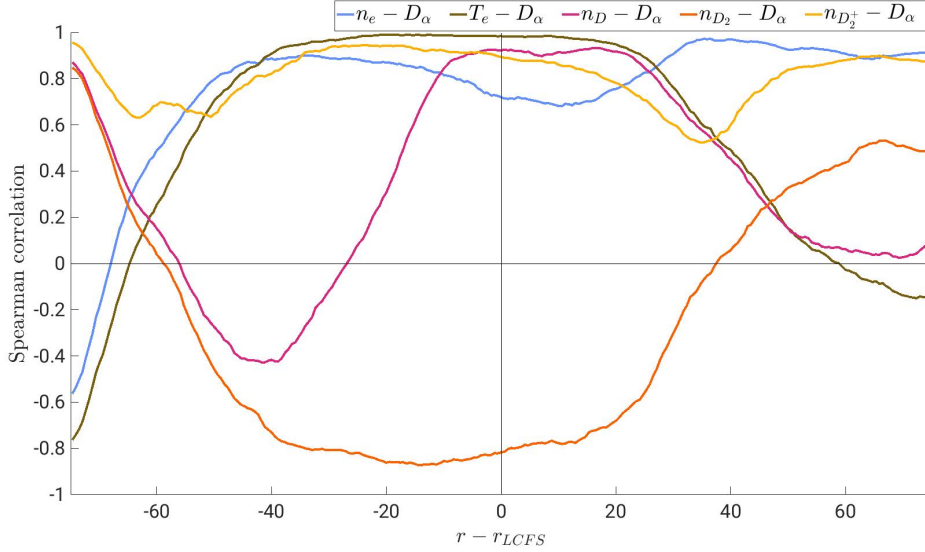


Figure 4.8: Radial plot of the Spearman correlation function between the quantities involved in the D_α emission, at the LFS equatorial midplane (all quantities are averaged in time and along the toroidal direction).

Finally, Fig. 4.8 shows the correlation functions between the total D_α emission rate, D_α , the electron temperature T_e and the density of each of the species involved in the reactions that emit light in the D_α line. The correlation with D_α can be interpreted through the analysis of $D_{\alpha, \text{Exc}}$, since it dominates over the other sources of D_α emission in the edge and near SOL, and $D_{\alpha, \text{Diss}(D_2^+)}$, which is dominant in the far SOL. It is observed that, as for $D_{\alpha, \text{Exc}}$ (see Fig. 4.5), the D_α emission is anti-correlated with n_e and T_e near the core, where neutrals can hardly penetrate and a strong correlation between D_α and n_D is observed. For the same reason, D_α is strongly correlated with n_{D_2} and $n_{D_2^+}$ in this region, even though these species contribute weakly to the overall emission via dissociative processes. In the edge, D_α emission is strongly correlated with n_e and T_e and the correlation between D_α and n_D , similarly to $D_{\alpha, \text{Exc}}$, is negative, since ionization dominates over dissociation. The correlation between D_α and n_{D_2} and between D_α and $n_{D_2^+}$ in the edge are explained by the fact that n_{D_2} is strongly anti-correlated with n_e and T_e , while $n_{D_2^+}$ is strongly correlated with these plasma quantities. In the near SOL, D_α is correlated with n_e , T_e and n_D , since dissociation dominates. On the other hand, since the D_α emission rate in the far SOL is mostly determined by $D_{\alpha, \text{Diss}(D_2^+)}$, D_α is also strongly correlated with $n_{D_2^+}$ and n_e in this region. The correlation between D_α and T_e drops radially outwards, becoming anti-correlation next to the outer wall. We remark that this

4.4. Analysis of the correlation between the D_α emission and the plasma and neutral quantities

represents a crucial difference with respect to the Spearman correlation between the D_α emission rate and T_e of the single-component simulation in Ref. [64] with important implications on the interpretation of GPI measurements, suggesting a different way of interpreting GPI measurements in the region next to the gas puff source. Moreover, the correlations of D_α with n_D and n_{D_2} near the gas puff source are determined by the correlation between the dominant $D_{\alpha, \text{Diss}(D_2^+)}$ contribution and the densities of neutral species n_D and n_{D_2} (not shown in Fig. 4.7). This is determined by the fact that $D_{\alpha, \text{Diss}(D_2^+)}$ is strongly correlated with n_e , thus the correlation between D_α and the densities of neutral species descends from their correlation with n_e . Fig. 4.5 shows a small correlation between n_e and n_D , explaining that D_α and n_D are not clearly correlated. On the other hand, Fig. 4.6 shows that n_e and n_{D_2} are correlated, thus leading to a correlation between D_α and n_{D_2} in the close proximity to the gas puff. These conclusions agree with the results observed in Fig. 4.8.

To summarise, we can divide the domain in four different regions according to the correlation between the D_α emission rate and the plasma and neutral quantities, namely n_e , T_e and n_D . 1) The far SOL, where D_α emission is mostly determined by the contribution of dissociation of D_2^+ ions and which is characterized by the D_α emission being strongly correlated with n_e , but uncorrelated or even slightly anti-correlated with T_e and, in general, uncorrelated with n_D . 2) The near SOL and LCFS, where D_α emission due to excitation of D atoms dominates over the contributions from dissociative processes and a strong correlation between D_α emission and the plasma quantities, n_e and T_e , is observed. Moreover, since the sources of D due to dissociative processes are more important than D sinks due to ionization, D_α is strongly correlated with n_D (similar to the conclusions found in Ref. [46]). 3) The edge region, where D_α is also strongly correlated with n_e and T_e , but ionization of D dominates with respect to dissociative processes, hence leading to an anti-correlation between D_α and n_D (similar to the results reported in Ref. [64]). 4) The region of the core, where D_α emission is constrained by the residual values of the density of D atoms that can penetrate in this region, resulting in D_α being correlated with n_D , but anti-correlated with n_e and T_e .

To illustrate the implications of these observations in Fig. 4.9, we consider snapshots of the normalized fluctuations of the plasma and neutral quantities, namely n_e , T_e , n_D , n_{D_2} and $n_{D_2^+}$, and the D_α emission, at a given time and toroidal location, focusing on the poloidal region around the LFS equatorial midplane. The normalized fluctuations for the electron density, n_e , are defined as $(n_e - \langle n_e \rangle) / \langle n_e \rangle$, and similarly for the other quantities. The results in Fig. 4.9 confirm that n_e and T_e are strongly correlated in the whole domain, except in the close proximity to the core, where the correlation is less evident. The fluctuations of the molecular density, n_{D_2} , are uncorrelated with n_e and T_e in the SOL, but clearly anti-correlated with the perturbations of n_e and T_e around the LCFS and in the edge region, consistently with the observations in Fig. 4.6. On the other hand, the fluctuations of $n_{D_2^+}$ are strongly correlated with the electron density and temperature fluctuations, except next to the outer wall, where $n_{D_2^+}$ is correlated with n_e , but anti-correlated with T_e (because dissociation of D_2^+ is more important than ionization of D_2 at the temperatures typically found in this region), and in the close proximity to the core, where D_2 molecules can hardly penetrate and hence ionization of D_2

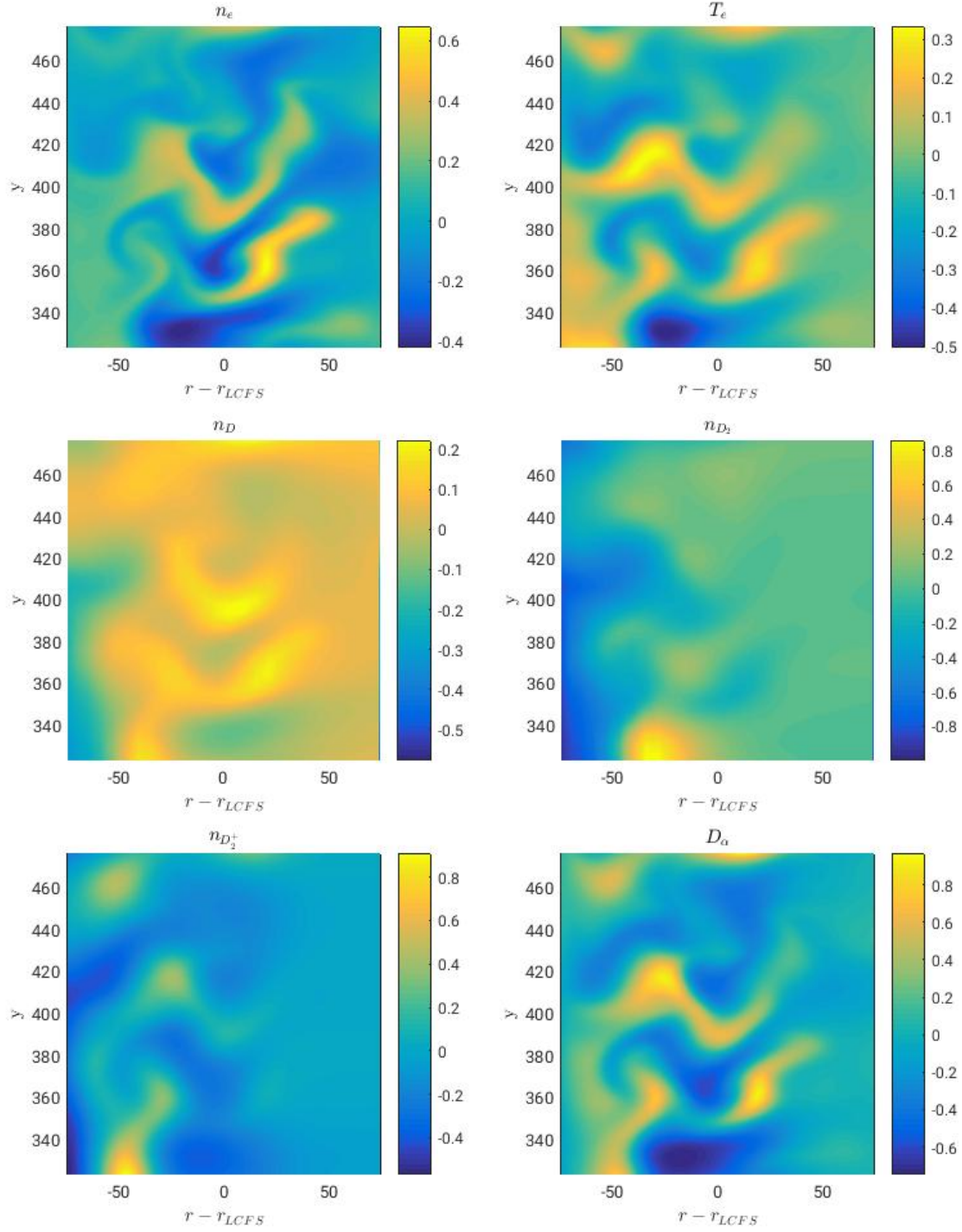


Figure 4.9: Typical poloidal snapshots of the fluctuations of n_e , T_e , n_D , n_{D_2} , $n_{D_2^+}$ and the D_α emission rate at the LFS equatorial midplane, where the gas puff is located.

is small. Regarding the n_D fluctuations, one can distinguish the different regions mentioned above: the region close to the outer wall, where n_D is uncorrelated with n_e and T_e , the edge,

where the n_D fluctuations are anti-correlated with the fluctuations of n_e and T_e , and the LCFS with the SOL, where n_D fluctuations are positively correlated with electron density and temperature perturbations. Close to the core, the shadowing effect first reported in Ref. [64], especially at $y \simeq 420\rho_{s0}$ is observed. In fact, the positive perturbation of n_e , T_e enhances the ionization of D atoms, thus reducing n_D locally and also further inside towards the core, since D atoms can no longer penetrate radially. As a result, n_D does not increase when n_e and T_e decrease. We therefore conclude that the non-local shadowing effect attenuates the anti-correlation. Finally, we observe that the total D_α emission rate, D_α , is strongly correlated with n_e and T_e in almost the whole domain, except for the far SOL where the link between D_α and T_e is not clear. We remind that this is related to the fact that D_α emission is dominated by the contribution of dissociation of D_2^+ ions, with the total D_α emission being mostly correlated with $n_{D_2^+}$ and n_e in this region, while nothing can be said regarding the correlation between D_α and T_e . We again highlight that the location and radial spread of these regions is affected by the values of the electron density and temperature, thus leading to a shorter mean free path of the D_2 molecules puffed into the domain.

4.5 Impact of neutral fluctuations

Similarly to the procedure followed in Ref. [64], we evaluate the impact of neutral density fluctuations on the D_α emission by using the average density of neutral particles when computing the emission rates and compare them with the self-consistent D_α emission profile that takes into account the instantaneous neutral density. This is of importance for the $D_{\alpha,\text{Exc}}$ and $D_{\alpha,\text{Diss}(D_2)}$ contributions, which rely on the excitation of neutral atoms and molecules, respectively, but not for the $D_{\alpha,\text{Diss}(D_2^+)}$ contribution, which is associated with the excitation of D_2^+ plasma ions. For the two excitation channels affected by the density of neutral species, the D_α emission based on the averaged neutral density profiles can be expressed as

$$D_{\alpha,\text{Exc}\langle n_D \rangle} = n_e \langle n_D \rangle r_{\alpha,\text{Exc}}(n_e, T_e) \quad (4.10)$$

and

$$D_{\alpha,\text{diss},D_2\langle n_{D_2} \rangle} = n_e \langle n_{D_2} \rangle r_{\alpha,\text{Diss}(D_2)}(n_e, T_e), \quad (4.11)$$

where we considered the time and toroidally averaged D atom density, $\langle n_D \rangle$, the average D_2 molecule density, $\langle n_{D_2} \rangle$. The resulting total D_α emission evaluated using the average density of neutral species is therefore given by

$$D_{\alpha\langle n_n \rangle} = D_{\alpha,\text{Exc}\langle n_D \rangle} + D_{\alpha,\text{diss},D_2\langle n_{D_2} \rangle} + D_{\alpha,\text{Diss}(D_2^+)}. \quad (4.12)$$

Chapter 4. Numerical simulations of Gas Puff Imaging

In Fig. 4.10, snapshots of the D_α and $D_{\alpha\langle n_n \rangle}$ emission is presented, as well as their relative difference, $(D_\alpha - D_{\alpha\langle n_n \rangle})/D_\alpha$. The contributions of the two excitation channels involving neutral particles are also analysed. We highlight that $D_{\alpha,Exc}$ and $D_{\alpha,Exc\langle n_D \rangle}$ have similar profiles, but discrepancies of the order of 20% – 30% can be seen in the near SOL and edge regions. The difference becomes particularly important close to the core, where it reaches values of the order of 50%. Similar considerations hold for the comparison between $D_{\alpha,Diss(D_2)}$ and $D_{\alpha,diss,D_2\langle n_{D_2} \rangle}$. Since the D_α emission is mostly determined by the contribution from excitation of D atoms in the edge and near SOL, while the dominant component in the far SOL, $D_{\alpha,Diss(D_2^+)}$, does not depend on the density of neutral species, the plots for the total D_α emission are similar to those obtained for $D_{\alpha,Exc}$. Therefore, our results support the conclusions expressed in Ref. [64], namely that neutral fluctuations have a non-negligible impact on the D_α emission rates.

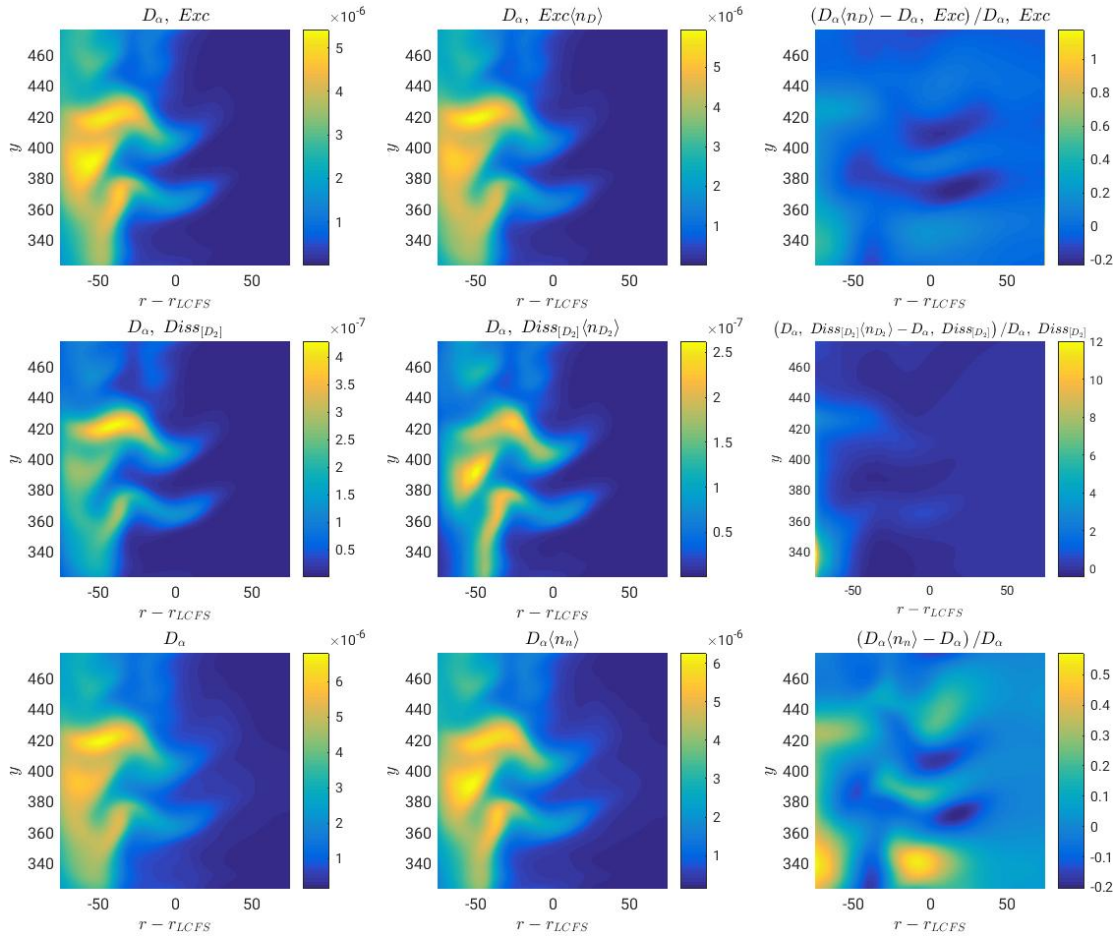


Figure 4.10: Snapshots of the $D_{\alpha,Exc}$ contribution (top), the $D_{\alpha,Diss(D_2)}$ component (middle) and the total D_α emission rate (bottom). The emission rate taking into account neutral fluctuations (left), the same quantity calculated by neglecting the atom density fluctuations (middle), and relative difference between the two (right) are plotted.

The analysis is further extended by evaluating the effect of neutral density fluctuations on the

statistical moments of the D_α emission, namely the standard deviation, skewness and kurtosis, presented in Fig. 4.11, and also the properties of turbulence, i.e. the auto-correlation time, τ_{auto} , the radial and poloidal correlation lengths, L_{rad} and L_{pol} , displayed in Fig. 4.12. We also consider the same quantities from the contributions of the D_α emission, taking into account and excluding neutral fluctuations. These quantities play an important role on turbulence characterization and are often used as proxy to analyse the n_e and T_e fluctuations.

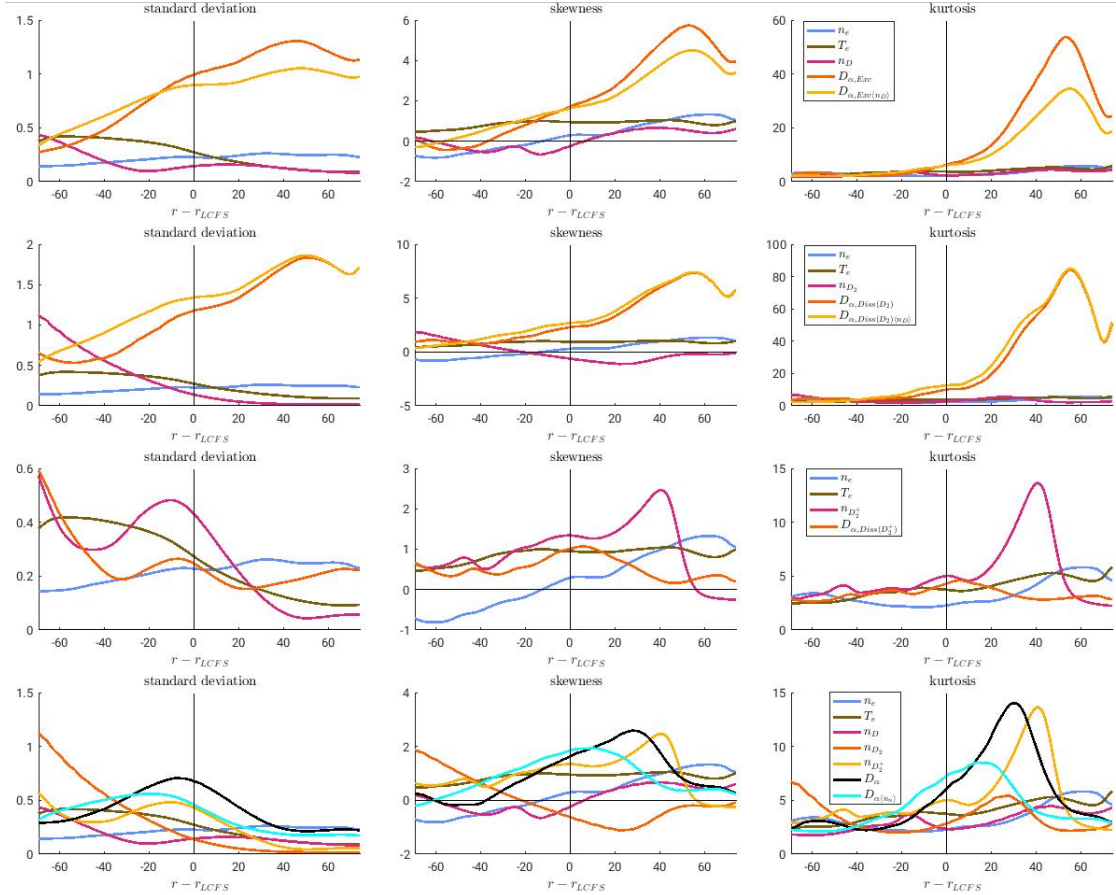


Figure 4.11: Radial profiles of the statistical moments of each component of the D_α emission rate, representing the standard deviation (left), skewness (middle) and kurtosis (right), computed at the LFS equatorial midplane. The first row refers to the $D_{\alpha,\text{Exc}}$ contribution, the second row presents results for the $D_{\alpha,\text{Diss}(D_2)}$ component, the third row displays the plots for the $D_{\alpha,\text{Diss}(D_2^+)}$ contribution and the fourth row refers to the total D_α emission.

We therefore start our analysis by considering the statistical moments of n_e and T_e , as well as of n_D , n_{D_2} and $n_{D_2^+}$ as these affect the properties of the D_α emission. The standard deviation of n_e does not change considerably throughout the domain, being of the order of 30% its equilibrium value, as expected from previous theoretical and experimental studies. In contrast, the standard deviation of T_e in the edge is about two to three times larger than in the SOL, having a sharp gradient in the region around the LCFS. The standard deviation of $n_{D_2^+}$ decreases is considerably large at the edge-core interface, decreases slightly in the proximity of the core,

then it increases a bit close to the LCFS and decreases significantly in the SOL, becoming negligible close to the outer wall. Focusing on the neutral species, we note that the standard deviation of n_D is large at the edge-core interface, decreases significantly in the edge, increases slightly around the LCFS and remains approximately constant in the SOL, being comparable to the standard deviation of T_e . Finally, the standard deviation of n_{D_2} at the edge-core interface is much larger than the standard deviation of the other variables and decreases sharply across the edge, becoming negligible in most of the SOL.

Turning to the analysis of the skewness, we remark that the skewness of T_e is positive and approximately constant over the whole domain, while n_e and n_D have negative skewness in the edge and positive in the SOL. This is different from the result found in Ref. [64] for the skewness of n_D , which is yet another consequence of the introduction of molecular dynamics. In fact, in the multi-component simulation, plasma fluctuations have different impact on n_D in the edge and SOL. In the SOL, large positive perturbations of n_e and T_e make dissociation of D_2 molecules more frequent and hence decisively increase n_D , while large negative perturbations do not change n_D significantly, which justifies the positive skewness in the SOL. In the edge, however, D atoms have a higher density than D_2 molecules. Therefore, large positive fluctuations of n_e and T_e increase the level of ionization of D atoms and hence result in a sharp decrease of n_D , while large negative plasma fluctuations do not lead to equally important positive fluctuations of n_D , thus justifying the negative values of skewness observed in the edge region. For comparison, in the single-species simulations, since there are no volumetric sources of n_D , large positive plasma perturbations are always associated with an increase of the ionization levels and consequent sharp decrease of n_D , while large negative perturbations have a less significant impact on n_D , thus suggesting negative values of skewness in the whole domain (in reality, the plots in Ref. [64] show that skewness is negative in the SOL, where ionization of D atoms is important, and increases radially inwards, since n_D decreases and hence the effect of the plasma perturbations on ionization of D becomes less important). The skewness of n_{D_2} is positive in the edge and negative in the SOL, similarly to what was reported for the skewness of n_D in Ref. [64]. In addition, the kurtosis of n_e , T_e and n_D have a similar behaviour, being larger in the SOL compared to the edge region, remaining between 0 and 5.

We now turn our attention to the D_α emission. Fig. 4.11 shows that the standard deviation of the $D_{\alpha,Exc}$ emission rate is larger than the one of n_e , T_e and n_D in most of the domain and has a different radial dependence. This observation is related to the complex dependency of the emissivity coefficient r_α on n_e and T_e , which may result in a very different behaviour of the statistical properties of $D_{\alpha,Exc}$ compared to n_e and T_e . It is also found that $D_{\alpha,Exc\langle n_D \rangle}$ is 20% to 30% smaller than $D_{\alpha,Exc}$ in the SOL, while this relation is reversed in the edge, where $D_{\alpha,Exc\langle n_D \rangle}$ is about 20% larger. The relation between the two quantities in the SOL contrasts with the one reported in Ref. [64], which is related to the fact that molecular dynamics are now taken into account, thus affecting the impact of neutral fluctuations on the D_α emission. We observe that the standard deviation of $D_{\alpha,Exc\langle n_D \rangle}$ is larger in the SOL compared to the edge region. The skewness of $D_{\alpha,Exc}$ and $D_{\alpha,Exc\langle n_D \rangle}$ is of the same order of magnitude as the

skewness of n_e , T_e and n_D in the edge, but grows radially and becomes much larger than the skewness of the other quantities in the SOL, which is also not observed in Ref. [64] (we remark that $D_{\alpha, \text{Exc}}$ is very small in the far SOL, where the D_α emission is mostly determined by $D_{\alpha, \text{Diss}(D_2^+)}$). Moreover, we notice that $D_{\alpha, \text{Exc}}$ and $D_{\alpha, \text{Exc}(n_D)}$ display similar behaviour in the SOL, but different behaviour in the edge, especially close to the core. This agrees with the conclusion reported in Ref. [64] on the effect of neutral perturbations on D_α emission, confirming that the impact of n_D fluctuations on D_α emission increases with the distance from the gas puff. In fact, n_D fluctuations have a strong influence on the qualitative behaviour of the $D_{\alpha, \text{Exc}}$ emission in the edge and towards the core. The interpretation of the kurtosis is identical to that of the skewness.

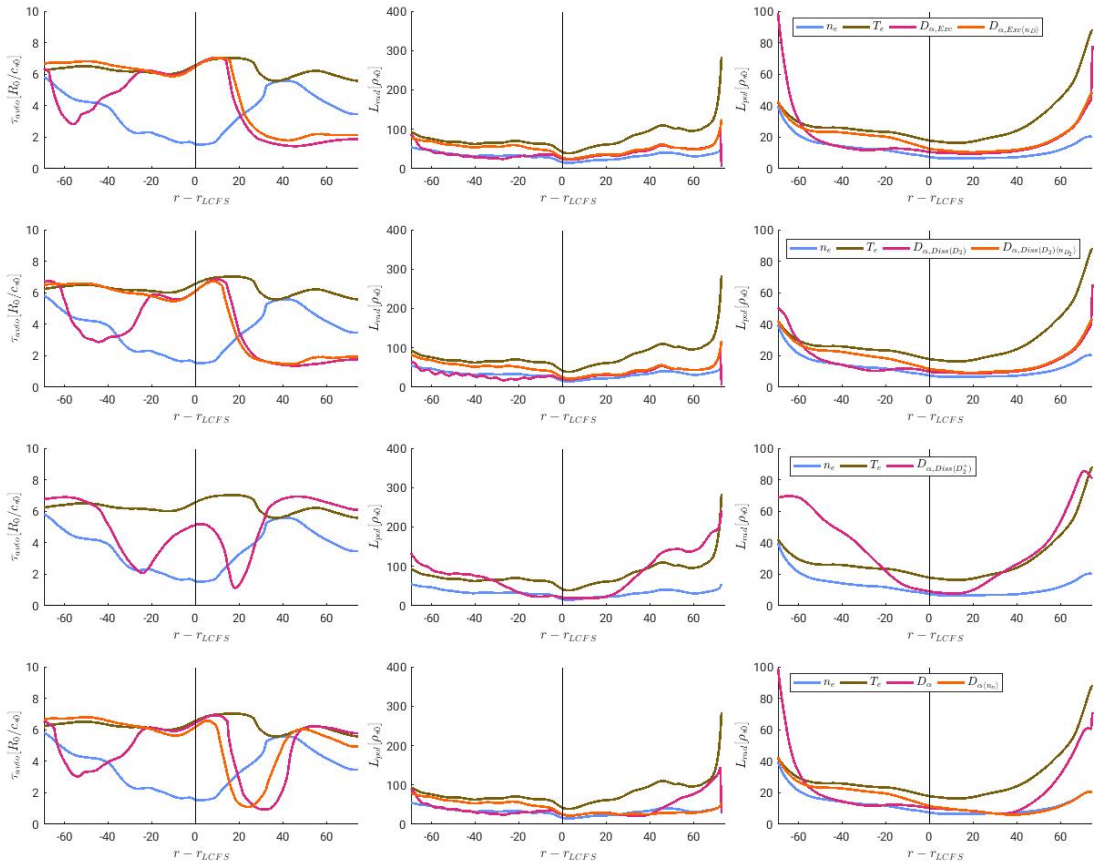


Figure 4.12: Radial profiles of the turbulence properties of each component of the $D_{\alpha, \text{Exc}}$ emission rate, representing the auto-correlation time (left), poloidal correlation length (middle) and radial correlation length (right), computed at the LFS equatorial midplane. The first row refers to the $D_{\alpha, \text{Exc}}$ contribution, the second row presents results for the $D_{\alpha, \text{Diss}(D_2)}$ component, the third row displays the plots for the $D_{\alpha, \text{Diss}(D_2^+)}$ contribution and the fourth row refers to the total D_α emission.

Providing a small contribution to the overall D_α emission, $D_{\alpha, \text{Diss}(D_2)}$ displays very similar standard deviation, skewness and kurtosis as $D_{\alpha, \text{Diss}(D_2)(n_{D_2})}$ in the SOL, with the difference between these quantities being larger in the edge, especially close to the core, which resembles

the results obtained in for the statistical moments of the D_α emission. As a matter of fact, while Ref. [64] considers D_α emission generated by neutral atoms that are puffed into the system and then ionized by the plasma, here the $D_{\alpha,\text{Diss}(D_2)}$ component of D_α emission is similarly due to D_2 molecules puffed into the system and depleted via dissociation and ionization processes. We also highlight that the large values of the statistical moments in the SOL around $r = 50\rho_{s0}$, and in particular the kurtosis, are related to the fact that $D_{\alpha,\text{Diss}(D_2)}$ is very small in this region, and hence large values are strongly influenced by statistical fluctuations.

In contrast to $D_{\alpha,\text{Exc}}$ and $D_{\alpha,\text{Diss}(D_2)}$, the statistical moments of $D_{\alpha,\text{Diss}(D_2^+)}$ are of the same order as the values of the statistical moments of n_e , T_e and $n_{D_2^+}$. We remark that, since $D_{\alpha,\text{Diss}(D_2^+)}$ dominates over the other D_α emission components in the far SOL, the small values of the standard deviation, skewness and kurtosis of $D_{\alpha,\text{Diss}(D_2^+)}$ in the SOL ensure that the values of these statistical moments for the total D_α emission remain small. We also highlight that the skewness and kurtosis of $D_{\alpha,\text{Diss}(D_2^+)}$ follow those of $n_{D_2^+}$ in the edge, while the skewness and kurtosis decrease in the SOL and become smaller than those of the other quantities.

Finally, we analyse the statistical moments of the total D_α emission, D_α , both including and neglecting the fluctuations of the density of neutral species, D and D_2 , and the statistical moments of all plasma and neutral quantities involved. The standard deviation of D_α is smaller than the standard deviation of T_e at the edge-core interface, increases across the edge region, peaks at the LCFS, decreases in the SOL and remains approximately constant in the close proximity of the edge, being similar to the standard deviation of n_e in this region. We highlight that the radial profile of the standard deviation of D_α is very different from the one of the standard deviation of both n_e and T_e , but it can still be used as a proxy of the standard deviation of n_e in the far SOL. This difference is once again related to the complex dependency of the emissivity coefficient in $D_{\alpha,\text{Exc}}$ on n_e and T_e , and it is also partially explained by the non-negligible contribution of $D_{\alpha,\text{Diss}(D_2^+)}$, which depends mostly on the profile of $n_{D_2^+}$. In fact, the standard deviation of D_α follows, to some extent, the same behaviour exhibited by the standard deviation of $n_{D_2^+}$. Regarding the standard deviation of $D_{\alpha\langle n_n \rangle}$, although it has a similar profile to the one of the standard deviation of D_α , we note that it is slightly larger than the standard deviation of D_α in the proximity of the core and smaller than it in the rest of the domain, which makes it more similar with the standard deviation of T_e . Therefore, the standard deviation of $D_{\alpha\langle n_n \rangle}$ could, to some extent, be used as a proxy of the standard deviation of T_e , particularly in the SOL. Regarding the skewness of D_α , we remark that it almost verifies in the close proximity of the core, decreases slightly radially outwards and then increases significantly in the edge and near SOL, decreasing sharply in the far SOL, where it becomes smaller than the skewness of both n_e and T_e . Since it has a very different behaviour from the skewness of n_e and T_e , the skewness of D_α can hardly be envisaged as a proxy for these quantities. In fact, it has a similar profile to the skewness of $n_{D_2^+}$, particularly close to the outer wall, where the contribution from $D_{\alpha,\text{Diss}(D_2^+)}$ becomes dominant. On the other hand, the skewness of $D_{\alpha\langle n_n \rangle}$ has a smoother profile than the skewness of D_α , remaining closer to the skewness of T_e in most of the domain, but its behaviour is still too different from the profiles of the skewness of n_e and T_e for it to be used as a proxy of these quantities. Very

similar observations apply to the analysis of the kurtosis of D_α and $D_{\alpha\langle n_n \rangle}$, which are small in the close proximity of the core, increase significantly when approaching the LCFS and in the near SOL, and then decrease sharply in the far SOL, with a similar behaviour to the kurtosis of $n_{D_2^+}$. Although the kurtosis of D_α and $D_{\alpha\langle n_n \rangle}$ has a smoother profile than the kurtosis of D_α , both of them have a very different behaviour compared to the kurtosis of n_e and T_e , which prevent them from being used as proxies for these quantities in most of the domain.

Fig. 4.11 also shows that the neutral density fluctuations do not affect significantly the statistical moments of D_α in the SOL, but the discrepancy between the standard deviation, skewness and kurtosis of D_α and $D_{\alpha\langle n_n \rangle}$ is larger in the edge and displays different behaviour close to the core. This reinforces the conclusion that the n_D fluctuations can have an important impact on the $D_{\alpha,Exc}$ emission, particularly in the edge, and thus must be taken into account when interpreting experimental results from GPI diagnostics, as highlighted in Ref. [64].

Focusing now on the results of the analysis of the auto-correlation time and of the poloidal and radial correlation lengths, presented in Fig. 4.12, we note that the auto-correlation time, τ_α , is the time interval such that

$$C_{ii}(\tau_\alpha) = \frac{1}{2}, \quad (4.13)$$

with C_{ii} the auto-correlation function between two signals at the same location separated by a τ_α time interval. In turn, the radial and poloidal correlation lengths, L_{rad} and L_{pol} , are evaluated as

$$L = 1.66 \frac{\delta}{\sqrt{-\ln C_{ij}}}, \quad (4.14)$$

where C_{ij} is the cross-correlation function between the signals measured at the same time and at the positions labelled i and j , and δ the distance between these two positions. Similarly to Ref. [64], we observe that there is no significant dependence of the correlation lengths on the value of δ , as long as $1.5\rho_{s0} \lesssim \delta \lesssim 10\rho_{s0}$, and we choose $\delta = 2.9\rho_{s0}$ for the evaluation of the radial correlation length and $\delta = 7.8\rho_{s0}$ for the evaluation of the poloidal correlation length. The simulation shows that the fluctuations of the neutral densities have a stronger impact on the turbulence properties in the edge region compared to the SOL. As a matter of fact, the auto-correlation time and the poloidal and radial correlation lengths of $D_{\alpha,Exc}$ and $D_{\alpha,Exc\langle n_D \rangle}$ are approximately the same in the SOL, but considerably different in the edge. A similar conclusion holds for the comparison of the turbulence properties of $D_{\alpha,Diss(D_2)}$ and $D_{\alpha,diss,D_2\langle n_{D_2} \rangle}$. We also note that the auto-correlation time and the poloidal and radial correlation lengths for $D_{\alpha,Diss(D_2^+)}$ display a similar behaviour compared to the profiles of $D_{\alpha,Exc}$ and $D_{\alpha,Diss(D_2)}$. The turbulence properties of the total D_α emission, are therefore marginally affected by the neutral density fluctuations in the SOL, but strongly impacted in the edge, as shown in Fig. 4.12.

Since the GPI diagnostic is used to infer the turbulence properties of the plasma quantities, namely n_e and T_e , it is interesting to compare the auto-correlation time and correlation lengths of the D_α emission with the ones of n_e and T_e , which are also presented in Fig. 4.12. The plots of τ_α show that the auto-correlation time of the D_α emission rate is in general longer than the one for n_e . Regarding the auto-correlation time of T_e , we note that D_α can be used as its proxy in the edge, but not in the SOL. In fact, only in the proximity of the LCFS and close to the wall, where the D_α emission is mostly determined by the contribution of dissociation of D_2^+ , the auto-correlation time of the D_α emission follows the one of T_e . On the other hand, L_{rad} and L_{pol} based on the D_α emission provide a good estimate for the same quantities for n_e , while it underestimates the T_e measurements. The same conclusions hold for $D_{\alpha\langle n_n \rangle}$, thus the correlation lengths of $D_{\alpha\langle n_n \rangle}$ can be used to infer L_{rad} and L_{pol} of the electron density.

4.6 Conclusion

In this chapter we present the results of a simulation of GPI diagnostics carried out with the multi-component GBS model introduced in Ch. 3 with the goal of supporting a proper interpretation of the D_α emission in the context of GPI diagnostics, ultimately to allow for an accurate reconstruction of the plasma and neutral profiles and a reliable inference of the properties of plasma turbulence. This simulation extends the study reported in Ref. [64] to the case of a multi-component deuterium plasma, thus taking into account the dynamics associated with molecular species, D_2 and D_2^+ . It also follows up on the work presented in Ref. [46], that we extend by considering a three-dimensional plasma and simulating the neutrals by means of a kinetic model valid for all values of the neutral mean free path. Analogously to Ref. [64], a toroidally symmetric source of D_2 molecules at wall temperature is considered at the LFS equatorial midplane in order to mimic a diagnostic gas puff.

With respect to the analysis in Refs. [64] and [46] the contributions from dissociation of D_2 and D_2^+ species to the D_α emission rate is taken into account, in addition to the contribution from the excitation of D atoms. While the D_α emission is mostly determined by the contribution of atomic excitation in most of the domain, the dissociation of D_2^+ is dominant in the far SOL, near the gas puff source, where the contribution from atomic excitation is residual. These results suggest, for future work, to include the contribution from recombination processes when studying the D_α emission, especially for low SOL temperatures.

The work presented in this chapter also sheds some light on the correlations between the fluctuations of the components of the D_α emission rate, the plasma quantities and the neutral species densities, based on the application of the Spearman correlation function. In the configuration and parameter regime considered here, it is possible to divide the diagnosed volume in four regions, according to the correlations between the total D_α emission and the plasma and neutral quantities determining it. In the far SOL, D_α emission is strongly correlated with n_e , but no significant correlation with T_e or n_D is reported, which is a result of the D_α emission being mostly determined by the contribution from dissociation of D_2^+

ions. In the near SOL and around the LCFS, D_α emission is strongly correlated with n_e , T_e and n_D , being mostly determined by excitation of D atoms. On the other hand, radially inward across the edge region, the D_α emission becomes anti-correlated with the neutral density n_D , as a result of ionization sinks dominating over dissociation sources in that region. Finally, the very low density of neutral atoms in the proximity of the core results in the D_α emission being correlated with n_D and strongly anti-correlated with the plasma quantities n_e and T_e . However, the location and radial spread of the regions found is strongly dependent on the plasma density and temperature considered in the simulation, as the whole dynamics is expected to shift radially outwards if higher densities and temperatures are considered.

Regarding the impact of the neutral fluctuations on the D_α emission rate, the simulation results confirm the conclusions reported in Ref. [64], that the perturbations of the neutral quantities affect significantly the D_α emission, particularly in the edge and in the proximity of the core. This is shown for the statistical moments of the D_α emission rate and the related turbulence properties, which highlight the increasingly important role of the neutral fluctuations as one moves radially inwards.

5 Summary and conclusions

The boundary region of a tokamak plays a crucial role in determining the overall performance of the device, as it regulates the exhaust of particle and energy to the vessel walls, controls plasma fuelling, impurity levels and Helium ashes removal [12]. In the boundary, the plasma dynamics is significantly affected by the presence of neutral particles, which are generated by recycling processes taking place at the surrounding walls, external injection or volumetric recombination processes. The GBS code enables self-consistent three-dimensional simulations of the neutral-plasma interaction in the tokamak boundary, by using a set of drift-reduced Braginskii equations to model plasma turbulence and a kinetic advection equation for the neutral species [61]. While the plasma equations are solved by using a standard finite-difference scheme, the numerical solution of the neutral kinetic equation relies on the application of the method of characteristics, with the integral over the neutral path being numerically discretized, while considering the $\tau_n \ll \tau_{\text{turb}}$ and $k_{\parallel} \lambda_{\text{mfp},n} \ll 1$ limits. Leveraging the GBS code, the present thesis reports on the development of a mass-conserving multi-component self-consistent plasma and neutral model and its first applications that consider a limited plasma configuration, with a limiter on the equatorial HFS.

Ch. 2 presents the extension of the GBS model to achieve mass conservation to leading order in ρ_s/R_0 , detailing its numerical implementation and describing the first mass-conserving simulation results. Mass conservation is achieved by consistently considering toroidicity effects in the neutral and plasma models and by accounting for the radial variation of the inverse aspect ratio $\epsilon = a_0/R_0$. Moreover, the orderings $k_{\parallel}/k_{\perp} \ll 1$ and $k_{\perp} R_0 \gg 1$ are avoided and a set of boundary conditions implemented to make the plasma recycling processes at the walls verify mass conservation. The mass-conserving properties of the whole model are demonstrated by performing proper convergence tests. The results from mass-conserving simulations differ from the ones obtained by using a non-mass-conserving model, as mass-conserving simulations are characterized by a sharper transition between the closed and open field-line regions, noticeable in the profiles of both the plasma and neutral quantities, thus highlighting the impact of mass conservation on the simulation results. In addition, quantitative studies of particle fluxes performed with the mass-conserving model show that

Chapter 5. Summary and conclusions

the ion particle flux is mostly determined by the $E \times B$ drift, which balances the neutral particle flux. Finally, when performing a parameter scan on the plasma density, higher densities result in a weaker penetration of neutral particles across the edge and consequently a more pronounced drop of the neutral density from the SOL to the edge region. As a result, the flux of neutrals also drops more significantly from the LCFS to the core.

In Ch. 3, the mass-conserving self-consistent model of plasma turbulence and neutral dynamics is extended to include the molecular dynamics in the context of a deuterium plasma, i.e. by considering a plasma composed of electrons, D^+ ions, D atoms, D_2 molecules and D_2^+ ions. As a result of the introduction of the molecular dynamics, a number of new collisional processes are taken into account, including ionization, electron-neutral elastic collisions, charge-exchange and dissociative processes, which give rise to new collisional terms appearing in the equations describing both the plasma and the neutral dynamics. The plasma model is extended by considering a set of drift-reduced Braginskii equations for the D_2^+ ion species, that implement the Zhdanov closure. On the other hand, the neutral model is improved to take into account the description of D_2 molecules, which is done by solving a neutral kinetic equation for the molecular species, in addition to the atomic species, thus resulting in a system of two coupled linear integral equations for the atomic and molecular densities.

The results from the first simulation of a multi-component plasma using GBS are presented. The density profiles show a noticeable up-down asymmetry, which ultimately results in larger recycling rates and higher density of neutrals above than below the limiter plates. The simulation shows that the density of D_2^+ ions peaks inside the LCFS in the proximity of the limiter and is between three and four orders of magnitude smaller than the density of the main ion species, D^+ . In addition, the role of D_2 molecules on plasma fuelling is also addressed. It is observed that most of the D_2 particles generated in the SOL cross the LCFS and are dissociated into D atoms in the edge. Both D atoms and D_2 molecules are ionized due to the higher plasma densities and temperatures in the edge, where D_2^+ ions have very short lifetimes, being rapidly dissociated. An interesting result from the simulations is the shift of the ionization of D atoms radially inward with respect to the results from single-species simulations, as a result of the significant generation of D atoms due to the dissociation of D_2 molecules inside the LCFS. As a result of the dissociation of D_2 in the region around the LCFS and the association of D atoms at the limiter and vessel walls, the density of D atoms peaks in the SOL region close to the LCFS, where the radial flux of D atoms reverses sign, as opposed to the monotonic increase of the density of D atoms towards the wall observed in single-component GBS simulations.

Ch. 4 reports on the investigation of light emission in GPI performed by exploiting the self-consistent multi-component model developed in Ch. 3. The research presented in this Ch. 4 constitutes a follow-up of the studies reported in Refs. [64] and [46], by featuring three-dimensional simulations of a mass-conserving multi-component deuterium plasma in the tokamak boundary in the presence of a diagnostic gas puff located at the equatorial outboard midplane. The molecules puffed at wall temperature into the domain interact with

the boundary plasma, and this interaction results also in light emission. The studies presented in this chapter focus on the D_α line emission and take into account the contributions from excitation of D atoms and dissociative processes acting on D_2 molecules and D_2^+ molecular ions, with the component associated with atomic excitation being dominant in most of the domain, except in the proximity of the gas puff source, where dissociation of D_2^+ ions is dominant. The simulation results reveal that the fluctuations of the neutral density have a significant impact on the D_α emission rate in the edge, which is supported by the analysis of the radial profiles of the standard deviation, the skewness, the kurtosis, the auto-correlation time and the radial and poloidal correlation lengths.

The results presented in Ch.4 also highlight that the simulation domain can be split radially into four different regions, according to the correlation functions between the D_α emission rate and the plasma and neutral quantities determining it, namely the electron density, n_e , the electron temperature, T_e , and the density of neutral atoms, n_D . More precisely, a strong correlation is observed between the D_α emission and n_e in the far SOL, but D_α emission is found not to be strongly correlated with T_e or n_D . In the near SOL and around the LCFS, D_α emission is strongly correlated with n_e , T_e and n_D . In most of the edge region, D_α is also strongly correlated with both n_e and T_e , but anti-correlated with n_D , since dissociation of D_2 molecules dominates over ionization of D atoms in the SOL, while ionization becomes dominant in the edge. Finally, towards the core region, the very low neutral density results in the D_α emission being mostly determined by n_D , which in turn translates into a strong correlation between D_α and n_D , and significant anti-correlations between D_α and both n_e and T_e . These results provide useful insights on the interpretation of the D_α emission in the context of GPI diagnostics, as it can guide the interpretation of plasma and neutral quantities from light emission measurements.

As a final note, we remark that the studies presented in this thesis constitute a step forward towards the realistic self-consistent simulation of the complex dynamics in the boundary region of a tokamak. While mass-conservation is an essential feature for the accurate simulations of the neutral-plasma interaction, the ability to simulate multi-ion species and to address the dynamics of several neutral particles is considered a key element to study relevant issues concerning the physics of boundary plasmas, such as fuelling and GPI diagnostics.

The results published in this thesis focus on a limited plasma. The extension to diverted configurations, more widely used in nowadays tokamaks given their advantages on reducing the heat load on the plasma facing components, should be relatively straightforward. Since divertor plates are placed, with respect to the limiter plates, further away from the tokamak core, the inclusion of neutral dynamics is expected to be even more crucial in a diverted geometry. The implementation of the multi-species model in diverted configurations will also allow for the conduction-limited and detachment regimes to be addressed by GBS simulations. The later will most likely require the inclusion of impurities, which in turn will call for an extension of the model to include new charged and neutral species, by following a similar approach to the one presented in the present thesis.

A Proof of mass conservation in the formal solution of the neutral kinetic equation

We prove that the formal solution of Eq. (2.47), presented in Eq. (2.51), satisfies the conservation relation

$$\nabla \cdot \Gamma_n = -n_n v_{iz}. \quad (\text{A1})$$

For the sake of simplicity, we consider an infinitely extended domain (no boundary conditions) and plasma related quantities constant. These assumptions lead to an ion velocity distribution constant in space, $\mu_i = \mu_i(\mathbf{v})$, and constant collisional frequencies ($v_{cx}, v_{iz} = \text{const.}$). The extension of the proof to the most general case is straightforward.

We start by noting that the neutral flux in Eq. (A1) is given by $\Gamma_n = \int d^3\mathbf{v} f_n \mathbf{v}_p$ in the poloidal plane (the component of the neutral flux along the toroidal direction is not considered in the $\lambda_{mfp,n} k_{\parallel} \ll 1$ and $|\nabla\psi \times \nabla\varphi| \ll |F(\psi)\nabla\varphi|$ limits studied here). Making use of Eq. (2.48) to express f_n , the neutral flux can be written as

$$\Gamma_n(\mathbf{x}_p) = \int_0^\infty d\nu_p \nu_p \int_0^{2\pi} d\vartheta \int_{-\infty}^\infty d\nu_t \int_0^\infty dr' \frac{R(\mathbf{x}'_p)}{R(\mathbf{x}_p)} S(\mathbf{x}'_p, \mathbf{v}) \exp\left(-\frac{\nu_{\text{eff}}}{\nu_p} r'\right) (\cos\vartheta \mathbf{e}_R + \sin\vartheta \mathbf{e}_Z), \quad (\text{A2})$$

where $S(\mathbf{x}'_p, \mathbf{v}) = n_n(\mathbf{x}'_p) v_{cx} \mu_i(\mathbf{v})$ within the hypothesis made here, and the neutral velocity \mathbf{v}_p is decomposed in (R, Z) coordinates as $\mathbf{v}_p = \nu_p (\cos\vartheta \mathbf{e}_R + \sin\vartheta \mathbf{e}_Z)$.

We remark that the \mathbf{x}_p and \mathbf{x}'_p locations are identified by their (R, Z) coordinates, and they are related by the distance r' and the angle ϑ as

$$R(\mathbf{x}'_p) = R(\mathbf{x}_p) - r' \cos\vartheta \quad (\text{A3})$$

and

Appendix A. Proof of mass conservation in the formal solution of the neutral kinetic equation

$$Z(\mathbf{x}'_p) = Z(\mathbf{x}_p) - r' \sin \vartheta. \quad (\text{A4})$$

Eqs. (A3-A4) can be inverted to obtain the definitions of r' and ϑ as a function of R and Z , that is

$$r'^2 = (R(\mathbf{x}_p) - R'(\mathbf{x}'_p))^2 + (Z(\mathbf{x}_p) - Z'(\mathbf{x}'_p))^2, \quad (\text{A5})$$

$$\cos \vartheta = \frac{R(\mathbf{x}_p) - R'(\mathbf{x}'_p)}{r'}, \quad (\text{A6})$$

and

$$\sin \vartheta = \frac{Z(\mathbf{x}_p) - Z'(\mathbf{x}'_p)}{r'}. \quad (\text{A7})$$

We note that, for a given location \mathbf{x}'_p described by coordinates $(R(\mathbf{x}'_p), Z(\mathbf{x}'_p))$, the location of the neutral particle source \mathbf{x}_p can be described by the variables r' and ϑ , according to Eqs. (A3-A4). Therefore, $(R(\mathbf{x}'_p), Z(\mathbf{x}'_p), r', \vartheta)$ must be regarded as four independent variables that fully describe each pair of source and target points.

We now apply the divergence operator to the neutral flux in Eq. (A2) at the \mathbf{x}_p location. This can be written in (R, Z) coordinates as

$$\nabla \cdot \mathbf{\Gamma}_n(\mathbf{x}_p) = \frac{\partial \Gamma_{n,R}}{\partial R(\mathbf{x}_p)} + \frac{\partial \Gamma_{n,Z}}{\partial Z(\mathbf{x}_p)}. \quad (\text{A8})$$

Since the variables r' and ϑ are independent of $R(\mathbf{x}_p)$ and $Z(\mathbf{x}_p)$, the R, Z -dependence in Eq. (A2) comes exclusively from the source $S(\mathbf{x}'_p, \mathbf{v})$, namely through the neutral density $n_n(\mathbf{x}'_p)$, and from the geometric factor $R(\mathbf{x}'_p)/R(\mathbf{x}_p)$. We then make use of Eqs. (A3) and (A4) and apply the chain rule (at constant r' and ϑ) to write $\partial/\partial R(\mathbf{x}'_p) = \partial/\partial R(\mathbf{x}_p)$ and $\partial/\partial Z(\mathbf{x}'_p) = \partial/\partial Z(\mathbf{x}_p)$. By taking the derivatives with respect to the R, Z coordinates of the source location \mathbf{x}'_p , we obtain

$$\begin{aligned} \nabla \cdot \mathbf{\Gamma}_n(\mathbf{x}_p) = & \int_0^\infty dv_p v_p \int_0^{2\pi} d\vartheta \int_{-\infty}^\infty dv_t \int_0^\infty dr' v_{cx} \mu_i(\mathbf{v}) \\ & \left[\frac{\partial}{\partial R(\mathbf{x}'_p)} \left(\frac{R(\mathbf{x}'_p)}{R(\mathbf{x}_p)} n_n(\mathbf{x}'_p) \right) \cos \vartheta + \frac{\partial}{\partial Z(\mathbf{x}'_p)} \left(\frac{R(\mathbf{x}'_p)}{R(\mathbf{x}_p)} n_n(\mathbf{x}'_p) \right) \sin \vartheta \right] \exp \left(-\frac{v_{\text{eff}}}{v_p} r' \right). \end{aligned} \quad (\text{A9})$$

Since the integrals are performed with respect to r' and ϑ , it is convenient to express the derivatives appearing in Eq. (A9) in terms of these variables. Again, by using the chain rule, we obtain from Eqs. (A5-A7)

$$\frac{\partial n_n}{\partial R(\mathbf{x}'_p)} = \frac{\partial r'}{\partial R(\mathbf{x}'_p)} \frac{\partial n_n}{\partial r'} + \frac{\partial \vartheta}{\partial R(\mathbf{x}'_p)} \frac{\partial n_n}{\partial \vartheta} = -\cos \vartheta \frac{\partial n_n}{\partial r'} + \frac{\sin \vartheta}{r'} \frac{\partial n_n}{\partial \vartheta}, \quad (\text{A10})$$

$$\frac{\partial n_n}{\partial Z(\mathbf{x}'_p)} = \frac{\partial r'}{\partial Z(\mathbf{x}'_p)} \frac{\partial n_n}{\partial r'} + \frac{\partial \vartheta}{\partial Z(\mathbf{x}'_p)} \frac{\partial n_n}{\partial \vartheta} = -\sin \vartheta \frac{\partial n_n}{\partial r'} - \frac{\cos \vartheta}{r'} \frac{\partial n_n}{\partial \vartheta}, \quad (\text{A11})$$

Applying Eqs. (A10) and (A11) into Eq. (A9) yields

$$\nabla \cdot \mathbf{\Gamma}_n(\mathbf{x}_p) = - \int_0^\infty d\nu_p \nu_p \int_0^{2\pi} d\vartheta \int_{-\infty}^\infty d\nu_t \int_0^\infty dr' \nu_{cx} \mu_i(\mathbf{v}) \frac{\partial}{\partial r'} \left(\frac{R(\mathbf{x}'_p)}{R(\mathbf{x}_p)} n_n(\mathbf{x}'_p) \right) \exp \left(-\frac{\nu_{\text{eff}}}{\nu_p} r' \right). \quad (\text{A12})$$

Finally, the integral along r' appearing in Eq. (A12) is computed via integration by parts, yielding

$$\begin{aligned} & \int_0^\infty dr' \frac{\partial}{\partial r'} \left(\frac{R(\mathbf{x}'_p)}{R(\mathbf{x}_p)} n_n(\mathbf{x}'_p) \right) \exp \left(-\frac{\nu_{\text{eff}}}{\nu_p} r' \right) \\ &= -n_n(\mathbf{x}_p) + \int_0^\infty dr' \frac{R(\mathbf{x}'_p)}{R(\mathbf{x}_p)} n_n(\mathbf{x}'_p) \frac{\nu_{\text{eff}}}{\nu_p} \exp \left(-\frac{\nu_{\text{eff}}}{\nu_p} r' \right) \end{aligned} \quad (\text{A13})$$

Using Eq. (A13) to develop Eq. (A12), we can write

$$\begin{aligned} \nabla \cdot \mathbf{\Gamma}_n(\mathbf{x}_p) &= \nu_{cx} n_n(\mathbf{x}_p) \int_0^\infty d\nu_p \nu_p \int_0^{2\pi} d\vartheta \int_{-\infty}^\infty d\nu_t \mu_i(\mathbf{v}) \\ &- \nu_{\text{eff}} \int_0^\infty d\nu_p \nu_p \int_0^{2\pi} d\vartheta \int_{-\infty}^\infty d\nu_{\parallel} \int_0^\infty dr' \frac{R(\mathbf{x}'_p)}{R(\mathbf{x}_p)} \frac{\nu_{cx} n_n(\mathbf{x}'_p) \mu_i(\mathbf{v})}{\nu_p} \exp \left(-\frac{\nu_{\text{eff}}}{\nu_p} r' \right). \end{aligned} \quad (\text{A14})$$

Then, since $\int_0^\infty d\nu_p \nu_p \int_0^{2\pi} d\vartheta \int_{-\infty}^\infty d\nu_t \mu_i(\mathbf{v}) = 1$, the first term on the right-hand side of Eq. (A14) yields simply $\nu_{cx} n_n(\mathbf{x}_p)$. For the second term, one recognises the neutral density at the \mathbf{x}_p location as given by Eq. (2.51). Therefore,

$$\nabla \cdot \mathbf{\Gamma}_n(\mathbf{x}_p) = \nu_{cx} n_n(\mathbf{x}_p) - \nu_{\text{eff}} n_n(\mathbf{x}_p). \quad (\text{A15})$$

Since $\nu_{\text{eff}} = \nu_{cx} + \nu_{iz}$, Eq. (A1) is recovered.

B Evaluation of the average electron energy loss and reaction product energies in collisional processes

The Franck-Condon principle [114, 115] states that electronic excitation occurs over a timescale considerably shorter than the characteristic timescale associated with vibration or dissociation of the diatomic species. In turn, the vibration or dissociation timescales are much shorter than the electron deexcitation timescale. As a result, when an electron impacts a D_2 molecule or a D_2^+ ion, an electronic excitation is observed with no significant change in the inter-atomic distance (vertical transition). If the excited state is not stable, the molecule dissociates before deexcitation takes place. In this case, the difference between the excitation energy and the dissociation energy is converted into kinetic energy of the products (ionization and dissociative energies are discussed in [116]). We note that the exact energies of the products of dissociation reactions depend on the vibrational level of the D_2 molecule or D_2^+ ion. Considering the excitation of a D_2 molecule in a given initial state, the set of vibrational levels accessible for the molecule in the final state are the ones lying within the region of the potential energy surface accessed by that particular vertical transition, known as the Franck-Condon region. The mean energy of the reaction products is thus the average over the Franck-Condon region, taking into account all accessible vibrational states.

In the present thesis, we model the products of dissociative reactions by considering that they are reemitted isotropically in the reference frame of the incoming massive particle (D_2 or D_2^+), thus approximating their velocity distribution as a Maxwellian centered at the velocity of the incoming D_2 or D_2^+ . The temperature of the Maxwellian, together with the average electron energy loss for each process, are obtained from the values presented in [85]. Since these energies depend on the intermediate excited state of the D_2 or D_2^+ particle, different values are found for different channels within the same dissociative process. This requires that an average is performed over all possible excited states, taking into account the respective cross section of each process. We present these calculations in detail for each process, following [85].

The energy loss and the energy of the reaction products may depend on the electronic levels (n) and sub-levels (l) of the reaction products, on the molecular orbital (MO) of the intermediate state, if bonding or antibonding, and on the energy of the incident electron. The energy

Appendix B. Evaluation of the average electron energy loss and reaction product energies in collisional processes

values are experimentally determined for all relevant dissociation channels. These quantities are then averaged over all vibrational states ν of the D_2 molecules or D_2^+ ion and over the Franck-Condon region, from [85].

We start by considering the dissociation of D_2 molecules, i.e.



For this reaction, the values of the electron energy loss, $\langle \Delta E_e \rangle$, and reaction product energies, $\langle E_D \rangle$, depend significantly on the electronic state of the products. Hence, considering that there are $i = 1, \dots, N$ electronic states of the reaction products and, associated, N different sub-processes contributing to the dissociation of D_2 , the average electron energy loss $\langle \Delta E_e \rangle$ is obtained by performing a weighed average of $\langle \Delta E_e \rangle_i$, the energy loss for the sub-process i , based on the $\langle \sigma \nu \rangle_i$ reaction rate, yielding

$$\langle \Delta E_e \rangle = \frac{\sum_{i=1}^N [\langle \sigma \nu \rangle_i \langle \Delta E_e \rangle_i]}{\sum_{i=1}^N [\langle \sigma \nu \rangle_i]}, \quad (B.2)$$

For simplicity, we evaluate all quantities at the reference temperature, $T_e = 20\text{eV}$. Similarly, the average value for the energy of the reaction products is obtained as

$$\langle E_D \rangle = \frac{\sum_{i=1}^N [\langle \sigma \nu \rangle_i \langle E_D \rangle_i]}{\sum_{i=1}^N [\langle \sigma \nu \rangle_i]}, \quad (B.3)$$

with $\langle E_D \rangle_i$ the average energy of the products for the sub-process i .

The values of $\langle \sigma \nu \rangle_i$, $\langle \Delta E_e \rangle_i$, $\langle E_D \rangle_i$ are presented in Table B.1 for all sub-processes. The additional information between brackets refers to the minimum and maximum of the range of energies accessible to $\langle \Delta E_e \rangle_i$ and $\langle E_D \rangle_i$, following the values listed in [85]. We highlight that $D(1s)$ denotes a D atom in the fundamental state (electron at the lowest orbital $1s$), while $D^*(2s)$ and $D^*(2p)$ denote an atom in the excited state $n = 2$ with the electron in an orbital of type s or p , respectively, and $D^*(n = 3)$ represents an atom in the excited state $n = 3$. Following [85], we assume that the energy is equally distributed over the reaction products, regardless of the fact that their electronic states are the same. Based on the values in Table B.1, from Eqs. (B.2) and (B.3), we obtain $\langle \Delta E_e \rangle \simeq 14.3\text{eV}$ and $\langle E_D \rangle \simeq 1.95\text{eV}$, respectively, at $T_e = 20\text{eV}$. These are the values mentioned in Table 3.2.

Focusing now on the dissociative-ionization of D_2 ,

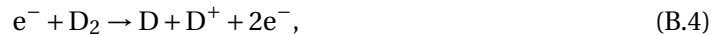


Table B.1: $\langle \sigma \nu_e \rangle$ product, average electron energy loss and average energy of reaction products for each sub-process of D_2 dissociation.

| Reaction | $\langle \sigma \nu_e \rangle_i$ | $\langle \Delta E_e \rangle_i$ | $\langle E_D \rangle_i$ |
|---|--|--------------------------------|-------------------------|
| $e^- + D_2 \rightarrow e^- + D(1s) + D(1s)$ | $3.8 \times 10^{-9} \text{cm}^3/\text{s}$ | 10.5eV | 3eV |
| $e^- + D_2 \rightarrow e^- + D(1s) + D^*(2s)$ | $5.3 \times 10^{-9} \text{cm}^3/\text{s}$ | 15.3eV | 0.3eV |
| $e^- + D_2 \rightarrow e^- + D^*(2p) + D^*(2s)$ | $9.2 \times 10^{-10} \text{cm}^3/\text{s}$ | 34.6eV | 4.85eV |
| $e^- + D_2 \rightarrow e^- + D(1s) + D^*(n=3)$ | $5.7 \times 10^{-10} \text{cm}^3/\text{s}$ | 21.5eV | 5.7eV |

we consider three cases. If the incoming electron has an energy $E_e < E_{\text{th(g)}}$, with $E_{\text{th(g)}} = 18\text{eV}$, no dissociation takes place. If $E_{\text{th(g)}} < E_e < E_{\text{th(u)}}$, with $E_{\text{th(u)}} = 26\text{eV}$, the electron can ionize the molecule, resulting in an unstable D_2^+ ion, which then dissociates into a D atom and a D^+ ion. The short-lived D_2^+ has the electron in a bonding molecular orbital (MO) with σ -symmetry, thus exhibiting *gerade* (g) symmetry (German for even) state, denoted as $D_2^+(\Sigma_g)$. If $E_e > E_{\text{th(u)}}$, the intermediate D_2^+ ion has the electron in a higher-energy antibonding MO with σ -symmetry, which exhibits *ungerade* (u) symmetry (German for odd), thus denoted as $D_2^+(\Sigma_u)$. As a result of the different energy levels of the intermediate D_2^+ ion, the energy of the final products will also be different, as well as the average electron energy loss. According to the results presented in [85], these energies still depend on the energy of the incoming electron within each sub-process. To simplify the evaluation of the $\langle \Delta E_e \rangle$ and the energy of the products, we consider the energy to be evenly distributed by the reaction products (D and D^+) and we consider the two cases separately. For $E_{\text{th(g)}} < E_e < E_{\text{th(u)}}$, all dissociative-ionization events originate an intermediate state $D_2^+(\Sigma_g)$, while for $E_e > E_{\text{th(u)}}$ all events generate an intermediate state $D_2^+(\Sigma_u)$. The values for the electron energy loss and reaction product energies being considered for each case are evaluated for [85] and listed in Table B.2. We note that this is just an approximation, as even with $T_e < E_{\text{th(u)}}$ there are electrons with energies superior to the threshold that will generate a D_2^+ ion in a $D_2^+(\Sigma_u)$ state, and vice-versa. Nevertheless, this approximation avoids us to evaluate $\langle \Delta E_e \rangle$ and $\langle E_D \rangle$ at every single value of T_e .

For the dissociation of D_2^+ , i.e.



different sub-processes are taken into account, following an approach similar to the one

Table B.2: Average electron energy loss and average energy of reaction products for the two cases of dissociative-ionization of D_2 .

| Reaction | $\langle \Delta E_e \rangle$ | $\langle E_D \rangle = \langle E_{D^+} \rangle$ |
|--|------------------------------|---|
| $e^- + D_2 \rightarrow e^- + [D_2^+(\Sigma_g) + e^-] \rightarrow D + D^+ + 2e^-$ | 18.25eV | 0.25eV |
| $e^- + D_2 \rightarrow e^- + [D_2^+(\Sigma_u) + e^-] \rightarrow D + D^+ + 2e^-$ | 33.6eV | 7.8eV |

Appendix B. Evaluation of the average electron energy loss and reaction product energies in collisional processes

| Reaction | $\langle \sigma \nu_e \rangle_i$ | $\langle \Delta E_e \rangle_i$ | $\langle E_D \rangle = \langle E_{D^+} \rangle_i$ |
|--|--|--------------------------------|---|
| $e^- + D_2^+ \rightarrow D^+ + D(1s) + e^-$ | $1.2 \times 10^{-7} \text{ cm}^3/\text{s}$ | 10.5eV | 4.3eV |
| $e^- + D_2^+ \rightarrow D^+ + D^*(n=2) + e^-$ | $1.0 \times 10^{-7} \text{ cm}^3/\text{s}$ | 17.5eV | 1.5eV |

Table B.3: $\langle \sigma \nu_e \rangle$ product, average electron energy loss and average energy of reaction products for each sub-process of D_2^+ dissociation.

adopted to treat the dissociation of D_2 . We perform a weighed average of the electron energy loss and the reaction products energy by using Eqs. (B.2) and (B.3), respectively. The values of $\langle \sigma \nu_e \rangle_i$, $\langle \Delta E_e \rangle_i$ and $\langle E_D \rangle = \langle E_{D^+} \rangle_i$ for each sub-process are presented in Table B.3. The weighed averaged values for the electron energy loss and reaction products energy at the reference temperature, $T_e = 20\text{eV}$, yield $\langle \Delta E_e \rangle = 13.7\text{eV}$ and $\langle E_D \rangle = \langle E_{D^+} \rangle = 3.0\text{eV}$, as listed in Table B.3.

Regarding the dissociative-ionization of D_2^+ , i.e.



we follow [85], where the average energy of the resulting D^+ ions is obtained from an average performed over all vibrational states ($\nu = 0 - 9$) of the D_2^+ ion and over the Franck-Condon region. This yields $\langle E_{D^+} \rangle = 0.4\text{eV}$, while the average electron energy loss is $\langle \Delta E_e \rangle = 15.5\text{eV}$.

We finally focus on the dissociative-recombination of D_2^+ , which generates a D atom in the fundamental state (electron in orbital 1s) and a D atom in an excited state (electron with principal quantum number $n \geq 2$), i.e.



We assume that the energy of the products is evenly distributed among the two D atoms and is given by

$$\langle E_{D(1s)} \rangle \simeq \langle E_{D^*(n \geq 2)} \rangle \simeq \frac{1}{2} \left(E_e + \frac{\text{Ry}}{n^2} \right), \quad (\text{B.8})$$

with $\text{Ry} = 13.6\text{eV}$ the Rydberg unit of energy (corresponding to the electron binding energy in a hydrogen atom in the fundamental state). Since this expression depends on the energy of the incoming electron, E_e , and the electronic level n of the excited atom, D^* , we assume an energy of the incident electron of $E_e \simeq 20\text{eV}$, the typical value in the region around the LCFS at the HFS, and consider that these atoms are most likely in the accessible state of lowest energy $n = 2$ (considering a higher excited state would not change the value of the energy of the products by a significant amount). Under these assumptions, we get $\langle E_{D(1s)} \rangle \simeq \langle E_{D^*(n \geq 2)} \rangle \simeq 11.7\text{eV}$.

C Zhdanov collisional closure

We focus on the derivation of the parallel friction forces and the parallel heat fluxes, denoted respectively by $R_{\parallel\alpha} = \mathbf{R}_\alpha \cdot \mathbf{b}$ and $q_{\parallel\alpha} = \mathbf{q}_\alpha \cdot \mathbf{b}$ for a given species α , with $\mathbf{R}_\alpha = \int m_\alpha \mathbf{v}' C_\alpha d\mathbf{v}$ and $\mathbf{q}_\alpha = \int (m_\alpha v'^2)/2 \mathbf{v}' f_\alpha d\mathbf{v}$, where we introduce the thermal component of the velocity, $\mathbf{v}' = \mathbf{v} - \mathbf{v}_\alpha$, with $\mathbf{v}_\alpha = \int \mathbf{v} f_\alpha d\mathbf{v}$ the fluid velocity of the α species, and the collision operator $C_\alpha = \sum_\beta C_{\alpha\beta}(f_\alpha, f_\beta)$, with $C_{\alpha\beta}$ describing collisions of species α with species β . We consider the collisional closure derived by Zhdanov in [65], relying on the approach proposed in [66] and discussed in [93] for its numerical implementation.

Following [65], the parallel component of the friction forces and heat fluxes of the species α is related to the parallel gradients of the temperature and parallel velocity of all species through

$$\begin{bmatrix} q_{\parallel\alpha} \\ R_{\parallel\alpha} \end{bmatrix} = \sum_\beta Z_{\alpha\beta} \begin{bmatrix} \nabla_{\parallel} T_\beta \\ w_{\parallel\beta} \end{bmatrix}, \quad (\text{C.1})$$

where T_β denotes the temperature of plasma species β and $w_{\parallel\beta}$ is the parallel component of the fluid velocity of species β with respect to the center of mass of the plasma, $\mathbf{w}_\beta = \mathbf{v}_\beta - \mathbf{v}_{\text{CM}}$, with $\mathbf{v}_{\text{CM}} = (\sum_\beta n_\beta m_\beta \mathbf{v}_\beta) / (\sum_\beta n_\beta m_\beta)$. The matrix $Z_{\alpha\beta}$ relates the parallel heat fluxes and friction forces with the parallel gradients of temperature and parallel velocity. We remark that Eq. (C.1) simplifies the general result obtained by Zhdanov [65] to the case of singly-ionized states, neglecting possible multiplicity of charge states for the chemical species present in the plasma.

In order to compute the matrix $Z_{\alpha\beta}$, we consider the $21N$ -moment approximation of the distribution function [65], thus including the moments up to the fifth order moment. We first express \mathbf{R}_α and \mathbf{q}_α in terms of these moments of the distribution function, namely the first order moment, \mathbf{w}_α , the third order moment, $\mathbf{h}_\alpha = q_{\parallel\alpha}$, and the fifth order moment, $\mathbf{r}_\alpha = m_\alpha/4 \int (c^4 - 14c^2/\gamma_\alpha + 35\gamma_\alpha) \mathbf{c} f_\alpha d\mathbf{c}$, where we introduce the velocity with respect to the center of mass of the plasma, $\mathbf{c} = \mathbf{v} - \mathbf{v}_{\text{CM}}$, and the parameter $\gamma_\alpha = m_\alpha/(kT_\alpha)$, with $T_\alpha = \int (m_\alpha v'^2/2) f_\alpha d\mathbf{v}$. Since only the expressions for the parallel component of the friction

Appendix C. Zhdanov collisional closure

forces and heat fluxes are needed, we consider only the parallel component of these equations. The heat flux, $q_{\parallel\alpha}$, simply corresponds to the third order moment, $h_{\parallel\alpha}$, while the friction forces, $R_{\parallel\alpha}$, are obtained in terms of $w_{\parallel\alpha}$, $h_{\parallel\alpha}$ and $r_{\parallel\alpha}$ [117], yielding

$$q_{\parallel\alpha} = h_{\parallel\alpha}, \quad (\text{C.2})$$

$$R_{\parallel\alpha} = \sum_{\beta} \left[G_{\alpha\beta}^{(1)} (w_{\parallel\alpha} - w_{\parallel\beta}) + \frac{\mu_{\alpha\beta}}{kT} G_{\alpha\beta}^{(2)} \left(\frac{h_{\parallel\alpha}}{m_{\alpha} n_{\alpha}} - \frac{h_{\parallel\beta}}{m_{\beta} n_{\beta}} \right) + \left(\frac{\mu_{\alpha\beta}}{kT} \right)^2 G_{\alpha\beta}^{(8)} \left(\frac{r_{\alpha}}{m_{\alpha} n_{\alpha}} - \frac{r_{\beta}}{m_{\beta} n_{\beta}} \right) \right]. \quad (\text{C.3})$$

where m_{α} and n_{α} are respectively the mass and density of species α , $\mu_{\alpha\beta} = (m_{\alpha} m_{\beta}) / (m_{\alpha} + m_{\beta})$ is the reduced mass, and $G_{\alpha\beta}^{(n)}$ are polynomial functions of the local plasma density and temperature, their exact expressions being presented in [65] (chapter 8.1, pp. 163-164). Eqs. (C.2) and (C.3) can then be written in matrix form as

$$\begin{bmatrix} q_{\parallel\alpha} \\ R_{\parallel\alpha} \end{bmatrix} = \sum_{\beta} A_{\alpha\beta} \begin{bmatrix} h_{\parallel\beta} \\ r_{\parallel\beta} \end{bmatrix} + \sum_{\beta} B_{\alpha\beta} \begin{bmatrix} \nabla_{\parallel} T_{\beta} \\ w_{\parallel\beta} \end{bmatrix}, \quad (\text{C.4})$$

where the matrices A and B are defined to satisfy Eqs. (C.2) and (C.3). We now aim at expressing the moments \mathbf{h}_{α} and ∇r_{α} in terms of \mathbf{w}_{α} and ∇T_{α} . This can be achieved by solving a system of moment equations similar to the one presented in [65] (chapter 8.1, pp. 162-163), including the time evolution of the moments (\mathbf{w}_{α} , \mathbf{h}_{α} and ∇r_{α}) and the time evolution of basic thermodynamic variables (ρ , \mathbf{v}_{CM} and T). We neglect time derivatives and nonlinear terms. For simplicity, we also assume that, for two massive particle species D^+ and D_2^+ , the condition $|T_{D_2^+} - T_{D^+}| \ll T_{D_2^+}$ is fulfilled, which allows us to write $T_{D_2^+} = T_{D^+} = T$. Moreover, as long as $T_e / T_{D^+} \gg m_e / m_{D^+}$ is verified, T can also be replaced by T_e , following [65] (the simulation results shown in Fig. 3.3 meet these conditions). We therefore impose $T_{D_2^+} = T_{D^+} = T_e = T$, while no assumption is made on the temperature and pressure gradients, i.e. temperature gradients can be different from species to species [65].

The parallel projection of the system of moment equations can then be written as (see [117])

$$\begin{aligned} \frac{5}{2} n_{\parallel\alpha} k \nabla T_{\alpha} = \sum_{\beta} \left[\frac{5}{2} \frac{\mu_{\alpha\beta}}{m_{\alpha}} G_{\alpha\beta}^{(2)} (w_{\parallel\alpha} - w_{\parallel\beta}) + G_{\alpha\beta}^{(5)} \frac{h_{\parallel\alpha}}{p_{\alpha}} \right. \\ \left. + G_{\alpha\beta}^{(6)} \frac{h_{\parallel\beta}}{p_{\beta}} + \frac{\mu_{\alpha\beta}}{kT} \left(G_{\alpha\beta}^{(9)} \frac{r_{\parallel\alpha}}{p_{\alpha}} + G_{\alpha\beta}^{(10)} \frac{r_{\parallel\beta}}{p_{\beta}} \right) \right], \end{aligned} \quad (\text{C.5})$$

$$0 = \sum_{\beta} \left[\frac{35}{2} \left(\frac{\mu_{\alpha\beta}}{m_{\alpha}} \right)^2 G_{\alpha\beta}^{(8)} (w_{\parallel\alpha} - w_{\parallel\beta}) + 7 \frac{\mu_{\alpha\beta}}{m_{\alpha}} \left(G_{\alpha\beta}^{(9)} \frac{h_{\parallel\alpha}}{p_{\alpha}} + G_{\alpha\beta}^{(10)} \frac{h_{\parallel\beta}}{p_{\beta}} \right) + \frac{m_{\alpha}}{kT} G_{\alpha\beta}^{(11)} \frac{r_{\parallel\alpha}}{p_{\alpha}} + \frac{m_{\beta}}{kT} G_{\alpha\beta}^{(12)} \frac{r_{\parallel\beta}}{p_{\beta}} \right], \quad (\text{C.6})$$

where p_{α} is the pressure of species α . Rewriting Eqs. (C.5-C.6) in matrix form, one obtains

$$\sum_{\gamma} P_{\alpha\gamma} \begin{bmatrix} \nabla_{\parallel} T_{\gamma} \\ w_{\parallel\gamma} \end{bmatrix} = \sum_{\beta} M_{\alpha\beta} \begin{bmatrix} h_{\parallel\beta} \\ r_{\parallel\beta} \end{bmatrix}, \quad (\text{C.7})$$

which can be inverted to express the parallel third and fourth order fluid moments in terms of the parallel gradient of temperature and relative parallel velocity as

$$\begin{bmatrix} h_{\parallel\beta} \\ r_{\parallel\beta} \end{bmatrix} = \sum_{\alpha} \sum_{\gamma} M_{\alpha\beta}^{-1} P_{\alpha\gamma} \begin{bmatrix} \nabla_{\parallel} T_{\gamma} \\ w_{\parallel\gamma} \end{bmatrix}. \quad (\text{C.8})$$

Finally, making use of Eq. (C.8) to express $h_{\parallel\alpha}$ and $r_{\parallel\alpha}$ in Eq. (C.4) in terms of the parallel temperature gradients and relative velocities, one obtains the expressions for the parallel heat flux and friction forces in the matrix form presented in Eq. (C.1), that is

$$\begin{bmatrix} q_{\parallel\alpha} \\ R_{\parallel\alpha} \end{bmatrix} = \left(A_{\alpha\lambda} M_{\gamma\lambda}^{-1} P_{\gamma\beta} + B_{\alpha\beta} \right) \begin{bmatrix} \nabla_{\parallel} T_{\beta} \\ w_{\parallel\beta} \end{bmatrix}. \quad (\text{C.9})$$

Since the matrices A , B , P and M are fully determined by Eqs. (C.2), (C.3), (C.5) and (C.6), the expressions of the parallel heat flux and friction forces can be found. Following Zhdanov [65], these matrices can be expressed in terms of the local values of plasma quantities, namely densities n_e , n_{D^+} and $n_{D_2^+}$ and temperatures T_e and T_{D^+} (we again assume $T_{D_2^+} = T_{D^+}$, mass ratios and characteristic time scales τ_{eD} and τ_{DD} , with τ_{eD} defined as the inverse of the collision frequency for momentum transfer between electrons and D^+ ions, and τ_{DD} the ion timescale defined as the inverse of the collision frequency for momentum transfer between D^+ ions. We retain only terms of leading order in $\sqrt{m_e/m_D}$, while terms proportional to the fast electron timescale τ_{eD} are neglected when compared to terms proportional to τ_{DD} , which considerably simplifies the final expressions. We also highlight that, besides imposing the quasi-neutrality relation $n_e = n_{D^+} + n_{D_2^+}$, we take into account the fact that the density of the molecular ion species is much smaller than the density of the main ion species D^+ for typical tokamak boundary conditions, i.e. $n_{D_2^+}/n_{D^+} \ll 1$, keeping therefore only leading order terms in $n_{D_2^+}/n_{D^+}$. As a result, the friction forces between molecular ions and other species are neglected, as well as molecular ion temperature gradient terms, while friction and thermal force contributions involving D^+ and e^- species are kept in the expressions of the parallel components of the heat fluxes and friction forces. The expressions obtained for the friction

Appendix C. Zhdanov collisional closure

forces and heat fluxes finally yield

$$\begin{aligned}
q_{\parallel e} &= -\frac{3.16n_e T_e \tau_{eD}}{m_e} \nabla_{\parallel} T_e + 0.71n_e T_e (v_{\parallel e} - v_{\parallel D^+}), \\
q_{\parallel D^+} &= -\frac{4.52n_e T_{D^+} \tau_{DD}}{m_D} \nabla_{\parallel} T_{D^+}, \\
q_{\parallel D_2^+} &= -\frac{1.80n_e T_{D^+} \tau_{DD}}{m_D} \nabla_{\parallel} T_{D^+}, \\
R_{\parallel e} &= -0.71n_e \nabla_{\parallel} T_e - \frac{0.51m_e n_e}{\tau_{eD}} (v_{\parallel e} - v_{\parallel D^+}), \\
R_{\parallel D^+} &= 0.71n_e \nabla_{\parallel} T_e - \frac{0.51m_e n_e}{\tau_{eD}} (v_{\parallel D^+} - v_{\parallel e}), \\
R_{\parallel D_2^+} &= 0,
\end{aligned} \tag{C.10}$$

The expressions in Eqs. (C.10) can be simplified by applying the relation between the electron and ion characteristic times,

$$\frac{\tau_{DD}}{\tau_{eD}} = \frac{1}{\sqrt{2}} \sqrt{\frac{m_D}{m_e}} \left(\frac{T_e}{T_{D^+}} \right) \sim \frac{1}{\sqrt{2}} \sqrt{\frac{m_D}{m_e}}, \tag{C.11}$$

having again assumed $T_{D^+} \sim T_e$. This enables one to write τ_{DD} appearing in Eq. (C.10) in terms of τ_{eD} . Following Braginskii's approach [17] and considering that the electron characteristic time is $\tau_e = \tau_{eD}$, we then write Eqs. (C.10) in terms of the resistivity, defined as [33, 34]

$$\nu = 0.51 \frac{m_e}{m_D} \frac{R_0}{c_{s0}} \frac{1}{n_e \tau_{eD}}, \tag{C.12}$$

The parallel friction forces and heat fluxes, as they appear in Eqs. (3.22-3.24) and Eqs. (3.25-3.27), respectively, are therefore written in normalized units as

$$\begin{aligned}
R_{\parallel e} &= -0.71n_e \nabla_{\parallel} T_e - \nu n_e (v_{\parallel e} - v_{\parallel D^+}), \\
R_{\parallel D^+} &= 0.71n_e \nabla_{\parallel} T_e - \nu n_e (v_{\parallel D^+} - v_{\parallel e}), \\
R_{\parallel D_2^+} &= 0, \\
q_{\parallel e} &= -\frac{1.62}{\nu} n_e T_e \nabla_{\parallel} T_e + 0.71n_e T_e (v_{\parallel e} - v_{\parallel D^+}), \\
q_{\parallel D^+} &= -\frac{2.32}{\sqrt{2}\nu} \sqrt{\frac{m_e}{m_D}} n_e T_{D^+} \nabla_{\parallel} T_{D^+}, \\
q_{\parallel D_2^+} &= -\frac{0.92}{\sqrt{2}\nu} \sqrt{\frac{m_e}{m_D}} n_e T_{D^+} \nabla_{\parallel} T_{D^+}.
\end{aligned} \tag{C.13}$$

We note that, similarly to the single-ion species model implemented in GBS [33], the ohmic

heating terms are neglected.

D List of kernel functions

The kernels used in Eqs. (3.80-3.83) for n_{D_2} , Γ_{out,D_2} , n_D and Γ_D are defined as

$$K_{p \rightarrow p}^{D_2, D_2^+}(\mathbf{x}_\perp, \mathbf{x}'_\perp) = K_{p \rightarrow p, \text{dir}}^{D_2, D_2^+}(\mathbf{x}_\perp, \mathbf{x}'_\perp) + \alpha_{\text{refl}} K_{p \rightarrow p, \text{refl}}^{D_2, D_2^+}(\mathbf{x}_\perp, \mathbf{x}'_\perp), \quad (\text{D.1})$$

$$K_{b \rightarrow p}^{D_2, \text{reem}}(\mathbf{x}_\perp, \mathbf{x}'_{\perp b}) = K_{b \rightarrow p, \text{dir}}^{D_2, \text{reem}}(\mathbf{x}_\perp, \mathbf{x}'_{\perp b}) + \alpha_{\text{refl}} K_{b \rightarrow p, \text{refl}}^{D_2, \text{reem}}(\mathbf{x}_\perp, \mathbf{x}'_{\perp b}), \quad (\text{D.2})$$

$$K_{b \rightarrow p}^{D_2, \text{refl}}(\mathbf{x}_\perp, \mathbf{x}'_{\perp b}) = K_{b \rightarrow p, \text{dir}}^{D_2, \text{refl}}(\mathbf{x}_\perp, \mathbf{x}'_{\perp b}) + \alpha_{\text{refl}} K_{b \rightarrow p, \text{refl}}^{D_2, \text{refl}}(\mathbf{x}_\perp, \mathbf{x}'_{\perp b}), \quad (\text{D.3})$$

$$K_{p \rightarrow b}^{D_2, D_2^+}(\mathbf{x}_{\perp b}, \mathbf{x}'_\perp) = K_{p \rightarrow b, \text{dir}}^{D_2, D_2^+}(\mathbf{x}_{\perp b}, \mathbf{x}'_\perp) + \alpha_{\text{refl}} K_{p \rightarrow b, \text{refl}}^{D_2, D_2^+}(\mathbf{x}_{\perp b}, \mathbf{x}'_\perp), \quad (\text{D.4})$$

$$K_{b \rightarrow b}^{D_2, \text{reem}}(\mathbf{x}_{\perp b}, \mathbf{x}'_{\perp b}) = K_{b \rightarrow b, \text{dir}}^{D_2, \text{reem}}(\mathbf{x}_{\perp b}, \mathbf{x}'_{\perp b}) + \alpha_{\text{refl}} K_{b \rightarrow b, \text{refl}}^{D_2, \text{reem}}(\mathbf{x}_{\perp b}, \mathbf{x}'_{\perp b}), \quad (\text{D.5})$$

$$K_{b \rightarrow b}^{D_2, \text{refl}}(\mathbf{x}_{\perp b}, \mathbf{x}'_{\perp b}) = K_{b \rightarrow b, \text{dir}}^{D_2, \text{refl}}(\mathbf{x}_{\perp b}, \mathbf{x}'_{\perp b}) + \alpha_{\text{refl}} K_{b \rightarrow b, \text{refl}}^{D_2, \text{refl}}(\mathbf{x}_{\perp b}, \mathbf{x}'_{\perp b}), \quad (\text{D.6})$$

Appendix D. List of kernel functions

$$K_{p \rightarrow p}^{\text{D}, \text{D}^+}(\mathbf{x}_\perp, \mathbf{x}'_\perp) = K_{p \rightarrow p, \text{dir}}^{\text{D}, \text{D}^+}(\mathbf{x}_\perp, \mathbf{x}'_\perp) + \alpha_{\text{refl}} K_{p \rightarrow p, \text{refl}}^{\text{D}, \text{D}^+}(\mathbf{x}_\perp, \mathbf{x}'_\perp), \quad (\text{D.7})$$

$$K_{p \rightarrow p}^{\text{D}, \text{D}_2^+}(\mathbf{x}_\perp, \mathbf{x}'_\perp) = K_{p \rightarrow p, \text{dir}}^{\text{D}, \text{D}_2^+}(\mathbf{x}_\perp, \mathbf{x}'_\perp) + \alpha_{\text{refl}} K_{p \rightarrow p, \text{refl}}^{\text{D}, \text{D}_2^+}(\mathbf{x}_\perp, \mathbf{x}'_\perp), \quad (\text{D.8})$$

$$K_{p \rightarrow p}^{\text{D}, \text{diss}(\text{D}_2^+)}(\mathbf{x}_\perp, \mathbf{x}'_\perp) = K_{b \rightarrow b, \text{dir}}^{\text{D}, \text{reem}}(\mathbf{x}_{\perp b}, \mathbf{x}'_{\perp b}) + \alpha_{\text{refl}} K_{b \rightarrow b, \text{refl}}^{\text{D}, \text{reem}}(\mathbf{x}_{\perp b}, \mathbf{x}'_{\perp b}), \quad (\text{D.9})$$

$$K_{p \rightarrow p}^{\text{D}, \text{diss-rec}(\text{D}_2^+)}(\mathbf{x}_\perp, \mathbf{x}'_\perp) = K_{b \rightarrow b, \text{dir}}^{\text{D}, \text{reem}}(\mathbf{x}_{\perp b}, \mathbf{x}'_{\perp b}) + \alpha_{\text{refl}} K_{b \rightarrow b, \text{refl}}^{\text{D}, \text{reem}}(\mathbf{x}_{\perp b}, \mathbf{x}'_{\perp b}), \quad (\text{D.10})$$

$$K_{p \rightarrow p}^{\text{D}, \text{diss}(\text{D}_2)}(\mathbf{x}_\perp, \mathbf{x}'_\perp) = K_{b \rightarrow b, \text{dir}}^{\text{D}, \text{reem}}(\mathbf{x}_{\perp b}, \mathbf{x}'_{\perp b}) + \alpha_{\text{refl}} K_{b \rightarrow b, \text{refl}}^{\text{D}, \text{reem}}(\mathbf{x}_{\perp b}, \mathbf{x}'_{\perp b}), \quad (\text{D.11})$$

$$K_{p \rightarrow p}^{\text{D}, \text{diss-iz}(\text{D}_2)}(\mathbf{x}_\perp, \mathbf{x}'_\perp) = K_{b \rightarrow b, \text{dir}}^{\text{D}, \text{reem}}(\mathbf{x}_{\perp b}, \mathbf{x}'_{\perp b}) + \alpha_{\text{refl}} K_{b \rightarrow b, \text{refl}}^{\text{D}, \text{reem}}(\mathbf{x}_{\perp b}, \mathbf{x}'_{\perp b}), \quad (\text{D.12})$$

$$K_{b \rightarrow p}^{\text{D}, \text{reem}}(\mathbf{x}_\perp, \mathbf{x}'_{\perp b}) = K_{b \rightarrow b, \text{dir}}^{\text{D}, \text{reem}}(\mathbf{x}_{\perp b}, \mathbf{x}'_{\perp b}) + \alpha_{\text{refl}} K_{b \rightarrow b, \text{refl}}^{\text{D}, \text{reem}}(\mathbf{x}_{\perp b}, \mathbf{x}'_{\perp b}), \quad (\text{D.13})$$

$$K_{b \rightarrow p}^{\text{D}, \text{refl}}(\mathbf{x}_\perp, \mathbf{x}'_{\perp b}) = K_{b \rightarrow b, \text{dir}}^{\text{D}, \text{reem}}(\mathbf{x}_{\perp b}, \mathbf{x}'_{\perp b}) + \alpha_{\text{refl}} K_{b \rightarrow b, \text{refl}}^{\text{D}, \text{reem}}(\mathbf{x}_{\perp b}, \mathbf{x}'_{\perp b}), \quad (\text{D.14})$$

$$K_{p \rightarrow b}^{\text{D}, \text{D}^+}(\mathbf{x}_{\perp b}, \mathbf{x}'_\perp) = K_{b \rightarrow b, \text{dir}}^{\text{D}, \text{reem}}(\mathbf{x}_{\perp b}, \mathbf{x}'_{\perp b}) + \alpha_{\text{refl}} K_{b \rightarrow b, \text{refl}}^{\text{D}, \text{reem}}(\mathbf{x}_{\perp b}, \mathbf{x}'_{\perp b}), \quad (\text{D.15})$$

$$K_{p \rightarrow b}^{\text{D}, \text{D}_2^+}(\mathbf{x}_{\perp b}, \mathbf{x}'_\perp) = K_{b \rightarrow b, \text{dir}}^{\text{D}, \text{reem}}(\mathbf{x}_{\perp b}, \mathbf{x}'_{\perp b}) + \alpha_{\text{refl}} K_{b \rightarrow b, \text{refl}}^{\text{D}, \text{reem}}(\mathbf{x}_{\perp b}, \mathbf{x}'_{\perp b}), \quad (\text{D.16})$$

$$K_{p \rightarrow b}^{\text{D,diss}(\text{D}_2^+)}(\mathbf{x}_{\perp b}, \mathbf{x}'_{\perp}) = K_{b \rightarrow b, \text{dir}}^{\text{D, reem}}(\mathbf{x}_{\perp b}, \mathbf{x}'_{\perp b}) + \alpha_{\text{refl}} K_{b \rightarrow b, \text{refl}}^{\text{D, reem}}(\mathbf{x}_{\perp b}, \mathbf{x}'_{\perp b}), \quad (\text{D.17})$$

$$K_{p \rightarrow b}^{\text{D,diss-rec}(\text{D}_2^+)}(\mathbf{x}_{\perp b}, \mathbf{x}'_{\perp}) = K_{b \rightarrow b, \text{dir}}^{\text{D, reem}}(\mathbf{x}_{\perp b}, \mathbf{x}'_{\perp b}) + \alpha_{\text{refl}} K_{b \rightarrow b, \text{refl}}^{\text{D, reem}}(\mathbf{x}_{\perp b}, \mathbf{x}'_{\perp b}), \quad (\text{D.18})$$

$$K_{p \rightarrow b}^{\text{D,diss}(\text{D}_2)}(\mathbf{x}_{\perp b}, \mathbf{x}'_{\perp}) = K_{b \rightarrow b, \text{dir}}^{\text{D, reem}}(\mathbf{x}_{\perp b}, \mathbf{x}'_{\perp b}) + \alpha_{\text{refl}} K_{b \rightarrow b, \text{refl}}^{\text{D, reem}}(\mathbf{x}_{\perp b}, \mathbf{x}'_{\perp b}), \quad (\text{D.19})$$

$$K_{p \rightarrow b}^{\text{D,diss-iz}(\text{D}_2)}(\mathbf{x}_{\perp b}, \mathbf{x}'_{\perp}) = K_{b \rightarrow b, \text{dir}}^{\text{D, reem}}(\mathbf{x}_{\perp b}, \mathbf{x}'_{\perp b}) + \alpha_{\text{refl}} K_{b \rightarrow b, \text{refl}}^{\text{D, reem}}(\mathbf{x}_{\perp b}, \mathbf{x}'_{\perp b}), \quad (\text{D.20})$$

$$K_{b \rightarrow b}^{\text{D, reem}}(\mathbf{x}_{\perp b}, \mathbf{x}'_{\perp b}) = K_{b \rightarrow b, \text{dir}}^{\text{D, reem}}(\mathbf{x}_{\perp b}, \mathbf{x}'_{\perp b}) + \alpha_{\text{refl}} K_{b \rightarrow b, \text{refl}}^{\text{D, reem}}(\mathbf{x}_{\perp b}, \mathbf{x}'_{\perp b}), \quad (\text{D.21})$$

$$K_{b \rightarrow b}^{\text{D, refl}}(\mathbf{x}_{\perp b}, \mathbf{x}'_{\perp b}) = K_{b \rightarrow b, \text{dir}}^{\text{D, refl}}(\mathbf{x}_{\perp b}, \mathbf{x}'_{\perp b}) + \alpha_{\text{refl}} K_{b \rightarrow b, \text{refl}}^{\text{D, reem}}(\mathbf{x}_{\perp b}, \mathbf{x}'_{\perp b}), \quad (\text{D.22})$$

where the kernel functions for a given path = {dir, refl} are defined as

$$K_{p \rightarrow p, \text{path}}^{\text{D}_2, \text{D}_2^+}(\mathbf{x}_{\perp}, \mathbf{x}'_{\perp}) = \int_0^\infty \frac{1}{r'_{\perp}} \Phi_{\perp}[\mathbf{v}_{\perp, \text{D}_2^+}, T_{\text{D}_2^+}](\mathbf{x}'_{\perp}, \mathbf{v}_{\perp}) \exp \left[-\frac{1}{v_{\perp}} \int_0^{r'_{\perp}} v_{\text{eff}, \text{D}_2}(\mathbf{x}_{\perp}'') dr''_{\perp} \right] dv_{\perp}, \quad (\text{D.23})$$

$$K_{b \rightarrow p, \text{path}}^{\text{D}_2, \text{reem}}(\mathbf{x}_{\perp}, \mathbf{x}'_{\perp b}) = \int_0^\infty \frac{v_{\perp}}{r'_{\perp}} \cos \theta' \chi_{\perp, \text{in}, \text{D}_2}(\mathbf{x}'_{\perp b}, \mathbf{v}_{\perp}) \exp \left[-\frac{1}{v_{\perp}} \int_0^{r'_{\perp}} v_{\text{eff}, \text{D}_2}(\mathbf{x}_{\perp}'') dr''_{\perp} \right] dv_{\perp}, \quad (\text{D.24})$$

Appendix D. List of kernel functions

$$K_{b \rightarrow p, \text{path}}^{\text{D}_2, \text{refl}}(\mathbf{x}_\perp, \mathbf{x}'_{\perp b}) = \int_0^\infty \frac{1}{r'_\perp} \Phi_{\perp}[\mathbf{v}_{\text{refl}(\text{D}_2^+)}, T_{\text{D}_2^+}](\mathbf{x}', \mathbf{v}) \exp \left[-\frac{1}{v_\perp} \int_0^{r'_\perp} v_{\text{eff}, \text{D}_2}(\mathbf{x}''_\perp) dr''_\perp \right] dv_\perp, \quad (\text{D.25})$$

$$K_{p \rightarrow b, \text{path}}^{\text{D}_2, \text{D}_2^+}(\mathbf{x}_{\perp b}, \mathbf{x}'_\perp) = \int_0^\infty \frac{v_\perp}{r'_\perp} \cos \theta \Phi_{\perp}[\mathbf{v}_{\perp, \text{D}_2^+}, T_{\text{D}_2^+}](\mathbf{x}'_\perp, \mathbf{v}_\perp) \exp \left[-\frac{1}{v_\perp} \int_0^{r'_\perp} v_{\text{eff}, \text{D}_2}(\mathbf{x}''_\perp) dr''_\perp \right] dv_\perp, \quad (\text{D.26})$$

$$K_{b \rightarrow b, \text{path}}^{\text{D}_2, \text{reem}}(\mathbf{x}_{\perp b}, \mathbf{x}'_{\perp b}) = \int_0^\infty \frac{v_\perp^2}{r'_\perp} \cos \theta \cos \theta' \chi_{\perp, \text{in}, \text{D}_2}(\mathbf{x}'_{\perp b}, \mathbf{v}_\perp) \exp \left[-\frac{1}{v_\perp} \int_0^{r'_\perp} v_{\text{eff}, \text{D}_2}(\mathbf{x}''_\perp) dr''_\perp \right] dv_\perp, \quad (\text{D.27})$$

$$K_{b \rightarrow b, \text{path}}^{\text{D}_2, \text{refl}}(\mathbf{x}_{\perp b}, \mathbf{x}'_{\perp b}) = \int_0^\infty \frac{v_\perp}{r'_\perp} \cos \theta \Phi_{\perp}[\mathbf{v}_{\text{refl}(\text{D}_2^+)}, T_{\text{D}_2^+}](\mathbf{x}', \mathbf{v}) \exp \left[-\frac{1}{v_\perp} \int_0^{r'_\perp} v_{\text{eff}, \text{D}_2}(\mathbf{x}''_\perp) dr''_\perp \right] dv_\perp, \quad (\text{D.28})$$

$$K_{p \rightarrow p, \text{path}}^{\text{D}, \text{D}^+}(\mathbf{x}_\perp, \mathbf{x}'_\perp) = \int_0^\infty \frac{1}{r'_\perp} \Phi_{\perp}[\mathbf{v}_{\perp, \text{D}^+}, T_{\text{D}^+}](\mathbf{x}'_\perp, \mathbf{v}_\perp) \exp \left[-\frac{1}{v_\perp} \int_0^{r'_\perp} v_{\text{eff}, \text{D}}(\mathbf{x}''_\perp) dr''_\perp \right] dv_\perp, \quad (\text{D.29})$$

$$K_{p \rightarrow p, \text{path}}^{\text{D}, \text{D}_2^+}(\mathbf{x}_\perp, \mathbf{x}'_\perp) = \int_0^\infty \frac{1}{r'_\perp} \Phi_{\perp}[\mathbf{v}_{\perp, \text{D}_2^+}, T_{\text{D}_2^+}](\mathbf{x}'_\perp, \mathbf{v}_\perp) \exp \left[-\frac{1}{v_\perp} \int_0^{r'_\perp} v_{\text{eff}, \text{D}}(\mathbf{x}''_\perp) dr''_\perp \right] dv_\perp, \quad (\text{D.30})$$

$$K_{p \rightarrow p, \text{path}}^{\text{D}, \text{diss}(\text{D}_2^+)}(\mathbf{x}_\perp, \mathbf{x}'_\perp) = \int_0^\infty \frac{1}{r'_\perp} \Phi_{\perp}[\mathbf{v}_{\perp, \text{D}_2^+}, T_{\text{D}, \text{diss}(\text{D}_2^+)}](\mathbf{x}'_\perp, \mathbf{v}_\perp) \exp \left[-\frac{1}{v_\perp} \int_0^{r'_\perp} v_{\text{eff}, \text{D}}(\mathbf{x}''_\perp) dr''_\perp \right] dv_\perp, \quad (\text{D.31})$$

$$K_{p \rightarrow p, \text{path}}^{\text{D}, \text{diss-rec}(\text{D}_2^+)}(\mathbf{x}_\perp, \mathbf{x}'_\perp) = \int_0^\infty \frac{1}{r'_\perp} \Phi_{\perp}[\mathbf{v}_{\perp, \text{D}_2^+}, T_{\text{D}, \text{diss-rec}(\text{D}_2^+)}](\mathbf{x}'_\perp, \mathbf{v}_\perp) \exp \left[-\frac{1}{v_\perp} \int_0^{r'_\perp} v_{\text{eff}, \text{D}}(\mathbf{x}''_\perp) dr''_\perp \right] dv_\perp, \quad (\text{D.32})$$

$$K_{p \rightarrow p, \text{path}}^{\text{D, diss}(D_2)}(\mathbf{x}_\perp, \mathbf{x}'_\perp) = \int_0^\infty \frac{1}{r'_\perp} \Phi_\perp[\mathbf{v}_\perp, D_2, T_{\text{D, diss}(D_2)}](\mathbf{x}'_\perp, \mathbf{v}_\perp) \exp\left[-\frac{1}{v_\perp} \int_0^{r'_\perp} v_{\text{eff}, \text{D}}(\mathbf{x}''_\perp) dr''_\perp\right] dv_\perp, \quad (\text{D.33})$$

$$K_{p \rightarrow p, \text{path}}^{\text{D, diss-iz}(D_2)}(\mathbf{x}_\perp, \mathbf{x}'_\perp) = \int_0^\infty \frac{1}{r'_\perp} \Phi_\perp[\mathbf{v}_\perp, D_2, T_{\text{D, diss-iz}(D_2)}](\mathbf{x}'_\perp, \mathbf{v}_\perp) \exp\left[-\frac{1}{v_\perp} \int_0^{r'_\perp} v_{\text{eff}, \text{D}}(\mathbf{x}''_\perp) dr''_\perp\right] dv_\perp, \quad (\text{D.34})$$

$$K_{b \rightarrow p, \text{path}}^{\text{D, reem}}(\mathbf{x}_\perp, \mathbf{x}'_{\perp b}) = \int_0^\infty \frac{v_\perp}{r'_\perp} \cos\theta' \chi_{\perp, \text{in}, \text{D}}(\mathbf{x}'_{\perp b}, \mathbf{v}_\perp) \exp\left[-\frac{1}{v_\perp} \int_0^{r'_\perp} v_{\text{eff}, \text{D}}(\mathbf{x}''_\perp) dr''_\perp\right] dv_\perp, \quad (\text{D.35})$$

$$K_{b \rightarrow p, \text{path}}^{\text{D, refl}}(\mathbf{x}_\perp, \mathbf{x}'_{\perp b}) = \int_0^\infty \frac{1}{r'_\perp} \Phi_\perp[\mathbf{v}_{\text{refl}(\text{D}^+)}, T_{\text{D}^+}](\mathbf{x}', \mathbf{v}) \exp\left[-\frac{1}{v_\perp} \int_0^{r'_\perp} v_{\text{eff}, \text{D}}(\mathbf{x}''_\perp) dr''_\perp\right] dv_\perp, \quad (\text{D.36})$$

$$K_{p \rightarrow b, \text{path}}^{\text{D, D}^+}(\mathbf{x}_{\perp b}, \mathbf{x}'_\perp) = \int_0^\infty \frac{v_\perp}{r'_\perp} \cos\theta \Phi_\perp[\mathbf{v}_\perp, \text{D}^+, T_{\text{D}^+}](\mathbf{x}'_\perp, \mathbf{v}_\perp) \exp\left[-\frac{1}{v_\perp} \int_0^{r'_\perp} v_{\text{eff}, \text{D}}(\mathbf{x}''_\perp) dr''_\perp\right] dv_\perp, \quad (\text{D.37})$$

$$K_{p \rightarrow b, \text{path}}^{\text{D, D}_2^+}(\mathbf{x}_{\perp b}, \mathbf{x}'_\perp) = \int_0^\infty \frac{v_\perp}{r'_\perp} \cos\theta \Phi_\perp[\mathbf{v}_\perp, \text{D}_2^+, T_{\text{D}_2^+}](\mathbf{x}'_\perp, \mathbf{v}_\perp) \exp\left[-\frac{1}{v_\perp} \int_0^{r'_\perp} v_{\text{eff}, \text{D}}(\mathbf{x}''_\perp) dr''_\perp\right] dv_\perp, \quad (\text{D.38})$$

$$K_{p \rightarrow b, \text{path}}^{\text{D, diss}(\text{D}_2^+)}(\mathbf{x}_{\perp b}, \mathbf{x}'_\perp) = \int_0^\infty \frac{v_\perp}{r'_\perp} \cos\theta \Phi_\perp[\mathbf{v}_\perp, \text{D}_2^+, T_{\text{D, diss}(\text{D}_2^+)}](\mathbf{x}'_\perp, \mathbf{v}_\perp) \exp\left[-\frac{1}{v_\perp} \int_0^{r'_\perp} v_{\text{eff}, \text{D}}(\mathbf{x}''_\perp) dr''_\perp\right] dv_\perp, \quad (\text{D.39})$$

$$K_{p \rightarrow b, \text{path}}^{\text{D, diss-rec}(\text{D}_2^+)}(\mathbf{x}_{\perp b}, \mathbf{x}'_\perp) = \int_0^\infty \frac{v_\perp}{r'_\perp} \cos\theta \Phi_\perp[\mathbf{v}_\perp, \text{D}_2^+, T_{\text{D, diss-rec}(\text{D}_2^+)}](\mathbf{x}'_\perp, \mathbf{v}_\perp) \exp\left[-\frac{1}{v_\perp} \int_0^{r'_\perp} v_{\text{eff}, \text{D}}(\mathbf{x}''_\perp) dr''_\perp\right] dv_\perp, \quad (\text{D.40})$$

Appendix D. List of kernel functions

$$K_{p \rightarrow b, \text{path}}^{\text{D, diss}(D_2)}(\mathbf{x}_{\perp b}, \mathbf{x}'_{\perp}) = \int_0^\infty \frac{v_{\perp}}{r'_{\perp}} \cos \theta \Phi_{\perp}[\mathbf{v}_{\perp, D_2}, T_{D, \text{diss}(D_2)}](\mathbf{x}'_{\perp}, \mathbf{v}_{\perp}) \exp \left[-\frac{1}{v_{\perp}} \int_0^{r'_{\perp}} v_{\text{eff}, D}(\mathbf{x}''_{\perp}) dr''_{\perp} \right] dv_{\perp}, \quad (\text{D.41})$$

$$K_{p \rightarrow b, \text{path}}^{\text{D, diss-iz}(D_2)}(\mathbf{x}_{\perp b}, \mathbf{x}'_{\perp}) = \int_0^\infty \frac{v_{\perp}}{r'_{\perp}} \cos \theta \Phi_{\perp}[\mathbf{v}_{\perp, D_2}, T_{D, \text{diss-iz}(D_2)}](\mathbf{x}'_{\perp}, \mathbf{v}_{\perp}) \exp \left[-\frac{1}{v_{\perp}} \int_0^{r'_{\perp}} v_{\text{eff}, D}(\mathbf{x}''_{\perp}) dr''_{\perp} \right] dv_{\perp}, \quad (\text{D.42})$$

$$K_{b \rightarrow b, \text{path}}^{\text{D, reem}}(\mathbf{x}_{\perp b}, \mathbf{x}'_{\perp b}) = \int_0^\infty \frac{v_{\perp}^2}{r'_{\perp}} \cos \theta \cos \theta' \chi_{\perp, \text{in}, D}(\mathbf{x}'_{\perp b}, \mathbf{v}_{\perp}) \exp \left[-\frac{1}{v_{\perp}} \int_0^{r'_{\perp}} v_{\text{eff}, D}(\mathbf{x}''_{\perp}) dr''_{\perp} \right] dv_{\perp}, \quad (\text{D.43})$$

$$K_{b \rightarrow b, \text{path}}^{\text{D, refl}}(\mathbf{x}_{\perp b}, \mathbf{x}'_{\perp b}) = \int_0^\infty \frac{v_{\perp}}{r'_{\perp}} \cos \theta \Phi_{\perp}[\mathbf{v}_{\text{refl}(D^+)}, T_{D^+}](\mathbf{x}', \mathbf{v}) \exp \left[-\frac{1}{v_{\perp}} \int_0^{r'_{\perp}} v_{\text{eff}, D}(\mathbf{x}''_{\perp}) dr''_{\perp} \right] dv_{\perp}. \quad (\text{D.44})$$

We remark that all velocity distributions given by a Maxwellian or a Knudsen cosine law are integrated along the parallel velocity, that is

$$\Phi_{\perp}[\mathbf{v}_{\perp, D_2^+}, T_{D_2^+}](\mathbf{x}'_{\perp}, \mathbf{v}_{\perp}) = \int_0^\infty \Phi_{\perp}[\mathbf{v}_{\perp, D_2^+}, T_{D_2^+}](\mathbf{x}'_{\perp}, \mathbf{v}_{\perp}) dv_{\parallel}, \quad (\text{D.45})$$

$$\Phi_{\perp}[\mathbf{v}_{\perp, D^+}, T_{D^+}](\mathbf{x}'_{\perp}, \mathbf{v}_{\perp}) = \int_0^\infty \Phi_{\perp}[\mathbf{v}_{\perp, D^+}, T_{D^+}](\mathbf{x}'_{\perp}, \mathbf{v}_{\perp}) dv_{\parallel}, \quad (\text{D.46})$$

$$\Phi_{\perp}[\mathbf{v}_{\perp, D_2}, T_{D, \text{diss}(D_2)}](\mathbf{x}'_{\perp}, \mathbf{v}_{\perp}) = \int_0^\infty \Phi_{\mathbf{v}_{\perp, D_2}, T_{D, \text{diss}(D_2)}}(\mathbf{x}'_{\perp}, \mathbf{v}_{\perp}) dv_{\parallel}, \quad (\text{D.47})$$

$$\Phi_{\perp}[\mathbf{v}_{\perp, D_2}, T_{D, \text{diss-iz}(D_2)}](\mathbf{x}'_{\perp}, \mathbf{v}_{\perp}) = \int_0^\infty \Phi_{\perp}[\mathbf{v}_{\perp, D_2}, T_{D, \text{diss-iz}(D_2)}](\mathbf{x}'_{\perp}, \mathbf{v}_{\perp}) dv_{\parallel}, \quad (\text{D.48})$$

$$\Phi_{\perp}[\mathbf{v}_{\perp, D_2^+}, T_{D, \text{diss}}(D_2^+)](\mathbf{x}'_{\perp}, \mathbf{v}_{\perp}) = \int_0^{\infty} \Phi[\mathbf{v}_{\perp, D_2^+}, T_{D, \text{diss}}(D_2^+)](\mathbf{x}'_{\perp}, \mathbf{v}_{\perp}) d v_{\parallel}, \quad (\text{D.49})$$

$$\Phi_{\perp}[\mathbf{v}_{\perp, D_2^+}, T_{D, \text{diss-rec}}(D_2^+)](\mathbf{x}'_{\perp}, \mathbf{v}_{\perp}) = \int_0^{\infty} \Phi[\mathbf{v}_{\perp, D_2^+}, T_{D, \text{diss-rec}}(D_2^+)](\mathbf{x}'_{\perp}, \mathbf{v}_{\perp}) d v_{\parallel}, \quad (\text{D.50})$$

$$\Phi_{\perp}[\mathbf{v}_{\text{refl}(D^+)}, T_{D^+}](\mathbf{x}', \mathbf{v}) = \int_0^{\infty} \Phi[\mathbf{v}_{\text{refl}(D^+)}, T_{D^+}](\mathbf{x}', \mathbf{v}) d v_{\parallel}, \quad (\text{D.51})$$

$$\Phi_{\perp}[\mathbf{v}_{\text{refl}(D_2^+)}, T_{D_2^+}](\mathbf{x}', \mathbf{v}) = \int_0^{\infty} \Phi[\mathbf{v}_{\text{refl}(D_2^+)}, T_{D_2^+}](\mathbf{x}', \mathbf{v}) d v_{\parallel}, \quad (\text{D.52})$$

$$\chi_{\perp, \text{in}, D_2}(\mathbf{x}'_{\perp, \text{b}}, \mathbf{v}_{\perp}) = \int_0^{\infty} \chi_{\text{in}, D_2}(\mathbf{x}'_{\perp, \text{b}}, \mathbf{v}_{\perp}) d v_{\parallel}, \quad (\text{D.53})$$

$$\chi_{\perp, \text{in}, D}(\mathbf{x}'_{\perp, \text{b}}, \mathbf{v}_{\perp}) = \int_0^{\infty} \chi_{\text{in}, D}(\mathbf{x}'_{\perp, \text{b}}, \mathbf{v}_{\perp}) d v_{\parallel}. \quad (\text{D.54})$$

E Numerical solution of the neutral equations

The coupled neutral equations for D_2 and D , Eqs. (3.80-3.83), may be discretized as a linear matrix system, $\mathbf{x} = A\mathbf{x} + \mathbf{b}$, with the unknown \mathbf{x} representing the density and boundary flux of the D_2 and D species. Indicating with N_P the number of points that discretize the poloidal plane and N_B the number of points discretizing the boundary, \mathbf{x} is a vector of size $2(N_P + N_B)$, A is a $2(N_P + N_B) \times 2(N_P + N_B)$ matrix and \mathbf{b} is a $2(N_P + N_B)$ vector that includes all contributions not proportional to the neutral density or flux, namely the effect of recombination of D^+ and D_2^+ with electrons, the effect of dissociative processes to which D_2^+ ions are subject and the contributions from the flux of D^+ and D_2^+ ions to the boundary.

The matrix M , and the vectors \mathbf{x} and \mathbf{b} can then be written as

$$\mathbf{x} = \begin{bmatrix} n_D \\ \Gamma_{\text{out},D} \\ n_{D_2} \\ \Gamma_{\text{out},D_2} \end{bmatrix}, M = \begin{bmatrix} M_{11} & M_{12} & M_{13} & M_{14} \\ M_{21} & M_{22} & M_{23} & M_{24} \\ M_{31} & M_{32} & M_{33} & M_{34} \\ M_{41} & M_{42} & M_{43} & M_{44} \end{bmatrix}, \mathbf{b} = \begin{bmatrix} b_1 \\ b_2 \\ b_3 \\ b_4 \end{bmatrix}, \quad (\text{E.1})$$

where M_{11} is a matrix of size $N_P \times N_P$,

$$M_{11} = \nu_{\text{cx},D} K_{p \rightarrow p}^{\text{D},\text{D}^+}, \quad (\text{E.2})$$

that discretizes the kernel $K_{p \rightarrow p}^{\text{D},\text{D}^+}$ defined in Eq. (3.84) at the spatial points where n_D is evaluated. The matrix

$$M_{21} = \nu_{\text{cx},D} K_{p \rightarrow b}^{\text{D},\text{D}^+}, \quad (\text{E.3})$$

Appendix E. Numerical solution of the neutral equations

has size $N_B \times N_P$ and discretizes the kernel $K_{p \rightarrow b}^{D, D^+}$ defined in Eq. (D.15) at the points where Γ_D is evaluated. The other matrices appearing in the definition of M are defined similarly,

$$M_{31} = \left[\frac{n_{D_2^+}}{n_D} v_{\text{cx}, D_2^+ - D} \right] K_{p \rightarrow p}^{D_2, D_2^+}, \quad (\text{E.4})$$

$$M_{41} = \left[\frac{n_{D_2^+}}{n_D} v_{\text{cx}, D_2^+ - D} \right] K_{p \rightarrow b}^{D_2, D_2^+}, \quad (\text{E.5})$$

$$M_{12} = (1 - \alpha_{\text{refl}})(1 - \beta_{\text{assoc}}) K_{b \rightarrow p}^{D, \text{reem}}, \quad (\text{E.6})$$

$$M_{22} = (1 - \alpha_{\text{refl}})(1 - \beta_{\text{assoc}}) K_{b \rightarrow b}^{D, \text{reem}}, \quad (\text{E.7})$$

$$M_{32} = (1 - \alpha_{\text{refl}}) \frac{\beta_{\text{assoc}}}{2} K_{b \rightarrow p}^{D_2, \text{reem}}, \quad (\text{E.8})$$

$$M_{42} = (1 - \alpha_{\text{refl}}) \frac{\beta_{\text{assoc}}}{2} K_{b \rightarrow b}^{D_2, \text{reem}}, \quad (\text{E.9})$$

$$M_{13} = v_{\text{cx}, D_2 - D^+} K_{p \rightarrow p}^{D, D^+} + v_{\text{diss}, D_2} K_{p \rightarrow p}^{D, \text{diss}(D_2)} + v_{\text{diss-iz}, D_2} K_{p \rightarrow p}^{D, \text{diss-iz}(D_2)}, \quad (\text{E.10})$$

$$M_{23} = v_{\text{cx}, D_2 - D^+} K_{p \rightarrow b}^{D, D^+} + v_{\text{diss}, D_2} K_{p \rightarrow b}^{D, \text{diss}(D_2)} + v_{\text{diss-iz}, D_2} K_{p \rightarrow b}^{D, \text{diss-iz}(D_2)}, \quad (\text{E.11})$$

$$M_{33} = v_{\text{cx}, D_2} K_{p \rightarrow p}^{D_2, D_2^+}, \quad (\text{E.12})$$

$$M_{43} = v_{\text{cx}, D_2} K_{p \rightarrow b}^{D_2, D_2^+}, \quad (\text{E.13})$$

$$M_{14} = 0, \quad (\text{E.14})$$

$$M_{24} = 0, \quad (\text{E.15})$$

$$M_{34} = (1 - \alpha_{\text{refl}}) K_{b \rightarrow p}^{D_2}, \quad (\text{E.16})$$

$$M_{44} = (1 - \alpha_{\text{refl}}) K_{b \rightarrow b}^{D_2}, \quad (\text{E.17})$$

The vector \mathbf{b} is defined through the vectors b_1 and b_3 of size N_P ,

$$b_1 = n_{D[\text{rec}(D^+)]}(\mathbf{x}_\perp) + n_{D[\text{diss}(D_2^+)]}(\mathbf{x}_\perp) + n_{D[\text{out}(D^+)]}(\mathbf{x}_\perp), \quad (\text{E.18})$$

$$b_3 = n_{D_2[\text{rec}(D_2^+)]}(\mathbf{x}_\perp) + n_{D_2[\text{out}(D_2^+)]}(\mathbf{x}_\perp) + n_{D_2[\text{out}(D^+)]}(\mathbf{x}_\perp), \quad (\text{E.19})$$

and the vector b_2 and b_4 of size N_B ,

$$b_2 = \Gamma_{\text{out}, D[\text{rec}(D^+)]}(\mathbf{x}_\perp) + \Gamma_{\text{out}, D[\text{diss}(D_2^+)]}(\mathbf{x}_\perp) + \Gamma_{\text{out}, D[\text{out}(D^+)]}(\mathbf{x}_\perp), \quad (\text{E.20})$$

$$b_4 = \Gamma_{\text{out}, D_2[\text{rec}(D_2^+)]}(\mathbf{x}_\perp) + \Gamma_{\text{out}, D_2[\text{out}(D_2^+)]}(\mathbf{x}_\perp) + \Gamma_{\text{out}, D_2[\text{out}(D^+)]}(\mathbf{x}_\perp). \quad (\text{E.21})$$

Appendix E. Numerical solution of the neutral equations

It is remarked that the vector \mathbf{b} can also be written as $\mathbf{b} = N\mathbf{x}_i$, where \mathbf{x}_i refers to the densities and boundary fluxes of the D^+ and D_2^+ ion species,

$$\mathbf{x}_i = \begin{bmatrix} n_{D^+} \\ \Gamma_{\text{out},D^+} \\ n_{D_2^+} \\ \Gamma_{\text{out},D_2^+} \end{bmatrix}, \quad (\text{E.22})$$

and the matrix N can be expressed as

$$N = \begin{bmatrix} N_{11} & N_{12} & N_{13} & N_{14} \\ N_{21} & N_{22} & N_{23} & N_{24} \\ N_{31} & N_{32} & N_{33} & N_{34} \\ N_{41} & N_{42} & N_{43} & N_{44} \end{bmatrix}, \quad (\text{E.23})$$

with entries

$$N_{11} = v_{\text{rec},D^+} K_{p \rightarrow p}^{D,D^+}, \quad (\text{E.24})$$

$$N_{21} = v_{\text{rec},D^+} K_{p \rightarrow b}^{D,D^+}, \quad (\text{E.25})$$

$$N_{31} = v_{\text{rec},D_2^+} K_{p \rightarrow p}^{D_2,D_2^+}, \quad (\text{E.26})$$

$$N_{41} = v_{\text{rec},D_2^+} K_{p \rightarrow b}^{D_2,D_2^+}, \quad (\text{E.27})$$

$$N_{12} = (1 - \alpha_{\text{refl}})(1 - \beta_{\text{assoc}}) K_{b \rightarrow p}^{D,\text{reem}} + \alpha_{\text{refl}} K_{b \rightarrow p}^{D,\text{refl}}, \quad (\text{E.28})$$

$$N_{22} = (1 - \alpha_{\text{refl}})(1 - \beta_{\text{assoc}}) K_{b \rightarrow b}^{D,\text{reem}} + \alpha_{\text{refl}} K_{b \rightarrow b}^{D,\text{refl}}, \quad (\text{E.29})$$

$$N_{32} = (1 - \alpha_{\text{refl}}) \frac{\beta_{\text{assoc}}}{2} K_{b \rightarrow p}^{\text{D}_2, \text{reem}}, \quad (\text{E.30})$$

$$N_{42} = (1 - \alpha_{\text{refl}}) \frac{\beta_{\text{assoc}}}{2} K_{b \rightarrow b}^{\text{D}_2, \text{reem}}, \quad (\text{E.31})$$

$$N_{13} = v_{\text{diss}, \text{D}_2^+} K_{p \rightarrow p}^{\text{D}, \text{diss}(\text{D}_2^+)} + 2v_{\text{diss-rec}, \text{D}_2^+} K_{p \rightarrow p}^{\text{D}, \text{diss-rec}(\text{D}_2^+)}, \quad (\text{E.32})$$

$$N_{23} = v_{\text{diss}, \text{D}_2^+} K_{p \rightarrow b}^{\text{D}, \text{diss}(\text{D}_2^+)} + 2v_{\text{diss-rec}, \text{D}_2^+} K_{p \rightarrow b}^{\text{D}, \text{diss-rec}(\text{D}_2^+)}, \quad (\text{E.33})$$

$$N_{33} = v_{\text{rec}, \text{D}_2^+} K_{p \rightarrow p}^{\text{D}_2, \text{D}_2^+}, \quad (\text{E.34})$$

$$N_{43} = v_{\text{rec}, \text{D}_2^+} K_{p \rightarrow b}^{\text{D}_2, \text{D}_2^+}, \quad (\text{E.35})$$

$$N_{14} = 0, \quad (\text{E.36})$$

$$N_{24} = 0, \quad (\text{E.37})$$

$$N_{34} = (1 - \alpha_{\text{refl}}) K_{b \rightarrow p}^{\text{D}_2, \text{reem}}, \quad (\text{E.38})$$

$$N_{44} = (1 - \alpha_{\text{refl}}) K_{b \rightarrow b}^{\text{D}_2, \text{reem}} + \alpha_{\text{refl}} K_{b \rightarrow b}^{\text{D}_2, \text{refl}}. \quad (\text{E.39})$$

Appendix E. Numerical solution of the neutral equations

We remark that a convergence study to estimate the error introduced by the discretization of the neutral equation was carried out for a single neutral species model and it is reported in [36].

Bibliography

- [1] V. Smil. Energy Transitions: Global and National Perspectives, 2017.
- [2] BP Statistical. BP statistical review of world energy 2020. Technical report, BP p.l.c., 2020.
- [3] J. Houghton. *Global Warming: The Complete Briefing. 4th edition*. Cambridge University Press, 2009.
- [4] S. Simons, J. Schmitt, B. Tom, H. Bao, B. Pettinato, and M. Pechulis. *Thermal, Mechanical, and Hybrid Chemical Energy Storage Systems*. Elsevier Inc., 2021.
- [5] P. A. Kharecha and J. E. Hansen. Prevented mortality and greenhouse gas emissions from historical and projected nuclear power. *Environmental Science and Technology*, 47:4889, 2013.
- [6] International Atomic Energy Agency and Nuclear Energy Agency. Uranium 2020 - Resources, Production and Demand, 2020.
- [7] BP Statistical. BP Statistical Review of World Energy. Technical report, BP p.l.c., 2016.
- [8] European Commission. Directorate General for Research. *Fusion research : an energy option for Europe's future*. European Communities, 2005.
- [9] J. Parisi and J. Ball. *The Future of Fusion Energy*. World Scientific Europe Publishing Ltd., 2019.
- [10] J. Reijonen, T. P. Lou, B. Tolmachoff, and K. N. Leung. Compact neutron source development at LBNL. *Charged Particle Detection, Diagnostics, and Imaging*, 4510:80, 2001.
- [11] J. D. Lawson. Some criteria for a power producing thermonuclear reactor. *Proceedings of the Physical Society. Section B*, 70, 1957.
- [12] P. C. Stangeby. *The Plasma Boundary of Magnetic Fusion Devices*. IOP, Bristol, 2000.
- [13] Y. Yu, L. Wang, B. Cao, H. Wang, and J. Hu. Fuel retention and recycling studies by using particle balance in EAST tokamak. In *Physica Scripta*, page 014070, 2017.

Bibliography

- [14] S. M. Motevalli, S. Ostadi, and F. Fadaei. Effects of wall recycling and fuel injections rate on particle balance behavior in the tokamak fusion. *Indian Journal of Physics*, 95:943, 2020.
- [15] C. C. Petty and the Diii-D Team. DIII-D research towards establishing the scientific basis for future fusion reactors. *Nuclear Fusion*, 59:112002, 2019.
- [16] M. Z. Tokar. Modelling of detachment in a limiter tokamak as a nonlinear phenomenon caused by impurity radiation. *Plasma Physics and Controlled Fusion*, 36:1819, 1994.
- [17] S. I. Braginskii. Transport processes in a plasma. In *Reviews of Plasma Physics*, volume 1. Consultants Bureau, New York, 1965.
- [18] B. J. Braams. Radiative Divertor Modelling for ITER and TPX. *Contributions to Plasma Physics*, 36:276, 1996.
- [19] M. Baelmans, D. Reiter, and R. R. Weynants. New Developments in Plasma Edge Modeling with Particular Emphasis on Drift Flows and Electric Fields. *Contributions to Plasma Physics*, 36:117, 1996.
- [20] R. Simonini, G. Corrigan, G. Radford, J. Spence, and A. Taroni. Models and Numerics in the Multi-Fluid 2-D Edge Plasma Code EDGE2D/U. *Contributions to Plasma Physics*, 34:368, 1994.
- [21] H. Bufferand, G. Ciraolo, L. Isoardi, G. Chiavassa, F. Schwander, E. Serre, N. Fedorczak, P. Ghendrih, and P. Tamain. Applications of SOLEDGE-2D code to complex SOL configurations and analysis of Mach probe measurements. *Journal of Nuclear Materials*, 415:S589, 2011.
- [22] R. Zagórski, H. Gerhauser, and H. A. Claassen. Numerical simulation of the TEXTOR edge plasma including drifts and impurities. *Contributions to Plasma Physics*, 38:61, 1998.
- [23] A. Yu Pigarov, S. I. Krasheninnikov, W. P. West, T. D. Rognlien, J. A. Boedo, D. G. Whyte, C. J. Lasnier, T. W. Petrie, M. J. Schaffer, and J. G. Watkins. DIII-D edge plasma simulations with UEDGE code including non-diffusive anomalous cross-field transport. *Journal of Nuclear Materials*, 313-316:1076, 2003.
- [24] D. Stotler and C. Karney. Neutral Gas Transport Modeling with DEGAS 2. *Contributions to Plasma Physics*, 34:392, 1994.
- [25] D. Reiter, M. Baelmans, and P. Börner. The EIRENE and B2-EIRENE codes. *Fusion Science and Technology*, 47:172, 2005.
- [26] J. Mandrekas. GTNEUT: A code for the calculation of neutral particle transport in plasmas based on the transmission and escape probability method. *Computer Physics Communications*, 161:36, 2004.

-
- [27] K. Shimizu, T. Takizuka, S. Sakurai, H. Tamai, H. Takenaga, H. Kubo, and Y. Miura. Simulation of divertor detachment characteristics in JT-60 with superconducting coils. *Journal of Nuclear Materials*, 313-316:1277, 2003.
- [28] J. D. Lore, J. M. Canik, Y. Feng, J. W. Ahn, R. Maingi, and V. Soukhanovskii. Implementation of the 3D edge plasma code EMC3-EIRENE on NSTX. *Nuclear Fusion*, 52:054012, 2012.
- [29] R. Schneider, X. Bonnin, K. Borrass, D. P. Coster, H. Kastelewicz, D. Reiter, V. A. Rozhansky, and B. J. Braams. Plasma edge physics with B2-Eirene. *Contributions to Plasma Physics*, 46:3, 2006.
- [30] B. D. Dudson, M. V. Umansky, X. Q. Xu, P. B. Snyder, and H. R. Wilson. BOUT++: A framework for parallel plasma fluid simulations. *Computer Physics Communications*, 180:1467, 2009.
- [31] B. D. Dudson and J. Leddy. Hermes: Global plasma edge fluid turbulence simulations. *Plasma Physics and Controlled Fusion*, 59, 2017.
- [32] M. Wiesenberger, L. Einkemmer, M. Held, A. Gutierrez-Milla, X. Sáez, and R. Iakymchuk. Reproducibility, accuracy and performance of the FELTOR code and library on parallel computer architectures. *Computer Physics Communications*, 238:145, 2019.
- [33] P. Ricci, F. D. Halpern, S. Jolliet, J. Loizu, A. Masetto, A. Fasoli, I. Furno, and C. Theiler. Simulation of plasma turbulence in scrape-off layer conditions: The GBS code, simulation results and code validation. *Plasma Physics and Controlled Fusion*, 54:124047, 2012.
- [34] F. D. Halpern, P. Ricci, S. Jolliet, J. Loizu, J. Morales, A. Masetto, F. Musil, F. Riva, T. M. Tran, and C. Wersal. The GBS code for tokamak scrape-off layer simulations. *Journal of Computational Physics*, 315:388, 2016.
- [35] P. Paruta, P. Ricci, F. Riva, C. Wersal, C. Beadle, and B. Frei. Simulation of plasma turbulence in the periphery of diverted tokamak by using the GBS code. *Physics of Plasmas*, 25:112301, 2018.
- [36] M. Giacomini, P. Ricci, A. Corrado, G. Fourestey, D. Galassi, E. Lanti, and D. Mancini. The GBS code for the self-consistent simulation of plasma turbulence and kinetic neutral dynamics in the tokamak boundary. *submitted to Computer Physics Communications*, 2021.
- [37] M. Francisquez, B. Zhu, and B. N. Rogers. Global 3D Braginskii simulations of the tokamak edge region of IWL discharges. *Nuclear Fusion*, 57, 2017.
- [38] A. Stegmeir, D. Coster, A. Ross, O. Maj, K. Lackner, and E. Poli. GRILLIX: A 3D turbulence code based on the flux-coordinate independent approach. *Plasma Physics and Controlled Fusion*, 60, 2018.

Bibliography

- [39] A. S. Thrysøe, M. Løiten, J. Madsen, V. Naulin, A. H. Nielsen, and J. J. Rasmussen. Plasma particle sources due to interactions with neutrals in a turbulent scrape-off layer of a toroidally confined plasma. *Physics of Plasmas*, 25, 2018.
- [40] C. Baudoin, P. Tamain, H. Bufferand, G. Ciraolo, N. Fedorczak, D. Galassi, P. Ghendrih, and N. Nace. Turbulent heat transport in TOKAM3X edge plasma simulations. *Contributions to Plasma Physics*, 58:484, 2018.
- [41] E. L. Shi, G. W. Hammett, T. Stoltzfus-Dueck, and A. Hakim. Gyrokinetic continuum simulation of turbulence in a straight open-field-line plasma. *Journal of Plasma Physics*, 83, 2017.
- [42] C. S. Chang and S. Ku. Spontaneous rotation sources in a quiescent tokamak edge plasma. *Physics of Plasmas*, 15, 2008.
- [43] S. Ku, C. S. Chang, and P. H. Diamond. Full-f gyrokinetic particle simulation of centrally heated global ITG turbulence from magnetic axis to edge pedestal top in a realistic tokamak geometry. *Nuclear Fusion*, 49, 2009.
- [44] J. Leddy, B. Dudson, and H. Willett. Simulation of the interaction between plasma turbulence and neutrals in linear devices. *Nuclear Materials and Energy*, 12:994, 2017.
- [45] A. S. Thrysøe, L. E. H. Tophøj, V. Naulin, J. J. Rasmussen, J. Madsen, and A. H. Nielsen. The influence of blobs on neutral particles in the scrape-off layer. *Plasma Physics and Controlled Fusion*, 58, 2016.
- [46] A. S. Thrysøe, J. Madsen, V. Naulin, and J. J. Rasmussen. Influence of molecular dissociation on blob-induced atom density perturbations. *Nuclear Fusion*, 58, 2018.
- [47] D. M. Fan, Y. Marandet, P. Tamain, H. Bufferand, G. Ciraolo, P. Ghendrih, and E. Serre. Effect of turbulent fluctuations on neutral particles transport with the TOKAM3X-EIRENE turbulence code. *Nuclear Materials and Energy*, 18:105, 2019.
- [48] A. Zeiler, J. F. Drake, and B. Rogers. Nonlinear reduced Braginskii equations with ion thermal dynamics in toroidal plasma. *Physics of Plasmas*, 4:2134, 1997.
- [49] P. Ricci, C. Theiler, A. Fasoli, I. Furno, K. Gustafson, D. Iraj, and J. Loizu. Methodology for turbulence code validation: Quantification of simulation-experiment agreement and application to the TORPEX experiment. *Physics of Plasmas*, 18:032109, 2011.
- [50] P. Ricci, B. N. Rogers, and S. Brunner. High- and low-confinement modes in simple magnetized toroidal plasmas. *Physical Review Letters*, 100:225002, 2008.
- [51] P. Ricci and B. N. Rogers. Transport scaling in interchange-driven toroidal plasmas. *Physics of Plasmas*, 16:062303, 2009.
- [52] B. N. Rogers and P. Ricci. Low-frequency turbulence in a linear magnetized plasma. *Physical Review Letters*, 104, 2010.

-
- [53] W. Gekelman, H. Pfister, Z. Lucky, J. Bamber, D. Leneman, and J. Maggs. Design, construction, and properties of the large plasma research device - The LAPD at UCLA. *Review of Scientific Instruments*, 62:2875, 1991.
- [54] P. Ricci and B. N. Rogers. Turbulence phase space in simple magnetized toroidal plasmas. *Physical Review Letters*, 104, 2010.
- [55] Federico D. Halpern, S. Jolliet, J. Loizu, A. Masetto, and P. Ricci. Ideal ballooning modes in the tokamak scrape-off layer. *Physics of Plasmas*, 20:052306, 2013.
- [56] A. Masetto, F. D. Halpern, S. Jolliet, J. Loizu, and P. Ricci. Finite ion temperature effects on scrape-off layer turbulence. *Physics of Plasmas*, 22:012308, 2015.
- [57] F. Riva, P. Ricci, F. D. Halpern, S. Jolliet, J. Loizu, and A. Masetto. Verification methodology for plasma simulations and application to a scrape-off layer turbulence code. *Physics of Plasmas*, 21:062301, 2014.
- [58] P. Paruta, C. Beadle, P. Ricci, and C. Theiler. Blob velocity scaling in diverted tokamaks: A comparison between theory and simulation. *Physics of Plasmas*, 26:032302, 2019.
- [59] C. F. Beadle and P. Ricci. Understanding the turbulent mechanisms setting the density decay length in the tokamak scrape-off layer. *Journal of Plasma Physics*, 86, 2020.
- [60] M. Giacomini, L. N. Stenger, and P. Ricci. Turbulence and flows in the plasma boundary of snowflake magnetic configurations. *Nuclear Fusion*, 60, 2020.
- [61] C. Wersal and P. Ricci. A first-principles self-consistent model of plasma turbulence and kinetic neutral dynamics in the tokamak scrape-off layer. *Nuclear Fusion*, 55:123014, 2015.
- [62] D. A. Russell, J. R. Myra, and D. P. Stotler. A reduced model of neutral-plasma interactions in the edge and scrape-off-layer: Verification comparisons with kinetic Monte Carlo simulations. *Physics of Plasmas*, 26, 2019.
- [63] C. Wersal, P. Ricci, and J. Loizu. A comparison between a refined two-point model for the limited tokamak SOL and self-consistent plasma turbulence simulations. *Plasma Physics and Controlled Fusion*, 59:044011, 2017.
- [64] C. Wersal and P. Ricci. Impact of neutral density fluctuations on gas puff imaging diagnostics. *Nuclear Fusion*, 57:116018, 2017.
- [65] V. M. Zhdanov. Transport Processes in Multicomponent Plasma. *Plasma Physics and Controlled Fusion*, 2002.
- [66] H. Bufferand, P. Tamain, S. Baschetti, J. Bucalossi, G. Ciraolo, N. Fedorczak, P. Ghendrih, F. Nespoli, F. Schwander, E. Serre, and Y. Marandet. Three-dimensional modelling of edge multi-component plasma taking into account realistic wall geometry. *Nuclear Materials and Energy*, 18:82, 2019.

Bibliography

- [67] A. Corrado and P. Ricci. Moving toward mass-conserving simulations of plasma turbulence and kinetic neutrals in the tokamak boundary with the GBS code. *Physics of Plasmas*, 28:022310, 2021.
- [68] A. Masetto, F. D. Halpern, S. Jolliet, J. Loizu, and P. Ricci. Turbulent regimes in the tokamak scrape-off layer. *Physics of Plasmas*, 20, 2013.
- [69] D. M. Fan, Y. Marandet, P. Tamain, H. Bufferand, G. Ciraolo, P. Ghendrih, and E. Serre. Self-consistent coupling of the three-dimensional fluid turbulence code TOKAM3X and the kinetic neutrals code EIRENE. *Contributions to Plasma Physics*, 58:490, 2018.
- [70] F. D. Halpern and P. Ricci. Velocity shear, turbulent saturation, and steep plasma gradients in the scrape-off layer of inner-wall limited tokamaks. *Nuclear Fusion*, 57, 2017.
- [71] A. Arakawa. Computational design for long-term numerical integration of the equations of fluid motion: Two-dimensional incompressible flow. Part I. *Journal of Computational Physics*, 1:119, 1966.
- [72] S. Jolliet, F. D. Halpern, J. Loizu, A. Masetto, and P. Ricci. Aspect ratio effects on limited scrape-off layer plasma turbulence. *Physics of Plasmas*, 21:022303, 2014.
- [73] M. Knudsen. Das Cosinusgesetz in der kinetischen Gastheorie. *Annalen der Physik*, 353:1113, 1916.
- [74] J. Loizu, P. Ricci, F. D. Halpern, and S. Jolliet. Boundary conditions for plasma fluid models at the magnetic presheath entrance. *Physics of Plasmas*, 19:122307, 2012.
- [75] A. Masetto, F. D. Halpern, S. Jolliet, J. Loizu, and P. Ricci. Finite ion temperature effects on scrape-off layer turbulence. *Physics of Plasmas*, 22, 2015.
- [76] F. D. Halpern, P. Ricci, S. Jolliet, J. Loizu, and A. Masetto. Theory of the scrape-off layer width in inner-wall limited tokamak plasmas. *Nuclear Fusion*, 54, 2014.
- [77] A. Corrado and P. Ricci. A self-consistent multi-component model of plasma turbulence and kinetic neutral dynamics for the simulation of the tokamak boundary. *submitted to Nuclear Fusion*, 2021.
- [78] C. S. Pitcher. *Tokamak Plasma Interaction with Limiters*. PhD thesis, University of Toronto, 1988.
- [79] C. Zhang, C. Sang, L. Wang, M. Chang, D. Liu, and D. Wang. Effect of carbon and tungsten plasma-facing materials on the divertor and pedestal plasma in EAST. *Plasma Physics and Controlled Fusion*, 61:115013, 2019.
- [80] Y. Feng, F. Sardei, and J. Kisslinger. 3D fluid modelling of the edge plasma by means of a Monte Carlo technique. *Journal of Nuclear Materials*, 266:812, 1999.

-
- [81] K. Sawada and T. Fujimoto. Effective ionization and dissociation rate coefficients of molecular hydrogen in plasma. *Journal of Applied Physics*, 78:2913, 1995.
- [82] K. D. Lawson, M. Groth, D. Harting, S. Menmuir, D. Reiter, S. Brezinsek, G. Corrigan, P. Drewelow, C. F. Maggi, A. G. Meigs, J. Simpson, M. F. Stamp, S. Wiesen, and contributors. A study of the atomic and molecular power loss terms in EDGE2D-EIRENE simulations of JET ITER-like wall L-mode discharges. *Nuclear Materials and Energy*, 12:924, 2017.
- [83] H. Bufferand, C. Baudoin, J. Bucalossi, G. Ciraolo, J. Denis, N. Fedorczak, D. Galassi, P. Ghendrih, R. Leybros, Y. Marandet, N. Mellet, J. Morales, N. Nace, E. Serre, P. Tamain, and M. Valentinuzzi. Implementation of drift velocities and currents in SOLEDGE2D-EIRENE. *Nuclear Materials and Energy*, 12:852, 2017.
- [84] D. Reiter. The data file AMJUEL: Additional Atomic and Molecular Data for EIRENE. Technical report, FZ, Forschungszentrum Julich GmbH FRG, 2011.
- [85] R. K. Janev and Langer W. D. *The Janev-Langer Hydrogen-Helium database, 1987 Contents*. Springer, 1987.
- [86] D. P. Stotler, C. H. Skinner, R. V. Budny, A. T. Ramsey, D. N. Ruzic, and R. B. Turkot. Modeling of neutral hydrogen velocities in the tokamak fusion test reactor. *Physics of Plasmas*, 3:4084, 1996.
- [87] M. Wensing, B. P. Duval, O. Février, A. Fil, D. Galassi, E. Havlickova, A. Perek, H. Reimerdes, C. Theiler, K. Verhaegh, and M. Wischmeier. SOLPS-ITER simulations of the TCV divertor upgrade. *Plasma Physics and Controlled Fusion*, 61:085029, 2019.
- [88] R. K. Janev. *Atomic and Molecular Processes in Fusion Edge Plasmas*. Plenum Press, New York, 1995.
- [89] J. S. Yoon, M. Y. Song, J. M. Han, S. H. Hwang, W. S. Chang, B. Lee, and Y. Itikawa. Cross sections for electron collisions with hydrogen molecules. *Journal of Physical and Chemical Reference Data*, 37:913, 2008.
- [90] H. K. Chung. Data for Atomic Processes of Neutral Beams in Fusion Plasma, Summary Report of the First Research Coordination Meeting. Technical report, IAEA Nuclear Data Section, 2017.
- [91] P. S. Krstić. Inelastic processes from vibrationally excited states in slow $H^+ + H_2$ and $H + H_2^+$ collisions: Excitations and charge transfer. *Physical Review A - Atomic, Molecular, and Optical Physics*, 66:042717, 2002.
- [92] P. S. Krstić. Vibrationally resolved collisions in cold hydrogen plasma. In *Nuclear Instruments and Methods in Physics Research, Section B: Beam Interactions with Materials and Atoms*, page 58, 2005.

Bibliography

- [93] M. Raghunathan, Y. Marandet, H. Bufferand, G. Ciraolo, P. Ghendrih, P. Tamain, and E. Serre. Generalized Collisional Fluid Theory for Multi-Component, Multi-Temperature Plasma Using The Linearized Boltzmann Collision Operator for Scrape-Off Layer/Edge Applications. *Plasma Physics and Controlled Fusion*, 29:1, 2021.
- [94] A. Poulsen, J. J. Rasmussen, M. Wiesenberger, and V. Naulin. Collisional multispecies drift fluid model. *Phys. Plasmas*, 032305:27, 2020.
- [95] D. Tskhakaya, S. Kuhn, and Y. Tomita. Formulation of boundary conditions for the unmagnetized multi-ion-component plasma sheath. *Contributions to Plasma Physics*, 46:649, 2006.
- [96] D. Galassi, H. Reimerdes, C. Theiler, M. Wensing, H. Bufferand, G. Ciraolo, P. Innocente, Y. Marandet, and P. Tamain. Numerical investigation of optimal divertor gas baffle closure on TCV. *Plasma Physics and Controlled Fusion*, 2020.
- [97] J. Loizu, P. Ricci, F. D. Halpern, S. Jolliet, and A. Masetto. On the electrostatic potential in the scrape-off layer of magnetic confinement devices. *Plasma Physics and Controlled Fusion*, 55:124019, 2013.
- [98] J. L. Terry, R. Maqueda, C. S. Pitcher, S. J. Zweben, B. Labombard, E. S. Marmar, A. Y. Pigarov, and G. Wurden. Visible imaging of turbulence in the SOL of the Alcator C-Mod tokamak. *Journal of Nuclear Materials*, 290-293:757, 2001.
- [99] R. J. Maqueda, G. A. Wurden, S. Zweben, L. Roquemore, H. Kugel, D. Johnson, S. Kaye, S. Sabbagh, and R. Maingi. Edge turbulence measurements in NSTX by gas puff imaging. *Review of Scientific Instruments*, 72:931, 2001.
- [100] S. J. Zweben, D. P. Stotler, J. L. Terry, B. Labombard, M. Greenwald, M. Muterspaugh, C. S. Pitcher, K. Hallatschek, R. J. Maqueda, B. Rogers, J. L. Lowrance, V. J. Mastrocola, and G. F. Renda. Edge turbulence imaging in the Alcator C-Mod tokamak. *Physics of Plasmas*, 9:1981, 2002.
- [101] I. Shesterikov, Y. Xu, M. Berte, P. Dumortier, M. Van Schoor, M. Vergote, B. Schweer, and G. Van Oost. Development of the gas-puff imaging diagnostic in the TEXTOR tokamak. *Review of Scientific Instruments*, 84, 2013.
- [102] S. J. Zweben, B. D. Scott, J. L. Terry, B. LaBombard, J. W. Hughes, and D. P. Stotler. Comparison of scrape-off layer turbulence in Alcator C-Mod with three dimensional gyrofluid computations. *Physics of Plasmas*, 16:082505, 2009.
- [103] F. D. Halpern, J. L. Terry, S. J. Zweben, B. LaBombard, M. Podesta, and P. Ricci. Comparison of 3D flux-driven scrape-off layer turbulence simulations with gas-puff imaging of Alcator C-Mod inner-wall limited discharges. *Plasma Physics and Controlled Fusion*, 57:054005, 2015.

-
- [104] D. Moulton, Y. Marandet, P. Tamain, P. Ghendrih, and R. Futtersack. Density and Temperature Correlations in the SOL; Implications for Gas Puff Imaging of Turbulence. *Contributions to Plasma Physics*, 54:4, 2014.
- [105] H. P. Summers, W. J. Dickson, M. G. O'Mullane, N. R. Badnell, A. D. Whiteford, D. H. Brooks, J. Lang, S. D. Loch, and D. C. Griffin. Ionization state, excited populations and emission of impurities in dynamic finite density plasmas: I. The generalized collisional-radiative model for light elements. *Plasma Physics and Controlled Fusion*, 2006.
- [106] E. De La Cal and the Tj-Ii Team. Visualising the electron density structure of blobs and studying its possible effect on neutral turbulence. *Nuclear Fusion*, 56:106031, 2016.
- [107] D. A. Russell, J. R. Myra, D. A. D'Ippolito, T. L. Munsat, Y. Sechrest, R. J. Maqueda, D. P. Stotler, and S. J. Zweben. Comparison of scrape-off layer turbulence simulations with experiments using a synthetic gas puff imaging diagnostic. *Physics of Plasmas*, 18:022306, 2011.
- [108] D. P. Stotler, B. LaBombard, J. L. Terry, and S. J. Zweben. Neutral transport simulations of gas puff imaging experiments. *Journal of Nuclear Materials*, 313-316:1066, 2003.
- [109] Y. Marandet, A. Mekkoçaoui, D. Reiter, P. Börner, P. Genesio, F. Catoire, J. Rosato, H. Capes, L. Godbert-Mouret, M. Koubiti, and R. Stamm. Transport of neutral particles in turbulent scrape-off layer plasmas. *Nuclear Fusion*, 51:083035, 2011.
- [110] A. Mekkaoui, Y. Marandet, D. Reiter, P. Boerner, P. Genesio, J. Rosato, H. Capes, M. Koubiti, L. Godbert-Mouret, and R. Stamm. A coarse-grained transport model for neutral particles in turbulent plasmas. *Physics of Plasmas*, 19:122310, 2012.
- [111] Y. Marandet, P. Tamain, R. Futtersack, P. Ghendrih, H. Bufferand, P. Genesio, and A. Mekkaoui. Influence of neutral particles on scrape-off layer turbulence with application to the interpretation of fast camera data. *Journal of Nuclear Materials*, 438:S518, 2013.
- [112] D. Wunderlich, M. Giacomini, R. Ritz, and U. Fantz. Yacora on the Web: Online collisional radiative models for plasmas containing H, H₂ or He. *Journal of Quantitative Spectroscopy and Radiative Transfer*, 240:106695, 2020.
- [113] C. Spearman. The Proof and Measurement of Association Between Two Things. *The American Journal of Psychology*, 15:72, 1904.
- [114] J. Franck. Elementary processes of photochemical reactions. *Transactions of the Faraday Society*, 21:536, 1926.
- [115] E. U. Condon. Nuclear motions associated with electron transitions in diatomic molecules. *Physical Review*, 32:858, 1928.

Bibliography

- [116] J. Liu, E. J. Salumbides, U. Hollenstein, Jeroen C. J. K., Kjeld S. E. Eikema, W. Ubachs, and F. Merkt. Determination of the ionization and dissociation energies of the hydrogen molecule. *Journal of Chemical Physics*, 130:174306, 2009.
- [117] V. M. Zhdanov and P. N. Yushmanov. Diffusion and heat transfer in a multicomponent completely ionized plasma. *Journal of Applied Mechanics and Technical Physics*, 1980.

Acknowledgements

Now that my PhD has finally come to an end, it is also the time to look back and think about the journey I made in the last four and a half years. I am glad to see how I grew up and evolved throughout this time, both scientifically and personally, which would not have been possible if I had not been surrounded and inspired by so many meaningful people in my life.

I would like to start by thanking Paolo, my thesis supervisor throughout this whole PhD journey, who has helped me bring my scientific skills to the next level while providing me full support to solve the unexpected problems I faced on my way to get here. Even during the hard times, I always felt that you trusted on me to successfully complete this mission and leave my contribution to the field. In the meanwhile, you were also a good friend who genuinely cared for my well-being, prioritizing the human component over work.

In the beginning of my PhD, I was fortunate to inherit the model created by Christoph, my predecessor, who led me to the discovery of the magic world of neutrals and GBS in general. I want to thank you for your guidance through the early stages of my PhD and for always having been available to answer my questions throughout the last 4 years, going back to what you did a long time ago just to help me, which I am deeply grateful for! I would also like to thank Fabio and Paola for their crucial help with GBS during the first years of my PhD: I learnt a lot from you and I was always glad to see you were always willing to help with a smile. Another person who helped me decisively through this GBS journey was Maurizio, who started a few months after me but soon became an expert into the code and helped me deal with many technical issues throughout my PhD. Thank you for that, for being such a good friend, and for coming with Alessandra to visit me in Lisbon!

I would also like to thank Christian for the useful discussions throughout my PhD and for being in the committee of my candidacy and thesis defense exams, Mirko for helping me to solve technical questions regarding the dynamics of a multi-species plasma, and particularly Kevin, for the long discussions we had and his precious advice that ultimately made it the last chapter of my thesis possible! Thank you all for sharing your knowledge with me, and thank you also to every single person at SPC who in one way or the other helped me overcome the challenges I faced during this PhD!

A very special thanks goes also to Rogério, who besides being a reference as a physicist was also

Acknowledgements

the person who first suggested me the idea of embracing the challenge of doing a PhD at SPC. After that, you and Sandra received me with your arms wide open and somehow became a family for me in Switzerland. Thank you very much for everything we shared! I would also like to thank the other member of this Portuguese family, Eduardo, who has been accompanying me in this journey across Plasma Physics for almost 7 years now and has always been keen to help me out of my scientific struggles. Thank you for your generosity, for being such a good friend and for the long journey we tackled together!

During my PhD I was glad to have the opportunity to share the office with two amazing people who ended up becoming two of my best friends, honouring the oldest historical alliance in Europe! In fact, during the two years we shared an office, Hamish became a sort of older brother to me and inspired me with his attitude towards life, as well as his love for the mighty Marchairuz! On the other hand, Carrie is the paradigm of the fearless adventurer who fights to turn her mountain dreams into reality, which has encouraged me to find a healthy work-life balance and pursue the cycling challenges that make me wonder. At the same time, we have supported each other through our GBS struggles and managed to change the botanic landscape in our office. Thank you, to both of you, also for your terrific British sense of humour, which now runs in my veins!

I would also like to thank the whole SPC community as a whole, for making our laboratory such a pleasant place to work. I would like to thank Laurent for my experience as an assistant to his Numerical Physics course, and also to all my colleagues who did the assistantship together with me, I learnt a lot from that experience! I would also like to thank my PhD colleagues who teamed-up with me during the preparation of the exams for the doctoral courses, I have good memories from those times! Then, I would like to thank many people individually and remember all the stories I lived with each of you, but there are so many nice people to thank... Nevertheless, I will have to say a special word to Pedro, for his contagious passion for science and heart-warming friendship; to Ajay for the cinema sessions and peculiar sens of humour; to Laurie, Ugo and Lorenzo for stimulating my passion for cycling; to Madhu, for helping me with his wise advice and caring attitude towards others; to Simon for the countless adventures we lived together on two wheels across Switzerland and for all we shared together through our beautiful friendship, in SPC or Grischn, in Lavaux or Verbania; to Guillermo and Karen, Arsène and Ashley, for being such compassionate people and inspiring me with your stories; to Mike, for being a chilled, super positive and determined (maybe too much sometimes...) adventure companion; to Mateusz, for your remarkable kindness, wise advice and inspiring passion for sports; to Baptiste, for his example passionate dedication to the scientific progress and his subtle jokes; to Antoine, for his inspiring commitment to environmentalist causes; to Aylwin, for his ever-lasting energy and contagious kindness; to Umar, for being always there when I need a friend even when I failed him; to Claudia, for being so kind and supportive, to the point of coming to watch the world cup final with me and celebrate Portugal's triumph over Italy; to António, for having shared so much with me, so many interesting talks about so many different subjects, and being always there with his friendly shoulder for me; and to all the others, who have made this PhD experience in Lausanne so special and meaningful to me!

I would also like to thank my friends in Switzerland, who made my life so much happier throughout the last four and a half years! I am deeply grateful to Samuel, for being the best friend one could ever wish and having introduced me to so many other spectacular friends from the Portuguese clan; to Raúl, for being such a sensitive and caring friend while sharing memorable moments with me; to Clara, for the mates, alfajores and contagious joy; to Cata, for the endless chats and fabulous friendship; to Ana Rita, for the successful partnership in the "Contacto" game and her generosity; to Ricardo, for his amazing photos and extreme kindness; to Raquel, for her hospitality and funny stories; to Leonardo, for the warm welcome and the patience when explaining molecular biology to me; to Ahmed, for always welcoming me when I invaded his place; to my footbag friends, who welcomed me in the core of their beautiful family and made me feel at home while developing new skills; to Harsh, for his deep insights into life, his understanding and his friendly inspiring advice; to Giada, for unveiling new perspectives and sharing with me new ways of being in harmony with the world.

I want to thank my friends from Portugal who were always present throughout this period, when I visited home or when they came to see me in Lausanne. Although our stories are different, all of them have a privileged place in my mind for the long-lasting friendship and the role they keep playing in my life! I would therefore like to thank particularly to Marco, Luzia, Carlos, Gonçalo, Rodrigo Vicente, Manel, Barão, André Raposo, Cristiano, Simão, André Santos, Rodrigo Farias, and many others, for all the chats and adventures that we kept sharing in these last four and a half years and for being a part of what I am! Special thanks to the whole beach soccer family I have in Portugal (and a bit across Europe), as I am glad to keep you as my close friends after all what we lived together!

It is also the time to look back to the people who played an important role in my academical formation, without who I would never have started a PhD at SPC. There were many agents, but I would like to highlight the role played by Luís, my high school teacher who first stimulated my passion for Physics, Nuno, my professor at university who revealed to me the marvels of controlled nuclear fusion, and Paulo, my Master's Thesis supervisor who taught me everything I knew about scientific research when I first came here. Thank you very much for helping me arrive here today!

Finally, I want to thank my family for always being there for me through this important period of my life! All of you played an important role in my life, and were important in your own way. Still, I will make a special note for my mum, who provided me tireless daily support throughout the whole time, even when her whole life was in a turmoil; my dad for always sharing interesting views and ideas that helped me keep my mind wide open all the time; my sister, with whom I keep a very beautiful relation and keep sharing deeply meaningful moments even though apart from each other; and to my resilient granny, who keeps being the best grandma one could ever desire and the best companion ever to watch and discuss beach soccer!

Lausanne, 9 October 2011

André Calado Coroado

André Calado Coroado

Date of birth: 09.06.1993

Email: andrecoroado@gmail.com



Education and experience

2017-2021: PhD in Plasma Physics, Swiss Plasma Center, École Polytechnique Fédérale de Lausanne (EPFL), Switzerland.

- Theoretical research in plasma physics and controlled fusion, based on numerical simulations carried out on high performance computers
- Teaching assistant for numerical physics
- Supervisor of two master level student projects

2011-2016: MSc in Engineering Physics, Instituto Superior Técnico (IST), Portugal.

- Scientific initiation scholarship (2015-2016), performing research on the resonant interaction between energetic particles and shear Alfvén waves in tokamaks.

PhD thesis

Self-consistent simulation of multi-component plasma turbulence and neutral dynamics in the tokamak boundary, supervised by Prof. Paolo Ricci.

Master thesis

Analytical studies of energetic particles in tokamaks, supervised by Dr. Paulo Rodrigues and Prof. Nuno Loureiro.

Languages

Portuguese (native), English (fluent), Spanish (fluent), French (intermediate), Italian (elementary)

Peer-reviewed publications

A. Coroado and P. Ricci. "Moving toward mass-conserving simulations of plasma turbulence and kinetic neutrals in the tokamak boundary with the GBS code." *Physics of Plasmas* (2021)

A. Coroado and P. Ricci. "A self-consistent multi-component model of plasma turbulence and kinetic neutral dynamics for the simulation of the tokamak boundary." *Submitted to Nuclear Fusion* (2021)

M. Giacomini, P. Ricci, A. Corrado, G. Fourestey, D. Galassi, E. Lanti, D. Mancini. "The GBS code for the self-consistent simulation of plasma turbulence and kinetic neutral dynamics in the tokamak boundary." *Submitted to Computer Physics Communications* (2021)

P. Rodrigues and A. Corrado. "Local up-down asymmetrically shaped equilibrium model for tokamak plasmas." *Nuclear Fusion* (2018)

Conference contributions (as first author)

A. Corrado, P. Ricci, C. Beadle, M. Giacomini, P. Paruta, F. Riva, C. Wersal. "First-principles simulation of plasma fuelling in a tokamak." *Poster presented at the 46th European Physical Society Conference on Plasma Physics. Milan, Italy, 2019.*

A. Corrado, P. Ricci, C. Beadle, P. Paruta, F. Riva, C. Wersal. "Numerical simulations of plasma fuelling in tokamaks using the GBS code." *Poster presented at the Joint Varenna-Lausanne International Workshop 2018. Varenna, Italy, 2018.*

A. Corrado, P. Ricci, C. Beadle, P. Paruta, F. Riva, C. Wersal. "Plasma refuelling at the SOL simulated with the GBS code." *Poster presented at the Joint Annual Meeting of SPS and ÖPG 2017. Geneva, Switzerland, 2017.*

Interests

Exact sciences, environmental science, geography, writing, cycling, beach soccer.